

VNIVERSITAT ID VALÈNCIA



2017

Christoph Tönnis

Tesis doctoral

VNIVERSITAT ID VALÈNCIA

Departament de Física Atòmica Molecular i Nuclear

Institut de Física Corpuscular



DOCTORAT EN FÍSICA

**Indirect search for dark matter in the
Sun and the Galactic Centre with the
ANTARES neutrino telescope**

PhD thesis dissertation by:

Christoph Tönnis

Under the supervision of:

Juan José Hernandez Rey

Juan de Dios Zornoza Gómez

Valencia, February 2017

DEPARTAMENT DE FÍSICA ATÓMICA MOLECULAR I
NUCLEAR
INSTITUTO DE FÍSICA CORPUSCULAR
DOCTORAT EN FÍSICA



VNIVERSITAT DE VALÈNCIA

**Indirect search for dark matter in
the Sun and the Galactic Centre
with the ANTARES neutrino
telescope**

Christoph Tönnis

Under the supervision of:
Juan José Hernandez Rey
Juan de Dios Zornoza Gómez

February 2017

D. JUAN JOSÉ HERNÁNDEZ REY, Profesor de Investigación del Consejo Superior de Investigaciones Científicas en el Instituto de Física Corpuscular i D. JUAN DE DIOS ZORNOZA GOMEZ, Investigador Ramón y Cajal de la Universitat de València en el Instituto de Física Corpuscular,

CERTIFIQUEN:

Que la present memòria, The indirect search for dark matter in the Sun and the Galactic Centre with the ANTARES neutrino telescope, ha sigut realitzada baix la seua direcció en el Institut de Física Corpuscular (Centre Mixt Universitat de València - CSIC) per D. Christoph Tönnis i constitueix la seua Tesi Doctoral en el Departament de Física Atòmica Molecular i Nuclear de la Universitat de València per a optar al grau de Doctor en Física.

I per a que conste, en compliment de la legislació vigent, signem el present Certificat a Paterna, a 6 de Marzo de 2017.

Signat Juan José Hernández Rey

Signat Juan de Dios Zornoza Gomez

Agradicimientos

En primer lugar quiero dar las gracias a todos aquellos a los que inevitablemente me voy a olvidar de agradecer. Si no te menciono en el resto del texto, entonces este párrafo va dirigido a ti.

En segundo lugar quiero dar las gracias a los que sería inexcusable olvidar: A Juan José Hernández Rey, Juan de Dios Zornoza Gomez y Juan Roman Zuñiga, que me han ayudado con sus comentarios, sus correcciones y su experiencia a la hora de realizar esta tesis, y a vencer la burocracia en todas sus formas.

A Javier Barrios Martí y Agustín Sánchez Losa, que me han ayudado mucho con mi análisis y que fueron compañeros maravillosos . . . aunque he escuchado muchas bromas de Agustín sobre lo absurdo de ser alemán.

Note of thanks

I also want to thank Guillaume Lambard, whose work formed a part of the basis of my own.

Danksagung

Zuletzt möchte ich meiner Familie danken, die mir jederzeit mit moralischer Unterstützung und Ermutigungen zur Seite gestanden hat, allen voran meinen Eltern Monika und Ferdinand.

Contents

1	Introduction	1
2	The ANTARES neutrino telescope	5
2.1	Detection principle	7
2.2	Visibility	9
2.3	Technical description	10
2.3.1	The Detector Line	10
2.3.2	The Optical Module	11
2.3.3	Data Acquisition System	12
2.3.4	Charge measurement	15
2.4	Optical properties of the medium	18
2.5	Backgrounds and background rejection	20
2.6	Triggers	21
3	Time calibration with LED optical beacons in ANTARES	25
3.1	ANTARES clock system	28
3.2	On shore calibration	29
3.3	Optical Beacons	30
3.4	Calibration with LED Optical Beacons	31
3.4.1	Early photon effect	32
3.4.2	Walk effect	32
3.4.3	DNL effect	33
3.4.4	Token ring effect	33
3.5	Calibration procedure	35
3.5.1	Manual revision	35
3.5.2	Calibrations from 2013 to 2015	37
4	Dark matter theory and phenomenology	41
4.1	Evidence for the existence of dark matter	41
4.1.1	The Cosmic Microwave Background	42
4.1.2	Structure hierarchy and Simulations	45

Contents

4.1.3	Gravitational lensing	47
4.1.4	The Bullet Cluster	48
4.1.5	The relative abundance of dark matter	49
4.2	Dark matter searches	49
4.2.1	Dark matter candidates	51
4.2.2	Types of dark matter searches	52
4.2.3	Direct detection	53
4.2.4	Accelerator bounds	54
4.2.5	Indirect detection	56
4.3	Searches using neutrinos	58
4.3.1	Searches towards the Sun	60
4.4	Dark matter cosmology and halo profiles	61
4.4.1	Relic density of WIMPs	61
4.4.2	WIMP capture in celestial objects	62
4.4.3	Halo profiles and the J-Factor	64
4.4.4	Halo profile parameters and the CLUMPY program	66
4.4.5	Signal neutrino spectra	68
4.4.6	Neutrino Oscillations	71
4.5	Supersymmetry	72
4.5.1	Superspace	73
4.5.2	The Algebra of Supersymmetry	74
4.5.3	Minimal supersymmetric extension of the Standard Model	75
4.5.4	Neutralinos	76
4.5.5	Supersymmetry breaking	78
5	Data reconstruction and detector simulation	79
5.1	Data reconstruction algorithms	79
5.2	Data selection	83
5.3	The Monte Carlo Simulation	85
5.3.1	Atmospheric muons	87
5.3.2	Atmospheric neutrinos	88
5.3.3	Detector response and light propagation	89
5.3.4	Statistical weights	90
5.4	Comparison to Data	92
5.4.1	AAFit	92
5.4.2	BBFit	93
5.5	The Acceptance	98
5.5.1	Implementation	101
6	The Analysis Method	103
6.1	Pseudo-experiments	104

6.2	The likelihood function	106
6.2.1	Extended likelihood function	107
6.2.2	Additional information	109
6.2.3	Ingredient production	110
6.2.4	Angular resolution	113
6.2.5	Reconstruction cuts	115
6.3	Sensitivity determination	117
6.3.1	The Test Statistic distribution	119
6.4	Moving sources	122
6.5	Extended sources	125
6.6	Unblinding procedure	128
7	Results of the search for dark matter annihilations in the Sun	131
7.1	Unblinding results	131
7.2	Optimum cuts	133
7.3	Initial sensitivities	135
7.4	Acceptance	136
7.5	Neutrino Flux	137
7.6	Systematics	138
7.7	Cross-Section	139
7.7.1	Comparison to the binned analysis	140
7.7.2	Comparison to other experiments	141
8	Results of the search for dark matter annihilations in the Galactic Centre	145
8.1	Unblinding results	146
8.2	Optimum cuts	147
8.3	Initial limits	149
8.4	Acceptance	150
8.5	Neutrino Flux	151
8.6	Systematics	152
8.7	Cross-Section	152
8.8	Comparison between halo models	153
8.9	Comparison to the binned analysis	155
8.10	Comparison to other experiments	155
9	Conclusion	159
9.1	Calibration	159
9.2	Search towards the Sun	159
9.3	Search towards the Galactic Centre	160

Contents

Appendix	161
1 Comparisons to simulation	161
2 Tables	165
3 List of Acronyms	168
3.1 Cosmology and Astrophysics	168
3.2 Dark matter	168
3.3 ANTARES	168
3.4 Statistics and Analysis	168
Resumen	169
1 El detector ANTARES	169
2 Datos y simulacion	171
3 Calibración temporal	173
4 Materia oscura	175
5 Método de análisis	178
6 Resultados	179

Chapter 1

Introduction

The main aim of this thesis is to search neutrino signals from annihilations of dark matter in the two most promising sources: the Sun and the Galactic Centre.

The search for dark matter is one of the mayor endeavours of contemporary physics and is approached with multiple complementary experimental techniques. Dark matter makes up around a quarter of the total energy content of the Universe and it has a very relevant effect on the formation of structures in the early Universe, the motion of stars in galaxies and other phenomena in cosmology and astrophysics. Through these phenomena the existence of dark matter is established. However, its exact properties, like the mass of the particles that compose it and their type, can not be extrapolated from these observations. Therefore, further searches are conducted to discover its nature. Chapter 4 contains a more detailed overview of the evidence concluding the existence of dark matter and its known properties. Also, the dark matter phenomenology that is relevant for the analyses conducted in this thesis and other types of searches, like direct searches, are introduced.

The searches conducted in this thesis are indirect searches using neutrinos that are produced by annihilations of dark matter in celestial objects, like the Sun and the Milky Way. This type of search is susceptible to different systematics than direct searches. Firstly the source extension affects the analysis. Thereby, the distribution of dark matter in the source has an important systematic effect on the analysis. Secondly, indirect searches look for signals from annihilations or decays and therefore their spectra have to be taken into account.

For this search the ANTARES neutrino telescope was used. ANTARES, installed on the ocean floor near Toulon, in southern France, is currently the largest neutrino telescope in the northern hemisphere. Neutrino telescopes consist of 3D arrays of photomultipliers that detect the Cherenkov light

induced by the particles produced by these neutrinos. From the position and time at which the photons are detected the spatial shape of the track or shower can then be reconstructed.

Due to the small cross sections of the neutrino interactions with matter, neutrino telescopes have to be very large. The ANTARES detector array has a floor area of around $180 \text{ m} \times 180 \text{ m}$ and uses 480 m long cable lines equipped with detector modules distributed on storeys. More details on the operating principle of neutrino telescopes and the technical details of ANTARES are given in Chapter 2.

The time calibration of ANTARES using so called Optical Beacons is part of this thesis as well. Each storey of ANTARES has six clocks, which are part of the data acquisition system. These clocks have to be calibrated to ensure a good angular resolution and reconstruction quality for the detector. With a timing accuracy of one nanoseconds an angular resolution of better than 0.3° can be achieved for neutrinos with an energy above 10 TeV. This can be done with multiple different methods, but the main one is the calibration with optical beacons. The optical beacons of ANTARES are cylindrical glass structures with multiple LEDs and electronic boards on the inside that are installed in a few selected storeys on each line. When flashed they illuminate the storeys above. The time differences between the flashing of the optical beacons and the photon hits in the optical modules from these flashes can be used to synchronise the clocks in the storeys. The technical details of the optical beacon system and the time calibration are elaborated in Chapter 3.

A likelihood-based method to construct limits and sensitivities is used. This analysis method uses a likelihood function to identify signals in datasets. The behaviour of the likelihood function is studied using simulated datasets, which are called pseudo-experiments. A detailed overview of the analysis is shown in Chapter 6. The analyses conducted for this thesis use multiple sets of data recorded with ANTARES and sets of data from Monte-Carlo simulations. This simulation and the sets of recorded and simulated data are further detailed in Chapter 5.

From this study the sensitivity of the analysis is calculated. After the analysis was applied to the recorded data, no signal was found and limits on models for dark matter were set.

For the search for dark matter annihilations in the Sun, limits on the spin-dependent and spin-independent annihilation cross-section are set. These limits are presented in Chapter 7. They are calculated by assuming an equilibrium between annihilation and capture of dark matter in the Sun. Furthermore, comparisons to the results of other experiments and to the results of previous analyses using ANTARES are also shown.

Finally, for the search in the Milky Way, limits on the thermally aver-

aged annihilation cross-section are set and presented in Chapter 8. The results are, as for the Sun, compared to other other types of dark matter experiments and to previous analyses using ANTARES.

Chapter 2

The ANTARES neutrino telescope

ANTARES (**A**stronomy with a **N**eutrino **T**elescope in **A**byss environment **R**ESearch) [1] is an underwater neutrino detector. Located 40 km off the shore of southern France at the bottom of the Mediterranean Sea at $42^{\circ}48'$ North $6^{\circ}10'$ East (see Fig. 2.2). ANTARES is anchored to the sea floor at 2475 m under the surface of the sea and extends up to a depth of 2025 m. A schematic of the detector can be seen in Fig. 2.1.

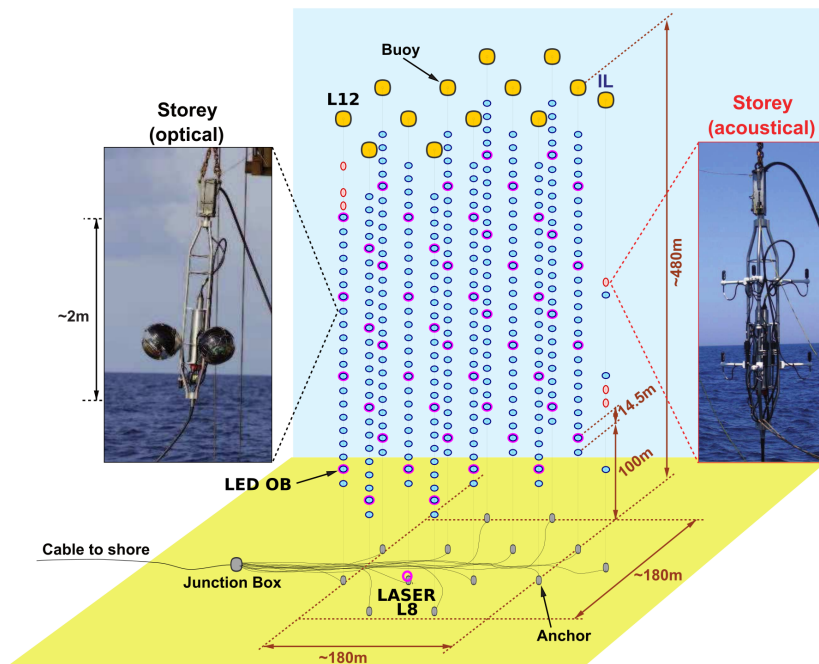


Figure 2.1: A schematic drawing of the ANTARES detector.

The detector consists of 12 detection lines with 25 storeys per line and

3 optical modules (OMs see section 2.3.2) per storey. Each OM has a 10'' photomultiplier and is inclined at 45° to the ground for the detection of upward-going muon tracks. The total number of PMTs is then 885 taking into account that in line 12 there are only 20 storeys. The detection lines are 450 m long with a difference of 12.5 m between storeys and 60-75 m apart horizontally. The detection lines are flexible and are held up by buoys at their top. For more details on the detector lines see section 2.3.

The light signals detected by the OMs (hits) are processed by a data acquisition system, which will be described in detail in section 2.3.3. The recorded hits are transmitted from a so-called Local Control Module (LCM) inside the storeys through the line and their anchors at the sea floor to the junction box. The junction box connects the detector to the observation station in La Seyne-sur-mer via an electro-optical cable. Not only the information of the hits is transmitted through this cable but also the high voltage is supplied to the detector through this cable and the junction box.

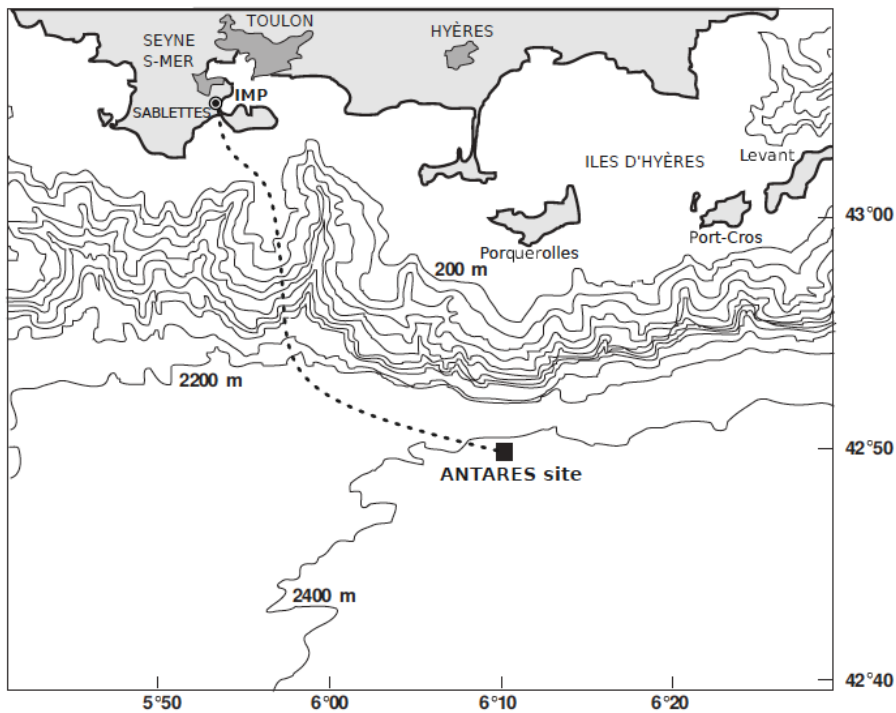


Figure 2.2: A map showing the position of the ANTARES detector.

The main backgrounds for a neutrino telescope are light from the environment (bioluminescence), which is very low at the depth of the

detector, and atmospheric muons. The light from the environment and the atmospheric muon background will be discussed in sections 2.1 and 2.5.

2.1 Detection principle

Neutrinos interact with only two of the fundamental forces: gravity and the weak force. Because of their very low mass it is practically impossible to detect them via gravity. This leaves only the detection of neutrinos using the weak force. Neutrinos are then not directly detected but rather via particles produced from neutrinos via the weak force. The earliest example of this form of neutrino detection is the detection of neutrinos via neutrino capture in chlorine atoms [2]. Another type of detector looks for leptons produced by neutrinos (typically using a water Cherenkov detector) when they interact with atoms. ANTARES is such a detector.

Due to the small cross-sections for weak interactions with neutrinos any neutrino detector needs to have an extremely large volume, especially for high neutrino energies (>100 GeV). For neutrino telescopes this is achieved by a larger spacing of the detector modules. Since the detector medium (i.e. sea water) does not have a very large opacity there is not a large loss of Cherenkov light through absorption and scattering even at a distance of several meters. The properties of the sea water is discussed in further detail in section 2.4.

Not all leptons detected in the detector volume are produced by neutrinos. This is a especially large problem in the case of muons, since there is a substantial amount of atmospheric muons (muons produced from interactions between cosmic rays and higher layers of the atmosphere) coming from above. Even though the water over the detector acts as a shield against atmospheric muons, there are still a large quantity of muons reaching the detector. The most effective way to reduce this background is to use the Earth effectively as a shield against muons by only looking for muons travelling upwards through the detector (upgoing muons).

Muons have a large movement range with typical track lengths of several hundreds of meters at high energies ($E > 10$ GeV). Muons produced outside the detector volume can therefore still be detected, as long as the muon reaches the detector. This increases the effective size of the detector by more than an order of magnitude. Since these muons move at almost the speed of light they will be faster than the light they emit. As a result the muon will induce Cherenkov light. Cherenkov light is emitted in a cone, which has an opening angle that depends on the optical density of the medium (e.g. sea water). The Cherenkov light of the muons covers

2.1 Detection principle

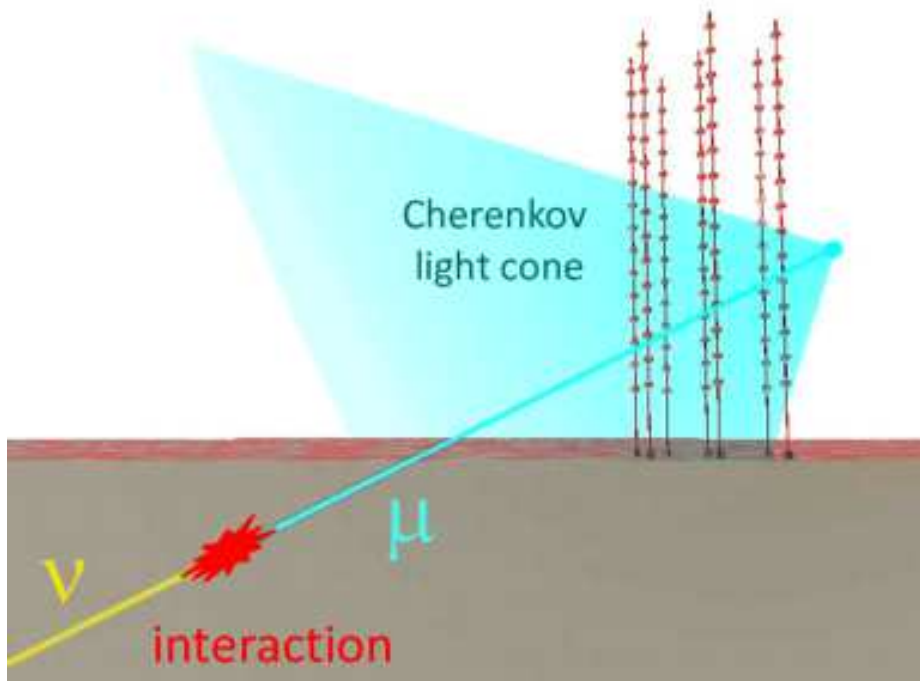


Figure 2.3: Illustration of the detection principle of neutrino telescopes [1].

the range of visible blue light and a part of this spectrum can be detected by the PMTs. In ANTARES the Cherenkov light emitted by these muons is measured with its array of OMs. In Fig. 2.3 there is an illustration of this mechanism. The only lepton that would lead to a notable track of Cherenkov light in sea water is the muon, but it is also possible to detect other signatures from other lepton flavours.

Electrons will produce an electromagnetic shower of a few meters in size. Most showers are smaller than the distance between two storeys and can not be detected with ANTARES. Additionally the medium free path length is very short, so that only neutrinos, that produce the electron inside the detector volume can be detected. The larger showers appear as spherical distributions of hits in the detector. The reconstruction of the direction of the primary particle is extremely difficult. Since the sensitivity of ANTARES to showers is very low they have not been included in the analyses in this thesis.

Tau leptons are very unstable and will almost immediately decay into an electron or muon. Before the decay the tauon will produce an electromagnetic shower like that expected from an electron. If the time resolution of

the detector is sufficiently good it is possible to separate the shower of the tau lepton and the subsequently produced electron as a so-called "double bang". This however is not possible with a small detector. For the same reason the electrons are not used the tau leptons are not used either.

2.2 Visibility

The detection of muon neutrinos, as described in the previous section, requires that the incoming neutrino direction be below the horizon to be observable, i.e. only upgoing events can be used. This has implications on the visibility of any source on the celestial sky (the sky parametrised in celestial coordinates). The maximum declination at which sources can be observed is dependent on the latitude of the detector, which is $42^{\circ}48'$ North for ANTARES. Within this range, each point in the sky has a visibility, defined as the percentage of live time that it can be observed. The ANTARES visibility map is shown in Fig. 2.4. At any given moment more than 50% of the celestial sky can be seen. This is not the case for detectors at extreme latitudes, like IceCube, which at any moment can see exactly half of the sky.

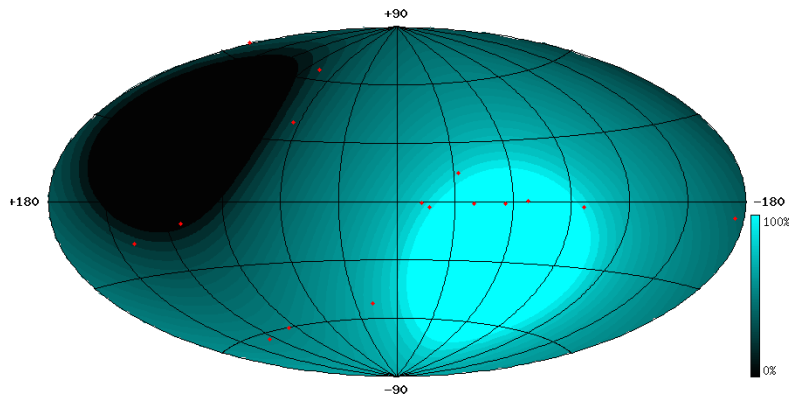


Figure 2.4: The visibility of the various places to ANTARES on the celestial sky .

The two most relevant objects in the sky for this thesis are the Sun and the Galactic Centre. The Galactic Centre is located at a declination of -29.01° with a visibility of about 75%. In local coordinates the Galactic Centre can be seen a significant fraction of time close to the horizon, where the background of misreconstructed atmospheric muons is high. The Sun moves in declination, with the highest declination at the summer solstice and the lowest at the winter solstice. The declination range covered by

2.3 Technical description

the Sun over a year is 23.45° to -23.45° .

Aside of the visibility further factors have also been considered, such as the non continuous live time of the detector and the varying detector efficiency, due to the temporary loss of lines and the incomplete deployment during the first years, have to be taken into account as well.

2.3 Technical description

The 12 lines of ANTARES are anchored to the sea floor by means of the so-called bottom string sockets (BSS) that consist of a 1.5 t iron weight. Inside the BSS the string power module supplies power to the line. There is also an acoustic transponder, which is part of the system used to measure the position of the lines [3], which changes over time since the lines are flexible and float in the sea current and the String Control Module that connects the JB to the electronics of the storeys on the string. The BSS connects the line to the JB via optical cables with two fibres for the clock signal, two for the data and two wires for the power supply. Additionally, the BSS contains a hydrophone for positioning purposes as well as a pressure sensor and a sound tachometer. The BSS has a mechanism to remotely release the line, so that it can be reeled in on the sea surface. The BSS in line 7 and 8 are also equipped with laser optical beacons used for time calibrations.

The JB is connected to the on-shore station by the main electro-optical cable (MEOC). The MEOC is 42 km long, 58mm thick and consists of 48 monomode optical fibres made from pure silicate.

2.3.1 The Detector Line

The detector lines themselves consist of electro-optical cables similar to the MEOC. Each line contains 25 storeys, one every 14.5 m starting 100 m above the BSS on each line in order to avoid biofouling [4] and accumulation of mud from the seabed by the sea current. The lines have a core consisting of copper and optic cables that connect the storeys with each other and with the BSS and are part of the power supply, the data transfer system and the surveillance system (slow control) of the detector. The cable of the line is covered by three layers of protective materials: polyethylene, aramid and polyurethane. These layers stabilise the line and insulate its core against the sea water. The topmost 3 storeys in line 12 are equipped with hydrophones for the AMADEUS project (acoustic detection of neutrinos [5]) and one contains the YODA device, which measures the oxygen concentration in sea water. All these storey parts are shown in Fig. 2.5.

There is also an additional 13th line, the so-called instrumentation line (IL) [6]. The storeys of this line measure the sea current with two acoustic doppler current profilers and the salinity, conductivity and speed of sound of the sea water. It also contains two infrared cameras, which are triggered by nearby PMTs to measure the level of bioluminescence. Three storeys on the IL are also equipped with hydrophones of the AMADEUS project.

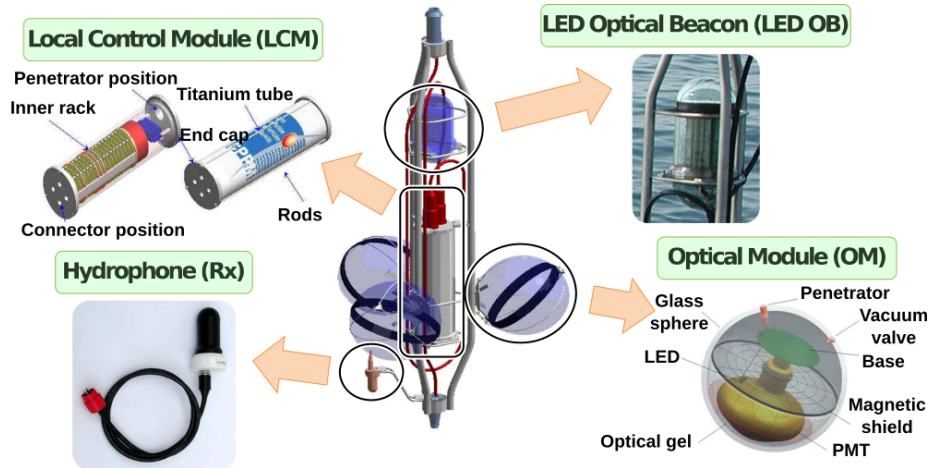


Figure 2.5: A schematic of the storeys and their (optional) parts.

2.3.2 The Optical Module

A regular storey is 2 m high and has a supporting frame made of titanium. There are three 17-inch borosilicate spheres that contain the three 10-inch PMTs, that detect the Cherenkov light of the bypassing muons. These sets of pressure-resistant spheres are called optical modules (OMs) [7]. The borosilicate of the OMs is 1.5 cm thick, leaving an inner diameter of the OM of 41.7 cm. The sphere can withstand a pressure of 260 atm at normal operation and a maximum pressure of 700 atm. The transparency to photons above 350 nm is greater than 95% and the refraction index is 1.47 for 300-600nm light signals. The sphere consists of two halves that are joined by a watertight tape and the surrounding pressure. Opposite to the window for the PMT there is a penetrator to connect the OM to the rest of the electronics. The hemisphere where the penetrator is blackened in order to avoid light detection from aback.

Behind the window there is a μ -metal grid to reduce the effect of the Earth's magnetic field on the PMT. The PMT is glued to the window by an optical gel. Attached to the side of the PMT there is a LED for calibration purposes and onto the inside of the blackened part of the glass

2.3 Technical description

sphere there is a manometer to check the pressure inside the OM.

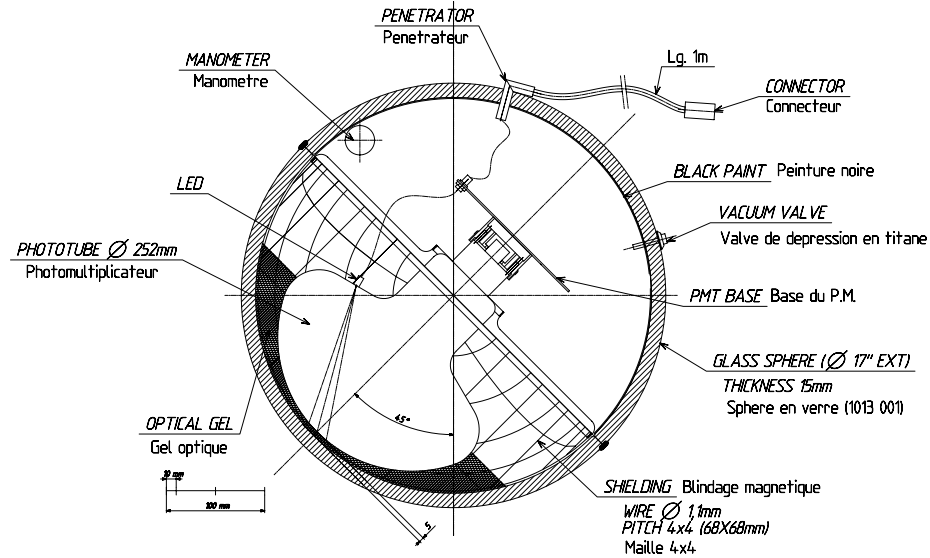


Figure 2.6: A schematic of the optical modules used in ANTARES.

The PMT model selected is the Hamamatsu R7081-20 [8]. This model has an operating voltage below 2 kV with a gain of $5 \cdot 10^7$, a spectral response between 300 and 650 nm with a peak in response at 420 nm and a one photoelectron peak-to-valley ratio higher than two. The Transit Time Spread (TTS) of the PMTs is below 3 ns (FWHM) and the dark noise rate is below 1 kHz for a 0.25 photoelectron threshold.

2.3.3 Data Acquisition System

The Data Acquisition and control System [9] used by ANTARES consists of a multitude of parts distributed over the detector. The first part of this system is the so-called Local Control Module (LCM), which is housed inside a titanium cylinder in the centre of the supporting frame of each storey. The LCM contains the basic electronics for the data readout, most importantly the Analogue Ring Sampler mainboards (ARS-MB). The storeys of ANTARES are grouped together into five sets of five storeys per line. The LCM of one storey per group is responsible for passing the recorded data from the storeys to the JB and further to the onshore station. These LCMs are called Master Local Control Modules or MLCMs. Every OM is connected to one MB and to the two ARS on each MB. Storeys with LED beacons contain another ARS to control it.

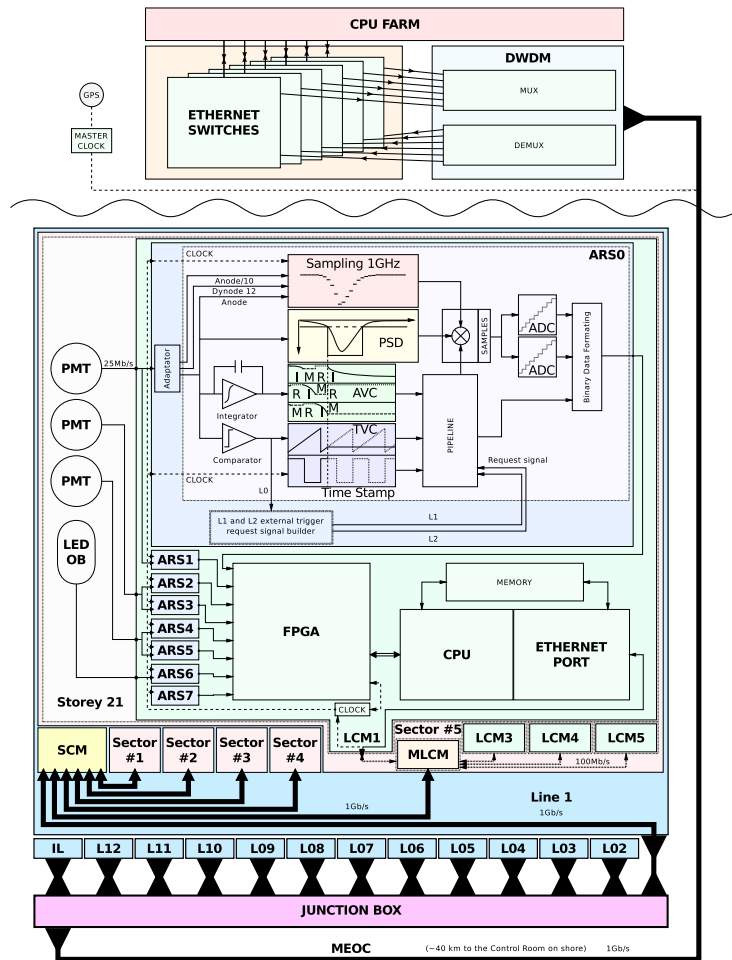


Figure 2.7: A schematic of the Data Acquisition System used in ANTARES [9].

The ARSs are $0.8 \mu\text{m}$ complementary (e.g. operating in pairs) metal oxide semiconductor chips that contain around 68000 transistors. The ARS is responsible for integrating the signal output of the PMTs and recording the time of an incident hit. The integration of a hit is started as soon as one pair of signal hits above a predefined threshold is registered (L0 hits, see section 2.6). An image of an ARS can be seen in Fig. 2.9.

For timing purposes ANTARES uses a 20 MHz clock signal distributed from the shore to the ARS. The ARS assigns a 25 ns time stamp to any recorded hit using the rising and the falling edge of the clock signal. In the ideal case the clock signal coincides with the raising flank of the PMT signal, but this is almost never the case. A time to voltage converter (TVC)

2.3 Technical description

inside the ARS can then give a more accurate additional measurement of the time of the incoming signals with an accuracy of 0.2 ns. The overall timing uncertainty is dominated by the 3 ns TTS. Inside the TVC there is an Analog to Digital Converter (ADC) that measures a ramp signal generated in the ARS in synchronisation with the clock signal. The ADC has a 8-bit output and therefore can give a timing information 256th of the clock period of 50 ns. The TVC value translates into time via the equation

$$t = 50\text{ns} \frac{\text{TVC} - \text{TVC}_{\min}}{\text{TVC}_{\max} - \text{TVC}_{\min}}. \quad (2.1)$$

where TVC_{\max} and TVC_{\min} are the maximum and the minimum of the range of the TVC. These values are not the 0th and 255th bin of the TVC though, since not all of the 256 bins of the TVC are available. Typically the ramp generator signal is digitised in a range of around 200 of the ADC bins. The actual range has to be measured individually for every TVC. This is done by feeding random time signals into the TVC with a flat distribution. From the range of the digitised values the range can then be read out. Due to the stability of the TVC this process does not have to be repeated after deployment.

After a time measurement is made the ramp shape has to be recovered, which leads to a dead time. For more information on this see Section 3.4. The TVC system is also shown in Fig. 2.8.

At the same time another part of the ARS starts integrating the signal received from the PMT over a duration of 35 ns. This integration process is illustrated in Fig. 2.10. The sampling frequency of this signal integration can be adjusted between 150 MHz and 1 GHz. The ARS can distinguish between a signal from a single photon and a signal from multiple photons, by analysing the wave form. In both cases the ARS provides the charge of the hit from the signal integration in the form of an analog signal. For multiple photons a waveform mode can be used with the ARS, which samples the waveform around 128 times every 0.6 ns. This massive amount of information can be used to calibrate the charge measurement of the ARS. Using the wave form mode would be impractical for physics analysis due to the large amount of data collected. Therefore only single photo electron data are used for physics runs.

An ADC then converts the signals from the TVC, the time stamp and the charge integration signal to a digital signal that is fed into a 16-bit binary shift register for temporary storage. The shift register can hold either 16 single photo electron signals or 4 waveform signals at a time.

All data is concentrated in the MLCM by Ethernet boards with a transmission speed of 100 Mb per second. The informations are then fed

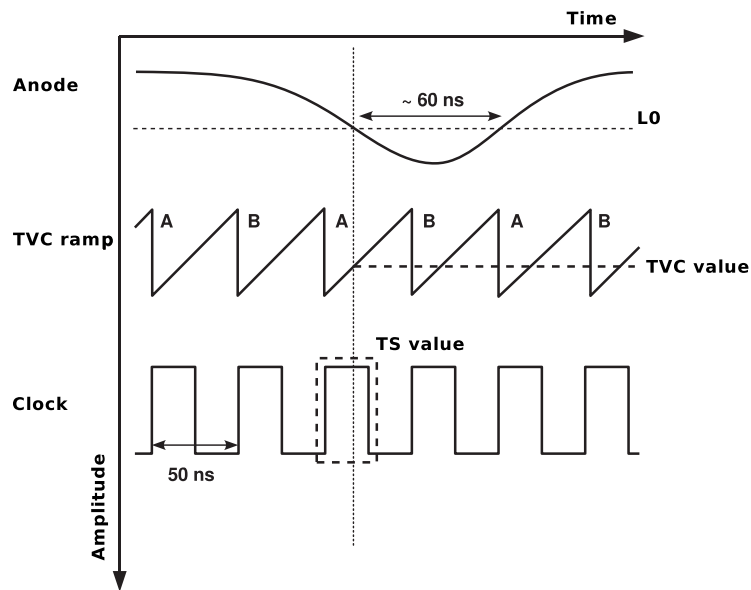


Figure 2.8: A schematic of the time measurement using the TVC. A TVC ramp is generated in synchronicity with the clock signal to allow a more fine determination of the time within a clock cycle.

into a dense wavelength division multiplexing system (DWDM), which transmits the hit informations to the BSS of the line. The DWDM system allows for the simultaneous communication with all lines by using different wavelengths for each line. The BBS are connected to the JB via optical fibres, which are routed together in the JB and continue from there to the shore station in La Seyne.

The data streams to the shore station are divided into frames of 104 ms. In the shore station the data stream is demultiplexed and distributed amongst multiple computers for further processing using 60 Gb Ethernet switches. The data are stored in ROOT files and transferred to the HPSS storage in the Centre de Calcul of IN2P3 in Lyon. The reconstruction of detected events is done using the SeaTray framework, an adapted version of the IceTray ?? software. The files with the reconstructed events are stored in an internal format of ANTARES called AntDST.

2.3.4 Charge measurement

In parallel to the measurement of the incident time of light signals in a PMT the intensity of the signals is recorded as well. This is done by the

2.3 Technical description

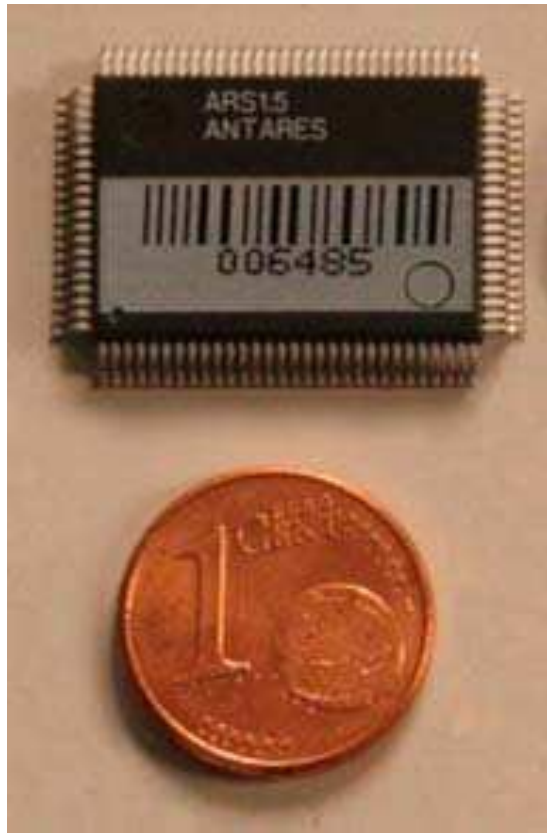


Figure 2.9: An image of one of the ARS.

ARS, which integrates the voltage signal from the PMTs as mentioned in the previous section. With a gain of around $5 \cdot 10^{17}$ a single primary photo-electron will yield a 45 mV signal at a 50Ω internal resistance.

The integration follows three steps: Integration (the analog integration with two capacitors), memorisation (keeping the analogous signal constant for digitisation) and reset. All phases have an adjustable total length between 8 and 30 ns. If the L0 condition is fulfilled (Section 2.6) the integration length can be extended even longer (up to 50 ns). This is done in order to capture the signal pulse shape. The whole process is illustrated in Fig. 2.10.

The integrated analog signal is digitised with an 8-bit ADC, which will be referred to as the Analog to Voltage Converter (AVC). As in the measurement of the incident time of a hit with the ramp generator (see Eq. 2.1) the integrated charge is calculated with the equation

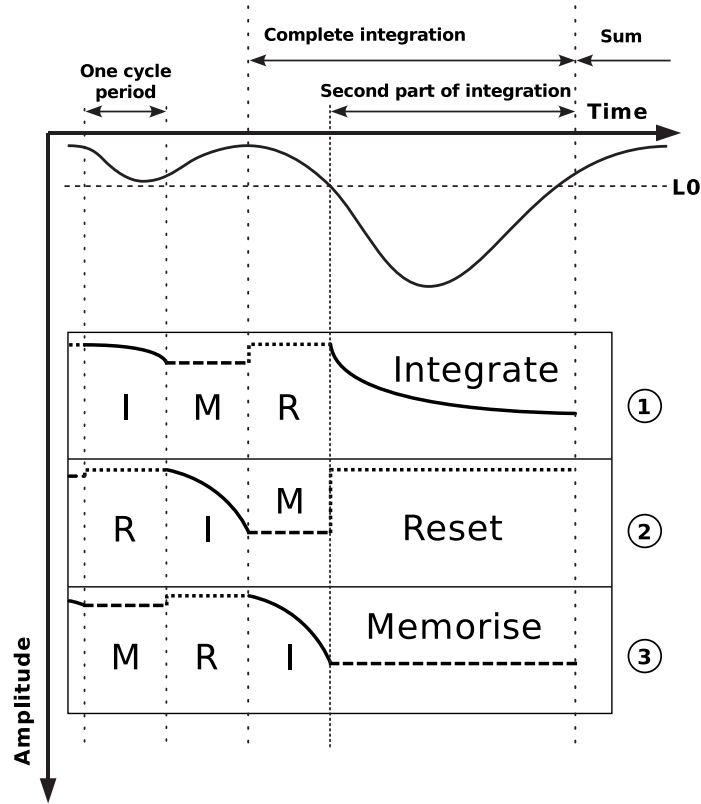


Figure 2.10: A schematic of the integration process in the ARS. Three capacitors go simultaneously through the different steps of the integration process. Upon fulfilling the L0 condition one of the capacitors will integrate the PMT signal.

$$q = \frac{AVC - AVC_{min}}{AVC_{max} - AVC_{min}}. \quad (2.2)$$

where AVC_{max} and AVC_{min} are the AVC peak for a single photo-electron and the AVC baseline respectively. Similarly to the measurement with the TVC, AVC_{max} and AVC_{min} have to be calibrated. AVC_{min} can be calibrated by measuring the AVC value at random times and AVC_{max} is measured using bioluminescence and ^{40}K decays. Due to biofouling the measured AVC_{max} degrades over time, which makes a tuning of the voltage supply of the PMT necessary in order to counteract this effect.

Before being stored, the AVC values are corrected for an effect called "cross-talk" between the AVC and the TVC. The TVC ramp generator influences the AVC output: the higher the voltage of the TVC is the

2.4 Optical properties of the medium

higher the AVC response typically becomes. To correct that the AVC value is lowered by

$$AVC_{corr} = AVC - S \cdot (TVC - TVC_{mean}). \quad (2.3)$$

where S is the Slope of the influence of the TVC on the AVC (i.e. $\frac{AVC}{TVC}$). TVC_{mean} is defined as $\frac{TVC_{max} - TVC_{min}}{2}$. Including this correction the relative error on the charge measurement with the AVC is estimated to be less than 10%.

2.4 Optical properties of the medium

For a proper understanding of the ANTARES operation it is crucial to know the properties of the medium used inside the detector [10]. Most importantly the scattering and absorption of Cherenkov light in sea water has to be known.

In order to quantify the effect of scattering and absorption in water the parameters $\lambda_{scatt}^{e,H}$ and λ_{abs} are defined. $\lambda_{scatt}^{e,H}$ is the effective scattering length. It is related to the normal scattering length, λ_{scatt} , through the average cosine of the scattering angular distribution $\langle \cos(\theta) \rangle$:

$$\lambda_{scatt}^{e,H} = \frac{\lambda_{scatt}}{1 - \langle \cos(\theta) \rangle}. \quad (2.4)$$

The absorption length and the effective scattering length can be combined into one parameter, the attenuation length λ_{att} . It can be expressed by:

$$\frac{1}{\lambda_{att}} = \frac{1}{\lambda_{scatt}^e} + \frac{1}{\lambda_{abs}}. \quad (2.5)$$

where λ_{abs} is the absorption length. These parameters were measured first prior to the deployment of ANTARES using an autonomous line equipped with a 1-inch diameter PMT [11, 12, 13]. This PMT was used to detect ultraviolet and blue light emitted by pulsed isotropic light sources placed at different distances. Furthermore, a prototype line [14] was installed in the ANTARES site before the main detector was deployed.

Once ANTARES was deployed the optical beacons that are also used for time calibrations (see section 3.3) were used to estimate the absorption and scattering length [15]. Finally, reconstructed muon tracks were also used to estimate these parameters. The results are shown in Table 2.1.

The impact of the uncertainty in these parameters is in general moderate. The most relevant parameter is the absorption length that can induce an error on the effective area from 5% at the highest energies (10^{6-7} GeV) to

2.4 Optical properties of the medium

Method	Wavelength	λ_{abs}	λ_{scatt}^e
Autonomous line	473 nm	60 m	265 m
Autonomous line	375 nm	26 m	122 m
Muon tracks	350 - 500 nm	55 m	200m

Table 2.1: The absorption length and effective scattering length measured in [11, 15]

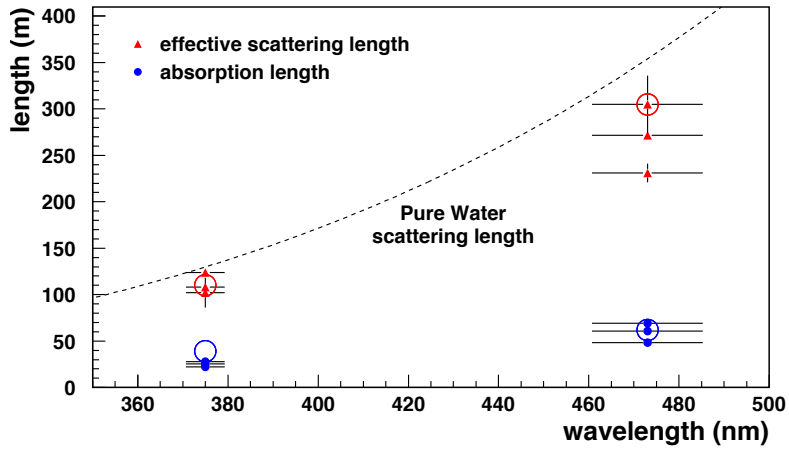


Figure 2.11: The scattering length for typical Cherenkov light measured at the ANTARES site in [11].

15% at the lowest ($\sim 10^2$ GeV). The effective scattering length influences mainly the angular resolution with an induced uncertainty of the order of $0.05^\circ - 0.1^\circ$.

A second property of the sea water that is very important to know for operating an undersea neutrino telescope is the group velocity of light in water v_g . This property is defined as the velocity of wave packets inside a medium, in this case sea water. It can be expressed as:

$$v_g = \frac{c}{n_g} - \frac{c \cdot k}{n_g^2} \frac{dn_g}{d\omega}. \quad (2.6)$$

In the above equation k is the wave number, n_g is the group refraction index and ω is the frequency of the wave packet. The group velocity of water is very important for the purpose of time calibration, where the expected time delays of calibration signals depend on this velocity, and

2.5 Backgrounds and background rejection

for the reconstruction of muon events, since the opening angle of the Cherenkov cone depends on the group velocity.

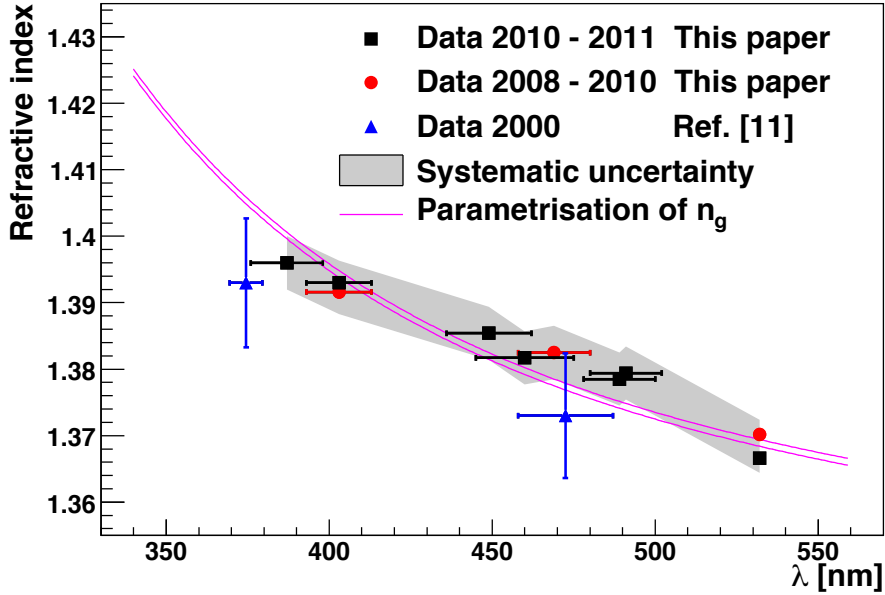


Figure 2.12: The group refraction index as measured in [12].

Using the optical beacon system an estimate of the group refractive index as a function of wavelength was performed [12]. The results, which are shown in Fig. 2.8 are in good agreement with a previous parametrisation depending on the temperature, salinity and pressure of the water in the ANTARES site (red lines in Fig. 2.12).

2.5 Backgrounds and background rejection

There are different types of background for the ANTARES neutrino telescope: Bioluminescence, photons from ^{40}K and other light from the environment, atmospheric muons and atmospheric neutrinos. This light can trigger the PMTs to emit a signal and in some very rare cases bioluminescence can look like an event with a small number of hits. Whilst the location of ANTARES reduces most environmental light, like sunlight or the lights of human settlement bioluminescence can not be avoided.

Bioluminescence is the light that is produced by microorganisms living in the sea water around the detector. It can be seen in the rate of detected

photon hits, which is persistently above what is expected for background radiation only. Hits produced by bioluminescence can interfere with the reconstruction of particle events since they can be falsely selected for the reconstruction. It is also possible that one of the hardware triggers is falsely set by bioluminescence, which increases the rate of data taking. Bioluminescence is a seasonal phenomenon and reaches its maximum during spring, where in some years the ANTARES detector had to be put into the reduced high voltage mode temporarily, in order to prevent damage of the PMTs due to the high amount of light hitting them. It also correlates to sea water temperature levels and sea current speeds making it sometimes necessary to change the data taking setup.

Atmospheric muons are produced in decays of mesons (e.g. pions) that themselves are products of cosmic rays interacting with higher layers of the atmosphere. Since these muons do not come from cosmic neutrinos they are a form of background. The most effective way of suppressing atmospheric muons is to exclude downgoing events. Since the mean free path length in solid material and the lifetime of muons is limited it is almost impossible for muons to pass through the Earth's mantle. This means that the Earth can be used as a shield against atmospheric muons by using an elevation cut on the events, which are considered for an analysis, as can be seen in Fig. 2.13. In the Figure the number of simulated atmospheric muons drops to almost zero and the total number of events drops by four orders of magnitude below the horizon.

2.6 Triggers

The typical rate at which a PMT in ANTARES detects hits reaches 50 kHz just from ^{40}K decays and bioluminescence. This alone would lead to an amount of 4 Tb of data every day, which is far too much to be processed timely. In order to reduce this amount of data, so-called triggers are used. Hits are only recorded when the conditions of at least one of the active triggers are fulfilled.

Most of the triggers work by recognizing time correlations between hits. They are designed to reduce the rate of triggered coincidental background hits to less than 10 % of the rate of background hits. During the operation of ANTARES the available triggers can be deactivated if there is a large background rate (triggers are deactivated when they yield more than 20 events per second).

The triggers used in the ANTARES data acquisition system constructed from coincidence filters that are organised into multiple so-called trigger levels. Before the first trigger level is applied, the measured hits are

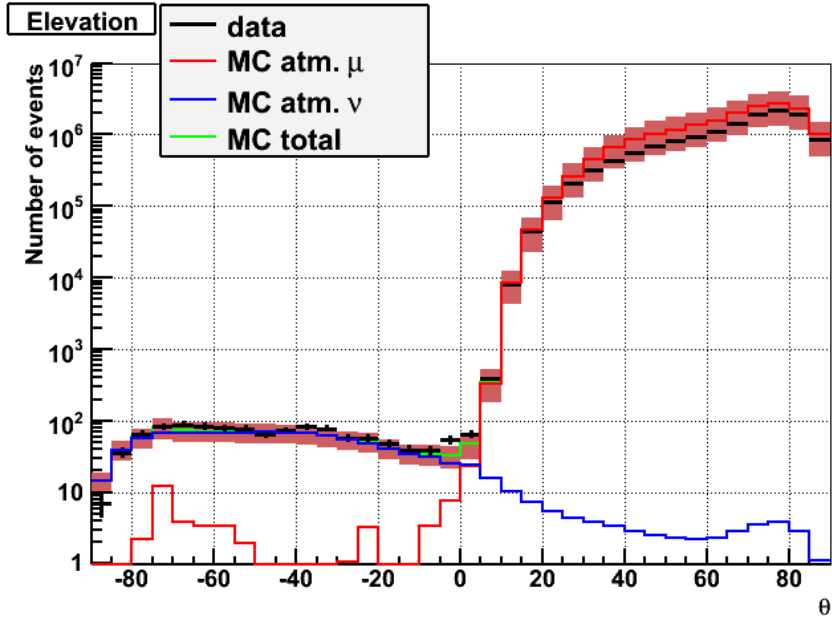


Figure 2.13: Number of events versus the event elevation. For $\theta < 0$ the track is reconstructed as upgoing, for $\theta > 0$ the track is downgoing.

calibrated according to the offsets of the clocks in the LCMs. After that hits with less than 0.3 photoelectrons are filtered out. Calibrated hits that pass this condition are referred to L0 hits. The L0 trigger is applied locally, the rest of the triggers are applied on the recorded data on-shore.

The next level of triggers requires two L0 hits to be registered in the same storey within the same storey or a single L0 hit to surpass a high threshold filter. This high threshold filter excludes hits with less than 3 photoelectrons (or less than 10 dependent on the data taking condition). Hits that pass this level are then called L1 hits.

The next trigger level is called the T-level. If a hit has at least one coincidental hit in an adjacent floor on the same line are called T2 hits. If there is a hit that has at least one coincidental hit in an adjacent or next to adjacent floor on the same line it is called a T3 hit. The coincidence windows for the T2 and T3 hits are 100 ns and 200 ns respectively. Triggers usually require multiple T2 and T3 hits to reduce the background.

Additional triggers can include conditions on the causally correlated hits. The causal correlation between two hits i and j is checked with the following inequality:

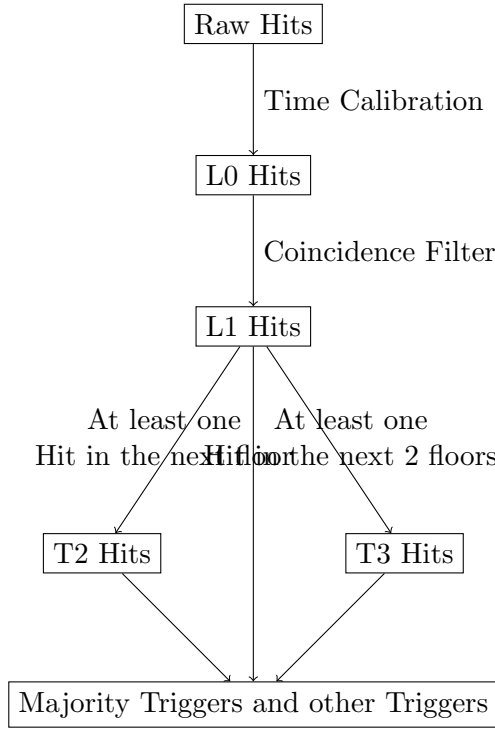


Figure 2.14: Diagram of the trigger levels used in ANTARES. The higher level triggers described in this sections are constructed using L1, L2 and L3 hits and appear as "Majority Triggers and other Triggers".

$$-\frac{R_{ij}}{c} \tan(\theta_C) \leq t_i - t_j \frac{z_i - z_j}{c} \leq \frac{R_{ij}}{c} \tan(\theta_C) \quad (2.7)$$

R_{ij} is the distance of the hits, z_i and z_j is the position of the hit i and j along the direction considered in the equation, t_i and t_j are the times of the hits and θ_C is the Cherenkov angle. The direction used in this check is usually predefined by the trigger.

The triggers used in our analyses are called 3D_SCAN, 3N and T3:

- The 3N trigger is used as a sort of standard trigger and searches for clusters of hits. A cluster is defined as the largest group of hits within a certain time window. This corresponds to the time it takes for a relativistic muon to traverse the entire detector. If the cluster has at least 5 hits it is tested for correlation. To do this the trigger uses a grid of 210 directions over the local sky. If at least 5 hits

2.6 Triggers

fulfill one of the causality conditions the trigger is set.

- The 3D_SCAN is almost identical to the 3N trigger. The only difference is that instead of checking for correlation with a grid of directions a simple time correlation is used. The 3D_SCAN trigger typically yields less than 5 events per second and is only deactivated at spring time before the detector is put into reduced high voltage mode.
- The T3 trigger makes a list of T3 hit pairs within a $2.2 \mu\text{s}$ time window (again corresponding to the passtime of a relativistic muon). If the number of consecutive hits exceeds a certain number the trigger gets set. For the standard T3 trigger this number is 1. This trigger is set off quickly and leads to trigger rates between 5 and 20 Hz depending on the conditions. This trigger is very often deactivated to prevent overloading the DAQ system. The standard T3 trigger is very useful for low energy searches since it can be set by events with very few hits.

Since events can be triggered by multiple triggers at the same time the amount of events received will not increase linearly with the number of trigger used. Especially very similar triggers display a large level of this overlap. Any event triggered by at least one of the triggers listed above was considered in the analysis.

Chapter 3

Time calibration with LED optical beacons in ANTARES

The ANTARES neutrino telescope is capable of achieving an angular resolution better than 0.3° for muon events above 10 TeV. This high level of accuracy relies on the measurement of the time of arrival of incoming light signals with an uncertainty of the order of a few nanoseconds. This can only be achieved with a well calibrated time system [16]. The details of the clock system used in ANTARES will be described in Section 3.1.

The main part of the clock system is responsible for the relative timing of PMT hits with respect to each other. This is treated independent of assigning an absolute time and date to a registered neutrino event. The absolute time is assigned by a GPS system on a separate hardware board.

This treatment of timing leads to two types of timing resolutions: the *relative time resolution* and the *absolute time resolution*. Only the relative time resolution is relevant for the angular resolution of ANTARES and so the relative timing is in the focus of the various methods of time calibration.

The absolute timing is relevant for determining if an event comes from a certain source on the celestial sky. The local coordinate system of ANTARES rotates with respect to the celestial sky due to the rotation of the Earth. Around every two minutes this rotation proceeds one degree. With accuracy of below 100ns the GPS system allows for a calculation of the celestial coordinates of an event with an accuracy below the angular resolution of ANTARES. Additionally there are time dependent analyses that rely on the time at which an event was detected. These analyses strongly rely on the absolute timing as well.

The relative timing has a set of unavoidable uncertainties that can not be corrected by the time calibration: The uncertainty on the transit time of electrons between the dynodes in the PMT called transit time

spread σ_{TTS} , uncertainties from the electronics σ_{elec} and an uncertainty on the light propagation in the sea water σ_{water} . They add up to a total uncertainty by the following equation:

$$\sigma_{tot}^2 = \frac{\sigma_{TTS}^2}{N_{pe}} + \frac{\sigma_{water}^2}{N_{\gamma}} + \sigma_{elec}^2, \quad (3.1)$$

where N_{pe} is the number of photo-electrons produced in the PMT and N_{γ} is the number of detected Cherenkov photons emitted along the muon track. The total uncertainty is of the size of 2ns in the worst case with one photo-electron in the PMTs and one photon per track. In most cases though a timing accuracy of the level of single nanoseconds is feasible.

The calibration of the clock system can be done in various ways. The four methods used for performing time calibrations for ANTARES are:

- **The internal clock calibration** As described in Section 2.3 a reference clock is installed to the on-shore station in la Seyne. This clock sends a 20 MHz reference signal to the LCMs in the detector modules. The LCMs send the reference signal back through the same wiring to the shore station. The time delay between the original clock signal from the shore station and of the moment, when the response signal reaches the shore station, is then compared between the LCMs of the detector to perform a time calibration that corrects for delays from the electronics that connect the individual LCMs to the on-shore station.
- **The internal optical module LEDs** Each of the OMs of the ANTARES detector is equipped with a blue LED installed to the back of the photocatode of the PMT inside of the OM. These LEDs allow the measurement of the relative transit time inside the PMT. This calibration has to be performed additionally to the calibrations of the offsets between the LCMs. More details on this system can be found in section 3.3.
- **Muon tracks** Every day ANTARES detects thousands of tracks from downgoing atmospheric muons (the rate is between 2 to 5 Hz). The reconstruction of muon track require a proper calibration of the ARS and the bigger the miscalibration is the larger the difference between the detected and the expected arrival times of the Cherenkov light becomes. The average of these time differences is called the time residual. The effect of the miscalibration of an individual ARS on the time residual can be determined by removing the hits from the corresponding OM from the reconstruction and calculate the difference. This difference in the time residual can be used to

perform a time calibration [17, 18]. It is even possible to calibrate the offset between entire lines using this method.

- **^{40}K decays** This radioactive isotope is responsible for a large part of the radioactive background detectable on Earth. It can be found almost everywhere on the surface of the Earth including the sea water. The main decay channel of ^{40}K is the β^- decay. A product of this decay is an electron with sufficient energy to emit up to 150 photons. If such a decay happens close to one of the ANTARES storeys the emitted photons will hit the different optical modules of the storey almost simultaneously. These coincident hits are numerous enough to be visible during the regular operation of the detector above the remaining background. This can be seen in Fig. 3.1.
- **The laser beacon system** The ANTARES detector is equipped with 3 lasers installed in the anchors of three lines. These lasers are used to illuminate nearby lines to measure and calibrate the inter line time offsets.
- **The optical beacon system** ANTARES is equipped with a set of so-called optical beacons (OBs). The OBs emit an optical signal that can be used for the calibration of time offsets between ARS on the same line. The OBs will be described in detail in section 3.3.

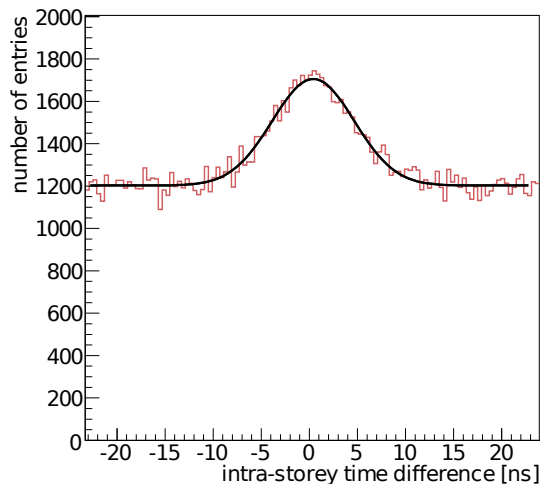


Figure 3.1: The time difference between hits in neighboring OMs. The black line shows a gaussian fit to the data shown in red.

The primary method of calibrating the offsets between the LCMs on the

3.1 ANTARES clock system

same line is the calibration with the optical beacons. For the calibration of offsets between lines the calibration with muon tracks is used.

3.1 ANTARES clock system

The ARS carries out several tasks. One of them is the time stamping of the PMT signals. The time is recorded using a time-to-digital converter (TDC) and a reference time from a clock signal. The clock signal is a 20 MHz square signal generated on-shore and is sent to the whole detector. The infrastructure distributing the reference signal is depicted in Fig. 3.2. Within each clock period, the ARS produces a linear ramp which is stopped with the arrival of the signal to produce a time stamp. The final output is the cycle of the clock plus a finer time within the clock period.

The time delays from the different fibre paths are calibrated by echoing the clock signal back to the shore station. The offsets accumulated in this round trip are twice the offsets from the signal transmission. The corrections from this frequent calibration are called clock phases. The clock phases are very stable over time and only vary a few picoseconds every year.

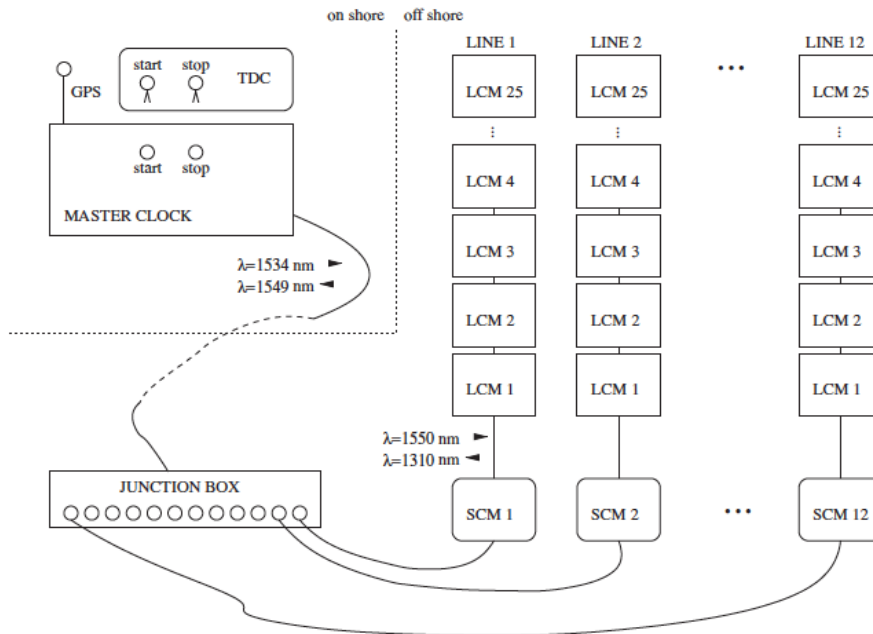


Figure 3.2: A schematic of the clock system used in ANTARES.

On top of the clock phases a further correction has to be done by

introducing another set of corrections called the ARS T0 value, or simply T0. They are equal to the time between the arrival of a photon and the finalisation of the hit charge integration by the ARS. These T0 values therefore correct for delays in the PMTs (transit time spread and aging effects of the PMTs) and for the varying times the different ARS need to integrate the charge generated by an incoming photon and also include the clock phases.

3.2 On shore calibration

Before the deployment of each line of the ANTARES detector a series of tests and a full calibration was performed. The time calibrations before deployment were performed in a dark room by simultaneously illuminating groups of OMs using a laser and a system of optical fibres. This process is illustrated in Fig. 3.3.

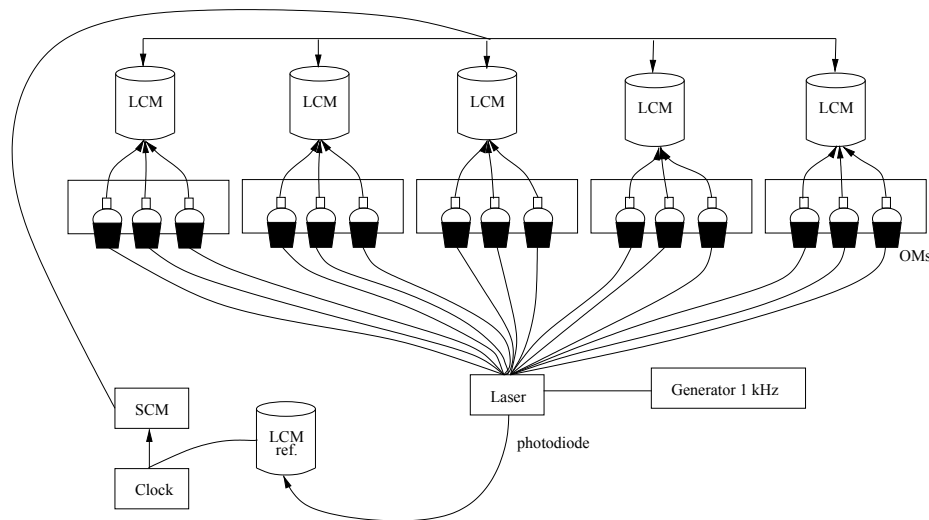


Figure 3.3: A schematic of the on-shore calibration in the Dark Room

These calibrations were carried out for bunches of five storeys. A pulsed Nd-YAG laser was used for this calibration. The Laser emits light with a wavelength of 532 nm in short and intense pulses ($E \sim 1\mu\text{J}$, FWHM $\sim 0.8\text{ns}$). The light of the laser is directed into a beam splitter which sends it through

3.3 Optical Beacons

optical fibers to the PMTs of the OMs via Lambertian diffusers that spread the light homogeneously across the whole area of the photokathodes. The length of the fibers are adjusted, so that the difference of the transition time of light through the fibers is below 0.3 ns. The time of emission of light is measured by an internal photodiode inside the laser and digitised by a reference LCM.

This calibration does not correct inter line offsets. These offsets have to be corrected in situ after deployment using one of the other calibration methods.

3.3 Optical Beacons

In each line of ANTARES the 2nd, the 9th, the 15th and the 21st storey, counted from the bottom of the lines, are equipped with one LED Optical Beacon (OB). These OBs are controlled from the LCM of the storeys where they are installed. The OBs are located above the optical modules of their storey.

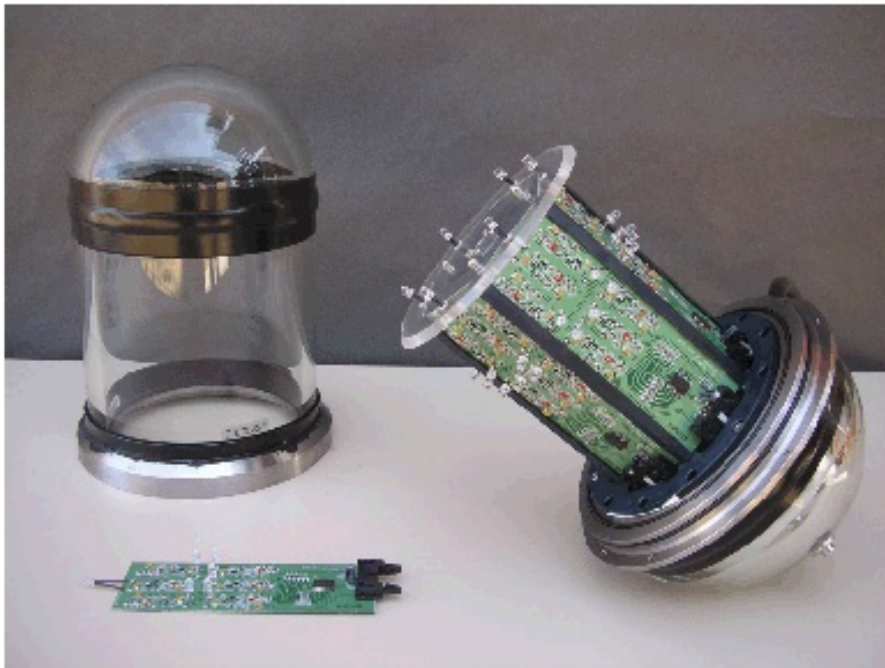


Figure 3.4: An optical beacon of the ANTARES detector

Inside each OB there are 6 hardware boards arranged into a hexagon and facing outwards. 6 LEDs are installed on each of these boards, which

makes a total of 36 LED per OB. One LED per board is installed at the top facing upwards. The boards are fixed by a hollow nylon casing with a small Hamamatsu H6780-03 photomultiplier tube inside. This PMT has a diameter of 8 mm, a rise-time of 0.8 ns and a transit time spread of 5.4 ns and is used to measure the flash time of the OB independently of the internal electronic signal triggering the light flash of the OB. On the top of the nylon casing an acrylic reflector is used as a light guide to increase the light received by this PMT. In Fig. 3.4 a picture of an OB can be seen.

The lower part of the OB houses the electronic boards that provide the voltage necessary to operate the LEDs and the slow control of the OB. The sides of the OB can be flashed individually and it is possible to activate only the LEDs at the top of the OB. If all the LEDs are flashed simultaneously the emitted light is very uniform.

The LEDs installed in the OBs are of the type Agilent HLMP-CB15-RSC00. The light emitted by these LEDs has a peak wavelength of 472 nm with a peak width of 35 nm. Their rise-time is between 1.9 and 2.2 ns. The caps of the LEDs, which would restrict the angle of the cone over which the LEDs can emit light to 15° , were removed to increase the angular occupancy of the LEDs.

The intensity of the light emitted by the LEDs can be adjusted by changing the DC voltage. The maximum voltage usable with the LEDs is 24 V. At this voltage the energy emitted per light pulse is 150 pJ in the form of $4 \cdot 10^8$ photons.

3.4 Calibration with LED Optical Beacons

For the time calibration using the LED OBs the time difference between the flashing of one OBs and the reception of light signals from that OB is measured. The time t_{OB} at which the OB is flashing is measured by the PMT inside the OB, whilst the time t_{OM} at which the light from the OB flash hits the OM is measured by the ARS connected to the OM. This time difference consists of the time offset that has to be calibrated and the travel time of the light signal from the OB to the OM. The correction to the clock of the calibrated OM, T_{corr} , can be expressed as:

$$T_{corr} = t_{OM} - t_{OB} - \frac{d_{OM-OB}}{v_g}. \quad (3.2)$$

where v_g is the group velocity of light in the sea water mentioned in section 2.4, d_{OM-OB} is the distance between the OB and the OM in question.

3.4 Calibration with LED Optical Beacons

There are several effects that influence the measured time offset and the way the incident times are measured. These effects are discussed in the following sections.

3.4.1 Early photon effect

If multiple photons arrive at a PMT in very quick succession, they can not be separated from each other by the OMs and the electronics. Due to the large amount of photons that are emitted per flash of the OBs, it is very likely for the PMTs close to the OBs to receive so many photons that they can not be differentiated. In such a case the time at which the photons are detected is set to the incident time of the first photon. A consequence of this is that the measured arrival time of the incident photons will be that of the earlier photons arriving at the PMT.

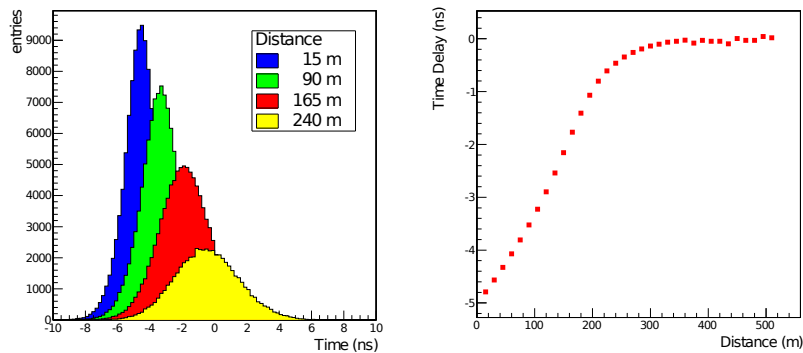


Figure 3.5: The results of a toy Monte Carlo simulating the early photon effect. On the left the time delay distributions for different OM–OB distances are shown. On the right the medians of such distributions are plotted versus the OM–OB distance can be seen. [19]

As can be seen in Fig. 3.5 the early photon effect can be neglected for sufficiently large distances. Therefore OMs that are further away from their corresponding OBs are calibrated without taking this effect into account.

3.4.2 Walk effect

The measured arrival time of a photon is set to the moment at which the charge produced inside the PMT gets over a certain threshold. For a weaker optical signal this threshold will be crossed at a later point during

its arrival than for stronger signals. This is called the walk-effect. The walk-effect is negligible for multi-photo-electron-hits and since most hits in the calibration with the LED OBs are multi-photo-electron-hits it can be ignored in that case, but it does become relevant for the interline calibration using the laser beacons.

3.4.3 DNL effect

The channels of the TVCs that record the incident time of the hits are not equally large. Therefore the TVCs do not give a uniform response to a uniform time signal. This can be seen in Fig. 3.6. The same time signal introduced to different TVCs can lead to different voltage outputs and is warped according to the different channel sizes. By this, a time offset is introduced by the TVCs that has to be taken into account. This behaviour is known as the differential non linearity (DNL) effect.

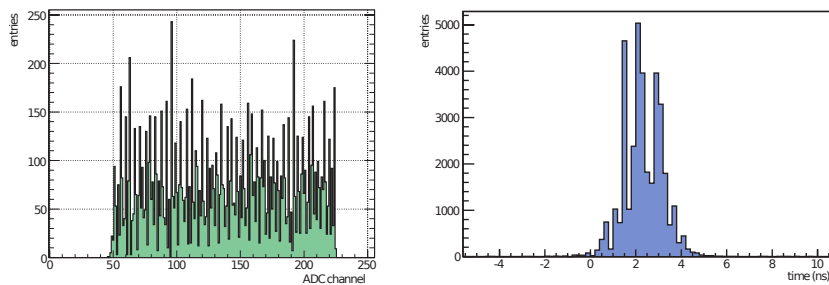


Figure 3.6: On the left the response of all TVCs to a uniform time signal is shown. On the right an example of the multiple peaks generated by the DNL effect for ARS 1 in floor 12 of line 12 can be seen. [19]

One manifestation of the DNL effect are multiple peaks in the time distributions used for the calibration. Each peak corresponds to one of the comparably large channels of the TVC in question. The DNL effect can change the TVC measurement by about 0.3 ns depending on the ARS. In tests this change can be reduced to 0.09 ns by means of corrections.

Since the DNL effect makes the shape of the detected pulses more irregular it makes automation of the calibration more difficult and increases the need for manual correction.

3.4.4 Token ring effect

Every PMT is connected to two ARS that are assigned in tandem to record incoming light signals. This assignment is managed by a protocol,

3.4 Calibration with LED Optical Beacons

that switches a "token" between the ARS. After the PMT receives a hit, the ARS that currently holds the token integrates the hit charge for the next 40 ns. Directly after this 40-ns time window the token is passed to the other ARS, which then continues the signal integration, if there is still a signal present, or waits for the next hit from the PMT.

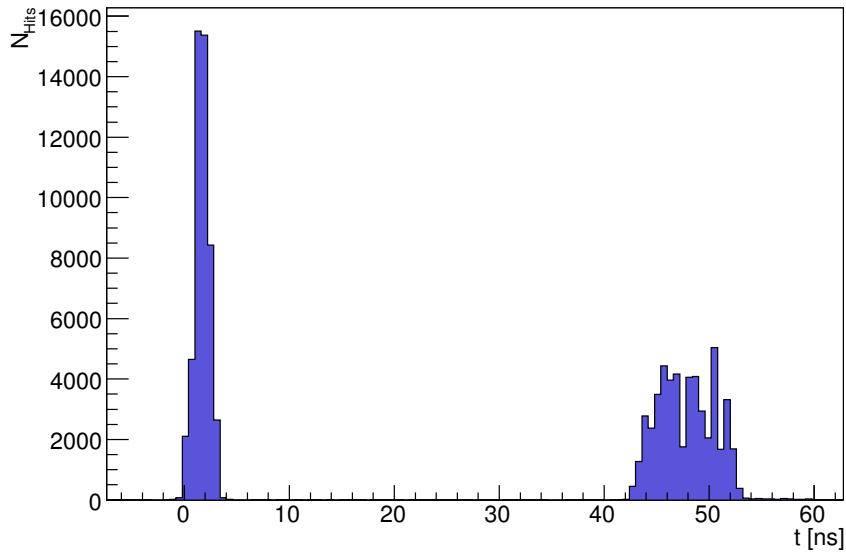


Figure 3.7: An example of the secondary peak produced by the token ring effect from ARS 0 in the fourth floor of line 4.

If too many photons impact on the PMT both ARS record the hits for the first 80 ns, one being used directly after the other. The ARS have a dead time that prevents them from recording any further hits for the next 250 ns after the 40-ns integration time for the last hit passed. So if both ARS have recorded the first hits, no further hits will be recorded for the next 210 ns. Additionally, the second ARS, that starts recording hits after the 40-ns window of the first ARS ends, will produce a secondary peak 40 ns after the primary peak in the time-delay histogram as can be seen in Fig. 3.7.

It can occur that the calibration program fits this secondary peak. In these situations a manual revision has to be made to prevent miscalibrations.

3.5 Calibration procedure

The calibration is carried out using an automatised process, whose results are manually revised and corrected afterwards. The time corrections are taken from histograms of the time difference expressed in equation 3.2. These histograms are automatically generated in a process called autobinning.

After constructing finely binned initial histograms a first fit is performed. Due to the DNL and the token ring effect this fit does not necessarily have a very good quality. If the quality of the fit is not good enough the binning is altered for coarser bins and the fit is performed again. This whole process is continued until a good fit is achieved or the bin size is larger than 4 ns. The fit function used in the autobinning is:

$$f(t) = \frac{A}{2\lambda} e^{\frac{\sigma^2}{2\lambda^2} - \frac{t-\mu}{\lambda}} \left(1 + \operatorname{erf} \left(\frac{\lambda(t-\mu) - \sigma^2}{\sqrt{2}\lambda\sigma} \right) \right). \quad (3.3)$$

This function is the convolution of an exponential and a gaussian function. A , μ and σ are respectively the amplitude, mean and width of the gaussian and λ is the decay constant of the exponential function.

This function can be adapted by the fitting process to a variety of shapes ranging from gaussian looking peaks, typical for OMS close to the OB, to noisy asymmetric peaks, more usual for OMs farther away from the OB. The repeated fitting gains a large level of stability by using the fitted parameters from the last step in the next fit as starting parameters. The first fit basically gives a first estimate of the fit parameters.

The range of the fit is defined relative to the bin with the largest content. The first fit uses all bins before and after the bin of maximum content until the bin content decreases to 20% of the maximum value. Later iterations take all bins until 5% of the maximum value is reached. If this value is never reached, the method to set the fit interval from the first fit is used instead. This can occur in case that there is a lot of scattered light, producing a large tail in the time difference histogram.

3.5.1 Manual revision

The results of the autobinning procedure have to be revised manually. There are different scenarios in which a manual correction is necessary:

- **Too few hits** There are a number of issues that can lead to an extremely small number of hits from the OB flashes. These range from problems with the internal PMT inside the OB registering the flash over insufficient power supply to the PMTs to the glass spheres

3.5 Calibration procedure

of the OMs accumulating a layer of dirt preventing the light of the flash to enter it. If the amount of hits is of the order of a few tens of hits the flash of the OM can not be properly seen in the time difference histograms and the ARS can not be calibrated.

- **Correction too large:** In some cases the token ring effect can produce a secondary peak that is fitted instead of the main peak from the OB flashes. It is also possible that due to high levels of noise a bad fit with a too large correction is produced.
- **Corrections for ARS pairs differ too much:** As mentioned before there are two ARS for each PMT of ANTARES for the purpose of recording hits. Since these ARS are almost identical, the corrections for the ARS pairs are expected to be very similar. Sometimes it can happen that there is a large amount of electric noise for one ARS and not for the other, or that there is a problem for both ARS that leads to very different corrections. On the other hand, it is possible that in the previous calibration one ARS could not be calibrated due to temporary issues and is then calibrated differently in the next calibration producing a difference in the correction for the pair of ARS. As a result, cases where ARS pairs are assigned corrections that differ by more than 1 ns have to be revised.
- **Noisy histogram:** There are cases where electronic noises in the data acquisition system, large amounts of scattered light or problems with the electronics in the OB can lead to very noisy time–difference histograms. In many of those cases no good fit can be achieved. It is also possible that a good fit to a peak that was produced by noise is performed, leading to an unreasonably large correction.
- **Badly fitted peak:** Many of the problems listed above can result in bad fits in the autobinining process. In most of these cases the fit has to be manually repeated or the calibration can not be performed at all. However, in some cases the main peak of the time–difference histograms is notable, but shows strong fluctuations that can be produced by electronic noise or the DNL effect. In those cases a good fit might be difficult, but the corrections from the autobinining effect can still be used for the calibration.

A manual revision involves changing the binning of the time difference histograms and performing the fit again by hand, if a calibration is still possible. Of the 1770 ARS that have to be calibrated about 30% require a manual revision. Most revisions are necessary due to too large corrections

from the autobinning with a good fit performed and only for around 80 ARS bad fits are performed with approximately 50 cases requiring a fit by hand.

The results of the calibrations of the OMs in the storeys 2 to 12 in line 2 from February 2015 are shown as an example in Fig. 3.8. The solid blue line in the figure is the expected time difference due to the travel time of the light from the OM flashes, the solid grey line is a fit to the time difference measured by the ARS. A delay of $0.09 \frac{\text{ns}}{\text{m}}$ is expected.

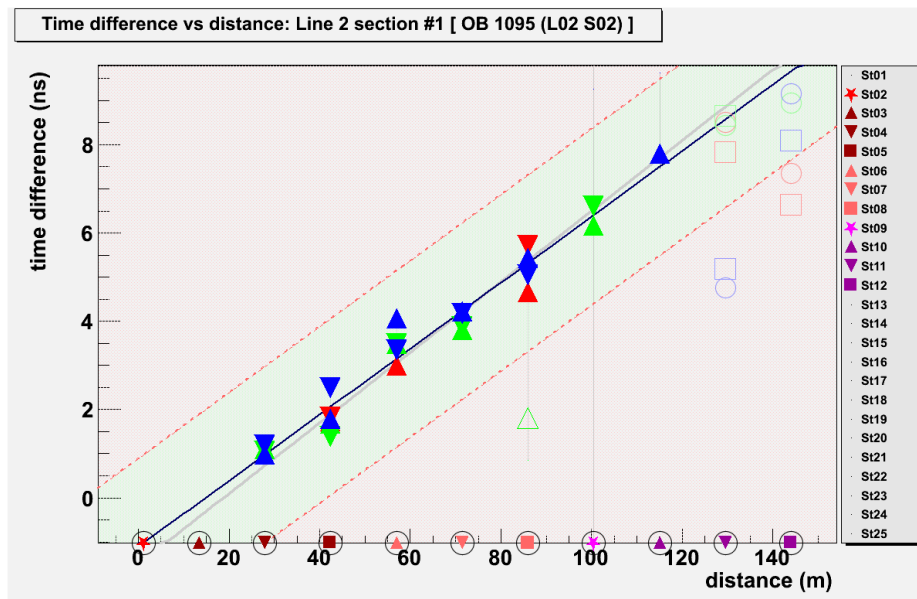


Figure 3.8: An overview of the calibration results for Line 2 from February 2015

The dashed red lines mark a 2 ns band around the expected time offset. The calibrations for the storeys 9 and 10 have been manually revised, since the original result of the autobinning showed too large corrections, which is indicated by the thin grey line above the markers for the ARS in those storeys. The ARS in the storeys 11 and 12 could not be calibrated, which is indicated by the hollow symbols used for their ARS offsets.

3.5.2 Calibrations from 2013 to 2015

As part of this thesis the calibrations using the LED OBs for the years 2014 and 2015 and part of the calibrations in 2013 have been performed. The calibration has to be carried out every two months on average. In the year 2013 there were calibrations in February, March and June, that where

3.5 Calibration procedure

Application start date	root mean square of corrections [ns]	number of corrected OMs
3.2. 2014	1.885	1059
31.3. 2014	2.53	1056
4.6. 2014	1.839	1000
28.7. 2014	2.227	1054
30.9. 2014	2.382	874
1.12. 2014	0.8996	589
18.12. 2015	2.073	830
27.4. 2015	2.097	853
29.6. 2015	2.086	866
31.8. 2015	2.119	805
26.10. 2015	2.052	798
21.12. 2015	2.107	809

Table 3.1: The results of the LED OB calibrations in 2014 and 2015.

performed within the thesis work, the other three calibrations of 2013 were performed by Agustin Sanchez Losa [19], who wrote the autobinning code. In 2014 calibrations were performed in February, March, June, July, September and December and the calibrations in 2015 in February, April, June, August, October and December. The corrections calculated from the calibrations in 2014 and 2015 are shown in the Figs.3.9.

The root mean square (rms) of the corrections obtained by the calibration process is a good measure of the size of the corrections. Since the ageing of the detector will effect the PMTs, and thereby their transit time spread, it is expected that the average time correction will slightly increase over time. In table 3.1 the evolution of the root mean squared (rms) of the time corrections can be seen. The corrections vary strongly between 0.8996 ns and 2.53 ns largely due to the varying number of ARS that can be calibrated in each calibration procedure. In the Fig. 3.9 the number of calibrated ARS can be seen as the number of entries in the histograms. Larger corrections are more likely to be excluded, since they often correspond to light peaks in an area of stronger noise, which makes the fitting more difficult. As a consequence calibrations with a larger number of uncorrected ARS tend to show a smaller rms.

It is also important to notice that the number of active storeys and lines is not constant. Due to technical issues, like failures in the power supply or problems in the communication with the LCMs, individual storeys or whole lines can be lost and become inaccessible for calibration or data

3.5 Calibration procedure

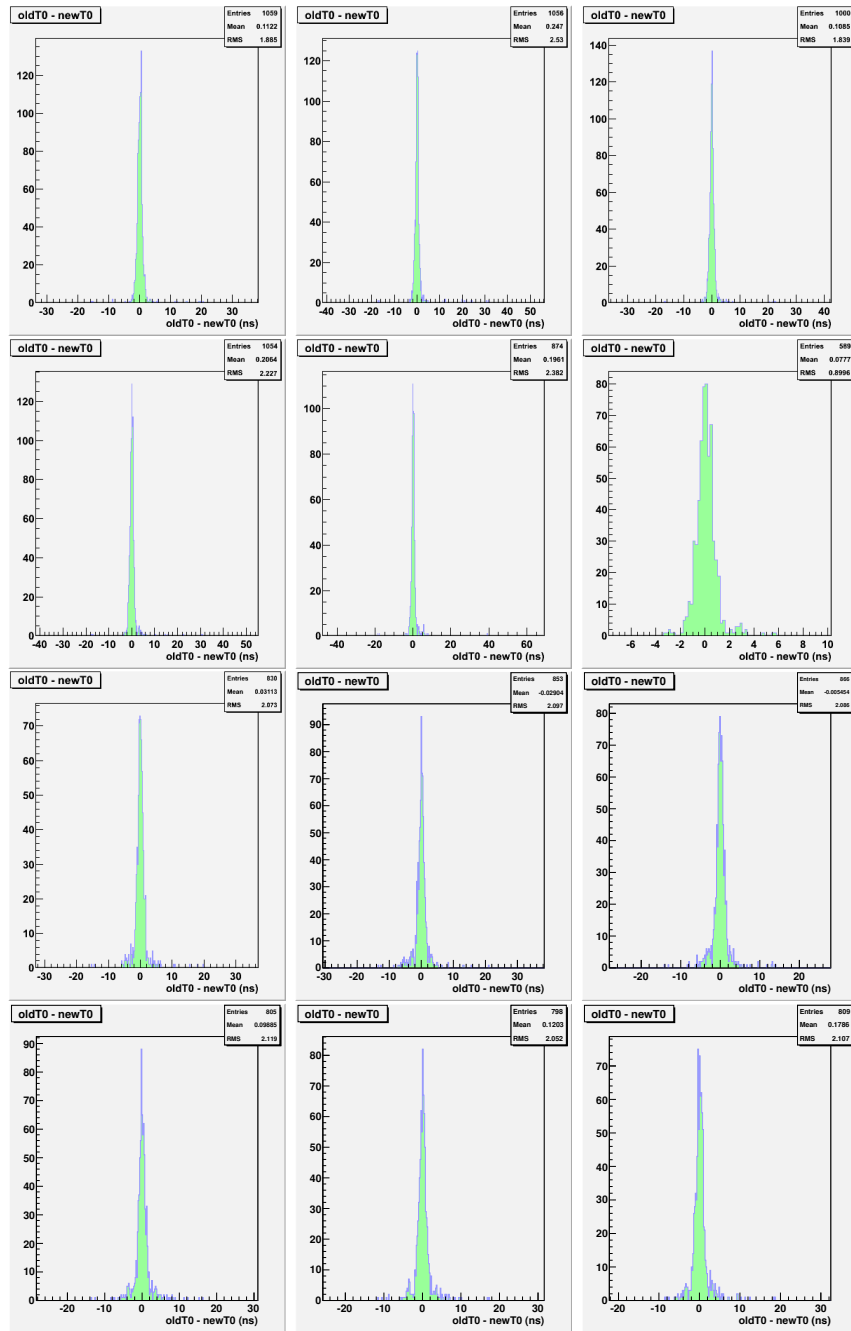


Figure 3.9: The time offsets from the calibrations in 2014 and 2015. The rms of these distributions are listed in table 3.1.

3.5 Calibration procedure

recording. In August 2014, for example, lines number 5 and 6 were lost and could not be recovered until December 2015. This can also cause changes in the rms of the time corrections.

Chapter 4

Dark matter theory and phenomenology

Whilst indirect searches for dark matter using neutrino telescopes are by nature very similar to point source searches in many regards, there are still a number of key differences. The main one is that the phenomenology of dark matter has to be taken into account. For this reason in this chapter some key aspects of dark matter theory and phenomenology will be laid out.

Firstly, the different independent lines of evidence that indicate the existence of dark matter are illustrated in section 4.1. Limits from accelerators and other experiments on dark matter and supersymmetry are presented in Section 4.2.4.

In section 4.4 the different aspects of the phenomenology of dark matter that are relevant for indirect searches like the expected neutrino spectra and the dark matter halo models are discussed. Finally, in Section 4.5 the basics of the supersymmetric extension of the Standard Model, a model that provides a very plausible candidate for dark matter, will be explained.

4.1 Evidence for the existence of dark matter

The first indication of the existence of dark matter was found by Jan Oort in 1932 when he observed the velocity of stars in the Milky Way [20]. One of the first times the term dark matter was spoken in the context of physics was by the Swiss physicist Fritz Zwicky, who inferred the existence of a large amount of non-luminous matter in the Coma galaxy cluster in 1933 by using the virial theorem to calculate the total amount of matter in the cluster and found the estimated mass to be significantly higher than the mass indicated by the luminosity of the cluster. He hypothesized that there was a type of non-luminous matter present, which he dubbed "dunkle Materie".

After these first indications of the existence of dark matter it took 67

4.1 Evidence for the existence of dark matter

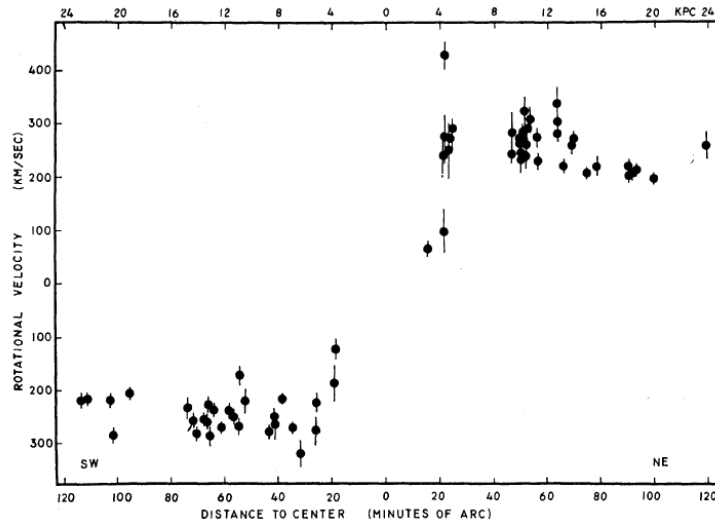


Figure 4.1: The rotation velocity distribution of stars and interstellar gas in the Messier 31 galaxy as measured by Vera C. Rubin and W. Kent Ford [21].

years for the first conclusive piece of empirical evidence to be provided. This evidence was the observed discrepancy between the rotation velocities of stars and interstellar gas in the galaxy Messier 31, also known as the Andromeda galaxy. If only visible, luminous matter was present in M31 the expectation would be that the velocity of the matter in the disk would decrease at large distances. As can be seen in Fig. 4.1 the observation showed an approximately constant velocity at large distances, indicating the presence of another type of non-visible matter.

Another hypothesis proposed to explain this phenomenon is the Modified Newton Dynamics (MOND [22]). The idea is to modify the equations of Newtonian mechanics to account for the observed effect. Whilst this can explain the rotation velocity of matter in galaxies it cannot account for other phenomena that are discussed below.

4.1.1 The Cosmic Microwave Background

The first observation of the cosmic microwave background was made in 1963 by Arno Penzias and Robert W. Wilson with the Holmdel horn antenna [23]. The existence of the cosmic microwave background (CMB) was hypothesized in 1948 by Ralph A. Alpher and Robert C. Herman [24].

The cosmic microwave background allows an insight into the earlier

CMB map LGMCA_WPR2 at 5 arcmin

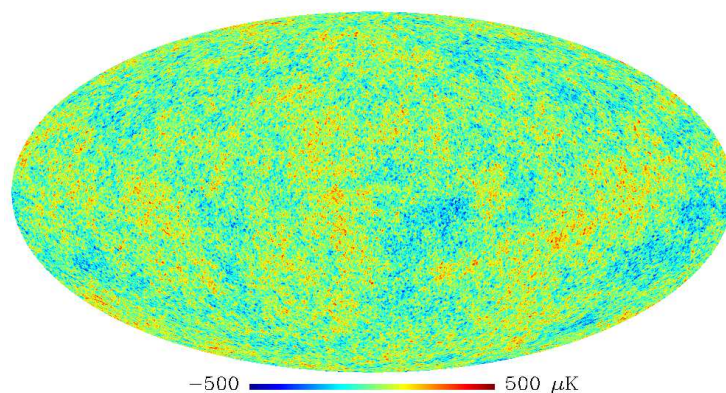


Figure 4.2: Temperature map of the cosmic microwave background obtained from Planck data [25]. The small scale temperature fluctuations indicate density fluctuations in the early Universe.

moments of the history of the Universe and gives rise to another piece of empirical evidence of the existence of dark matter. The small inhomogeneities in the temperature of the background indicate the presence of small accumulations of matter at the moment when the CMB was emitted.

In the early Universe small primordial perturbations of the density of the plasma were enhanced by gravity pulling in further matter. The high levels of radiation at this stage produced a large amount of pressure, which counteracted this effect. As a result, the density in these accumulations of plasma were oscillating. These changes in density act similar to an adiabatic compression and expansion, increasing the temperature in the accumulations and decreasing it in the regions from which the matter is drawn by gravity.

At the moment of "recombination", which is the time at which the protons and electrons in the early Universe became bound to form hydrogen atoms, the radiation, which up to this point was in thermal equilibrium with the baryonic matter, was released. Consequently, the remnants of this radiation, the CMB, had the same temperature as the plasma of the early Universe at the moment of recombination.

If only baryonic matter was present during recombination, the radiation pressure would have prevented variations at the observed scale. Dark matter however is not coupled to this radiation and would not experience the radiation pressure, allowing the formation of the observed fluctuations.

4.1 Evidence for the existence of dark matter

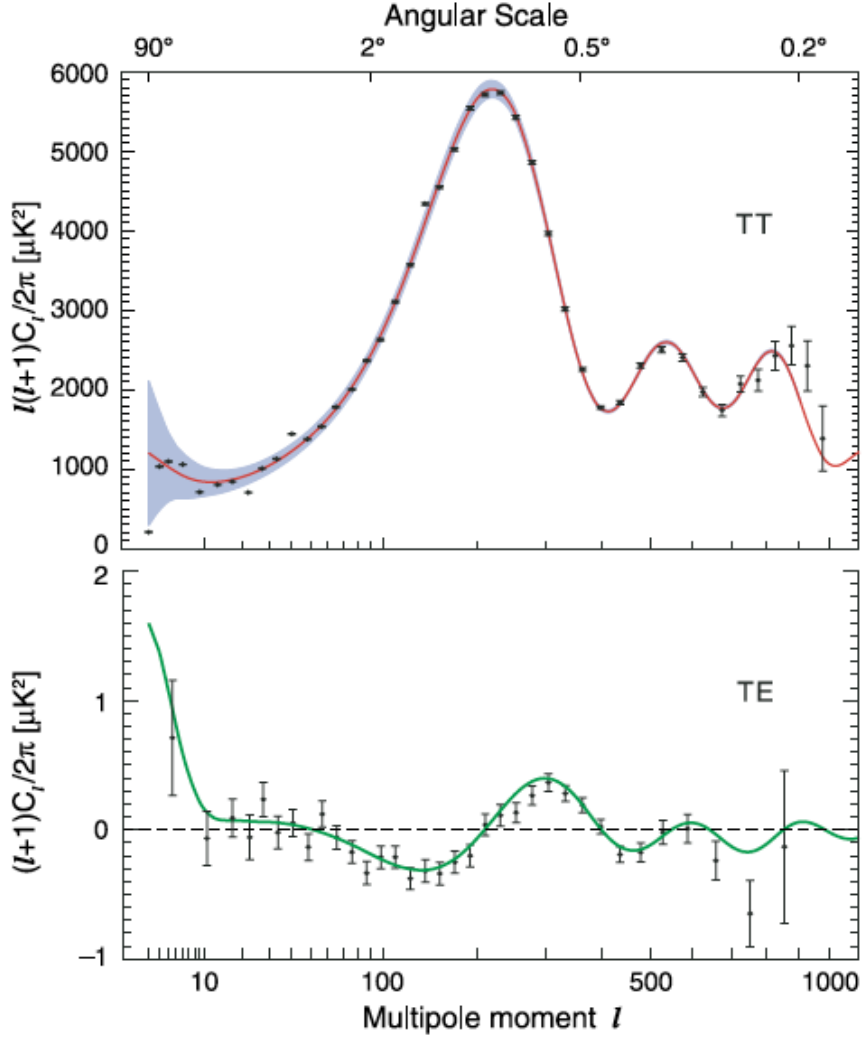


Figure 4.3: Power spectra of the cosmic microwave background for temperature (TT) and temperature-polarization correlation (TE) obtained from 5 years of WMAP data. [26]

The magnitude and size of these inhomogeneities can be quantified by a multipole power spectrum of the temperature calculated for the CMB. This spectrum can be seen in Fig. 4.3. Higher multipoles indicate smaller structures in the early Universe, whilst the dipole in the power spectrum is the result of the Doppler effect and the relative motion of the Earth with respect to the reference frame in which the CMB was emitted.

By fitting cosmological models to such power spectra it is possible to

obtain an estimate of the abundance of dark matter and other parameters that characterize the development of the early Universe. The estimate from the data of the Planck satellite and other experiments [27] for the dark matter density $\Omega_c h^2$ is 0.1184 ± 0.0012 with an estimate for the physical density of baryonic matter $\Omega_b h^2$ of 0.02227 ± 0.0002 .

4.1.2 Structure hierarchy and Simulations

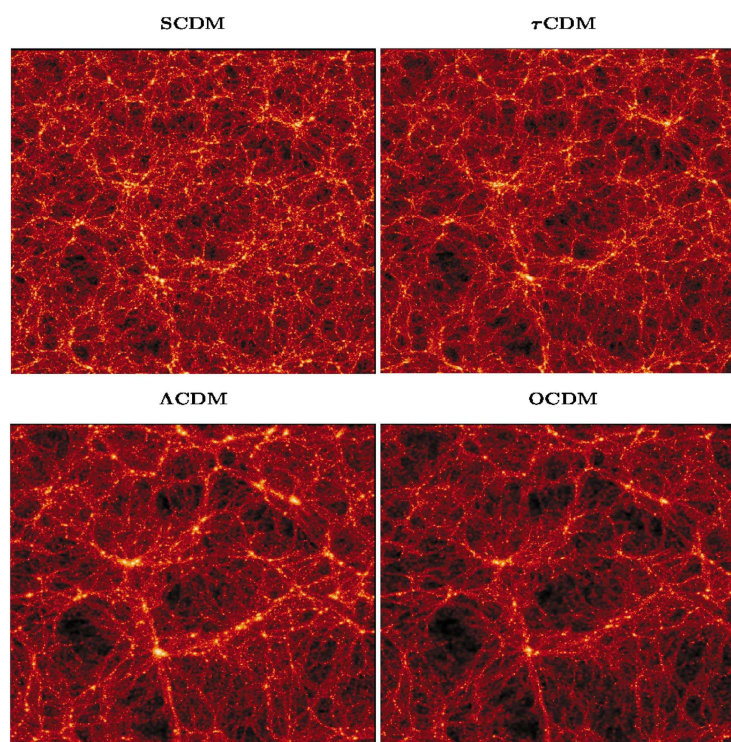


Figure 4.4: The dark matter density field for different models at a redshift of 1. The colour coding indicates the density.

The reason why it is necessary to include dark matter in cosmological models when fitting to the CMB is the so-called "structure hierarchy problem". The temperature fluctuation of the CMB shows the existence of small scale structures shortly after the recombination. This indicates that throughout the history of the Universe small structures formed first and from these, larger structures formed later on.

Taking into account the size of the temperature fluctuations in the CMB, there would not be enough time for the formation of the structure of the Universe as seen today if only baryonic matter were present. Another

4.1 Evidence for the existence of dark matter

type of matter that can accumulate early into small structures is therefore needed. In Fig. 4.4 (see also [28]) a visualization of four simulation runs is shown. These simulation runs used a large N-body simulation to study the effects of dark matter on the formation of structures in the early Universe. The figure shows the strong influence of dark matter on the formation of structures in the universe. The size of structures without any dark matter or in the presence of hot dark matter is too large. An overabundance of dark matter would lead to structures that are on average too small.

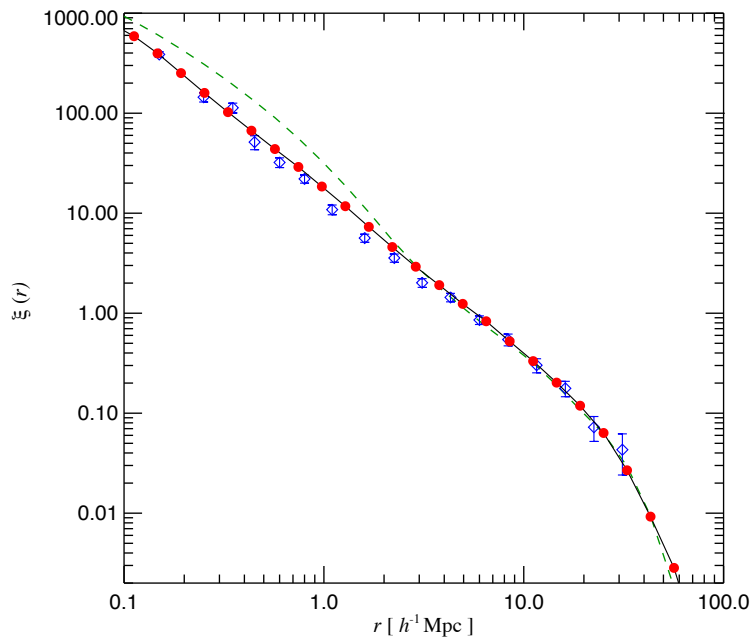


Figure 4.5: The expected two-point correlation function for galaxies in the current cosmological epoch. Red dots show measurements for model galaxies brighter than $M_k = -23$. Data for the large spectroscopic redshift survey 2dFGRS are shown as blue diamonds [28].

The amount of dark matter also influences the evolution of the formation of structures at early times and therefore the number of galaxies and galaxy clusters that are observed by galaxy surveys. Such surveys are expected to be particularly representative at small redshifts, where only very few galaxies and galaxy clusters will be overlooked.

In Fig. 4.5 the two-point correlation function for bright galaxies –which shows how clustered those bright galaxies are– is shown calculated from the Millennium simulation run and from the galaxy survey 2dFGRS. A good matching between the simulation and the actual data can be seen.

4.1.3 Gravitational lensing

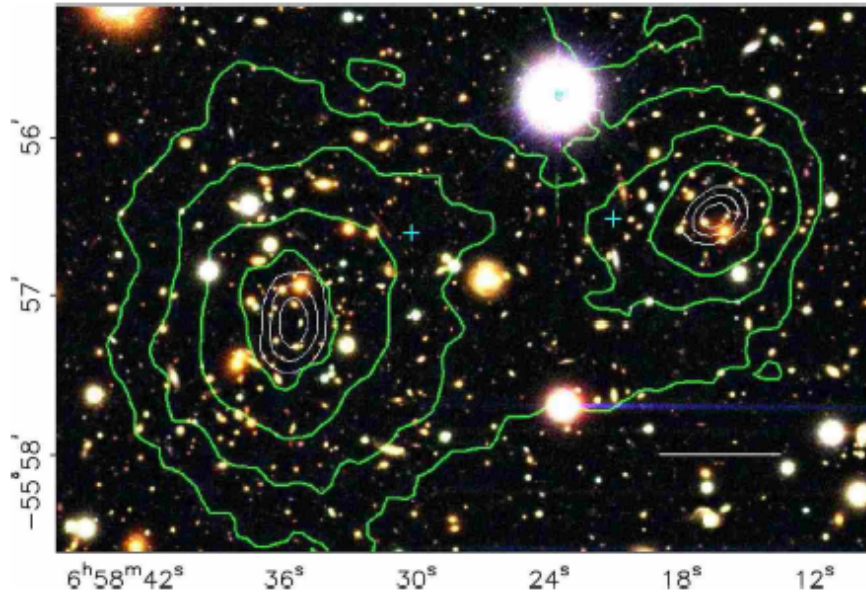


Figure 4.6: An image of the galaxy cluster 1E0657-558 obtained with the Magellan telescope. The white line indicates 200kpc at the distance of the cluster. The green lines show contours of the mass estimate generated from weak lensing observations [29].

Another piece of evidence that indicates the existence of dark matter can be obtained from gravitational lensing observations. Since massive objects generate a curved space-time, light that passes near these objects will be bent. Massive galaxies or galaxy clusters can operate as a lens that distorts the image of distant stars or other galaxies behind these objects. This effect is also known as weak gravitational lensing. The strength of the distortions allows to estimate the mass of the lensing object. The amount of matter necessary to explain the observations exceeds the amount of visible mass of the bodies in question, indicating the presence of dark matter. An example of an image, where weak lensing is present and has been used to estimate the mass of a celestial object can be seen in Fig. 4.6. From the image, a mass distribution was estimated from the weak lensing effect. The green lines in the image indicate the estimated contours of the mass distribution.

4.1.4 The Bullet Cluster

A further indication of the existence of dark matter can be obtained from the Bullet Cluster (See Fig. 4.7). The Bullet Cluster is the result of the collision of two clusters of galaxies. The ionised baryonic part of the matter of the Bullet Cluster can be seen at the collision site where it decelerated during the collision due to electromagnetic interactions. This can be seen in Fig. 4.7, where red patches indicate the distribution of ionised gas emitting x-rays. The unionised part of the baryonic matter of the two clusters however is not affected by electromagnetic forces and is therefore expected to pass through the collision site and move on largely unphased. The blue patches indicate a mass estimate generated from weak lensing similar to the estimate shown in Fig. 4.6. The mass estimate shows an amount of neutral matter much larger than is expected from unionised baryonic matter, indicating the presence of dark matter. Moreover, this is one of the hardest cases to explain by MOND theories.

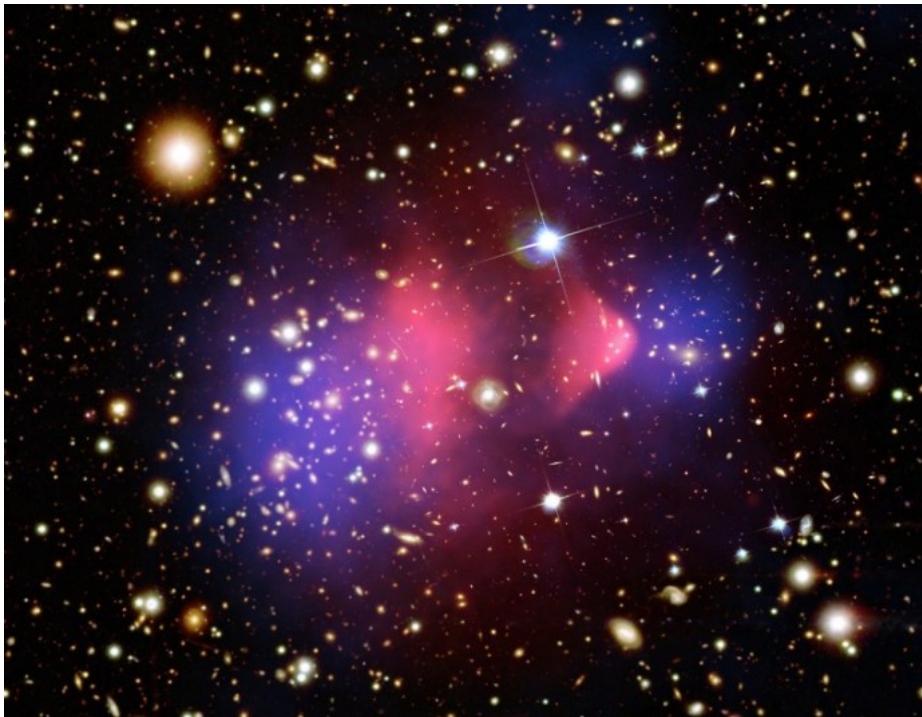


Figure 4.7: An image of the Bullet cluster. The mass distribution estimated by x-rays is displayed as a red hue, the mass distribution estimated by weak lensing as a blue hue [30].

4.1.5 The relative abundance of dark matter

The multipole expansion of the cosmic microwave background can be used to estimate the amount of dark matter present at the emission of the CMB and the amount that remains today in relation to the current total amount of baryonic matter. The relative composition of the early Universe and the Universe today is summarised in Fig. 4.8. At present dark matter composes 23% of the Universe which is around five times larger than the 4.6% of baryonic matter. The remainder of the energy density of the Universe is comprised of dark energy. At the moment when the CMB was emitted the amount of dark energy was smaller and dark matter contributed 63% of the total energy density in the Universe in comparison to the 37% of baryonic matter, neutrinos and photons. Therefore it is concluded that a part of the dark matter was converted into other forms of matter and energy throughout the further evolution of the Universe. If dark matter consists of particles, this conversion can happen via decay or annihilation of dark matter particles.

4.2 Dark matter searches

Before the different types of dark matter can be discussed, the different hypotheses about the nature have to be at least shortly described. As has been seen, there is an ample amount of evidence supporting the idea of dark matter. All evidence shown so far relies on the effect of the gravitational attraction of dark matter in different independent phenomena. Whilst this very strongly indicates the existence of dark matter it does not allow to infer many of the properties of dark matter since gravity is produced by all massive objects independent of their other properties like electromagnetic charge, spin or particle flavor.

There is a large number of possible candidates for what exactly constitutes dark matter. The following list summarises all the different candidates that will be discussed in the following subsection:

- Baryonic non-luminous matter (Massive Compact Halo Objects)
 - Brown dwarfs
 - Jupiters
 - Light black holes
- Non-baryonic particles
 - Light particles (< 1 keV, hot dark matter)
 - * Axions

4.2 Dark matter searches

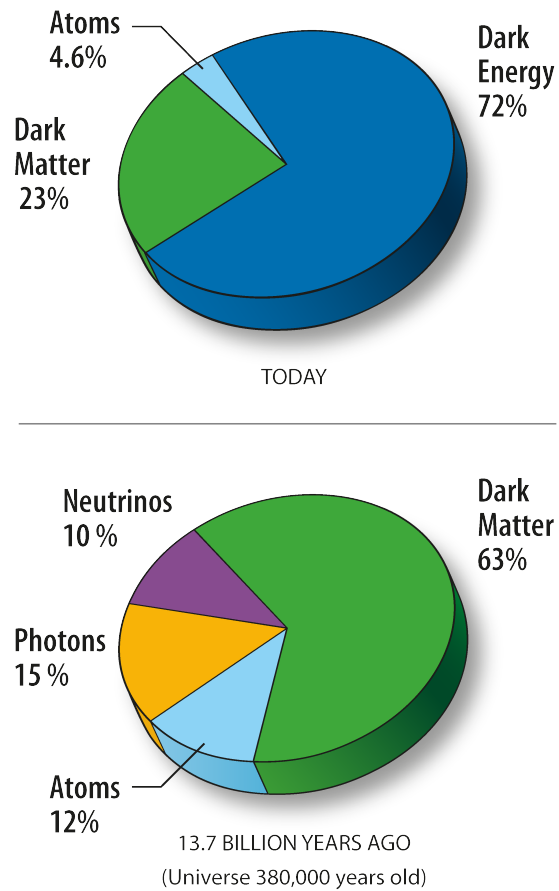


Figure 4.8: The current and past (at the time of recombination) energy composition of energy and matter in the Universe according to the WMAP data [31].

- * Neutrinos
- * Light goldstone bosons
- Medium mass particles (1 keV -10 GeV, warm dark matter)
 - * Sterile neutrinos
- Heavy particles (> 10 GeV, cold dark matter)
 - * Neutralinos
 - * Gravitinos

The above list is not exhaustive and there are many further exotic candidates for dark matter. Also not all the candidates listed can explain

all the evidence pointing towards dark matter and can be discarded.

4.2.1 Dark matter candidates

The observations concerning the CMB indicate that dark matter is composed largely of non-baryonic particles. A small fraction of the total dark matter existing today might be composed of Massive Compact Halo Objects (MACHOs), which are composed of baryonic matter. MACHOs include brown dwarfs, jupiters and small black holes with a mass of about 100 solar masses. Brown dwarfs are "stars" in the sense, that they consist of hydrogen and helium, but since the mass of a brown dwarf is very small there is no fusion going on in them. A jupiter is an even smaller gaseous object with 0.1% of the mass of the Sun, similar in size to the planet Jupiter in the Solar System. Another type of baryonic dark matter would be spaced out clouds of molecular hydrogen.

The non-baryonic candidates are in general exotic particles that are not predicted by the Standard Model. Candidate particles with masses at the order of 1 keV or below (also known as hot dark matter) can be excluded since they would lead to dark matter with a high temperature in the early Universe. Dark matter at high temperatures would experience thermodynamic pressure, which has an effect similar to the radiation pressure in the early Universe. This would then similarly prevent the formation of early small-scale structures so hot dark matter could not produce the structures observed in the Universe today. The so-called warm dark matter consists of particles with a mass between 1 keV and 10 GeV. Warm dark matter can predict the structures of the Universe more accurately than hot dark matter and can even resolve some problems found with heavier dark matter particles, but it introduces some problems of its own as well.

Hot (and warm) dark matter candidates would be neutrinos, sterile neutrinos and axions. Sterile neutrinos are, put simply, neutrinos with left-handed chirality and antineutrinos with right-handed chirality. Axions are Goldstone bosons that emerge out of a solution to the strong CP problem.

Candidate particles with a mass above a few MeV are referred to as cold dark matter. Most cold dark matter candidates are so-called WIMPs (Weakly Interacting Massive Particles). Amongst these WIMPs there are supersymmetric particles, namely the neutralino and the gravitino. The neutralino will be described in the following chapter, together with Supersymmetry in general. The gravitino simply is the superpartner to the graviton, which is a quantized excitation of the gravitational field. Such an excitation can be a transversal gravitational wave.

In this thesis the focus will be on the neutralino as a dark matter candidate.

4.2.2 Types of dark matter searches

There are different types of searches for dark matter that can be performed. To have any observable phenomenon that can be tested for in an experiment, an interaction between Standard Model particles and dark matter particles must occur. The simplest form of such an interaction is described by four particle Fermi-type diagrams with two Standard Model particles and two dark matter particles. Every such diagram is a rotation of the same basic diagram, which is shown in Fig. 4.9.

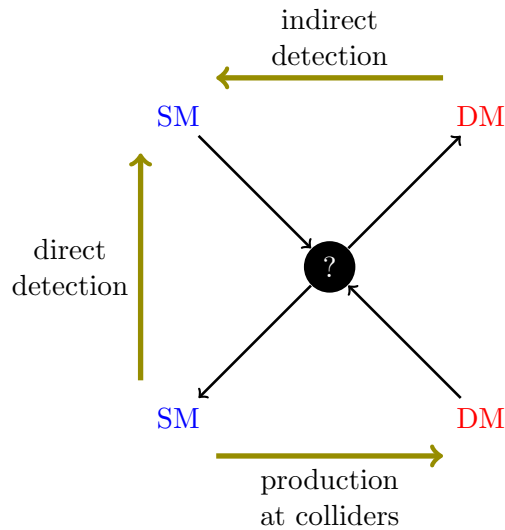


Figure 4.9: Diagram of the different types of dark matter searches and the associated interactions.

Direct detection experiments search for scattering of dark matter particles with Standard Model particles. This corresponds to reading the diagram in Fig. 4.9 vertically. Examples of direct detection experiments are given in Section 4.2.3. When read from left to right, the diagram describes the type of process by which dark matter can be looked for in particle accelerator experiments. The results of these searches are shown in Section 4.2.4. Read from left to right, the diagram describes indirect searches for dark matter. Examples for indirect detection experiments will be given in Section 4.2.5.

4.2.3 Direct detection

The currently most restrictive limits on dark matter scattering cross-sections stem from direct detection experiments. In general the direct detection experiments differ from each other by the medium used for the scattering and the means by which the recoil from the scattering is detected. The experiments XENON 100 [32] and LUX-ZEPLIN [33] use liquid Xenon as a scattering medium and detect the recoil using a time projection chamber. The target material is chosen to maximise the hypothetical scattering cross section between WIMPs and the material. Substances with a high atomic number serve this purpose very well.

In a time projection chamber (TPC), passing particles ionize the medium in the chamber via scattering. A high voltage generated by a series of cathodes on opposing walls in the TPC accelerates the particles (the electron that was knocked out of the atomic shell and the remaining atom) towards these cathodes. On their way to the cathodes the particles tend to produce further ions via scattering. The cathodes are then used to register the incoming shower of particles. The timing, position and strength of the measured impacts is then used to reconstruct the position where the initial ionisation happened and the amount of deposited energy.

In LUX and the upcoming XENON 1T (a larger version of the XENON 100 experiment) the outer part of the volume of the TPC is used as a veto (or active shielding) for atmospheric muons and other particles to reduce the background.

PICO [34, 35], on the other hand, uses a bubble chamber filled with superheated CF_3I and C_3F_8 . PICO detects recoil by bubbles forming in the target material as a result of the deposition of energy from the scattering. The bubbles are mainly detected via two high-speed, high-resolution cameras. Additionally the formation of bubbles is observed by piezoelectric acoustic transducers.

There is also a series of cryogenic dark matter detection experiments like CRESST [36], SuperCDMS [37] and EDELWEISS [38]. These detectors use cryogenically cooled Germanium or in the case of CRESST CaWO_4 crystals as target material. The detection of the recoil happens primarily via calorimeters measuring the deposited energy from the scattering but the scintillation light from the scattering is used as well.

The target materials of direct detection experiments show a very low density of unpaired spins, which makes them insensitive to the spin-dependent scattering cross-section (SDCS), which scales with the spin of the target material. The spin-independent scattering cross-section (SICS) on the other hand scales with the nucleon number of the target material, so that the SICS limit from the direct detection experiments are expected

to be significantly better than the SDCS limits.

4.2.4 Accelerator bounds

The supersymmetric parameter space has thus far been restricted by different accelerator searches. These accelerator searches look for different processes that can produce superpartner particles (especially neutralinos and charginos) by typically searching for resonances in certain decay products that are generated by the subsequent decay of the superpartner. The main production channels for these searches can be seen in Fig. 4.10.

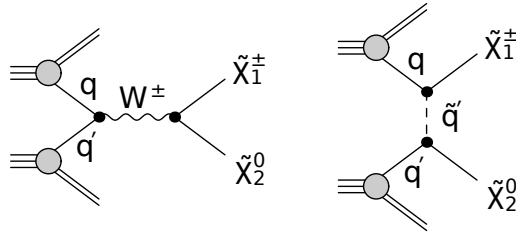


Figure 4.10: The main production channels for neutralinos and charginos in accelerator searches [39]. In both cases the incoming particles are fermions (protons in the case of the LHC) and the outgoing particles are in either case a chargino and the second to lightest neutralino. The second channel with a mediating squark (or slepton) gives the best sensitivity in accelerator searches.

If the lightest supersymmetric particle (LSP) were to be produced in such a process no further decay would happen and a large amount of missing energy and momentum would be noticed. For these processes, there are large irreducible backgrounds that make those futile in comparison. If however, the second to lightest neutralino is produced (or a chargino), further decays are to be expected, which is why the searches concentrate on these processes. The main decay channels can be seen in Fig. 4.11.

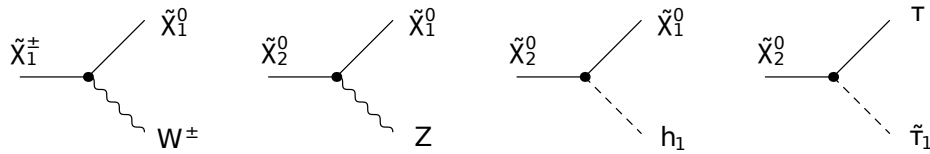


Figure 4.11: The main decay channels for neutralinos and charginos in accelerator searches [39].

The most stringent limits on the supersymmetric parameter space come

from the ATLAS [40] and CMS [41] experiments at the Large Hadron Collider (LHC) [42] at CERN. Since the parameter space of supersymmetry has many dimensions, and many of these parameters might be correlated due to the supersymmetry breaking mechanism, many exclusion limits are calculated by the accelerator experiments using different model assumptions. A summary of the different limits produced by CMS is shown in Fig. 4.12.

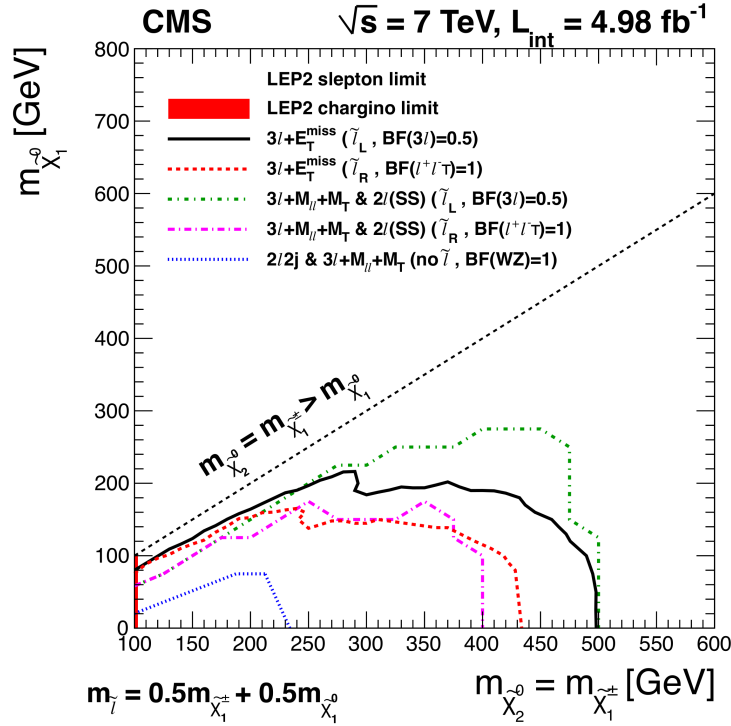


Figure 4.12: The exclusion limits from the CMS collaboration [43]. The most stringent limits come from a search for three-lepton events with large quantities of missing transversal energies and a left handed slepton mediating the production. The red limit is from a search using a production including a right handed slepton, the green and violet lines come from searches, that use for a specific transversal and longitudinal mass instead of a missing energy. The blue line searches for a production without slepton mediation.

There are similar limits produced with the ATLAS experiment [44]. In that search three-lepton events with large quantities of missing transversal energy have been used as well.

4.2.5 Indirect detection

Experiments for the indirect detection of dark matter look for signals of annihilations of dark matter particles. These searches concentrate on massive celestial objects in which an excess of dark matter is expected. Indirect searches are usually performed by astrophysics experiments as one of several analyses.

Indirect detection do not immediately detect dark matter particles but rather standard model particles that are either directly or indirectly the result of dark matter annihilations. Experiments that use photons for the indirect detection of dark matter would be, to name three examples, HESS [45], MAGIC [46] and the FERMI Large Area Telescope [47].

HESS is a terrestrial gamma-ray telescope that images atmospheric showers in the savannah of Namibia. It uses four 12-metre imaging atmospheric Cherenkov telescopes (IACTs) arranged into a square with a side length of 120 metres (called phase 1) and one 28-metre IACT in the centre of the square (called phase 2). HESS detects showers induced by high-energy cosmic radiation through Cherenkov light emitted from secondary particles. This Cherenkov light is focused on the cameras of the telescopes by a dish that consists of several reflector discs. Multiple telescopes allow then to reconstruct the spatial shape of the shower and give thereby an indication of the direction of the primary particle. The phase-1 telescopes use 960-pixel cameras with a total coverage of 5 degree and a pixel size of 0.16 degrees and have an area of 100 m². The phase-2 dishes have an area of 600 m². HESS can detect cosmic rays ranging from a few 10 GeV to a few 10 TeV and can provide competitive limits on DM.

MAGIC uses the same technique as HESS but has different dishes with an area of 236 m² and cameras, consisting of 1039 PMTs that are arranged into a 10-metre surface area giving them a coverage of 3.5 degrees. MAGIC consists of two of these large telescopes, which are installed at La Palma, on the Canary Islands.

FERMI LAT is a satellite-bound experiment that can detect high energy γ -rays like HESS or MAGIC. Unlike these two terrestrial experiments the LAT consists of a tube covered with a plastic anti-coincidence detector, a so-called converter-tracker [48] inside the tube and a calorimeter at the bottom. The converter-tracker consists of layers of high-Z material and silicone scintillation detectors that alternate between detecting the x and y-position of charged particles that pass the detector. Inside the converter-tracker, incoming high energy γ -rays produce electron-positron pairs, which are tracked by the scintillation detectors. When these pairs reach the bottom of the tube they are absorbed by the calorimeter, measuring their energy. The plastic anti-coincidence detector is used as a

veto against other charged particles that may enter the detector.

These experiments benefit from a very large sensitivity to their messenger particles but suffer from large uncertainties originating in the propagation of the photons from the source to the detector. There is also a problem with the significance of a potential signal.

There are already a large number of known and potential gamma ray sources in any galactic and extragalactic candidate bodies. This makes it very difficult to clearly pin a signal to annihilations of WIMPs.

Neutrino detectors can also be used for indirect searches. In this thesis the ANTARES neutrino telescope is used for an indirect search. Other searches were carried out using the IceCube neutrino telescope and SuperKamiokande. Using neutrinos for an indirect search has the benefit of only very small systematic uncertainties on the signal propagation. The main uncertainty of this type would be neutrino oscillations, which are discussed in Section 4.4.6.

Lastly, detectors for charged particles are used to search for dark matter as well. Since charged particles will be deflected by magnetic fields on their way to Earth, they can not be used for any search for a signal in any particular source and features in a diffuse flux are used to make inferences to dark matter models. An example of that would be the asymmetry between positrons and electrons in the diffuse flux detected by AMS [49].

Indirect searches can look into different celestial objects for dark matter annihilation and decay signals. Each type of objects has its own benefits and downsides:

- **The Sun:** The Sun is one of the closest targets for any indirect search. Unlike the case of larger objects that formed around filaments of dark matter, the Sun's dark matter has to be accumulated from the environment by gravitational capture. Since the Sun consists mostly of hydrogen, the dark matter annihilation signal is sensitive to spin dependent scattering. For searches using neutrinos the Sun is a very clean source since the neutrino background is expected to have a spectrum that is much softer than the dark matter signal spectrum.
- **The Galactic Center:** The Galactic Center (GC) yields the highest signal expectation. The limits generated for the GC can not be directly related to scattering cross sections since the dark matter in the GC is not accumulated through scattering, but is rather a thermal relic from the early Universe. The GC is a very extended source and has to be treated as such by the analysis. There is a large uncertainty on the exact shape of the dark matter halo of the

4.3 Searches using neutrinos

GC and depending on which halo model and parameters are chosen, the resulting limits can change by up to two orders of magnitude.

- **The Earth:** The Earth is both the closest and the weakest target for any indirect search. The main issue with the Earth as a target is that it can not be expected that there is an equilibrium between accumulation and annihilation. This equilibrium allows to calculate limits on scattering cross-sections for searches in the Sun. In the Earth however an annihilation cross-section has to be assumed (which introduces another systematic uncertainty) to calculate limits on the scattering cross section. Additionally the Earth is so close that the dark matter excess in its core has to be treated as an extended source. Nevertheless, depending on the assumed annihilation cross-section, the limits for the Earth can be reasonably good, although not as good as those for the Sun.
- **Dwarf Galaxies:** Dwarf galaxies typically have a very favorable ratio of visible mass to dark matter. Even faint dwarf galaxies yield a reasonable signal expectation. Due to their relative faintness most dwarf galaxies (especially the dwarf spheroidal galaxies or dSphs) are, relative to other extragalactic sources, rather close. The amount of dark matter in dwarf galaxies is also fairly well known so that there is only a small uncertainty.
- **Galaxy Clusters:** Galaxy clusters are extremely remote objects that are only interesting due to their immense mass. Most known galaxy clusters are found at redshifts larger than 0.2 and have masses ranging between 10^{13} and 10^{15} solar masses. Searches using neutrinos typically obtain limits in the same orders of magnitude for galaxy clusters as for dwarf galaxies.

4.3 Searches using neutrinos

Searches for dark matter using neutrinos have unique advantages over other search methods. Whilst there is a manifold of point sources emitting photons in the Milky Way and further away that could explain almost any possible signal found there is no such a problem for neutrinos in smaller sources (the Sun and the Earth). If a signal with a spectrum fitting the expectations for dark matter is found the chance that this really is dark matter is very high.

As mentioned before there are also very few uncertainties to indirect searches with neutrinos in comparison to other indirect searches. Photon

signals might be absorbed by any number of objects such as nebulae or dust clouds. Absorption and scattering within the source might also strongly alter or even block a possible signal. Neutrinos however can pass all these obstacles without interacting.

There are some unique problems with searches using neutrinos as well. Firstly the interaction cross sections for neutrinos are very small, which makes it necessary to use very large detectors. Therefore, despite the better understood background neutrino experiments typically lead to higher sensitivities than searches using photons. Neutrino detectors also usually have a rather high energy threshold (10 GeV for IceCube and 25 GeV for ANTARES for example) in comparison to other experiments and can thereby only look at higher WIMP masses with any good sensitivity.

There are currently three large neutrino detectors in operation that perform relevant indirect searches for dark matter: ANTARES, IceCube and SuperKamiokande. Whilst the technical details of ANTARES are laid out amply in Chapter 2, the details of IceCube will be described here.

IceCube is the currently largest neutrino telescope and located close to the geographic South Pole near the Amundsen station at the Pole. Its instrumented volume is close to one cubic kilometre and is located between 1.5 to 2.5 km below the surface of the polar ice. Similarly to ANTARES, IceCube uses PMTs to detect Cherenkov light induced by muons passing the detector volume. At the moment IceCube has 5160 digital optical modules (DOMs) with one PMT each. These DOMs are attached to 86 strings, 78 of these strings are organized into a triangular grid with a intraline distance of 125 m, the remaining 8 lines are put between the regular lines at an intraline distance of 55 m forming the so-called "Deep Core". These additional strings are also equipped with more sensitive PMTs and have a more dense spacing of the DOMs. For dark matter searches most of the sensitivity of IceCube comes from Deep Core, since the expected neutrino signal is expected to have a very low energy spectrum. The outer three layers of lines in IceCube are typically used as a veto to exclude atmospheric muons. However neutrinos that produce muons outside the detector volume, which later pass the detector are also excluded. Given the long range of muons, especially of high energy muons, the acceptance is greatly reduced by this veto.

SuperKamiokande is a water-Cherenkov detector constructed inside the Kamioka mine in the Gifu prefecture in Japan below 1 km of rock. The detector consists of a 41.4 m tall cylindrical water tank with a diameter of 39.3 m. The outer wall of the tank consists of stainless steel and it is filled with 50 kt of ultra pure water. The volume of the detector is divided into an inner and an outer detector by a stainless steel structure onto which a large number of PMTs are mounted. This structure is also

plated with polyethylene terephthalate sheets on its inside and Tyvek sheets on its outside. The outer tank walls are also covered by these sheets. As in ANTARES and IceCube, neutrinos are detected via muons that are produced by interactions between nucleons and passing high energy neutrinos. Due to the high density of PMTs, SuperKamiokande is sensitive to neutrinos of very low energy in comparison to neutrino telescopes. The main downside to SuperKamiokande is the comparably small volume of the detector which leads only to small effective areas. The data taking with SuperKamiokande started in April 1996 and was interrupted between July 2001 and October 2002 due to an accident during an upgrade to the detector hardware. In this accident half of the PMTs were severely damaged and could not be used anymore. To prevent further damage the remaining PMTs were put into fiber-reinforced plastic casings and the reconstruction of the detector started in October 2005 and was finished in July 2006. The detector is running since with its regained capacity.

There are also some detectors currently in planning: km³Net [50], IceCube gen-2 [51] and HyperKamiokande [52].

4.3.1 Searches towards the Sun

When looking at specific sources there are some advantages to these searches when it comes to neutrinos. Some of these advantages were already discussed above.

The expected background is very well understood. Neutrino fluxes from fusion processes have been used before to measure neutrino oscillations and are known to have energies significantly lower than the expected neutrino dark matter signal.

Moreover, the Sun takes a path through the Milky Way that makes the excess of dark matter that accumulates in its centre largely independent of halo substructures and other non-uniformities in the galactic halo, which otherwise is a big problem for direct searches. The annihilation rate also does not strongly depend on the velocity distribution of the dark matter excess, which is generally not known very well. Also, unlike direct searches, searches for dark matter in the Sun are more sensitive to the low end of the velocity distribution.

Whilst searches towards extragalactic sources and the milky way itself can only put limits on thermally averaged annihilation cross-sections, searches towards the Sun allow to put limits on the spin-dependent and spin-independent scattering cross-section. This can be done since for the Sun, an equilibrium between annihilation and accumulation, which depends on the scattering cross sections, can be assumed. This assertion is not very contrived when compared to the assumptions made for different

searches using other particles or sources.

4.4 Dark matter cosmology and halo profiles

There are several aspects of dark matter phenomenology that have a large effect on indirect searches. The expected signal spectra, for example, depend strongly on the annihilation behaviour of the WIMPs; source intensities and shapes depend very much on the dark matter halo models used. For this reason various aspects of dark matter phenomenology, theory and cosmology will be discussed in this Section.

4.4.1 Relic density of WIMPs

The first step towards the calculation of the relic density is the assumption of thermal equilibrium in the early matter-dominated era of the evolution of the Universe. This means that particles form at the same rate at which they annihilate. Starting from the primordial dark matter density, the relic density is calculated taking into account the dark matter annihilations and decay and the expansion of space-time. This leads to the Boltzmann equation for dark matter:

$$\begin{aligned} \frac{dn_i}{dt} = & -3Hn_i - \sum_{i=1}^N \langle \sigma_{ij} v_{ij} \rangle (n_i n_j - n_i^{eq} n_j^{eq}) \\ & - \sum_{i \neq j} \left[\langle \sigma'_{\chi_{ij}} v_{ij} \rangle (n_i n_X - n_i^{eq} n_X^{eq}) - \langle \sigma'_{X_{ji}} v_{ji} (n_j n_\chi - n_j^{eq} n_\chi^{eq}) \rangle \right] \\ & - \sum_{i \neq j} \left[\Gamma_{ij}(n_i - n_i^{eq}) - \Gamma_{ji}(n_j - n_j^{eq}) \right], \end{aligned} \quad (4.1)$$

where n_i is the number density of the dark matter particle of type i , n_i^{eq} is the number density of the dark matter particle of type i in equilibrium and v_{ij} is the relative velocity between the dark matter particles of the types i and j . The first term on the right-hand side describes the expansion of space via the Hubble parameter H . The second term takes into account the annihilation of dark matter, with the annihilation cross-section:

$$\sigma_{ij} = \sum_X \sigma(\chi_i \chi_j \rightarrow X). \quad (4.2)$$

The third term accounts for the scattering of dark matter with the cosmic microwave background with the cross-section:

$$\sigma'_{Xij} = \sum_Y \sigma(X \chi_i \rightarrow Y \chi_j). \quad (4.3)$$

4.4 Dark matter cosmology and halo profiles

And the last term describes the decay of dark matter with the decay rate:

$$\Gamma_{ij} = \sum_X \Gamma(\chi_i \rightarrow \chi_j X). \quad (4.4)$$

If dark matter consists only of the lightest supersymmetric particle the last two terms cancel out, since particles produced by scattering would quickly decay back into the LSP in most models. Since the LSP is much more likely to scatter than to annihilate, the distribution of particle types remains in thermal equilibrium:

$$\frac{n_i}{n} = \frac{n_i^{eq}}{n^{eq}}. \quad (4.5)$$

This simplifies the Boltzmann equation to:

$$\frac{dn}{dt} = -3Hn_i - \langle \sigma_{eff} v \rangle (n^2 - (n^{eq})^2) \quad (4.6)$$

where

$$\langle \sigma_{eff} v \rangle = \sum_{ij} \langle \sigma_{ij} v_{ij} \rangle \frac{n_i^{eq} n_j^{eq}}{n^{eq,2}}. \quad (4.7)$$

The relic density is then calculated using the solution to the Boltzmann equation and the following equation:

$$\Omega_\chi = \frac{m_\chi n}{\rho_{crit}}, \quad (4.8)$$

where ρ_{crit} is the matter density for which a flat cosmological evolution is achieved (in contrast to an open or closed cosmology). The equality

$$\Omega_\chi \approx \frac{1 \cdot 10^{-26}}{\langle \sigma_A v \rangle} \frac{1}{\text{cm}^3 \text{s}} \quad (4.9)$$

with the annihilation cross-section σ_A approximately holds for the thermally averaged annihilation cross-section of the dark matter particle.

4.4.2 WIMP capture in celestial objects

As described above WIMPs are generally assumed to be in equilibrium with the thermal background, which means that there will be WIMPs that loose most of their energy and can be captured gravitationally by massive objects like the Earth or the Sun. Within these objects annihilations of WIMPs will then occur, leading to a signal in the form of various particles, like photons or neutrinos. These annihilations and the capture

of WIMPs will lead to a dark matter density inside the object at which an equilibrium between these processes is achieved. This density n can then be expressed by

$$\frac{dn}{dt} = C - C_A n^2 - C_E n, \quad (4.10)$$

where C is the WIMP capture rate and C_A the annihilation rate. C_E is the rate at which WIMPs are lost by scattering. For the annihilation rate the following equation holds:

$$\Gamma_A = \frac{1}{2} \tanh^2 \left(\frac{t}{\tau} \right) \quad (4.11)$$

where $\tau = \sqrt{CC_A}$ is the time necessary for the system to reach the equilibrium. τ is typically much smaller than the lifetime of the massive object in question, so that it is reasonable to assume that the equilibrium has already been reached, in particular for the Sun. The capture rate then mostly depends on the WIMP mass, the mass of the object capturing the WIMPs, the local dark matter density at the capturing object, the mean velocity of the WIMPs at the capturing object, $v_{rms} = \sqrt{\langle v^2 \rangle}$, and the scattering cross-section with the matter of the capturing object (e.g. hydrogen, helium and oxygen for the Sun). This makes the form and magnitude of the galactic dark matter halo important for the case of the Sun. The local dark matter density that is typically used for comparisons is $0.3 \frac{\text{GeV}}{\text{cm}^3}$. The relevant scattering cross-sections for the capture of WIMPs in the Sun are the spin-dependent scattering cross-section with hydrogen, $\sigma_{H,sd}$, the spin-independent scattering cross-section with hydrogen, $\sigma_{H,si}$, and the spin-independent scattering cross-section with helium $\sigma_{He,si}$. The capture rate through the element i per shell dV of the Sun's volume can in general be expressed as [53, 54]

$$\frac{dC}{dV} = \int_0^{u_{max}} \frac{f(u)}{u} \omega \Omega_{v,i}(\omega) du, \quad (4.12)$$

where $\omega = \sqrt{u^2 + v_{esc}^2}$ is the velocity of the WIMP calculated with the escape velocity v_{esc} , u is the velocity of particles in the Sun, u_{max} is the maximum velocity at which WIMPs scatter to velocities above to escape velocity, and $\Omega_{v,i}(\omega)$ is the scattering probability of a WIMP with a nucleus of the element i at the velocity v . $\Omega_{v,i}(\omega)$ is proportional to the scattering cross-section and the abundance of the element the WIMP is scattering with. The velocity distribution $\frac{f(u)}{u}$ assumed for WIMPs in the Sun is a Maxwellian distribution with a rms velocity of $270 \text{ km} \cdot \text{s}^{-1}$:

4.4 Dark matter cosmology and halo profiles

$$\frac{f(u)}{u} = \sqrt{\frac{3}{2\pi}} \frac{n_x}{v_o v_{rms}} \left[e^{-\frac{3(u-v_o)^2}{2v_{rms}^2}} - e^{-\frac{3(u+v_o)^2}{2v_{rms}^2}} \right]. \quad (4.13)$$

The resulting conversion from neutrino fluxes to scattering cross-sections is shown in Fig. 4.13.

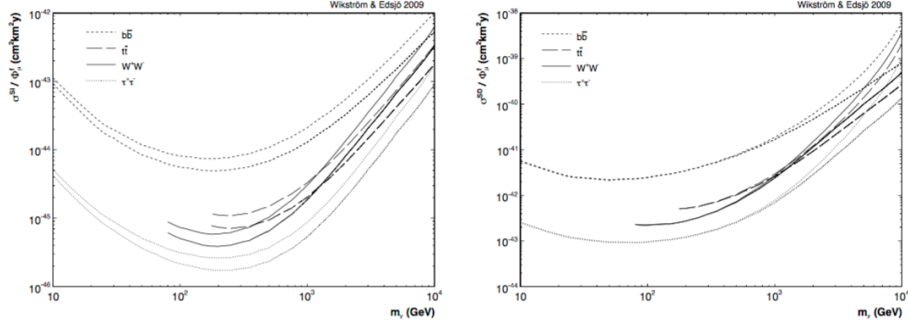


Figure 4.13: The conversion factors from neutrino fluxes to spin-independent (left) and spin-dependent (right) cross-sections. The upper lines show the results of a conservative calculation that includes gravitational effects from the gas giants and assumes less favorable form factors for the scattering and lower bounds for the abundances of more massive elements like oxygen in the Sun [53].

The scattering will be dominated by the spin-dependent scattering with hydrogen, since it is the most abundant element in the Sun, as can be seen in [55]. Spin-independent scattering will mainly happen with helium. In addition to the lower abundance of helium, the cross-section for the scattering with helium is suppressed in comparison to the spin-dependent scattering with hydrogen due to kinematics, which becomes stronger for heavier nuclei. Scattering with heavier elements can be ignored, since the abundance of these elements is even lower and the kinematic suppression higher.

4.4.3 Halo profiles and the J-Factor

Different profile functions (i.e. the density ρ_χ as a function of the distance to the centre r) can be used to model the amount and distribution of dark matter in galaxies and galaxy clusters, such as the Navarro-Frenck and White (NFW) profile [56]. These profiles are variants of the more general Zhao profile function [57]:

$$\rho_\chi(r) = \rho_s \left(\frac{r}{r_s}\right)^{-\gamma} \left[1 + \left(\frac{r}{r_s}\right)^\alpha\right]^{-\frac{\beta-\gamma}{\alpha}} \quad (4.14)$$

where ρ_s is the dark matter density at the scale radius r_s and α , β and γ are parameters that depend on the halo model used. The values of the NFW profile are $\alpha = 1, \beta = 3$ and $\gamma = 1$. These halo models are called "cusped" profiles, since they diverge for $r \rightarrow 0$ producing a cusp. Consequently these profiles would give a very concentrated signal, which would even appear as a point-like source for distant halos.

Aside of the NFW profile, a model from [58] was used, which is also a variant of the Zhao profile. In that halo model the same coefficients as for the NFW profile are used with the exception of γ , which is treated as a free parameter with a fitted value of γ is 0.79 ± 0.32 . This profile will be referred to as the McMillan model.

There are other halo models that do not use the Zhao profile as a starting point, such as the isothermal or the Burkert profile. The Burkert profile function is given by [59]:

$$\rho_\chi(r) = \frac{\rho_s}{\left(1 + \frac{r}{r_s}\right) \left(1 + \left(\frac{r}{r_s}\right)^2\right)}. \quad (4.15)$$

These profiles are also called "bulked" profiles, since they do not have a divergent cusp at $r = 0$. As a consequence these profiles appear much more sprawled out. This would make detecting signals for such a halo much more difficult.

Usually the NFW profile is used as a benchmark for comparison among different dark matter searches. In the case of a search in the Milky Way or other galaxies or galaxy clusters, an equilibrium between capture and annihilation or decay is not assumed. Instead, the density of dark matter and its distribution is determined by using typical velocity distributions of stars in a galaxy or of galaxies in a cluster to fit the parameters of a chosen halo profile function. This is very difficult for the Galactic Centre, since the visibility of stars is reduced due to the high density of matter in the galactic disc. This leads to larger astrophysical uncertainties in these profiles. In this thesis the program CLUMPY [60] has been used for the purpose of fitting the halo parameters to experimental data.

The resulting fitted halo profile describes the shape of the object where a signal of dark matter annihilations is searched for. More specifically,

4.4 Dark matter cosmology and halo profiles

a parameter called J-Factor describes the spatial distribution that is expected for the signal particles as seen from the detector. The J-Factor is defined as the squared dark matter density integrated along the line of sight from the detector. It can be expressed as:

$$J(\theta) = \int_0^{l_{\max}} \frac{\rho_\chi^2 \left(\sqrt{r_s^2 - 2lr_s \cos(\theta) + l^2} \right)}{r_s \rho_s^2} dl. \quad (4.16)$$

This definition generates a unitless J-Factor that does not scale with the overall amount of dark matter in the halo. The J-Factor is also necessary to convert signal particle fluxes into dark matter model parameters. The thermally-averaged annihilation cross-section $\langle \sigma v \rangle$ is related to the signal particle flux from the analysed object via the following equation:

$$\frac{d\phi_\nu}{dE} = \frac{\langle \sigma v \rangle}{2} J_{\Delta\Omega} \frac{r_s \rho_s^2}{4\pi m_\chi^2} \frac{dN_\nu}{dE}, \quad (4.17)$$

where $J_{\Delta\Omega}$ is the integrated J-Factor for an observation window $\Delta\Omega$ and $\frac{dN_\nu}{dE}$ is the number of neutrinos per annihilation in the energy bin dE . It is calculated by the integral:

$$J_{\Delta\Omega} = \int_{\Delta\Omega} J(\theta) d\Omega = \int_0^{2\pi} \int_0^{\theta_{cone}} J(\theta) \sin(\theta) d\theta d\phi, \quad (4.18)$$

where θ_{cone} is the opening angle of the cone-shaped observation window.

4.4.4 Halo profile parameters and the CLUMPY program

As mentioned before there are various difficulties in determining the shape of the dark matter distribution of the object under study, specifically in the case of the centre of the Milky Way. Programs like CLUMPY require input in the form of halo parameters in order to be able to produce J-Factors and halo-profile functions. In the case of CLUMPY, these parameters are the scaling radius, the local density (The scaling density depends on the local density and can be calculated from it. The local density can be estimated more directly and is therefore used to express the halo shape) and the mean velocity of the dark matter inside the halo. These parameters can be estimated by experimental data. Table 4.1 shows the estimates of ref. [61, 58], which will be used here.

The "old NFW" profile values are not used in this analysis, since they are quite outdated. They are put for reference, since they were the profile value used in previous analyses using ANTARES [62].

4.4 Dark matter cosmology and halo profiles

Parameter	NFW old	NFW new	Burkert	McMillan
r_s [kpc]	$16.1^{+17.0}_{-7.8}$	21.0	$9.26^{+5.6}_{-4.2}$	17.6 ± 7.5
ρ_{local} [GeV/cm ³]	0.3	$0.471^{+0.048}_{-0.061}$	$0.487^{+0.075}_{-0.088}$	0.39 ± 0.034

Table 4.1: Table of dark matter halo parameters for the Milky Way.

These parameters are then used by CLUMPY to produce J-Factors for the NFW profile, which has been chosen for comparison to other analyses. The Figs. 4.14 and 4.15 show the output generated by CLUMPY.

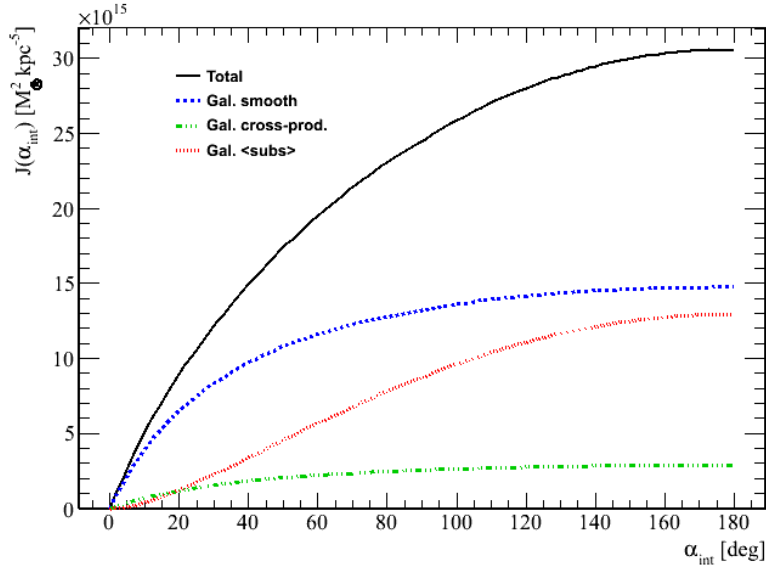


Figure 4.14: The integrated J-factor computed for the old NFW profile using CLUMPY versus the opening angle α_{int} of the observation window. The blue line is the smooth part of the halo, the red line shows the contribution from substructures (e.g. dark matter satellites) and green line shows the cross-product of the other contributions. The black line shows the sum of the individual contributions.

For the analyses conducted as part of this thesis, only the smooth contribution to the halo is considered, since there are large uncertainties in the contributions of halo substructures (clumps). The integrated J-Factor is proportional to the amount of signal that is expected for a certain size of the observation window. As can be seen in Fig. 4.14, the observation

4.4 Dark matter cosmology and halo profiles

window needs to be opened up to around 60° to gather 90% of the total signal, if only the smooth contribution to the halo is considered. Therefore the Galactic Centre can not be treated as a point-like source. Such a treatment is reasonable only if the source has an angular extension smaller than the angular resolution of the detector.

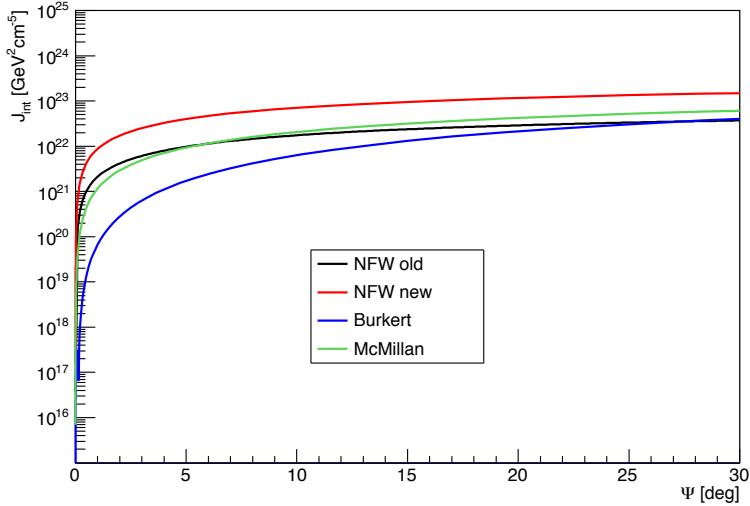


Figure 4.15: The integrated, smooth J-factor computed for the old NFW profile and the other three halo profiles used in this thesis as a function of the opening angle Ψ of the observation window.

Fig. 4.15 shows the smooth part of the integrated J-Factor for the old NFW in comparison to the other profiles and again, a large difference is visible.

4.4.5 Signal neutrino spectra

To compute acceptances and simulating signal events the expected spectra of signal particles (in this case neutrinos) has to be known. The spectra of the signal neutrinos depend on the processes that happen during and after the annihilation of the WIMPs. A WIMP annihilation will in first instance lead to a pair of Standard Model particles, one particle and one antiparticle, assuming that the WIMPs are the LSP. The kinetic energy of these annihilations is not necessarily very high, so that the particles that are produced initially in the annihilation need to be lighter than the annihilating WIMPs. If the WIMP is heavy enough there are many particle pairs it can annihilate to. The branching ratio for each type of

particle pair depends on the model used to describe the dark matter. In the case the WIMP is the neutralino, its field composition in terms of gauginos and higgsinos and its resulting mass determine its branching ratios.

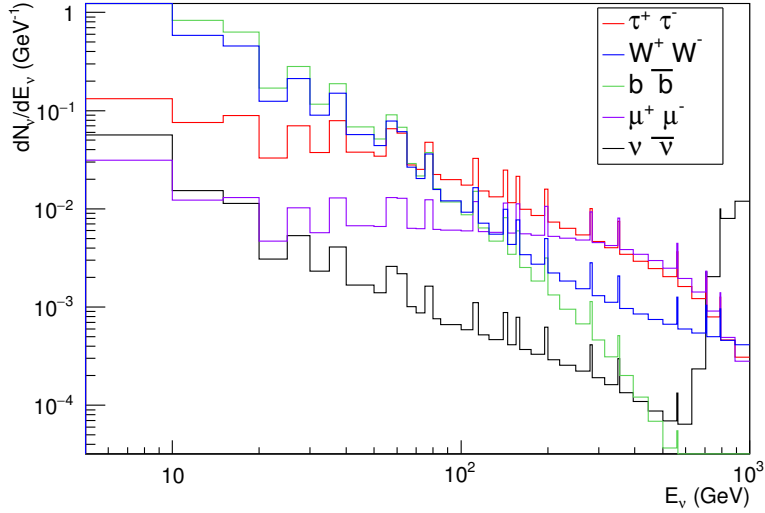


Figure 4.16: The number of neutrinos per WIMP annihilation, as a function of the neutrino energy for the different annihilation channels. These spectra have been calculated for WIMP annihilations in vacuum and a WIMP mass of 1 TeV. The peaks stem from a conversion from a logarithmic to a linear energy axis.

After the initial annihilation, the Standard Model particles that emerge will in most cases decay into lighter particles. In these secondary processes neutrinos can be produced. If the primary particle is a charged lepton the decay always produces a neutrino due to conservation of lepton flavour and the decay of weak gauge bosons have a high probability to produce charged leptons and neutrinos either directly or through the decay of hadrons. Gluons and quarks will produce hadronic showers that mostly produce neutrinos by the decay of mesons that emerge from the shower.

All these secondary processes depend only on the physics of the Standard Model sector. Therefore, the model dependency of the number of neutrinos and their energy spectra lies in the branching ratios of the initial annihilation. Each initial annihilation process is referred to as an annihilation channel. It is customary to calculate limits and sensitivities assuming that the corresponding annihilation has a 100 % branching ratio

4.4 Dark matter cosmology and halo profiles

into one annihilation channel.

The following annihilation channels have been considered:

$$\begin{aligned}
 WIMP + WIMP \rightarrow & \quad b + \bar{b} \\
 & \quad W^+ + W^- \\
 & \quad \tau^+ + \tau^- \\
 & \quad \mu^+ + \mu^- \\
 & \quad \nu + \bar{\nu}
 \end{aligned} \tag{4.19}$$

The $b\bar{b}$ channel will produce fewer neutrinos at smaller energies than the other channels since, as mentioned before, quarks will mostly produce neutrinos indirectly by hadronic showers. The remaining channels will in most cases directly produce a neutrino, with the W^+W^- channel giving the smallest amount of energy to the neutrino and the $\nu\bar{\nu}$ directly producing a neutrino without further decays (though the neutrino energy can later be reduced by scattering).

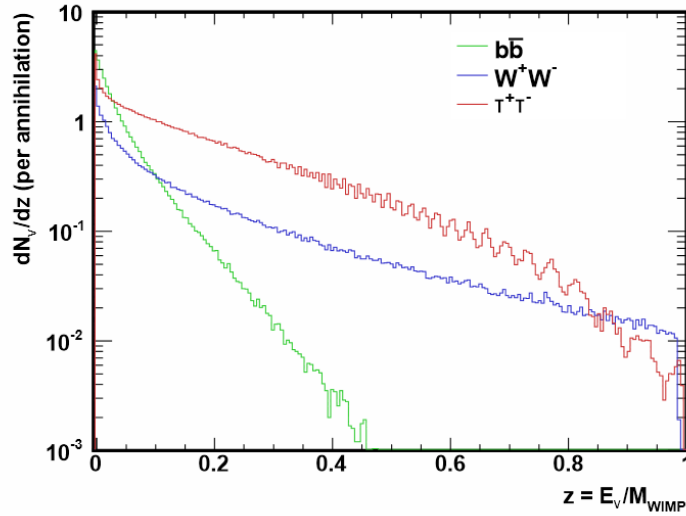


Figure 4.17: The number of neutrinos per WIMP annihilation, as a function of the neutrino energy for the different annihilation channels. These spectra have been calculated for WIMP annihilations in the Sun and a WIMP mass of 1 TeV. The peaks stem from a conversion from a logarithmic to a linear energy axis.

After the annihilation of the WIMPs and the decay of the annihilation

products, the produced neutrinos have to be propagated from the place of the annihilation or decay to the detector. Effects like the absorption of neutrinos in the source medium, which is particularly important for the Sun, have an impact on the resulting neutrino spectra at the detector. These effects lead to expected energies below the energy threshold of ANTARES for neutrinos from annihilations of WIMPs into neutrinos and muons in the Sun.

Neutrino oscillations will occur whilst the neutrinos propagate leading to a 1 : 1 : 1 ratio of neutrino flavours at the detector for sources larger than the oscillation length of the neutrinos.

As a result different signal neutrino spectra are obtained depending on the source considered. Fig. 4.16 shows the spectra at a terrestrial detector for neutrinos from WIMP annihilations in the vacuum. These spectra have been produced by the Cirelli workgroup [63, 64]. The spectra in Fig. 4.17 have been produced using WIMPSim [65].

4.4.6 Neutrino Oscillations

Neutrino oscillations is the phenomenon whereby the flavour of neutrinos changes during propagation. This can be explained by considering that at least two of the neutrino flavours have mass and assuming that the mass eigenstates are different from the flavour eigenstates. The mass and the flavour eigenstates are related by a mixing matrix U , which is called the Pontecorvo-Maki-Nakagawa-Sakata matrix. It can be written as:

$$U = \begin{pmatrix} U_{e_1} & U_{e_2} & U_{e_3} \\ U_{\mu_1} & U_{\mu_2} & U_{\mu_3} \\ U_{\tau_1} & U_{\tau_2} & U_{\tau_3} \end{pmatrix}, \quad (4.20)$$

where the e_i , μ_i and τ_i represent the fraction of the mass eigenstate number i , that belongs to the electron, muon or tau flavour eigenstate.

The oscillation length depends on the difference of the masses between the different neutrino mass eigenstates, the mixing angle θ between the flavour eigenstates, which determines the entries of U , and the neutrino energy. For a simplified 2-flavour-case the probability for the change of a neutrino of flavour α to flavour β due to neutrino oscillations is then:

$$P_{\alpha \rightarrow \beta}(L) = \sin^2(2\theta) \sin^2 \left(\frac{1.27 \Delta m^2 [eV^2] L [km]}{E_\nu [GeV]} \right). \quad (4.21)$$

The corresponding oscillation length (i.e. the half period of the sine in the above function) is consequently:

$$L_{osc} = 2.48 \frac{E_\nu [GeV]}{\Delta m^2 [eV^2]}. \quad (4.22)$$

The full 3-flavour-case the probability can be seen in [66]. The effect of neutrino oscillations is very simple for sources much larger or much further away than the oscillation length of the neutrinos. In this case the oscillations will average the flavours out, so that all flavours are equally prevalent in the resulting neutrino signal.

For closer and smaller sources the oscillations have to be explicitly calculated using equation 4.21. Additionally the effect of the solar plasma and the matter of the Earth on neutrino oscillations (MSW effect [67]) has to be taken into account. This is done using the WIMPSim program that has been used to calculate the muon neutrino signal energy spectra.

Besides neutrino oscillations WIMPSim has to take the absorption of neutrinos in the Earth into account. A plot of the probability of a neutrino to pass the Earth without being absorbed can be seen in Fig. 5.5.

With this all significant model dependencies of the indirect searches presented in this thesis have been presented. In addition to these effects the properties of the detector have an effect on the result of this search as well. The detector itself has been described in Chapter 2. The relevant detector properties like the effective area or the angular resolution have to be calculated from a simulation. This simulation and how these properties are calculated from them will be discussed in the following Chapter.

4.5 Supersymmetry

The term supersymmetry describes a symmetry between fermions and bosons. For such a symmetry to hold an equal number of fermionic and bosonic degrees of freedom are required, which implies that for every fermionic field there has to be exactly one bosonic field and vice versa, or in other words, every fermion has to have a boson (called sfermion) as a supersymmetric partner and every boson has to have a fermionic partner (called bosino).

In the case that supersymmetry exactly holds, sfermions would be produced in equal amounts as the Standard Model fermions in accelerators due to, for example, the decay of Z^0 bosons. Since this is not the case supersymmetry has to be broken in nature, if it exists at all. A straightforward way of breaking supersymmetry would be removing the mass degeneracy between supersymmetric particles and their Standard Model partners. This has to be achieved by a dynamical process which is also called soft or spontaneous symmetry breaking, in order to preserve

renormalisability. An example of soft symmetry breaking in the Standard Model is the Higgs mechanism.

One of the original motivations for supersymmetry is precisely to explain the fact that the mass of the Higgs boson is of the order of the electroweak scale. Being a scalar, the Higgs boson would receive a self-energy that would dominate its mass. These self-energy diagrams receive supersymmetric counterparts which cancel out their contribution, leading to a Higgs mass at the electroweak scale without unnatural fine tuning.

4.5.1 Superspace

In order to mathematically express supersymmetry it is necessary to produce a formalism for expressing quantum states, that can represent fermionic and bosonic degrees of freedom at the same time. Since fermionic fields anticommute but bosonic fields commute with each other and with fermionic fields one has to construct this formalism using mixed Grassmann algebras. These algebras consist of even elements b_j and odd elements a_i . The structure of these algebras is then as follows:

$$[a_i, b_j] = f(a, b) \quad (4.23)$$

$$[a_i, a_j]_+ = g(a, b) \quad (4.24)$$

$$[b_i, b_j] = h(a, b) \quad (4.25)$$

with the structure functions f , g and h .

One then introduces new coordinates θ and their complex conjugate $\bar{\theta}$ in addition to the spatial coordinates x and p . The resulting coordinate space is called superspace and the coordinates θ and $\bar{\theta}$, which are spinors of odd Grassmann parameters, describe whether a state function describes a fermion or a boson. One can then define two operators Q and \bar{Q} which act on the superspace coordinates of a state, so that

$$Q |Boson\rangle = |Fermion\rangle \quad (4.26)$$

$$\bar{Q} |Fermion\rangle = |Boson\rangle \quad (4.27)$$

holds. One can define additional operators that act on the superspace coordinate, but for simplicity we will only consider one set of operators. Using this formalism one can use functions of the superspace coordinates

4.5 Supersymmetry

to represent both fermions and bosons. The operators Q and \bar{Q} can be explicitly written as:

$$Q_A = -i \frac{\partial}{\partial \theta^A} + \sigma_{AB}^\mu \bar{\theta}^{\dot{B}} \frac{\partial}{\partial x_\mu} \quad (4.28)$$

$$\bar{Q}^{\dot{A}} = -i \frac{\partial}{\partial \bar{\theta}^{\dot{A}}} + \sigma^{\mu A \dot{B}} \theta_B \frac{\partial}{\partial x_\mu} \quad (4.29)$$

The eigenvalues of Q are in analogy to gauge theory called supercharges. Also in analogy to gauge theory one can define the covariant derivatives:

$$\mathcal{D}_A = \frac{\partial}{\partial \theta^A} - i \sigma_{AB}^\mu \bar{\theta}^{\dot{B}} \frac{\partial}{\partial x_\mu} \quad (4.30)$$

$$\bar{\mathcal{D}}^{\dot{A}} = \frac{\partial}{\partial \bar{\theta}^{\dot{A}}} - i \sigma^{\mu A \dot{B}} \theta_B \frac{\partial}{\partial x_\mu} \quad (4.31)$$

The σ^μ are here the Pauli spin matrices. Functions of superspace coordinates are called superfields. There are different types of superfields:

- right-handed chiral superfields, which are compatible with \mathcal{D}_A
- left-handed chiral superfields, which are compatible with $\bar{\mathcal{D}}^{\dot{A}}$
- Vector superfields V that fulfill $V^\dagger = V$

An expression a is compatible with an operator O if $O \cdot a = 0$ holds.

4.5.2 The Algebra of Supersymmetry

Now one has to construct the algebra of supersymmetry. Since spin is part of the rotational momentum the operators of supersymmetry, Q and \bar{Q} do not commute with the generators of rotation, which makes these generators part of the Poincaré algebra, which includes the generators of translations and rotations. Due to equations 4.28 and 4.29, Q and \bar{Q} are themselves fermionic Majorana spinors, which is also visible in equations 4.30 and 4.31. In the notation of equation 4.30 the operators Q have the form:

$$Q_A = \begin{pmatrix} Q_m \\ \bar{Q}^{\dot{m}} \end{pmatrix} \quad (4.32)$$

The index A is a spinor index, which makes Q_m and $\bar{Q}^{\dot{m}}$ two-component Weyl spinors. These operators are embedded in the Poincaré algebra in the following way:

$$[Q_m, \bar{Q}_{\dot{n}}]_+ = 2\sigma_{m\dot{n}}^i P_i \quad (4.33)$$

$$[\bar{Q}^{\dot{m}}, Q^n]_+ = 2\sigma^{im\dot{n}} P_i \quad (4.34)$$

$$[Q_m, Q_n]_+ = [\bar{Q}^{\dot{m}}, \bar{Q}^{\dot{n}}]_+ = 0 \quad (4.35)$$

$$[Q_m, P_i] = [Q^{\dot{m}}, P_i] = 0 \quad (4.36)$$

$$[M_{ij}, Q_m] = -(\sigma_{ij})_m^n Q_n \quad (4.37)$$

$$[M_{ij}, Q^{\dot{m}}] = -(\bar{\sigma}_{ij})^{\dot{m}}_{\dot{n}} \bar{Q}^{\dot{n}} \quad (4.38)$$

M_{ij} gives for $i = 1, 2, 3$ and $j = 1, 2, 3$ rise to the angular momentum operator $J_k = \frac{1}{2}\epsilon_{ijk}M_{ij}$ and for $i = 0$ or $j = 0$ the generator of Lorentz boosts. P_i is the 4-momentum operator and σ^i are the Pauli matrices.

4.5.3 Minimal supersymmetric extension of the Standard Model

Assuming a symmetry under the operations defined in the chapters above a lagrangian can be defined. This lagrangian describes a large number of particles, including the partner particles for the quarks, leptons and gauge bosons.

As with the electroweak interaction in the Standard Model, these fields, which are the eigenstates of the interaction, might not be the mass eigenstates, which are the eigenstates of particle propagation and will be identified as the recognizable particles. In general these interaction eigenstates have mass terms of the form $\psi_i M_{ij} \psi_j$ with a non diagonal mass matrix M_{ij} . In addition, the supersymmetric Higgs mechanism is still missing. The number of Higgs bosons has to be even and one receives at least two uncharged and two charged Higgs bosons and their four superpartners are required. If one then takes the uncharged Higgs bosons and the fields \tilde{W}_3 and \tilde{B} , a diagonalisation of their mass matrix gives four neutral majorana particles called neutralinos. Similarly the charged higgsinos and the fields $\tilde{W}_{1/2}$ give arise to the so-called charginos after diagonalisation.

Since no supersymmetric particle has been found yet, supersymmetry should be broken in nature. This can be achieved by different mechanisms. For this thesis it is sufficient to give a phenomenological description. Supersymmetry is broken as soon as the degeneracy of the masses of SM particles and their superpartners is removed. In order to preserve

4.5 Supersymmetry

Symbol	Particle	Symbol	Super- partner	Symbol	Mass- eigenstate
q	Quark	$\tilde{q}_{L,R}$	Squark	$\tilde{q}_{1,2}$	Squark
l	Lepton	$\tilde{l}_{L,R}$	Slepton	$\tilde{l}_{1,2}$	Slepton
ν	Neutrino	$\tilde{\nu}$	Sneutrino	$\tilde{\nu}$	Sneutrino
g	Gluon	\tilde{g}	Gluino	\tilde{g}	Gluino
W^\pm	W-Boson	\tilde{W}^\pm	Wino	$\tilde{\chi}_{1,2}^\pm$	Chargino
H^\pm	Higgs Boson	\tilde{H}^\pm	Higgsino		
B	B-Field	\tilde{B}	Bino	$\tilde{\chi}_{1,2,3,4}^0$	Neutralino
W_3	W-Boson	\tilde{W}_3	Wino		
$H_{1,2,3}$	Higgs Boson	$\tilde{H}_{1,2}$	Higgsino		

Table 4.2: Table of particles in the MSSM

the renormalisability this has to happen in a dynamic process, which is also known as soft symmetry breaking. The term that can break supersymmetry softly is given by [68]:

$$\begin{aligned}
\mathcal{L}_{soft} = & \epsilon_{ij} \left(\tilde{e}_R^* A_e Y_e \tilde{l}_L^i H_1^j - \tilde{d}_R^* A_d Y_d \tilde{q}_L^i H_1^j - \tilde{u}_R^* A_u Y_u \tilde{q}_L^i H_2^j \right) \\
& + H_1^{*i} m_1^2 H_1^i + H_2^{*i} m_2^2 H_2^i - \epsilon_{ij} (B\mu H_1^i H_2^j + h.c.) + \tilde{q}_L^{i*} M_q^2 \tilde{q}_L^i \\
& + \tilde{l}_L^{i*} M_l^2 \tilde{l}_L^i + \tilde{u}_L^{i*} M_u^2 \tilde{u}_L^i + \tilde{d}_L^{i*} M_d^2 \tilde{d}_L^i \\
& + \tilde{e}_L^{i*} M_e^2 \tilde{e}_L^i + \frac{1}{2} M_1 \tilde{B} \tilde{B} + \frac{1}{2} M_2 \left(\tilde{W}_3 \tilde{W}_3 + 2\tilde{W}^+ \tilde{W}^- \right) + \frac{1}{2} M_3 \tilde{g} \tilde{g}
\end{aligned} \tag{4.39}$$

The first line represents couplings to the Higgs sector and the Yukawa-couplings, Y . The second line is the Higgs potential. The third line contains the mass terms of sfermions and the last line contains the gaugino mass terms.

4.5.4 Neutralinos

In the MSSM the neutral higgsino fields, \tilde{H}_1 and \tilde{H}_2 , the bino field, $\tilde{\lambda}_0$, and wino field, $\tilde{\lambda}_3$, give rise to the so-called neutralinos by mixing. This mixing occurs since the neutralino mass matrix $\phi_i M_{ij}$ is non-diagonal,

so that the eigenstates of the interaction are different from the mass eigenstates, which are the eigenstates of propagation. For the neutralino fields, ϕ_i , the following equations hold: [69]

$$\phi_i = \begin{pmatrix} \tilde{\lambda}_0 \\ \tilde{\lambda}_3 \\ \tilde{H}_1 \\ \tilde{H}_2 \end{pmatrix} \quad (4.40)$$

$$M_{ij} = \begin{pmatrix} M_1 & 0 & -\frac{g'\nu_1}{\sqrt{2}} & \frac{g'\nu_2}{\sqrt{2}} \\ 0 & M_2 & \frac{g\nu_1}{\sqrt{2}} & -\frac{g\nu_2}{\sqrt{2}} \\ -\frac{g'\nu_1}{\sqrt{2}} & \frac{g\nu_1}{\sqrt{2}} & \delta_{33} & -\mu \\ \frac{g'\nu_2}{\sqrt{2}} & -\frac{g\nu_2}{\sqrt{2}} & -\mu & \delta_{44} \end{pmatrix} \quad (4.41)$$

where μ is the higgsino mass parameter, M_1 is the bino mass and M_2 is the wino mass. Terms proportional to g and g' couple the higgsinos to the wino and bino. δ_{33} and δ_{44} are top and bottom quark loop corrections to the higgsino masses. Their form is: [70]

$$\delta_{33} = -\frac{3}{16\pi^2} Y_b^2 m_b \sin(2\Theta_{\tilde{b}}) \text{Re} [B_0(Q, b, \tilde{b}_1) - B_0(Q, b, \tilde{b}_2)] \quad (4.42)$$

$$\delta_{44} = -\frac{3}{16\pi^2} Y_t^2 m_t \sin(2\Theta_{\tilde{t}}) \text{Re} [B_0(Q, t, \tilde{t}_1) - B_0(Q, t, \tilde{t}_2)] \quad (4.43)$$

where Y_t and Y_b are the Yukawa couplings of the top and bottom quarks, m_t and m_b are their masses and $\Theta_{\tilde{t}}$ and $\Theta_{\tilde{b}}$ are the flavour mixing angles.

The states that diagonalise the matrix (4.41) represent the neutralinos. The matrix diagonalising the mass matrix is denoted by N_{ij} . For the neutralino fields $\tilde{\chi}_i$ the following equation holds:

$$\tilde{\chi}_i = N_{i1}\tilde{\lambda}_0 + N_{i2}\tilde{\lambda}_3 + N_{i3}\tilde{h}_1 + N_{i4}\tilde{h}_2 \quad (4.44)$$

The entries of the matrix N_{ij} are the components of the neutralinos, that come from the higgsinos, the bino or the wino. N_{i1} is the bino

fraction, N_{i2} the wino fraction and $N_{i3} + N_{i4}$ are the higgsino fraction.

4.5.5 Supersymmetry breaking

As mentioned before supersymmetry has to be broken in Nature, if it is realised at all. This may happen via different mechanisms that remove the degeneracy of the masses of the Standard Model particles with their superpartners. These mechanisms typically involve processes at higher dimensions or in hidden sectors that produce additional mass terms for supersymmetric particles. In the most general case these mechanisms can give independent contributions to all masses in the supersymmetric sector, making all these masses independent parameters. This case is also called the phenomenological minimal supersymmetric extension to the Standard Model (pMSSM). The only assumptions made in this scenario are that there are no flavour changing neutral currents in the supersymmetric sector. The following list contains all 22 independent parameters of the pMSSM:

- The ratio of the Higgs field vacuum expectation values $\tan(\beta)$
- The Higgs masses $m_{H_{1,2}}$, that also called the up- and down-type Higgs masses $m_{H_u} = m_{H_2}$ and $m_{H_d} = m_{H_1}$
- The masses of the gauginos M_1 , for the bino, M_2 for the wino and M_3 for the gluino
- The universal masses of the first two generations of sfermions $m_{\tilde{q}}, m_{\tilde{u}_R}, m_{\tilde{d}_R}, m_{\tilde{e}_r}, m_{\tilde{l}}$
- The masses of the third generation of sfermions $m_{\tilde{Q}}, m_{\tilde{t}_R}, m_{\tilde{b}_R}, m_{\tilde{L}}, m_{\tilde{\tau}_R}$
- The trilinear couplings to sfermions $A_u, A_d, A_e, A_t, A_b, A_\tau$

For other models of these mechanisms assumptions are made that relate the masses of supersymmetric masses with each other at different energy scales, thereby reducing the number of independent parameters. One example would be the minimal super gravity (mSUGRA), where it is assumed, that the mechanisms breaking supersymmetry do so by gravitational phenomena. The result of this is the unification of the sfermion masses, the gaugino masses and the higgsino masses at the energy scale where the symmetry breaking occurs. This reduces the number of independent parameters to $\tan\beta$, the sign of the Higgs mass parameter $sign(\mu)$, the Higgsino and sfermion mass M_0 , the gaugino mass $M_{1/2}$ and the universal trilinear coupling A_0 .

Chapter 5

Data reconstruction and detector simulation

In this chapter both the detector simulation and the event reconstruction algorithms will be discussed.

First in Section 5.1 the two reconstruction algorithms used in this thesis will be explained. Muon tracks are reconstructed from photon hits recorded by the detector. The algorithms reconstruct the muon direction, energy, angular error estimates and many other parameters. This information contains the reconstructed track direction, muon energy and the expected angular resolution for the event. The reconstructions have to be applied to both recorded data and the simulation to be usable for the analysis.

Section 5.3 describes the Monte Carlo simulation of the detector, which is crucial for the calculation of limits and sensitivities and for the analysis process itself. The simulation also serves as a way of testing the understanding of the detector properties and the processes and effects that take place inside the detector. This is done by comparisons between the simulation and the recorded data in section 5.4.

One of the main uses of the simulation is determining the effective area. This is the effective size of the detector assuming an equivalent of 100% detection efficiency. From this the average effective size of the detector for a dark matter signal (the acceptance) can be calculated. How this is done is discussed in section 5.5.

5.1 Data reconstruction algorithms

The data recorded with ANTARES consists only of the registered hits. Both the incident time and the integrated charge of the hits are stored. The properties of the particle event have to be reconstructed from these hits using an event reconstruction algorithm. For the analyses conducted in this thesis only track-like events were used.

5.1 Data reconstruction algorithms

There are two reconstruction algorithms that have been used for the analyses: AAFit [71] and BBFit [72]. Each of these algorithms uses different reconstruction procedures, whose efficiency is different for different energies. After an initial fit to a hit distribution, a preliminary selection of hits has to be performed to reject background light. This hit selection is different for each strategy and mostly depends on coincidence criteria (i.e. the time between hits considering the distance of the relevant PMTs). After the first hit selection the different fits used by the reconstruction algorithms are performed.

The AAFit algorithm performs multiple consecutive reconstruction steps with a maximum likelihood fit as a final step. As a first step a preliminary χ^2 -like fit is performed. This fit provides a starting point for a likelihood fit. This procedure is repeated for different starting points and directions of the track. From all these fits the one with the best final likelihood value is selected. The entire process is illustrated in Fig. 5.1.

AAFit shows the highest efficiency of the two strategies at neutrino energies of 250 GeV or above. This stems largely from the hit selection of AAFit, which excludes events with hits on only one line. The parameter that measures the quality of the reconstruction is called λ and is proportional to the likelihood value from the final likelihood fit. It is defined as:

$$\lambda = \frac{\log(\mathcal{L})}{N_{DOF}} + 0.1 \cdot (N_{comp} - 1) \quad (5.1)$$

where N_{DOF} is the effective number of degrees of freedom in the fitting process and is equal to the number of hits minus the number of free parameters, which is five; N_{comp} is the number of convergences on the same final result from different initial steps. \mathcal{L} is the maximum value of the likelihood function used for this fit.

The estimate of the angular uncertainty, β , is calculated from the error matrix of the final fit that yields the errors on the zenith angle, σ_θ , and the azimuth angle, σ_ϕ . β can be expressed as:

$$\beta = \sqrt{\sin^2(\theta_{rec}) \sigma_\phi^2 + \sigma_\theta^2}. \quad (5.2)$$

There is a strong correlation between λ and β since a well performed fit will show a better angular resolution.

BBFit, the second reconstruction algorithm, performs a χ^2 -like fit. The hit selection does not exclude events with hits on only one line (single-line events) making this strategy better than AAFit for neutrino energies below 250 GeV. For single-line events only the zenith of the primary particle can be calculated, so that these events are best treated separately from the

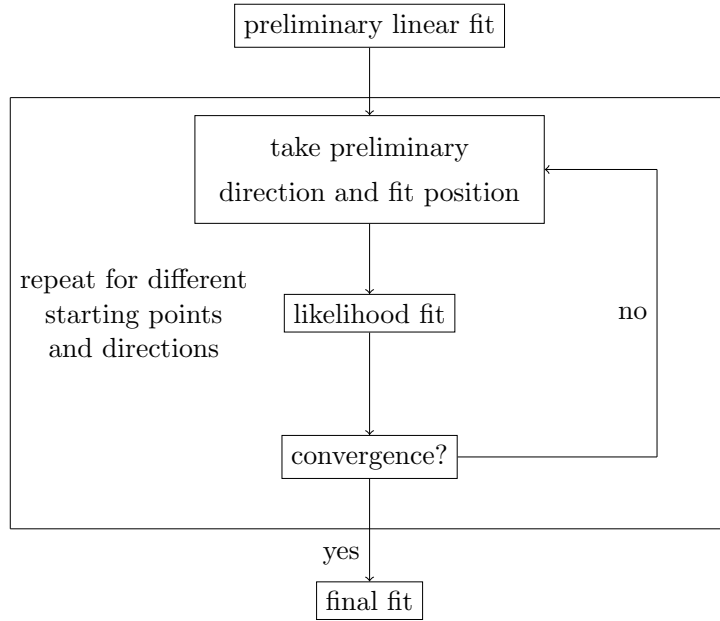


Figure 5.1: Flow diagram of the AAFit algorithm.

rest of the BBFit events. The final χ^2 value is used as the reconstruction quality parameter of this algorithm. χ^2 can be expressed as:

$$\chi^2 = \sum_{i=1}^{N_{hit}} \left(\frac{(t_i^{fit} - t_i)^2}{\sigma_i^2} + \frac{A(a_i)D(d_i^{fit})}{\langle a \rangle d_0} \right) \quad (5.3)$$

where N_{hit} is the number of hits selected for the reconstruction and t_i^{fit} is the expected incident time from the current iteration of the fit, whilst t_i is the measured time of the i th hit. $A(a_i)$ and $D(d_{fit})$ are the so-called factor functions of the hit charge a_i and the fitted distance of the current iteration d_{fit} . $\langle a \rangle$ is the average hit charge in the event and σ_i is the timing uncertainty.

The function $A(a_i)$ can be expressed as:

$$A(a_i) = \frac{a_0 a'_i}{\sqrt{a_0^2 + a_i'^2}} \quad (5.4)$$

where a'_i is the corrected hit charge and a_0 is the artificial saturation. The correction applied in a'_i takes into account the angular acceptance. The function $A(a_i)$ makes sure that the charge of a hit is artificially saturated at a_0 ($A(a_i \ll a_0) \sim a_0$). Similarly the function $D(d_i^{fit})$ assures that there

5.1 Data reconstruction algorithms

is a minimum distance d_0 that is used for the fit ($D(d_i^{fit} \ll d_0) \sim d_0$). $D(d_i^{fit})$ can be written as:

$$D(d_i^{fit}) = \sqrt{d_0^2 + d_i^{fit2}} \quad (5.5)$$

These saturations are used to penalise background hits: since Cherenkov light gets fainter with the distance to the OMs, the product of hit charge and hit distance will remain almost constant at $50 \text{ m} \times \text{Photoelectrons}$. This is not the case for background light, which can produce faint light close to the OMs. The factor functions also give a heuristic penalty to large charges and distances. The average charge $\langle a \rangle$ in the χ^2 parameter makes sure that this penalisation is reduced for high energy events, which tend to generate larger hit charges.

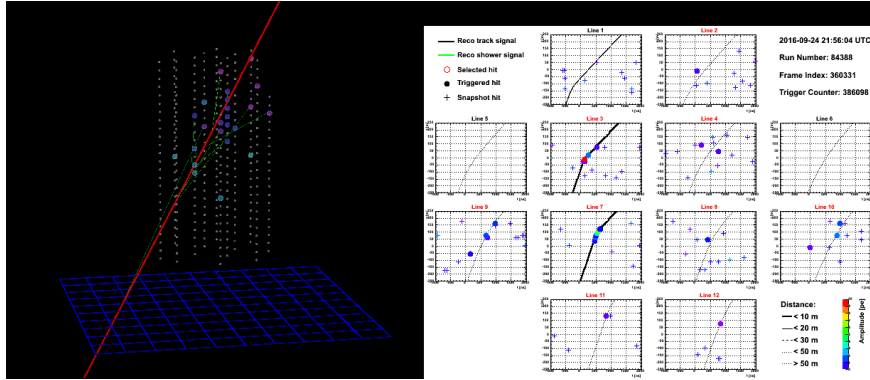


Figure 5.2: An image of the event display. Each plot shows the hits on one line. The Y-Axes show the position on the line, the X-axis shows the time at which the hit was recorded. The lines on some of the plots visualise the preliminary fit with BBFit. The left part of the image shows a 3D visualisation of the event [73].

BBFit assumes a rigid detector geometry (i.e. the storeys do not move in the water stream). This introduces further uncertainty but increases the reconstruction speed and allows the on-line execution of the reconstruction code. BBFit still can produce the best effective area for the lowest neutrino energies due to the inclusion of single line events.

As will be shown later, the BBFit multi-line event analysis does not yield sensitivities below those from AAFit and the BBFit single-line analysis.

BBFit is also used as an on-line reconstruction algorithm for the first reconstruction of detected events which is useful for a variety of purposes.

The ANTARES operation control tools contain a window called the event display, which shows the most recent event reconstructed using BBFit. An image of the event–display is shown in Fig. 5.2.

5.2 Data selection

The data recorded with ANTARES is organised in so–called runs. A run typically has a duration of 2 hours to 4 hours and 30 minutes. This splitting is done to allow the change of the detector setup (e.g. change the triggers used) and take the changing conditions and detector geometry into account.

Not every data run has been used for the analyses presented in this thesis. In some cases the level of bioluminescence or problems with the event triggers or electronics can lead to poor data quality for entire runs. In order to identify these runs, there is a parameter called the basic run quality, which is set to 0 for low quality runs. This value is given to a run, when it does not pass some basic quality checks or shows symptoms of problems with the data quality. The following list contains the criteria a run has to fulfil to be categorized with a basic quality of one or better:

- The run must have a duration of at least 1 second (as computed from the effective number of slices in the run, N_{slices}).
- During the run at least one ARS has to be active on average at every moment (e.g. at least one active frame on average over the whole run).
- No synchronisation issues.
- The difference between the total duration of the run and the effective time calculated from the timeslices ($N_{slices} \cdot T_{frame} N_{sampling}$) has to be below 450 seconds. limited time lost during the run: (Total time) - (Effective time) \leq 450 s.
- The 3N trigger rate has to be within acceptable limits: $10 \text{ mHz} < N_{Triggers3N} < 100 \text{ Hz}$.

There are further cuts on the data that have been used to reduce the atmospheric muon background. Those cuts however only exclude individual events and not entire runs. The final run selection can be made from the quality basic cut. The following table lists the runs and the detector configuration periods from which the data selection of the analyses presented here were made.

5.2 Data selection

Year	Number of lines	Run Numbers	Runs	Live time [<i>days</i>]
2007	5	25800-31048	1466	192.3
2008	10	31051-32491	301	36.2
	9	32525-34389	346	45.3
	10	34392-34427	21	1.9
	12	34432-38230	1318	96.6
2009	12	38241-38357	36	2.4
	11	38363-39589	504	45.5
	10	39590-41677	392	48.05
	9	41679-44109	516	87.3
	8	44112-44326	49	8.5
	10	44472-45538	166	18.3
2010	10	45540-51886	1399	147
	9	51897-52853	399	41.9
	12	52894-54252	614	51.1
2011	12	54253-61904	3118	275.4
2012	12	61908-68170	2418	223.7
2013	12	68692-73064	844	164.7
2014	10	73065-79221	975	262
2015	10	79226-83070	1010	353.9

Table 5.1: Table of the data used in the dark matter analyses

As can be seen, during the different detector configuration periods different numbers of lines were available. Every time the number of available detector lines changes or a new year begins a new detector configuration period starts.

The discrepancy between the duration of the configuration periods in real time and the total live time of the configuration periods (i.e. the total amount of time during which data was taken in the runs of said period) can be quite large and is not entirely due to the basic quality cut. During the data taking periods there were several interruptions of the detector operations, like power cuts in the on-shore station in La Seyne, power failures of the detector or loss of communication to parts of the detector. Up to once per day the detector operations also get interrupted for the

recovery of OMs to which communications were lost.

Additionally several runs were taken for the calibration of the detector and could not be used for the analysis. These runs can be up to 30 minutes long for the calibration with the internal LEDs. During spring the detector has to be set to "reduced high voltage", which means that the PMTs will be supplied with a reduced voltage, so that they will not have enough power to detect photons. This is done to protect the PMTs from damage, since in spring the level of bioluminescence would lead to an over-saturation of the PMTs which can potentially spoil their functionality. During this time no data runs can be taken. There have also been occasions where the detector had to be restarted due to problems with the electronics, the energy supply or the computers in the station in La Seyne-sur-Mer. All these issues lead to a substantial loss of live time. Runs for which no Monte Carlo simulation run are available have not been used in the analysis either.

The resulting number of runs is then 13067 with 1321 days of live time for the data from 2007 to 2012, 13911 runs with 1485.7 days of live time for the 2007 to 2013 data and 15896 runs with 2101.6 days of live time for the 2007 to 2015 data.

5.3 The Monte Carlo Simulation

To understand the behaviour of the detector and to calculate different detector properties and performances, Monte Carlo simulations are carried out. The effective area of the detector is one of the magnitudes that has to be calculated from the simulation. The effective area can be described as the effective size of the detector with a 100% detection efficiency. Since for real data the flux that produced these events is unknown, the effective area can not be calculated from these data and has to be obtained from the simulation.

The Monte Carlo simulation for ANTARES consists of three steps. First, a sample of neutrinos is simulated according to certain neutrino distributions. Amongst the calculated neutrino parameters are the neutrino energy and its direction. From these neutrinos, secondary particles like muons are generated by further Monte Carlo tools and propagated through the detector volume. There is a separate code to simulate atmospheric muons.

The second step is to simulate the detector response to the generated secondary particles. In this step, the production of light by the secondary particle is first simulated. This light is then propagated to the PMTs of the detector taking into account absorption and scattering. The last

5.3 The Monte Carlo Simulation

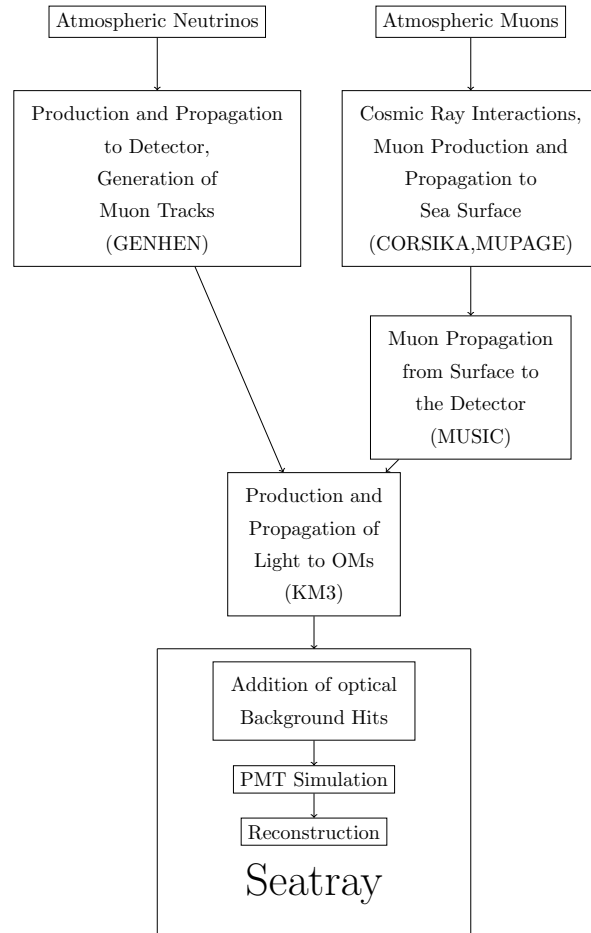


Figure 5.3: Flow diagram of the Monte Carlo simulation chain.

part of this step is the simulation of the PMTs response, their optical and quantum efficiency and the addition of hits from ambient light.

The last step is the reconstruction of the simulated particle events. The reconstruction algorithms used in this step are exactly the same as those described in section 5.1. This also means that there are simulation data for each reconstruction strategy.

Since the detector slowly moves with the water flow at the seabed, the simulation has to take into account the shifting detector geometry. In order to do this, the detector simulation and the recorded data is split into so-called runs. For each recorded run an individual simulation run is produced using the geometry measured for the run in question. The duration of the runs varies with a maximum length of 4 hours until 2013 and 8 hours since then.

5.3.1 Atmospheric muons

Atmospheric muons are a significant part of the background and need to be included in the simulation. Since in this work the background will be taken from time scrambled data the simulated atmospheric muons are only used as a cross-check by comparing its behaviour to that of data. For each run of recorded data, runs for both atmospheric muons and neutrinos has to be produced. These runs generate a sample that is expected to match the real data if the detector and the fluxes of atmospheric particles are modelled correctly by the simulation.

In a first step the unreconstructed muon tracks are generated with a code called MUPAGE [74, 75]. MUPAGE uses a parametrisation of the atmospheric muons inside a volume that contains the detector called the can. The can is chosen so that any muon track that does not cross the can is unlikely to produce hits in the detector. This reduces the CPU time required while ensuring that no relevant tracks are missed.

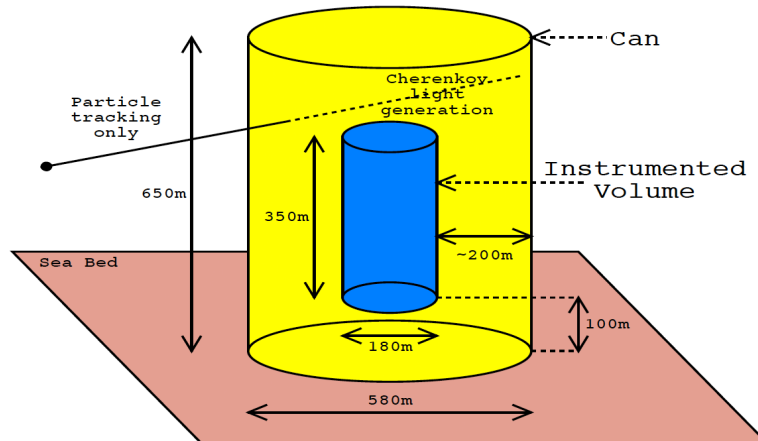


Figure 5.4: A schematic of the can used in MUPAGE.

The parametrisation used in MUPAGE has been generated with the simulation program CORSIKA [76, 77]. There is one parametrisation for each multiplicity of muon bundles. Using these parametrisations, muons of a depth between 1.5 and 5 km with zenith directions of up to 85 degrees can be simulated. The energy of the simulated atmospheric muons has been limited to values above 0.5 GeV. The propagation of the muons through the can is performed with a code called MUSIC [78].

In the MUPAGE simulation muons from atmospheric neutrinos were

5.3 The Monte Carlo Simulation

ignored since their contribution is estimated to be small and mostly present for muon energies above 10 TeV. The overall uncertainty of this part of the simulation is estimated to be around 50%. This uncertainty is the main reason for the observed discrepancies between real data and simulation in section 5.4.

5.3.2 Atmospheric neutrinos

Atmospheric neutrinos are generated using the GENHEN program package. The GENHEN package [79] is capable of simulating all neutrino flavours and both charged current and neutral current neutrino interactions. The neutrinos produce other particles in the vicinity of the detector when interacting with nearby nucleons. The parton model used to calculate the cross-sections of these interactions is the CTEQ6 parton distribution functions [80]. The probability for a neutrino of an energy E to cross the Earth at a certain zenith angle θ has been derived using the equation

$$P_{Earth}(\theta, E) = e^{-N_A \sigma_\nu(E) \rho(\theta)}. \quad (5.6)$$

N_A is the Avogadro number and $\sigma_\nu(E)$ is the interaction cross-section for neutrinos at an energy E when passing through the Earth. $\rho(\theta)$ is the effective density (i.e. the mass density integrated along the neutrino trajectory) for paths with a zenith angle θ in the local detector coordinate system. These probabilities can be seen in Fig. 5.5. The Earth is very permeable for low energy neutrinos and only becomes opaque for neutrinos coming almost directly from below with energies above roughly 10 TeV. Therefore, the opacity of the Earth is not a problem for any of the analyses performed in this thesis.

The neutrino fluxes for the simulation have been generated isotropically, which in the local coordinate system of the detector means that the flux is uniform in azimuth and in the cosine of the zenith. The spectrum of the neutrinos used for the neutrino production is the power law

$$\frac{dN_\nu}{dE}(E) = E^{-\gamma} \quad (5.7)$$

with a so-called spectral index γ . There are two different productions for the atmospheric neutrinos, for energies below and above 20 TeV. γ is 1.7 for the low energy production and 1.4 for the high energy production. This spectrum has been chosen so as to generate for each order of magnitude the same amount of neutrinos in both samples. For low energies, a larger spectral index has been chosen, since these samples have been generated with analyses of solar neutrinos in mind, which have a spectrum with a smaller index.

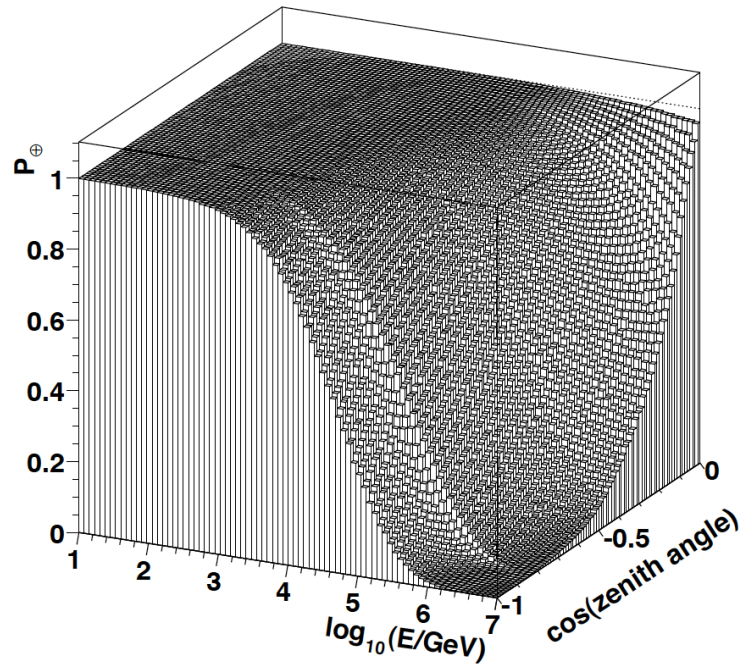


Figure 5.5: The probability for a neutrino to pass through the Earth as a function of the neutrino energy and the zenith angle. (Equation 5.6)

The maximum neutrino energy used in the simulation is 10^8 GeV. The range of the muons produced by these high energy neutrinos is expected to be several hundred metres and the amount of light produced is very large. Therefore, the simulation can not be restricted to only tracks within the can as in the simulation of atmospheric muons. Instead, a 25-km high cylinder with a 25-km radius is used as a volume restriction instead. These 25 km correspond to the maximum propagation range of the produced muons. The propagation of these muons is handled by MUSIC as in the case of the simulation of atmospheric muons.

5.3.3 Detector response and light propagation

To simulate the response of the detector to the crossing muons, the Cherenkov light induced by these muons has to be propagated through the sea water to the OMs. This is done with a code called KM3 [81]. KM3 has been written using the GEANT Monte Carlo tool [82]. It does not only contain the code for the light propagation but also includes a modified version of MUSIC to propagate the muons and derive the starting points

5.3 The Monte Carlo Simulation

for the light propagation. The propagation with KM3 takes scattering and absorption into account.

KM3 uses so-called photon tables. These tables contain distributions of PMT hits and arrival times for muons from different directions with different energies. They are produced using a full particle physics simulation of a large number of muons including the light propagation. The time and direction of photons are convolved at concentric distances from the track with different orientations of the OMs. This procedure has been chosen to reduce the computing time of the simulation for the individual runs. This allows to generate sufficiently high statistics within a reasonable amount of time. Therefore any implementation of further effects during the propagation have to be done with these photon tables.

After the propagation of the Cherenkov light, the optical background has to be added and the response of the detector has to be simulated. This is done with a package called SeaTray. SeaTray adds light from bioluminescence and ^{40}K decays. The ^{40}K decays are simulated as a 60 kHz signal of hits on each OM whilst the hit rates and distribution of bioluminescence are taken from actual data, since this background is much harder to model.

After adding the background light, a program called TriggerEfficiency is used to calculate the response of ANTARES. In the TriggerEfficiency code many different effects are implemented. On a basic level the triggers of the ANTARES detector described in Section 2.6 are implemented after the calibration and the environment conditions are accounted for. It also includes electronic noise and other electronic effects. TriggerEfficiency produces ANTARES event files that can be used as an input for the reconstruction algorithms as a last step of the simulation chain.

5.3.4 Statistical weights

In a typical Monte Carlo simulation events are accepted based on their likelihood to be present in a real data sample. For the simulation of a neutrino telescope this means that simulated neutrinos would only be accepted with a probability equal to the probability of a neutrino to produce a detectable interaction inside or in the vicinity of the detector (e.g. generate a muon by a weak interaction). Since this probability is small, a vast amount of simulated neutrinos would have to be rejected. There would also be a large amount of neutrinos that have to be excluded from the simulation due to absorption in the Earth. This would not be very efficient and therefore a different approach is chosen. Each event is given a set of statistical weights that are proportional to these probabilities. The weights also include parameters that take into account some limitations

of the simulation such as the limited energy range. The usage of weights also allows to simulate a smaller number of neutrinos and "stretch" the statistics using the weights.

In ANTARES these weights are called w_2 and w_3 , respectively. The weight w_2 is used to calculate detector properties, like the effective area or the point spread function. It can be expressed as:

$$w_2 = I_\theta \cdot I_{Energy} \cdot (1 - P_{Earth}) \cdot \sigma_{CC} \cdot Vol \cdot \rho_N \cdot E^\gamma \cdot T \quad (5.8)$$

where I_θ is a phase-space factor that takes into account the fact that the simulation is carried out only for part of the sky; I_{Energy} takes into account that the simulation is only run for limited energy ranges: A low-energy range from 0 to 20 TeV and a high-energy range from 20 TeV to 1 PeV, as mentioned above; P_{Earth} is the likelihood for the neutrino to be absorbed in the Earth from equation 5.6, which becomes larger at high energies and has a negligible effect for neutrinos from annihilations of WIMPs with masses below 10 TeV. σ_{CC} is the cross-section for charged current interactions between neutrinos and nucleons that produce a muon; Vol is the sensitive volume of the detector and ρ_N is the number density of nucleons in water. This combination of factors gives the probability that the neutrino has crossed the Earth and interacted in the sensitive volume of the detector. The factor E^γ is a correction to the energy spectrum used to produce the original neutrinos in the first step. T is the number of seconds in a year. T serves as a conversion of units from number of neutrinos per second to number of neutrinos per year.

The probability for a muon event to be reconstructed in the detector is included in the simulation by using the different reconstruction algorithms for the detector. If a simulated event can not be reconstructed by one of the algorithms it will not appear in the final data files.

The second weight, w_3 , which is used to generate comparisons between recorded data and the Monte Carlo simulation, contains all factors used in w_2 and can be written down in terms of the latter as:

$$w_3 = w_2 \cdot \Phi_{exp} \quad (5.9)$$

where Φ_{exp} is the expected neutrino flux through the detector at the Earth's surface. A comparison between simulation and data can now be made by filling a histogram of a chosen event parameter, such as the reconstructed track direction or the reconstructed energy, with the simulation data using w_3 as a weight. This histogram should reproduce the behaviour of the real data for the same runs within statistical uncertainties, provided that the simulation describes the detector well and the expected flux matches

the real flux. This, however, is not the case, so some deviations are to be expected.

In the case of the simulation of the atmospheric muons most of the factors of w_3 are calculated differently. The expected statistical properties of atmospheric muons (their spectrum, cross-sections etc...) are implemented in the particle generators in MUPAGE. Therefore, w_3 is set to 3 for all simulated atmospheric muons in the period of 2007 to 2012 and 10 for the simulation after 2012. The simulation of the atmospheric muons is expected to reproduce the data with a 20% accuracy.

5.4 Comparison to Data

Since the simulation is of key importance for the analyses, it has to be compared to the recorded data to verify that the data are modelled correctly. The comparisons made here have to check in particular whether the simulation data behave correctly with respect to the event parameters that have been used in the analysis. These parameters are the event position, the reconstruction quality λ for AAFit and χ^2 for BBFit, the angular error estimate, β , and the number of hits used in the reconstruction.

As mentioned in the previous section there is an expected discrepancy between the recorded data and the simulated atmospheric muons, which has to be taken into account when evaluating these comparisons. This discrepancy will lead to a systematic overestimation of the recorded data by the simulation. Since the simulation of atmospheric muons has not been used in the analysis, this discrepancy does not affect the accuracy of the analysis.

5.4.1 AAFit

In the comparisons for AAFit the angular error estimate has been cut to one degree or below and a quality cut of $\lambda > -5.4$ was used. Also, for all comparisons only upgoing events were used. These cuts were chosen since they are the optimum cuts from the Sun analysis, which uses the 2007 to 2012 sample.

Fig. 5.6 shows a comparison of the distribution of events as a function of the reconstruction quality parameter λ . Logically the reconstruction quality cut mentioned above was not used here. The histogram shows the estimate from the Monte Carlo simulation and the crosses show the real data with their statistical error. The shape of the plot shows good agreement between simulation and recorded data for high values of λ . Only for low values there is a notable discrepancy. At these values of λ the atmospheric muons dominate the statistics. This can be seen in

Fig. 1 in the appendix. This visible discrepancy can be explained by the inaccuracy of the simulation of atmospheric muons in particular when they are badly reconstructed.

In Fig. 5.7 a comparison of the distribution of the number of events as a function of the number of lines used in the reconstruction is shown. A consistent offset between real data and the simulation can be observed, with the simulation overestimating the recorded data. Despite this offset the behaviour of the simulated data agrees well with the recorded data.

Similarly in Fig. 5.8, which shows a comparison of the distribution of the number of events as a function of the number of hits used in the reconstruction, a persistent offset can be seen. The graphic shows again a good agreement between the shapes of the simulation and the data distributions. Only at very small numbers of hits, that is less than 14 hits, the simulation underestimates the recorded data.

In Fig. 5.9 an overall good agreement between the behaviour of the data and the simulation with regard to the elevation, $\cos(\theta)$, can be seen. Events close to an elevation of 1 (e.g. strongly upgoing events) have a better matching between data and simulation. At these elevations atmospheric muons are practically absent and the uncertainty in the simulation of atmospheric muons is expected to have a small influence.

5.4.2 BBFit

For the BBFit comparisons again only upgoing events were used. Both single-line and multi-line events were included in the comparisons with a cut on the reconstruction quality of $\chi^2 < 1.4$. The comparisons shown here are again using the 2007 to 2012 sample and the optimum cuts from the Sun analysis.

In Fig. 5.10 a comparison of the distribution of the number of events as a function of the reconstruction parameter χ^2 of the BBFit reconstruction algorithm is shown. For well reconstructed tracks, $\chi^2 < 1$, the agreement between real data and the simulation is good. For badly reconstructed tracks, however, atmospheric muons dominate and as for AAFit, a discrepancy can be seen. This can be checked in Fig. 4 in the appendix.

Fig. 5.11 shows a comparison of the distribution of the number of events as a function of the number of lines used for the reconstruction. A good overall agreement between data and simulation for single-line events, much better than for multi-line events, can be seen. This is also reflected by Fig. 5.12, which shows a comparison of the distribution of the number of events as a function of the number of hits used in the reconstruction, where the agreement between data and simulation is much better for events with

5.4 Comparison to Data

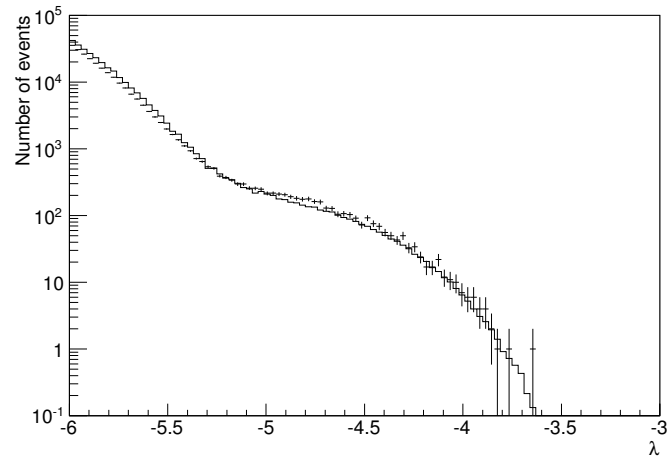


Figure 5.6: The number of events as a function of the event reconstruction quality λ for the AAFit algorithm. The events reconstructed in the 2007-2012 period are shown. The histogram shows the background estimate generated by Monte Carlo simulation, the crosses represent the recorded data.

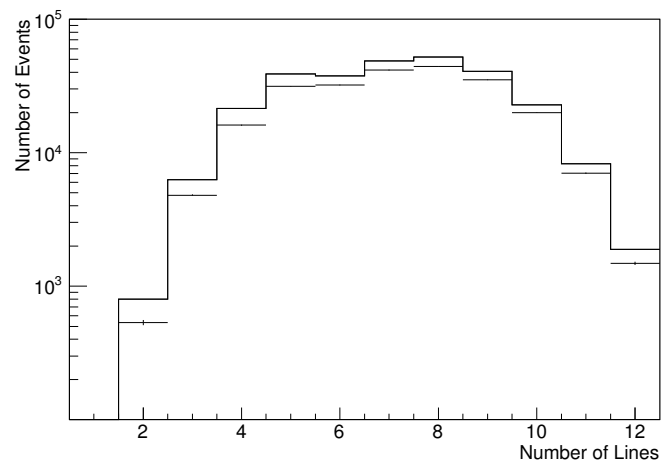


Figure 5.7: The number of events as a function of the number of lines used in the reconstruction. The events reconstructed in the 2007-2012 period with the AAFit algorithm are shown. The histogram shows the background estimate generated by Monte Carlo simulation, the crosses represent the recorded data.

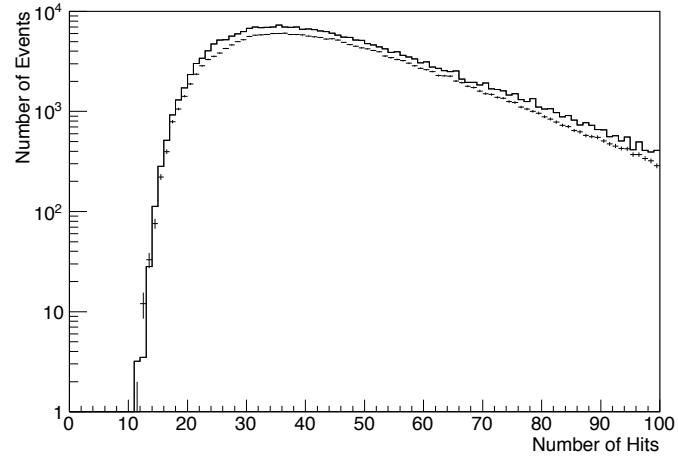


Figure 5.8: The number of events as a function of the number of hits used in the reconstruction. The events reconstructed in the 2007-2012 period with the AAFit algorithm are shown. The line shows the background estimate generated from the Monte Carlo simulation, the crosses represent the recorded data.

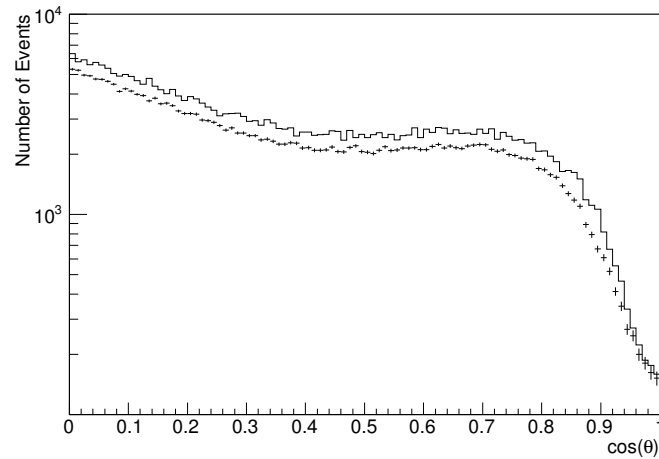


Figure 5.9: The number of events as a function of the event elevation. The events reconstructed in the 2007-2012 period with the AAFit algorithm are shown. The line shows the background estimate generated from the Monte Carlo simulation, the crosses represent the recorded data.

5.4 Comparison to Data

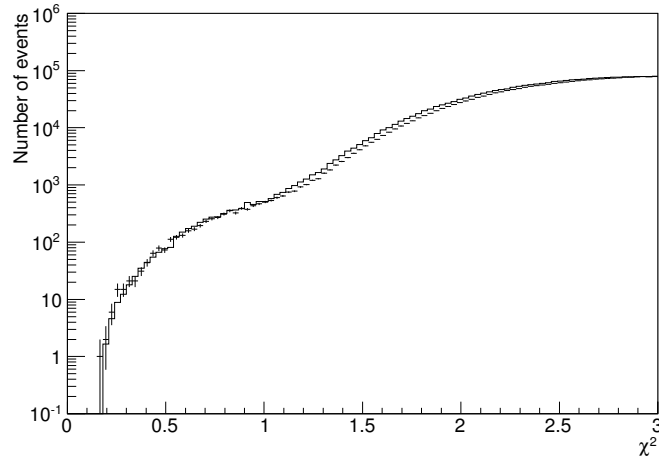


Figure 5.10: The number of events as a function of the event reconstruction quality χ^2 . The events reconstructed in the 2007-2012 period with the BBFit algorithm are shown. The line shows the background estimate generated from the Monte Carlo simulation, the crosses represent the recorded data.

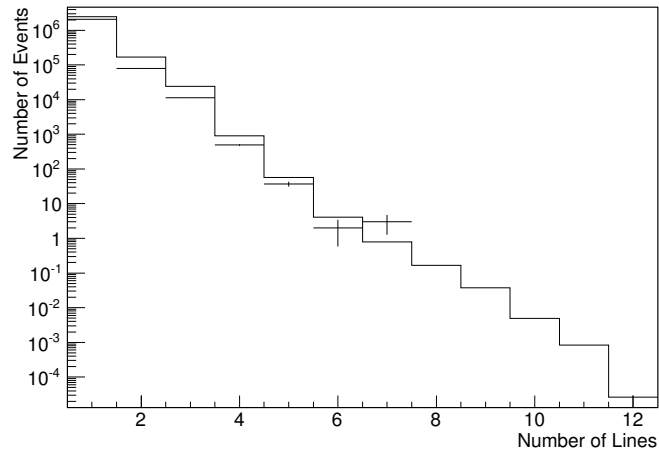


Figure 5.11: The number of events as a function of the number of lines used in the reconstruction. The events reconstructed in the 2007-2012 period with the BBFit algorithm are shown. The line shows the background estimate generated from the Monte Carlo simulation, the crosses represent the recorded data.

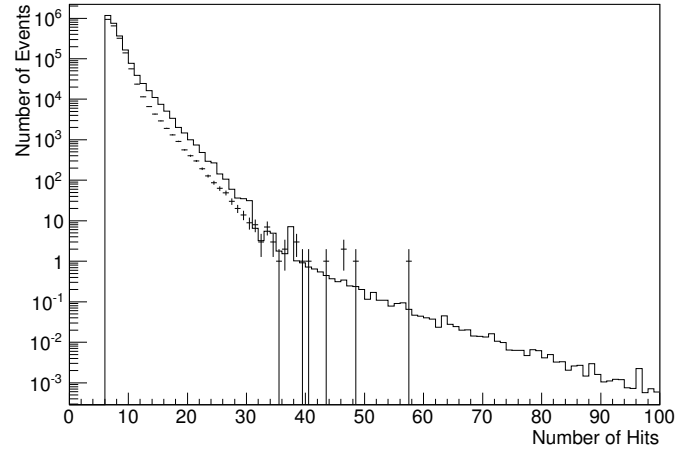


Figure 5.12: The number of events as a function of the number of hits used in the reconstruction. The events reconstructed in the 2007-2012 period with the BBFit algorithm are shown. The line shows the background estimate generated from the Monte Carlo simulation, the crosses represent the recorded data.

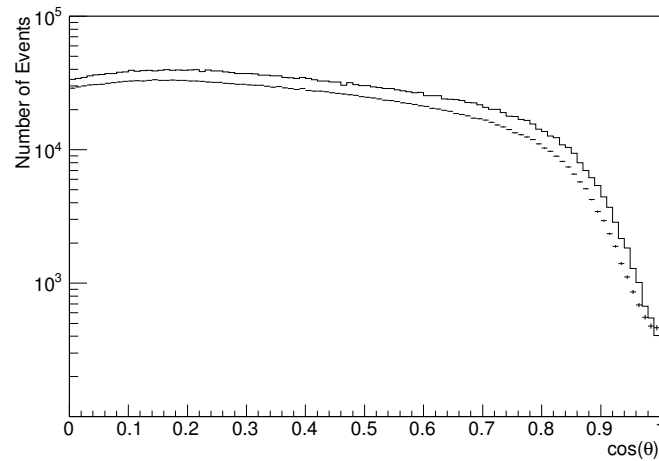


Figure 5.13: The number of events as a function of the event elevation. The events reconstructed in the 2007-2012 period with the BBFit algorithm are shown. The line shows the background estimate generated from the Monte Carlo simulation, the crosses represent the recorded data.

5.5 The Acceptance

fewer hits which is typical for single line events. Further comparisons for single–line events are found in the appendix 1. The difference for the multi–line events does not seem to depend on neither the number of hits nor the number of lines used for reconstruction. This indicates that, assuming the difference between the data and the simulation stems from the atmospheric muons, the simulation for the atmospheric neutrinos produces reasonable results. The comparison for the elevation in Fig. 5.13 shows great similarity to the comparison shown in Fig. 5.9. Again a good agreement for the overall behaviour of the data can be seen although a general offset is persistent for BBFit as well.

Again all comparisons presented here were performed using the runs from 2007 to 2012. Comparisons for 2013 and 2015 are in the appendix 1 as before.

After reviewing the comparison between the recorded data and the Monte Carlo simulation it is apparent, that the simulation does overestimate the data slightly but generally produces the right behaviour. As mentioned before the existing differences can be very well explained by the inaccuracy of the simulation of atmospheric muons. Only the simulation of atmospheric neutrinos is later used in the analysis for calculating the effective area and the point spread function.

5.5 The Acceptance

The acceptance measures the sensitivity to a signal with a certain spectrum and relates the number of detected signal events, μ_{det} , to the total signal neutrino flux, Φ_ν , through the following equation:

$$\Phi_\nu \cdot Acc = \mu_{det}. \quad (5.10)$$

In order to calculate the acceptance, the effective area A_{eff} has to be known first. The effective area can be defined using the following equation:

$$\int_{E_{th}}^{\infty} \frac{d\Phi_\nu(E_\nu)}{dE_\nu} \cdot A_{eff}(E_\nu) dE_\nu = \mu_{det}. \quad (5.11)$$

E_ν is the neutrino energy, E_{th} is the energy threshold of ANTARES. Since the neutrino flux producing the detected events in the recorded data is a priori unknown, the effective area has to be calculated from the simulation. This is done using the aforementioned statistical weights that are calculated for each simulated event.

In order to calculate the effective area some parts of w_2 in equation 5.8 have to be adapted to the analysis. The analyses in this thesis

look for a signal in specific sources, so I_{theta} has to be replaced by a factor representing the visibility. This factor is the probability density $V(\theta, \phi)d\Omega(\theta, \phi)$ to find the Sun at the direction specified by the zenith angle θ and the azimuth angle ϕ . This probability density has to be normalized as follows:

$$\int_{4\pi} V(\theta, \phi)d\Omega = 1 \quad (5.12)$$

where θ and ϕ are the azimuth and zenith angle in the local detector coordinate system. The second parameter that has to be modified is I_{Energy} . If the energy-dependent effective area is calculated, this phase space factor has to be corrected for the individual energy bins of the histogram for which the effective area is computed. I_{Energy} can be expressed as:

$$\int_{E_{min}}^{E_{max}} E^{-\gamma} dE = \frac{E_{max}^{1-\gamma} - E_{min}^{1-\gamma}}{1-\gamma} \quad (5.13)$$

where E_{min} and E_{max} are the minimal and maximal energy considered for the simulation, with the low energy simulation runs going from 0 to 20 TeV and the high energy runs going from 20 to 100 TeV. The modified I_{Energy} uses the bin edges as values for E_{min} and E_{max} instead of each bin receiving its own I_{Energy} . If the energy binning of the effective area histogram is fine enough, the modified I_{Energy} already corrects for the spectrum used for the generation of the neutrinos, which means that the factor E^γ has to be swapped for the expected signal spectrum from w_2 for the calculation of the acceptance as well. An example of the effective area for a signal with a flat spectrum from the Galactic Centre can be seen in Fig. 5.14 and 5.15 for the AAFit multi-line and the BBFit single-line events respectively.

Using the weight w_2 with the modifications mentioned above the effective area can be computed for the atmospheric neutrinos from the simulation data. The analysis uses reconstruction quality cuts, which exclude detected events and affect the effective area. Consequently the effective area has to be produced in dependence of not only the neutrino energy, but also the considered quality cut.

Unlike the effective area, the acceptance depends on the spectrum of the signal neutrinos arriving at the detector. It is calculated by convolving the effective area with the expected neutrino spectra. This is done according to the following equation:

5.5 The Acceptance

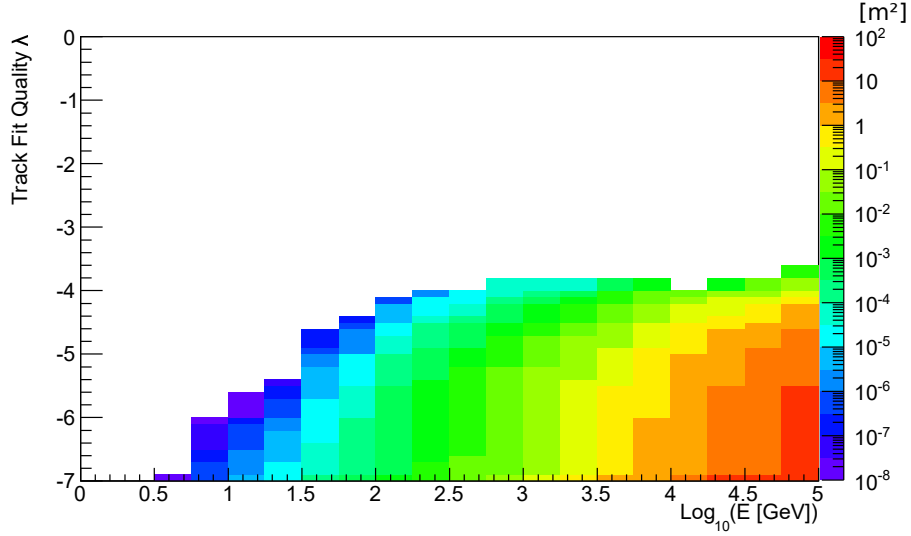


Figure 5.14: Effective area as a function of the quality cut and the neutrino energy for signals from the Galactic Centre. The AAFit reconstruction strategy has been used.

$$\begin{aligned}
 Acc(m_{WIMP}, Ch) = & \int_{E_{th}}^{m_{WIMP}} A_{eff}(E_{\nu_\mu}) \left. \frac{dN_{\nu_\mu}}{dE_{\nu_\mu}} \right|_{Det, Ch} dE_{\nu_\mu} \\
 & + \int_{E_{th}}^{m_{WIMP}} A_{eff}(E_{\bar{\nu}_\mu}) \left. \frac{dN_{\bar{\nu}_\mu}}{dE_{\bar{\nu}_\mu}} \right|_{Det, Ch} dE_{\bar{\nu}_\mu}
 \end{aligned} \quad (5.14)$$

where $A_{eff}(E_{\nu_\mu})$ is the effective area for the muon neutrino energy E_{ν_μ} (or muon antineutrino energy $E_{\bar{\nu}_\mu}$); $\left. \frac{dN_{\nu_\mu}}{dE_{\nu_\mu}} \right|_{Det, Ch}$ is the signal neutrino spectrum at the position of the detector for one particular annihilation channel Ch listed in equation 4.19 in section 4.4.5, E_{th} is the energy threshold of the detector and m_{WIMP} is the WIMP mass.

As the effective area, the acceptance has to be computed for each quality cut, so that the final result of these calculations will be histograms of the acceptance versus the quality cut for each combination of WIMP mass and annihilation channel.

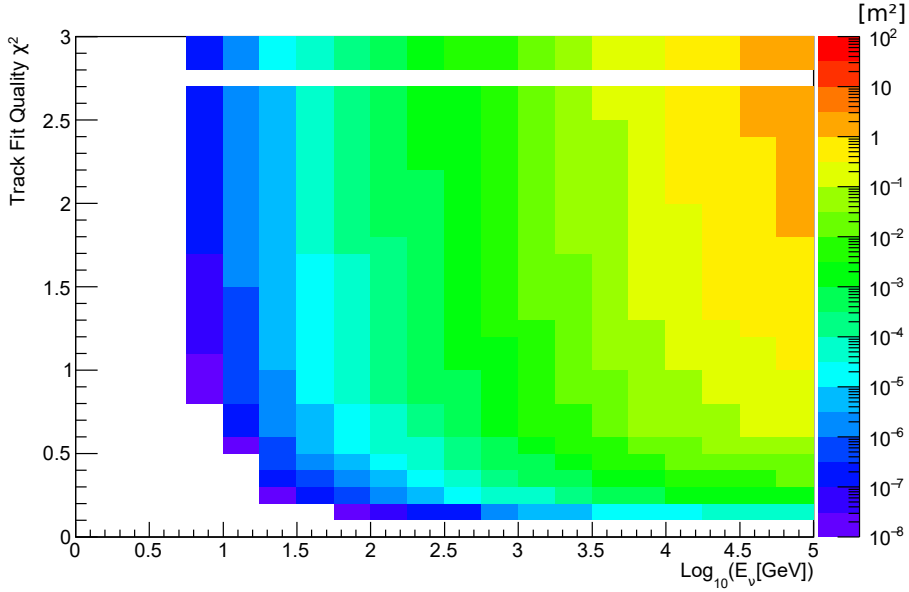


Figure 5.15: Effective area as a function of the quality cut and the neutrino energy for signals from the Galactic Centre. This effective area is produced for BBFit single line events.

5.5.1 Implementation

The calculation of the acceptance is implemented in several independent steps that allow several checks and controls of the accuracy of the procedure. In a first step, 2D histograms are calculated of the number of Monte Carlo events versus the reconstruction quality parameter χ^2 for BBFit or λ for AAFit and the true neutrino energy from the neutrino generation using the corrected w_2 mentioned above. In this calculation step the source visibility is taken into account as well.

For each reconstruction quality or angular error estimate bin, a separate histogram is generated multiplying the content with the correct I_{Energy} factor for each energy bin and making the new histograms cumulative in the reconstruction quality. At this stage the individual histograms represent the effective area for different quality or angular error cuts for ANTARES, which can be compared with other analyses as a sanity check.

In the next step, the effective area is just convolved with the expected neutrino signal spectrum according to equation 5.14. This process is particularly time consuming since a large number of histograms have to be treated. Finally, the histograms get integrated over the energy and a new histogram of the acceptance as a function of the reconstruction

5.5 The Acceptance

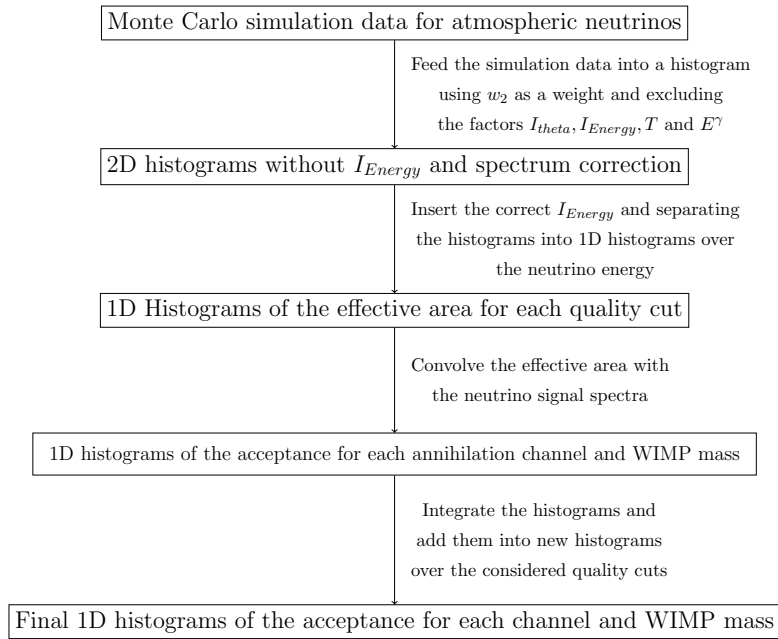


Figure 5.16: Diagram of the calculation process of the acceptance.

quality cut is produced.

This process is done individually for each detector configuration period laid out in section 5.2 with the results being scaled by the number of runs and events per period to obtain an acceptance per day of live time. These different histograms are then added with the effective live time in days as a weight to obtain the final acceptance for the whole data-taking period. The whole process is summarized in the chart shown in Fig. 5.16.

Chapter 6

The Analysis Method

In this thesis a likelihood-based method has been used for the calculation of limits and sensitivities. This method is also called "unbinned" method in contrast to the "binned" method used for the dark matter searches previously conducted with the ANTARES detector [83]. In the binned method a search cone or search "bin" around the analysed source is optimised. The amount of background events in this cone is then estimated from time-scrambled data or directly taken from the unblinded data. Sensitivity or, in the case of unblinded data, limits, are calculated from the background estimate.

In contrast, the likelihood method uses a so-called likelihood function to distinguish between background and signal. The likelihood uses the characteristics of events, such as the track direction, the number of hits used in the reconstruction or the reconstruction quality. All characteristics that behave differently for signal and background events can be useful for the likelihood function.

In order to quantify the efficiency of the likelihood function, random distributions of events, mimicking the expected behaviour of real data and the expected signal, are generated. The production process of these random skies, or pseudo-experiments, is explained in section 6.1. Using the likelihood function, which will be detailed in section 6.2, a parameter, called the test statistic (TS) is computed. The limits and sensitivities are then calculated from the distribution of the TS values of the pseudo-experiments (see section 6.3.1 for more details).

The limits and sensitivities that are generated from the TS distributions are first obtained in terms of detected events. Afterwards these limits and sensitivities can be converted to limits on the neutrino flux and on the annihilation or scattering cross-section, if no signal is found. The entire process is shown schematically in Fig. 6.1.

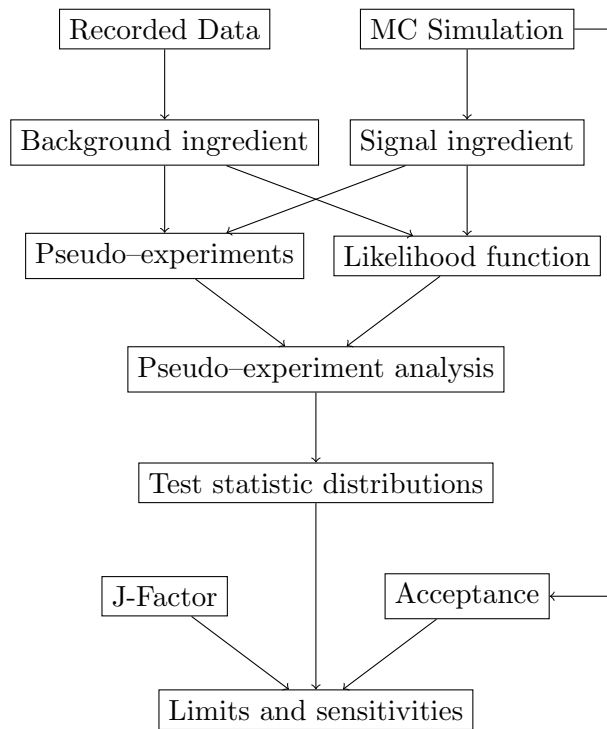


Figure 6.1: Diagram of the likelihood-based analysis procedure for dark matter searches.

6.1 Pseudo-experiments

The first step of the unbinned analysis method is the production of samples of randomly generated events, called random skies, that simulate the expected background and insert different numbers of fake signal events into them. These simulated skies, also called pseudo-experiments (PEs), are used to determine the response of the so-called likelihood function to the presence of a signal.

The PEs are generated using only a part of the accessible event information, which is also used in the likelihood function. The background events are generated according to the statistical behaviour of the blinded data. The blinding is achieved by time scrambling. Amongst the generated event informations, only the position of the events relative to the source is time dependent. In the case of the Galactic Centre analysis the blinding is done using celestial coordinates. The right ascension in celestial coordinates is the angle on the x-y-plane from the x-axis, which points towards the Sun during the spring equinox. In equatorial coordinates the declination

of the GC is time independent and the time scrambling is implemented using a purely random right ascension for each event.

The celestial coordinates used in this thesis are similar to regular equatorial coordinates with the difference that there is a 90 degree shift between the zenith in spherical coordinates and the declination coordinate. The declination is the angle to the equatorial x-y-plane, with negative declinations for celestial objects in the southern equatorial hemisphere. The entire coordinate system is illustrated in Figure 6.2.

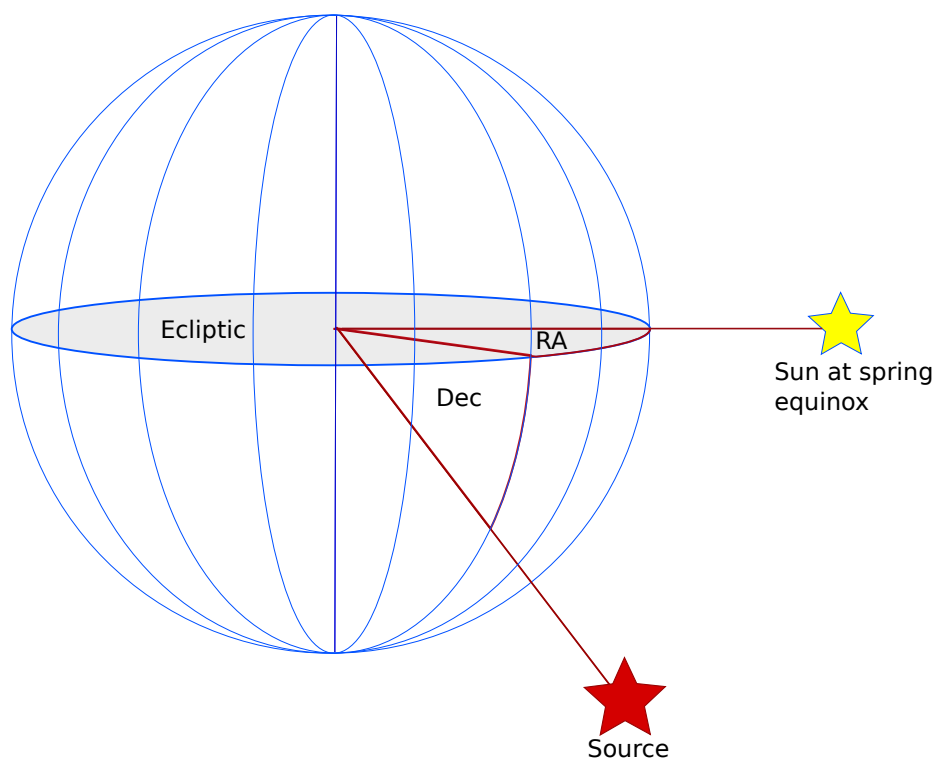


Figure 6.2: A schematic of the celestial coordinate system used in the analysis.

This however is not the case for the Sun that moves in equatorial coordinates and a different approach is chosen. The ingredients for the Sun analysis are calculated in local coordinates using randomly picked Sun positions that have been produced so as to be statistically representative of the movement of the Sun across the local sky. Instead of producing event positions on a local sky only the distance to the source is generated, so that the motion of the Sun does not have to be taken into account any further. A detailed description of the background statistics used for the Sun will be given in section 6.4

6.2 The likelihood function

The likelihood function is used to analyse the pseudo-experiments and determine the number of signal events in each experiment. To this end the likelihood function represents the probability that a pseudo-experiment contains a certain number of signal events according to the detector properties, the statistics of the background and the expected behaviour of the signal. The standard version of the likelihood function can be written as:

$$L(n_s) = \prod_{i=1}^{N_{tot}} \left(\frac{n_s}{N_{tot}} S(\psi_i, p_i, q_i) + \frac{N_{tot} - n_s}{N_{tot}} B(dec_i, p_i, q_i) \right) \quad (6.1)$$

or in its logarithmic form as:

$$\log_{10}(L(n_s)) = \sum_{i=1}^{N_{tot}} \log_{10} \left(\frac{n_s}{N_{tot}} S(\psi_i, p_i, q_i) + \frac{N_{tot} - n_s}{N_{tot}} B(dec_i, p_i, q_i) \right), \quad (6.2)$$

where N_{tot} is the total number of reconstructed events, n_s is the assumed number of signal events, ψ_i is the angular separation of the i -th event to the centre of the source, dec_i is the declination of the i -th event, p_i and q_i are additional event parameters like the reconstruction quality or the estimated neutrino energy. S represents the ANTARES point spread function (PSF) for the signal and B is a function that represents the behaviour of the background.

Any parameter supplied by the reconstruction could be used in the likelihood, but those that make the S and B functions more different are more useful, since the signal and background likelihoods will differ more. One of these useful parameters is the neutrino energy, which can be estimated from the reconstructed event. The number of selected hits in the reconstruction can be used as a proxy of the event energy.

A large fraction of the background consists of atmospheric muons that were wrongly reconstructed as upgoing. These events show a bad reconstruction quality and angular error estimate and can be effectively excluded by simple cuts on these parameters.

6.2.1 Extended likelihood function

Another likelihood function that can be used is the extended likelihood function [84]. This likelihood is sensitive to the number of events in the random sky. In an analysis, where the overall amount of events can indicate the presence of a signal, an improvement can be achieved. For a very extended source, like the GC, a large amount of signal events has to be introduced into the random skies before the signal becomes noticeable and the overall amount of events will become higher.

In each likelihood function a set $\{x_1, \dots, x_N\}$ of N measurements is considered. For ANTARES one measurement is an event. The likelihood function also has a set of variables $\{q_1, \dots, q_M\}$ that are used to maximise the likelihood in the analysis. In this thesis only the number of proposed signal events, n_s , is used as such a variable. A likelihood function can then generally be expressed as

$$L = \prod_{i=1}^N P(x_i, q_1, \dots, q_M), \quad (6.3)$$

with the $P(x_i, q_1, \dots, q_M)$ is the likelihood for event number i . In order to compare the likelihood values of different pseudo-experiments the likelihood has to be normalised. In the standard likelihood the normalisation is set for the likelihood for each individual event by:

$$\int P(p_i, q_1 \dots q_M) dp_i = 1. \quad (6.4)$$

This condition is different in the extended likelihood. The likelihood $P'(p_i, q_1 \dots q_M)$ for an event x_i is normalised to the expected number of measurements \mathcal{N} , which might differ from the actual number of measurements N . The normalisation is then

$$\int P'(p_i, q_1 \dots q_M) dp_i = \mathcal{N}(q_1 \dots q_M). \quad (6.5)$$

It is not obvious what effect replacing P by P' has on the likelihood function for the complete likelihood function. First the new normalisation is extremely large and further changes to the likelihood have to be done to handle it.

One way to do this is to take into account that an event that is detected at x_i can not be detected anywhere else. The range of the parameters x_i is divided into narrow segments, Δx_i . For sufficiently narrow Δx_i the probability to have two events inside one of these segments is negligible. With this division the likelihood to detect no event within an interval Δx is then

6.2 The likelihood function

$$P'_0(x) = e^{-\Delta x P'(x)} \quad (6.6)$$

and the probability to detect one event in Δx is

$$P'_1(x) = \Delta x P'(x) e^{-\Delta x P'(x)}. \quad (6.7)$$

The likelihood function for the complete range of x then is the product of all individual probabilities:

$$L = \prod_{i=1}^N \Delta x P'(x_i) \prod_{j=0}^{N_{bins}} e^{-\Delta x P'(x_j)}, \quad (6.8)$$

where N_{bins} is the number of intervals of x . Then the limit $\Delta x \rightarrow dx$ is taken and the first term becomes the probability density $P'(x)dx$ to find an event between x and $x + dx$. The second part becomes:

$$\prod_{j=0}^{N_{bins}} e^{-\Delta x P'(x_j)} = e^{-\sum_{j=0}^{N_{bins}} \Delta x P'(x_j)} \rightarrow e^{-\int P'(x)} = e^{-\mathcal{N}}. \quad (6.9)$$

Inserting equation 6.9 into equation 6.8 we obtain:

$$L = \left(\prod_{i=1}^N P'(x_i) \right) e^{-\mathcal{N}}. \quad (6.10)$$

\mathcal{N} can then be divided into the expected background, N_{bg} , and expected signal, n_s , whilst P' is split into a background and a signal part. This leads to the final form of the extended likelihood function:

$$\log [L(n_s)] = \sum_{i=1}^{N_{tot}} \log [n_s S(\psi_i, p_i, q_i) + N_{bg} B(dec_i, p_i, q_i)] - N_{bg} - n_s. \quad (6.11)$$

This likelihood is sensitive not only to the measurements $\{q_i\}$ but also to the sample size \mathcal{N} . In cases where large numbers of events are necessary for the detection of a signal, limits are lower using this likelihood.

6.2.2 Additional information

In any likelihood function different event parameters can be used. Sensitivities improve when parameters are added that can be used to distinguish between signal and background. For neutrino telescopes the direction of the neutrino is always used in the likelihood function and provides a very good way of distinguishing signal from background. For the analyses presented in this thesis, the neutrino energy estimated by the number of hits used in the reconstruction (an energy estimate) and the event reconstruction quality parameter (for BBFit) or the angular error estimate β (for AAFit) were also used.

As can be seen in Fig. 6.3 the benefit of using the number of hits and β in the likelihood only leads to a small improvement of the resulting sensitivities for the AAFit strategy. This can be explained by the large similarity between the spectra of the signal from WIMP annihilations and the limited energy resolution for muon tracks.

For BBFit it is expected that the inclusion of further parameters is not going to improve the analysis either, since the energy resolution for the BBFit reconstruction is even worse.

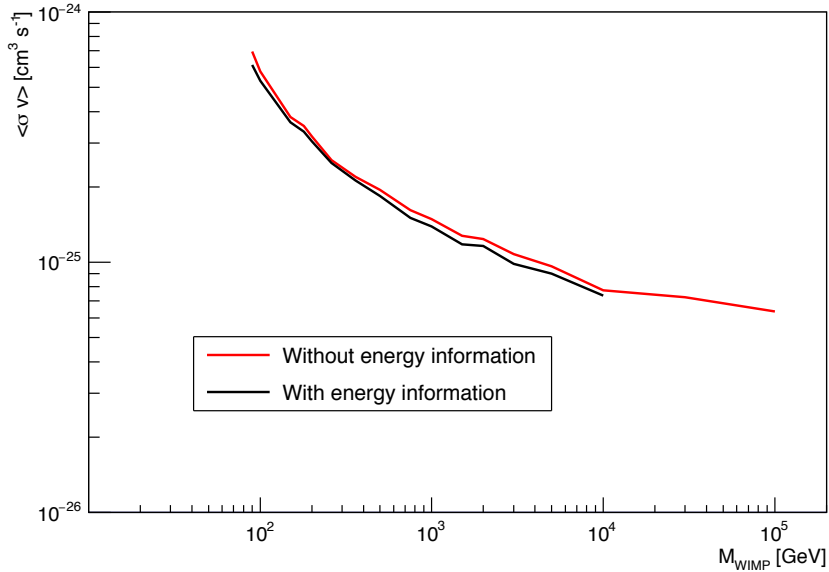


Figure 6.3: Thermally averaged annihilation cross-section sensitivities for the 2007-2012 AAFit data for a search in the GC [85]. Results using the number of hits (energy information) and β in the likelihood and those not using these parameters are shown.

6.2.3 Ingredient production

Both the production of pseudo-experiments and the likelihood function need different types of the so-called "ingredients". The "ingredients" are histograms that describe the statistical behaviour of signal and background. In the case of the background, these histograms are obtained from time-scrambled data.

The number of hits used in the reconstruction, the reconstruction quality parameter and the angular error estimate are time independent. The ingredients for these additional parameters can be obtained by simply filling a histogram with the raw data that is used for the analysis. An example of these ingredients for the additional parameters can be found in Figs. 6.4 and 6.5. The event position on the sky, however, is time dependent. Depending on the time at which an event is measured in the local sky the position on the celestial sky varies. If one uses celestial coordinates this change in relative position only occurs in right ascension. The ingredient for the declination of the events can therefore be obtained in the same way as the ingredient for the number of events used in the reconstruction.

Since the rotation speed of the Earth around its own axis is uniform every value for the right ascension of an event is equally likely, as long as the data sample is uniform in daytime. Therefore the ingredient does not have to be explicitly generated. In the case of the Sun, using celestial coordinates is highly inconvenient since the Sun moves in declination.

The ingredients for the signal events have to be produced from the Monte Carlo simulation using the statistical weights explained in section 5.3 and the expected neutrino signal spectrum at the position of the detector, which is explained in section 4.4.5. A modification of the weight w_2 , similar to that used to calculate the acceptance, is used for the signal ingredients. The simulation of the atmospheric muons is not used, since the muon simulation does not take the neutrino-nucleon interaction cross-section and its energy dependence and the resulting effect on the angular resolution and detection efficiency into account.

The ingredients for time-independent parameters are then generated filling histograms with the Monte Carlo events using the modified weight, analogous to the background ingredients. The position of the signal event, however, is generated differently to the background events. Signal events are produced by a source at a specific position in the sky and then are reconstructed with a limited angular resolution. The position of signal events is generated from a histogram that represents the likelihood of an event to be reconstructed at a certain angular distance from the true neutrino direction. This method of generating signal event positions

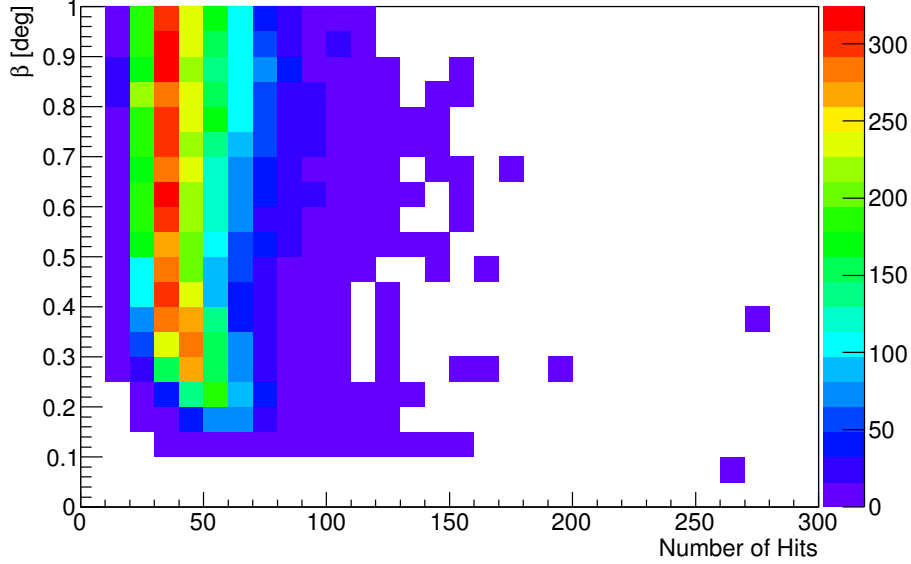


Figure 6.4: Distribution of the number of hits and the angular error estimate β for the background for the AAFit data with a quality cut of $\lambda > -5.6$.

assumes a point-like source, so in the case of an extended source the ingredient has to be modified.

For the likelihood function the ingredient for the angular separation to the core of the source has to be modified. For the PE generation the likelihood $\frac{dP(\Psi)}{d\Psi}$ for a signal event to be found at an angular separation Ψ to the source is needed. In the likelihood, however, the signal and the background parts have to be normalised in the same way. To do this, the likelihood $\frac{dP(\Psi)}{d\Omega}$ has to be normalised to the solid angle Ω , so that both parts of the likelihood are normalised to the solid angle. $\frac{dP(\Psi)}{d\Psi}$ and $\frac{dP(\Psi)}{d\Omega}$ are related by the following equation:

$$\frac{dP(\Psi)}{d\Psi} = \frac{d\Omega}{d\Psi} \frac{dP(\Psi)}{d\Omega} = 2\pi \sin(\Psi) \frac{dP(\Psi)}{d\Omega} \quad (6.12)$$

$\frac{dP(\Psi)}{d\Omega}$ is also called the point spread function (PSF).

Additionally the coordinates used for the ingredients have to be taken into account. In Fig. 6.6 $\frac{dP(\Psi)}{d\Omega}$ is shown in logarithmic scale. In these coordinates the relation

6.2 The likelihood function

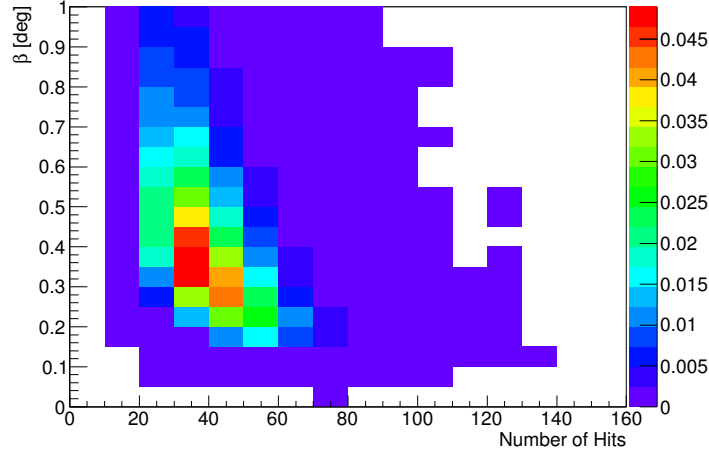


Figure 6.5: Distribution of the number of hits and the angular error estimate β for the expected signal for the $\tau^+\tau^-$ annihilation channel and a wimp mass of 5 TeV. The AAFit reconstruction algorithm and a quality cut of $\lambda > -5.6$ is used.

$$\frac{dP(\log_{10}(\Psi))}{d\log_{10}(\Psi)} = 2\pi \sin(\Psi) \ln(10) \Psi \frac{dP(\Psi)}{d\Omega} \quad (6.13)$$

has to be used. The normalisation of the signal ingredient for the likelihood function is then

$$\int_{4\pi} dP(\Psi) = \int_{4\pi} P(\Psi) d\Omega = 1. \quad (6.14)$$

An example of the PSF can be seen in Fig. 6.7. The normalisation of the background ingredient has likewise to be set by an integral over the solid angle. The declination ingredient for the background part in the likelihood function, $\frac{dP_{bg}(dec)}{d\Omega}$, has to fulfil the equation:

$$\int_{4\pi} \frac{dP_{bg}(dec)}{d\Omega} d\Omega = 1. \quad (6.15)$$

In this case $d\Omega$ has to be expressed in terms of celestial coordinates:

$$d\Omega = dRA \cdot d\sin(dec), \quad (6.16)$$

where RA is the right ascension.

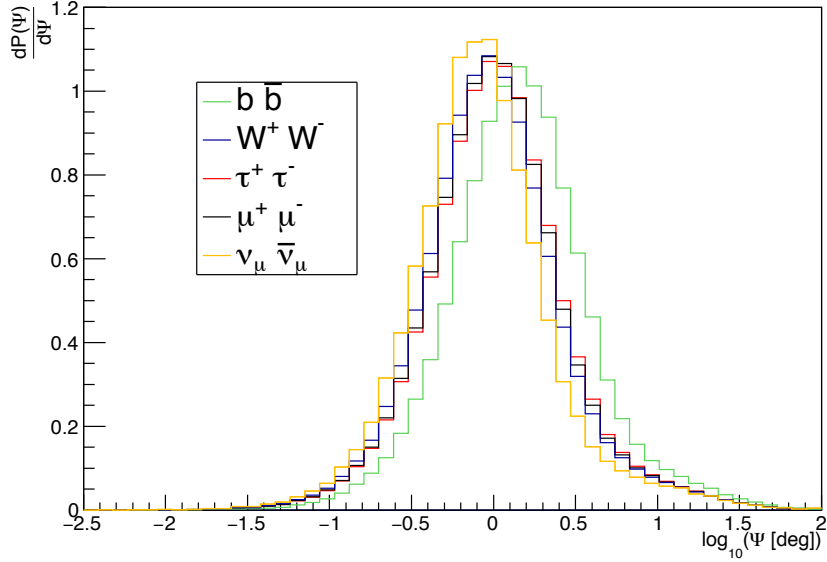


Figure 6.6: Example of the signal ingredient for the angular separation between event and the centre of the GC for the AAFit data with a quality cut of $\lambda > -5.2$. A WIMP mass of 1 TeV has been used.

Similar to the signal ingredient, coordinates have to be taken into account for the background ingredient as well. For coordinates that yield bins that are all equal in solid angle sizes no further correction is needed. A coordinate with that property is the cosine of the declination. This ingredient for this coordinate can be seen in Fig. 6.8.

6.2.4 Angular resolution

The PSF describes the angular inaccuracy in the reconstruction of the neutrino track. This includes the uncertainty in the reconstruction of the muon track and the difference between the muon track and that of its parent neutrino.

The difference between the muon and the neutrino direction will be referred to as the kinematic angular error. This inaccuracy is unavoidable and depends on the neutrino energy. The white squares in Fig. 6.9 show that for higher neutrino energies the kinematic angular error is smaller.

The inaccuracy of the reconstruction depends on the quality of the reconstruction algorithm that is used. The quality of the reconstruction

6.2 The likelihood function

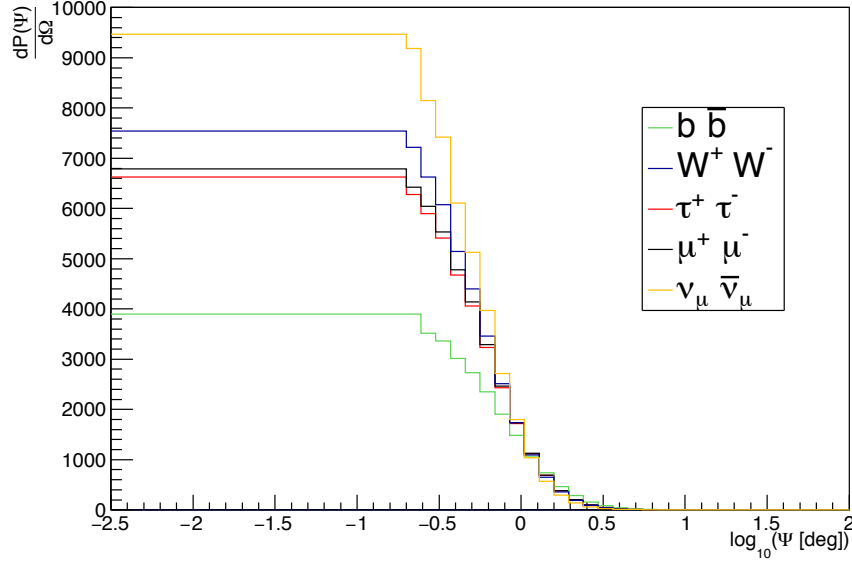


Figure 6.7: Point spread function for the AAFit reconstructed data with a quality cut of $\lambda > -5.2$ for the GC. A WIMP mass of 1 TeV has been used.

depends on the algorithm itself and the properties of the event and also decreases with growing energy at the energy range of the analyses in this thesis. At high neutrino energies this error makes up most of the angular uncertainty. The kinematic error is estimated to be below 1 degree for all energies, but can sink below 0.3 degrees for high energies.

Since the angular errors are energy dependent the expected signal spectra have to be taken into account. When constructing the PSF each simulated neutrino event has to be weighted by the spectrum for a certain WIMP mass and annihilation channel. This leads to one PSF per combination of WIMP mass and annihilation channel.

The highest average neutrino energies are achieved with the $\nu\bar{\nu}$ channel, which means that its angular resolution is typically the best of all channels for each WIMP mass. This optimum resolution is below one degree. Any source larger than this has to be considered as an extended source.

A good measure of the angular resolution for a given dark matter signal and reconstruction strategy is the median angular error (kinematic error and misreconstruction) that can be calculated from the Monte Carlo simulation. Fig. 6.10 shows a plot of the median of the total angular error for signal neutrinos from the Sun using multi-line events only. The

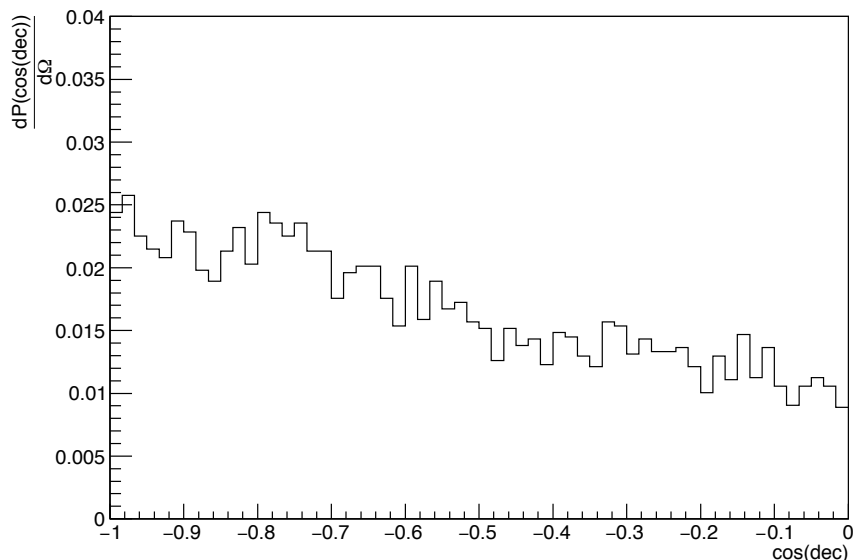


Figure 6.8: Background ingredient for the event declination for the AAFit data with a quality $\lambda > -5.2$. The ingredient is normalised over the solid angle to one.

angular error for most WIMP masses is between 2 and 4 degrees and only increases significantly for WIMP masses below 200 GeV for AAFit for the softest channel.

For single-line events the angular error is typically much larger and has to be determined differently. Since for single-line events only the zenith angle of the muon direction is known. The angular uncertainty is taken as the difference between the true and the reconstructed zenith angle.

6.2.5 Reconstruction cuts

In addition to the preliminary data selection described in Section 1.7 and the trigger selection, there are further cuts on the event reconstruction quality and other parameters that have been used to reject badly reconstructed events and atmospheric muons. These cuts reduce the typical angular error of the remaining set of events and therefore improve the angular resolution.

These quality cuts also reduce the effective area and the acceptance, as can be seen in Fig. 6.11 The values of these quality cuts are determined

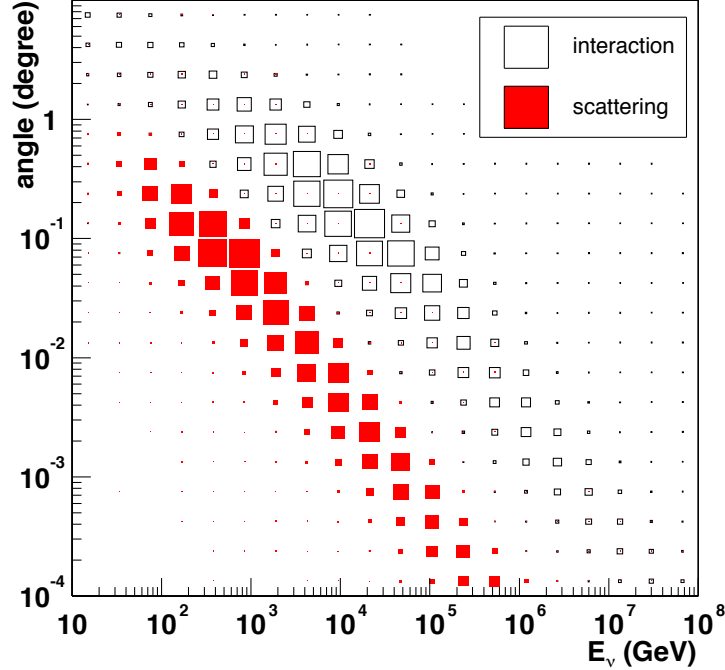


Figure 6.9: The angle between the original neutrino and the produced muon (white) and the change of muon direction due to scattering in water before entering the can (red) for different neutrino energies [71].

by an optimisation procedure. The analysis is repeated for several values of the reconstruction quality and angular error estimate. The cuts that lead to the best sensitivity are selected as the final cuts and are used for the calculation of limits. For each combination of annihilation channel and WIMP mass an individual cut is chosen, but typically the optimum cuts do not change much for different WIMP masses.

For the AAFit reconstruction strategy a cut on the angular error estimate, β , has been used in addition to the reconstruction quality cut. This cut is optimised in a similar way to the reconstruction quality cuts. The main difference in the optimisation process of the β cut is that only a few values of the cuts have been considered. This has been done since the computing time of the analysis is multiplied by the number of cuts treated and would exceed reasonable limits for a large number of cuts. The cuts considered were $\beta < 0.5^\circ$, $\beta < 1^\circ$, $\beta < 1.5^\circ$ and $\beta < 2^\circ$ and the final cut used in the analyses is $\beta < 1^\circ$. The average angular resolution

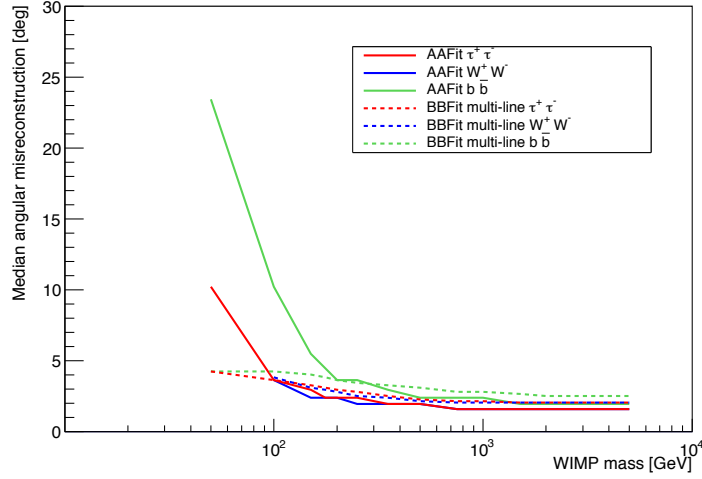


Figure 6.10: The median angular error as a function of the WIMP mass for the AAFit reconstructed data with a quality cut of $\lambda > -5.4$ and the BBFit multi-line data using a quality cut of $\chi^2 < 1.3$ for the different annihilation channels for the Sun.

obtained using the AAFit strategy is below this cut for WIMP masses above 100 GeV. The angular resolution is typically worse than one degree for WIMP masses below 100 GeV. The final sensitivities and limits of the analyses for low WIMP masses are obtained using the BBFit strategy. Therefore, the cut on β is not very strict for the mass range relevant for the analyses, which use AAFit.

6.3 Sensitivity determination

There are different ways to implement the calculation of sensitivities and limits from the TS distributions. These methods follow a common scheme, which is shown in 6.12.

Sensitivities are set in a process of hypothesis testing. Two types of hypotheses are proposed: the null-hypothesis, H_0 , and the alternative hypothesis, H_1 . H_0 is in this case the proposition that no signal is present in the analysed data set whilst H_1 means that at least some signal is present.

There are two types of errors that can occur when performing a hypothesis test. The first is a rejection of H_1 although some true signal is present in the sample (false negative), the second is a rejection of H_0 despite an

6.3 Sensitivity determination

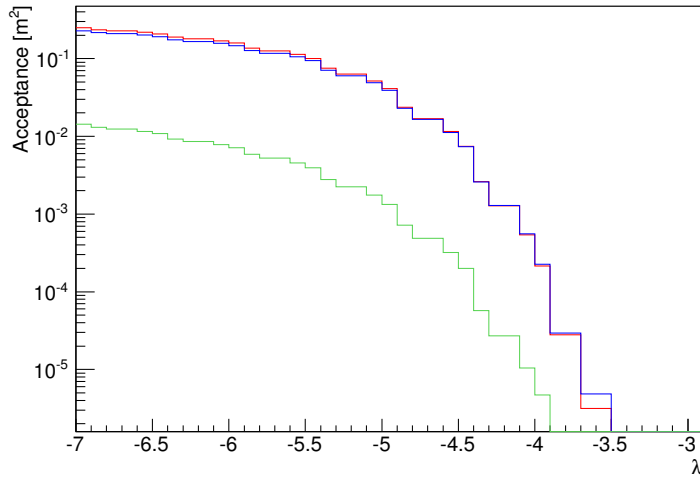


Figure 6.11: The acceptance versus the reconstruction quality parameter λ for the AAFit reconstruction. A WIMP mass of 1 TeV and a cut on the angular error estimate of $\beta < 1$ degree have been used. The colour coding indicates the annihilation channel: blue: W^+W^- red: $\tau^+\tau^-$ green: $b\bar{b}$

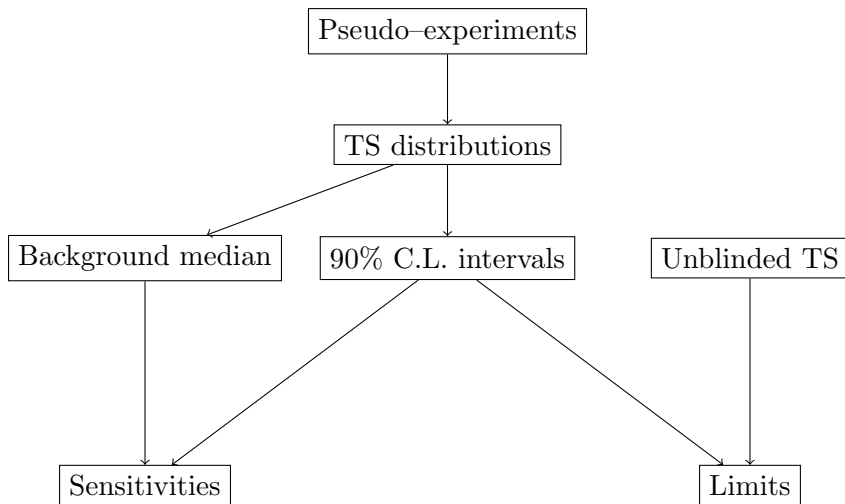


Figure 6.12: Diagram of the process to obtain sensitivities and limits.

absence of signal (false positive). The statistical strength of a test can be either expressed as a confidence level (CL) or the strength. The CL is the

fraction of time at which a false positive is avoided, the strength is the fraction at which a false negative is avoided.

In this thesis the sensitivities are set so that a CL of 90% is obtained, which means that while there is only a 10% probability to have a false positive, the chance of a false negative is increased. This approach is also called the model rejection factor (MRF) [86] approach.

To determine sensitivities, a frequentist approach that was first presented by Neyman [87] is used. In this approach intervals of a physical parameter n_{true} are defined by:

$$P(n_{true} \in [n_1, n_2]) = \alpha. \quad (6.17)$$

where α is the confidence level of the interval $[n_1, n_2]$ ¹. When this equation is fulfilled the interval is said to have proper coverage. For the purpose of the analyses in this thesis n_{true} is the true signal strength. However, the true signal strength is not directly measured and so, to construct these intervals, so-called "confidence belts" are used. These belts are series of intervals of a parameter x that can be measured and is correlated with n_{true} . These intervals are defined by the equation

$$P(x \in [x_1, x_2] | n_{true}) = \alpha \quad (6.18)$$

for each value of n_{true} . Although Neyman did not specify how to choose x_1 and x_2 , the intervals defined by

$$P(x > x_1 | n_{det}) = \alpha \quad (6.19)$$

are commonly referred to as "Neyman upper limits". This type of interval is used for this analysis.

If an interval in the confidence belt for a certain signal strength, n_{lim} , is entirely above the median of the distribution of x for $n_{true} = 0$ (background distribution) then n_{lim} is considered not to be in $[n_1, n_2]$. The sensitivity is then set to the lowest of these values of n_{lim} . The limit construction will be discussed in detail in section 6.6.

6.3.1 The Test Statistic distribution

For the parameter x from the previous section a function of the so-called test statistic is used. The test statistic (TS) of a pseudo-experiment is defined as:

¹In the frequentist approach n_{true} is not considered a random variable as in the Bayesian method, but a fixed, unknown parameter

6.3 Sensitivity determination

$$TS = \log_{10} \left(\frac{L(n_{opt})}{L(0)} \right), \quad (6.20)$$

where n_{opt} is the value of n_s at which the likelihood function, $L(n_s)$, takes its maximum value. The optimum value of n_s should be close to the amount of inserted signal events.

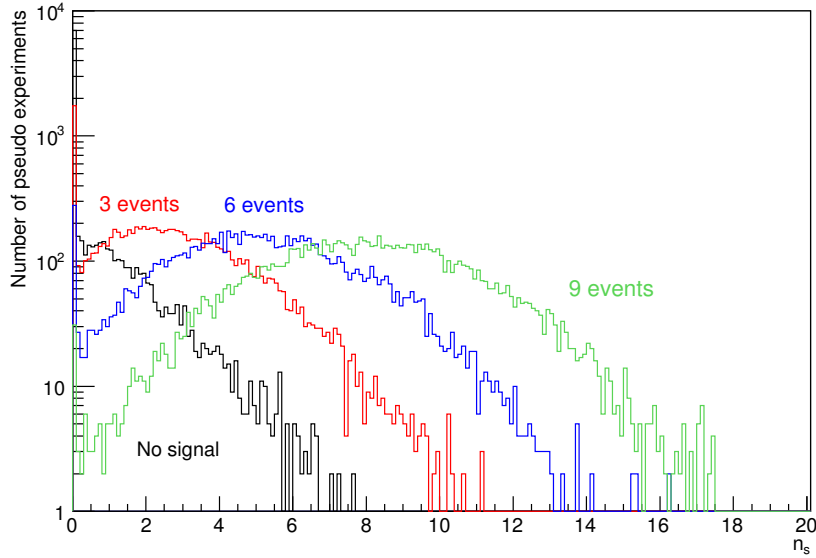


Figure 6.13: Distributions of the optimum n_s for different numbers of inserted signal events. These distributions were made for the AAFit strategy using a λ cut of -5.4 , a WIMP mass of 1 TeV and for the W^+W^- annihilation channel. The PEs were simulated for the Sun.

In Fig. 6.13 distributions of n_{opt} for different amounts of inserted signal events for the Sun are shown. As can be seen, n_{opt} underestimates the number of inserted signal events by around one event. This underestimation is worse for extended sources like the GC. Also a large population of PEs shows an n_{opt} of zero.

In Fig. 6.14 the distributions of TS values for different amounts of inserted signal are shown for the Sun (e.g. a point-like source). The distribution for pure background shows an exponential behaviour, in agreement with the Wilks theorem [88], and a large amount of pseudo-experiments with a next-to-zero TS value. These events make up more than 50% of the pseudo-experiments. For small amounts of signal events this population

is very large and has a big effect on the limits and sensitivities.

Pseudo-experiments are carried out for a large variety of numbers of inserted signal events. For point-like sources the maximum number of signal events considered is 40. For extended sources it is more difficult to identify signal in the PEs, so larger amounts of signal events (up to 140 events for the GC) depending on the source extension, are inserted.

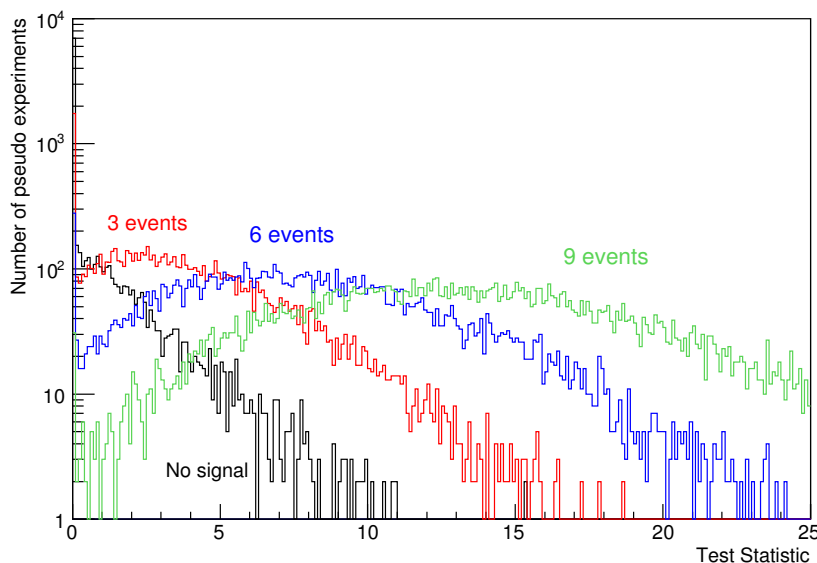


Figure 6.14: The TS distributions for several numbers of inserted signal events. This distribution was made for the AAFit strategy using a λ cut of -5.4 , a WIMP mass of 1 TeV and for the W^+W^- annihilation channel. The PE were simulated for the Sun.

The sources that are considered in this thesis are expected to generate a stable flux of signal neutrinos. Nevertheless, the amount of detected signal events undergoes statistical fluctuations. For this reason, TS distributions $P(TS|\mu)$ for a Poissonian mean μ of detected events instead of a fixed number of signal events have to be used to determine limits. These new distributions are calculated as

$$P(TS|\mu) = \sum_{i=0}^{n_{max}} P(TS|i) \times P(i|\mu), \quad (6.21)$$

where $P(TS|i)$ is the TS distribution for a fixed number of signal events i

6.4 Moving sources

and $P(i|\mu)$ is the probability to have i events given a Poissonian mean of μ .

Finally, the parameter x from Eq. 6.19 is defined by

$$x = \log(TS + C), \quad (6.22)$$

where C is the lowest of all TS values calculated for the given WIMP mass, quality cut and annihilation channel. C is introduced to avoid problems with negative TS values. These negative values occur because in the calculation of the TS the value of n_s in the likelihood function has a minimum of 0.001 (e.g. $n_{opt} > 0.001$ in Eq. 6.20). If the true optimum n_s is zero the TS that is calculated then yields a negative TS. Examples of distributions of x can be seen in Fig. 6.15.

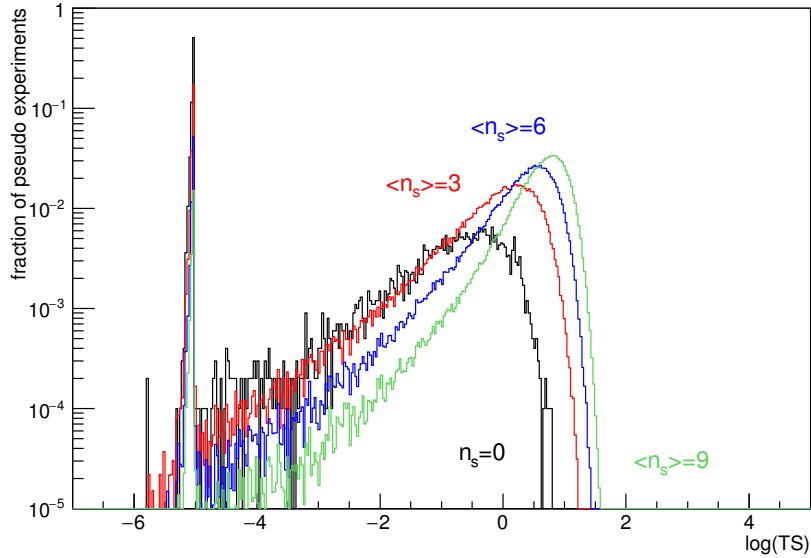


Figure 6.15: Distributions of x for different average numbers of inserted signal events. This distribution was made for the AAFit strategy using a λ cut of -5.4 , a WIMP mass of 1 TeV and for the W^+W^- annihilation channel.

6.4 Moving sources

Most of the astrophysical objects of interest have fixed coordinates. However, throughout the year, the declination of the Sun changes due to the

tilt between the rotation axis of the Earth around itself and the axis of the Earth's orbit around the Sun. During the year the Sun reaches its highest declination of 23.45° at the Summer solstice on the 20th of June and the lowest declination of -23.45° is reached during the Winter solstice on the 21st of December. In Fig. 6.16, a plot showing the fraction of time the Sun can be seen on the local sky is shown. The plot shows only the sky below the horizon and uses the zenith (θ) and the ϕ angle of the local coordinate system of ANTARES. North is at $\phi = 90^\circ$, South at $\phi = 270^\circ$ and East at $\phi = 0^\circ$.

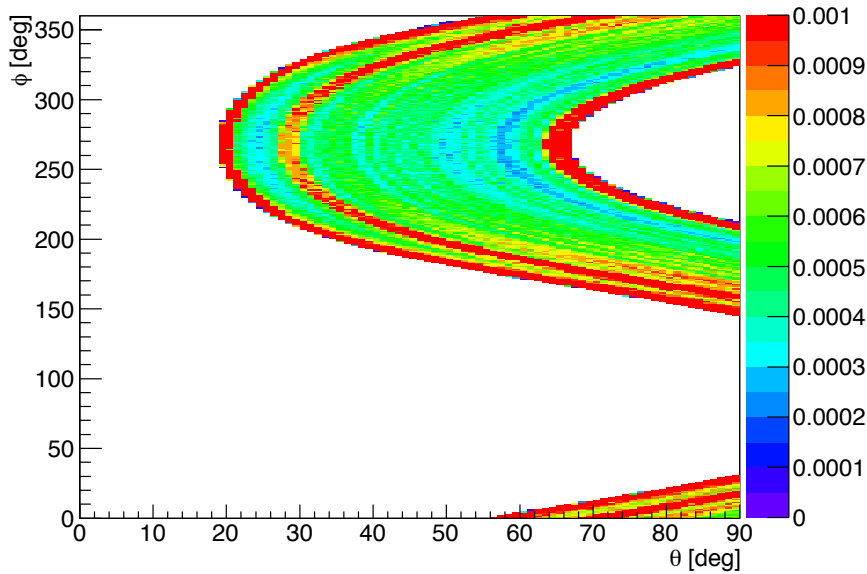


Figure 6.16: Fraction of time the Sun spends in each position on the local sky below the horizon. θ is the zenith of the local coordinate system of ANTARES. ϕ is the azimuth shifted by 90° . North is at $\phi = 90^\circ$, South at $\phi = 270^\circ$ and East at $\phi = 0^\circ$. The plot was produced for the data taking periods from 2007 to 2012 described in section 5.2.

If celestial coordinates are used for the PEs the Sun movement has to be tracked. This is necessary to calculate the angular separation between the source and the event for the signal part of the likelihood function in Eq. 6.1. To circumvent this issue a different coordinate system, which is centred at the Sun, is used so that events are produced directly with this angular separation as a coordinate instead of its position on the celestial sky. This way the distance to the source does not have to be calculated

when analysing the PE. The resulting likelihood function has the following form:

$$L(n_s) = \prod_{i=1}^{N_{tot}} (n_s S(\psi_i, p_i, q_i) + (N_{tot} - n_s) B(\psi, p_i, q_i)) e^{-N_{tot} - n_s} \quad (6.23)$$

using the same notation as in Eq. 6.1. Whilst the signal ingredient remains the same for this likelihood the background ingredient has to be changed. The new background ingredient has to give the likelihood for an event found at an angular distance to the source to be background. This is analogous to the signal ingredient, which gives the likelihood for an event found at a certain distance from the source to be signal. An example of this type of background ingredient is shown in Fig. 6.17. As can be seen, the logarithmic probability linearly increases with the logarithmic separation angle Ψ . This indicates that the background behaves as a power law. An approximately homogeneous background is expected to increase with the square of the angular separation to the source, so the observed behaviour agrees with the expectations. Additionally, events above the horizon are not included in this ingredient and for large angular distances most events are excluded by the horizon cut.

This ingredient used for the PE generation has to be calculated using an actual time scrambling. This has been implemented by using randomised positions of the Sun from a list of previously calculated positions that are representative of the motion of the Sun. This procedure is significantly more computing-time intensive than for celestial coordinates but since it has to be done only once for each quality cut, it does not affect the overall duration of the analysis significantly.

The ingredient used in the likelihood function for the background has to be modified as the corresponding ingredient for the signal, e.g. the PSF. Likewise, Eq. 6.12 has to be used for this modification and the normalization of this modified ingredient has to fulfil that:

$$\int dP(\Psi) = \int_{4\pi} P(\Psi) d\Omega = 1. \quad (6.24)$$

An example of this ingredient can be seen in Fig. 6.18. One advantage of this normalization is that it is identical for the background and the signal terms of the likelihood function. If there is any offset in the normalization of the ingredients it will equally affect in most cases the background and

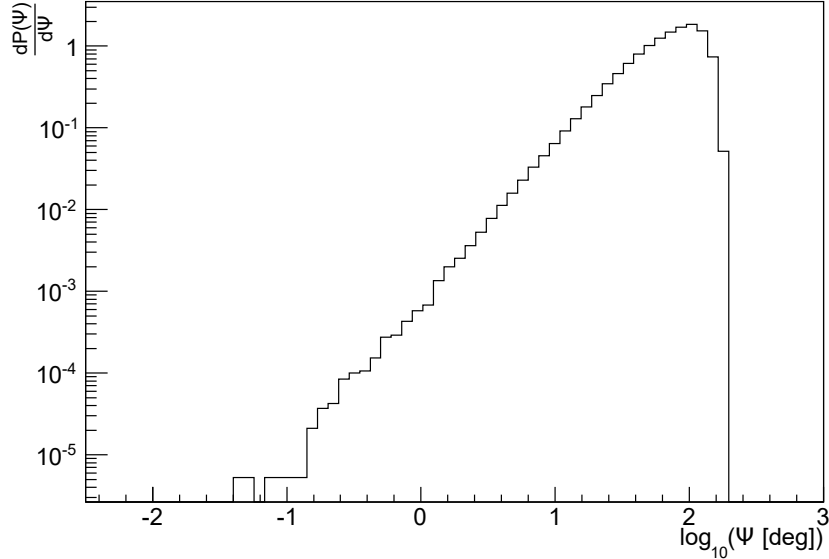


Figure 6.17: The background ingredient for the AAFit reconstruction with a quality cut of $\lambda > -5.6$ used for the generation of background events.

the signal part of the likelihood function and will offset the overall TS value, which does not affect the final limits. Another benefit is that the evaluation of the likelihood function is accelerated, since the distance to the source is already saved to the events in the pseudo-experiments and does not have to be calculated when evaluating the likelihood function. At an angle of 180 degrees an abnormally filled bin is seen. The size of these bins in solid angle scales with a factor of $\sin(\Psi) \cdot \Psi$. At 180 degrees the bin is therefore rather small and also points opposite to the source. So the position of this bin is above the horizon most of the time. This means that there will be only few events that fill this bin leading to a large statistical uncertainty. Since the bin content is corrected for the solid angle size of the bin a large correction is applied to the bin, which in connection with the large uncertainty lead to this anomalous behaviour.

6.5 Extended sources

The analysis method described so far assumes a point-like source, which is a reasonable assumption if the extension of the source is smaller than the angular resolution of the detector. The angular resolution of ANTARES

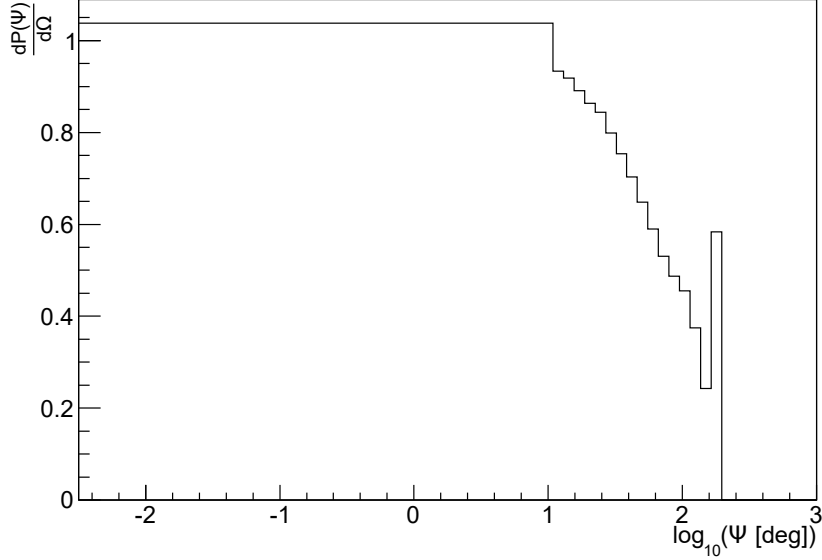


Figure 6.18: The ingredient for the angular separation of the event to the Sun. AAFit data with $\lambda > -5.6$ was used for the generation of background events.

varies depending on the neutrino energy and the reconstruction algorithm. For the relevant energy range the best angular resolution achieved is never below 2° .

The extension of a source in dark matter analyses can be estimated by the J-Factor described in Section 4.4.3. Fig. 4.14 shows an example of the J-Factor integrated over a cone with an opening angle α_{int} for the NFW profile. 90% of the maximum value for the smooth part of the halo (blue line) is reached at an angle of 90 degrees. Since the integrated J-Factor is proportional to the total amount of signal that can be seen within the observation cone defined by α_{int} , 90% of the maximally detectable signal will likewise be seen for this opening angle of 90 degrees. Therefore, the Galactic Centre is clearly extended and has to be treated as such in the analysis.

First, the source extension has to be properly implemented in the generation of pseudo-experiments. The fake signal events have to be scattered from the centre of the source according to the source morphology, for which the J-Factor can be used (Fig. 6.19). Then, the events have to be scattered a second time according to the limited angular resolution of the detector.

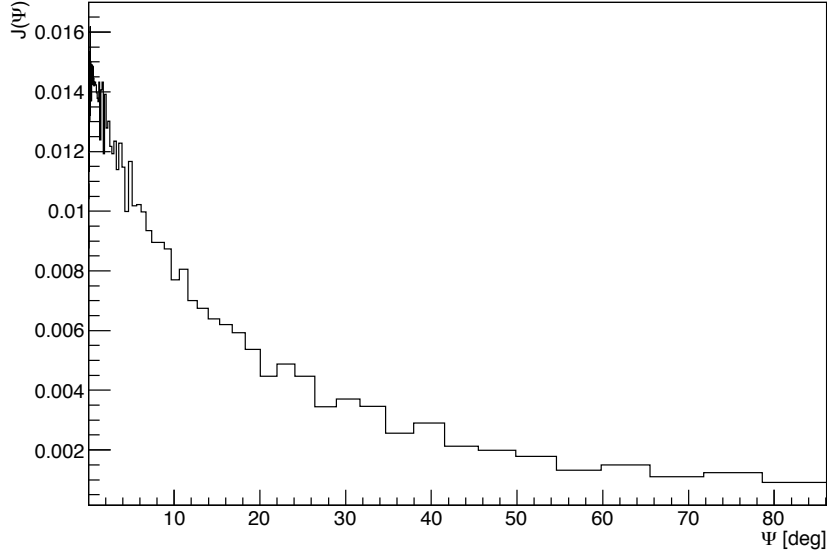


Figure 6.19: J-Factor, normalised to one, as a function of the angular separation from the GC, Ψ , multiplied by the solid angle element, $d\Omega$.

The likelihood function has to be modified as well. The signal term of the likelihood function has to use not only the PSF, but also the source morphology. For this, the PSF and the source morphology have to be convoluted. The result will be called the effective PSF.

This can be done by generating pseudo-experiments without background events, but with a large amount of signal events. The resulting distribution of the distances of the events to the centre of the source is then corrected according to equation 6.12. An example of the effective PSF can be seen in Fig. 6.20.

Since the signal events will be much more spread out for an extended source than for a point-like source, the number of signal events required for the likelihood function to recognize the signal is significantly larger. It is also much more likely that background events are misidentified as signal events. Therefore, the TS distributions for extended sources are in general wider.

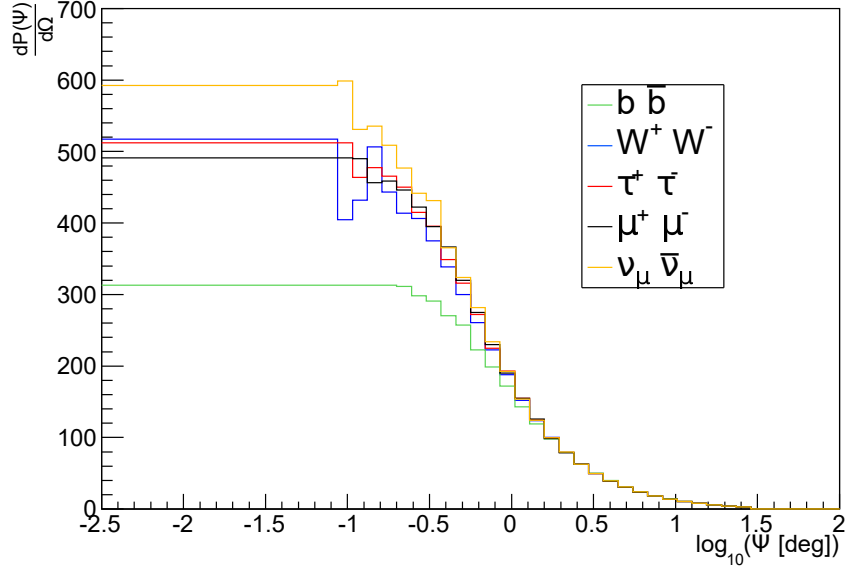


Figure 6.20: The effective PSF, i.e. a PSF that also takes the source morphology into account, for the Galactic Centre using the NFW halo profile. The colour coding indicates the annihilation channel used.

6.6 Unblinding procedure

In order to avoid biases that might skew the results the analysis is first performed and optimised on blinded data (i.e. data that does not contain all the relevant information of the detected events). This includes the optimisation of the reconstruction quality cuts, the angular error estimate cuts and other variables of the analysis.

The blinding of the data is achieved by the use of the pseudo-experiments generated from simulation and scrambled data only. The cuts are optimised with respect to the sensitivities constructed as previously described.

For the unblinding (e.g. the application of the established analysis to the actual data), the detected events are analysed using the likelihood function. For the Galactic Centre this means mainly that the true right ascension and declination of the events is used instead of randomly generated values. For the Sun the actual distance of the events to the Sun instead of that of randomly generated events is used.

Likewise the actually recorded values for the other event parameters are used in the likelihood functions. But since the time scrambling does

not strongly affect these parameters (they are time independent after all) only statistical fluctuations between the background estimate of these parameters and the unblinded values of the recorded events for these values.

In the unblinding the likelihood function is optimised using the unblinded data. The resulting TS value is then taken to compute the limit with the help of the probability intervals described in section 6.3. The interval with the lowest average signal strength n_{det} that is entirely above the TS value of the unblinded data becomes the limit. Naturally, the cuts used for the unblinded analyses are taken from the corresponding blinded analysis.

When the Neyman method is used for constructing limits it is not unlikely to obtain nonphysical limits, even when there is no large under-fluctuation of the data with respect to the background estimate. In the Neyman approach pseudo-experiments that are equally compatible with the null hypothesis can produce very different limits. In order to remove this feature in the limit setting method, the limits are truncated with the previously calculated sensitivity.

Chapter 7

Results of the search for dark matter annihilations in the Sun

The results of the analysis searching for dark matter in the Sun are presented in this chapter.

As described in great detail in chapter 6, the analysis starts with the simulation of pseudo-experiments, simulated maps of detected events with simulated signal events injected into them. The generation of PEs is described in Sec. 6.1. From these PEs, sensitivities in terms of the detected signal strength are then determined.

To construct the limits the analysis is applied to recorded data. This is called unblinding and the exact procedure of the unblinding is described in Sec. 6.6. The results of the unblinding are shown in Sec. 7.1. The unblinded analysis uses the quality cuts that were optimised using the blinded data and are presented in Sec. 7.2.

From the limits on the signal strength, limits on the neutrino flux are calculated using the acceptance (see Section 7.4) . These limits are then converted into limits on the spin-dependent and spin-independent scattering cross-sections.

The limits on the signal strength are shown in Section 7.3, those on the neutrino flux in Sec. 7.5, and the limits on the cross-sections and the comparisons to other experiments are finally shown in Section 7.7 and 7.7.2, respectively.

7.1 Unblinding results

As described in Section 6, the unblinding is performed by calculating the TS value of the unblinded data and comparing it with the background TS distribution. If the TS value is below the median of the background TS distribution, the data is compatible with the null hypothesis within the

7.1 Unblinding results

confidence level used in the analysis. Otherwise there is an excess above the background in the data. If the excess is large enough to be significant, a discovery can be claimed. Otherwise, limits that take the excess into account are set.

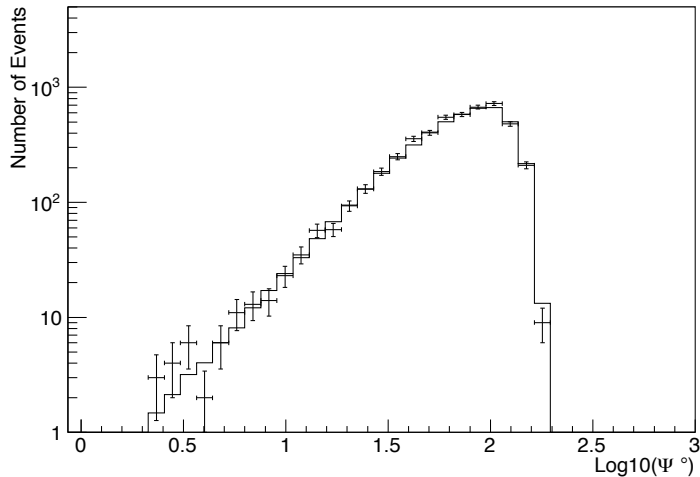


Figure 7.1: A comparison of the distribution of the angular distance of the reconstructed muon track to the source for the background estimate (histogram) and the data (crosses) for AAFit events. A quality cut of $\lambda > -5.4$ has been used. The error bars on the data are statistical errors only.

A good way to visualise the results of the unblinding is to compare the unblinded data to the background estimate used to generate the pseudo-experiments. The number of hits, angular error estimate and the reconstruction quality parameter do not depend on the event time and therefore should agree with the estimate. The only ingredient where a significant discrepancy can occur is the distribution of the angular separation to the source.

In Figs. 7.1, 7.2 and 7.3 no excess of events close enough to the source that could be identified as signal can be seen. The angular resolution used in the likelihood function is for most WIMP masses close to 2 degrees and therefore, fluctuations at angles much larger than that will not affect the analysis.

For most WIMP masses, the TS values of the unblinded data are very close to zero. This is expected to happen for pseudo-experiments generated with only background. An example of this can be seen in Fig. 6.15, where these populations are close to $\log_{10}(TS) = -5$.

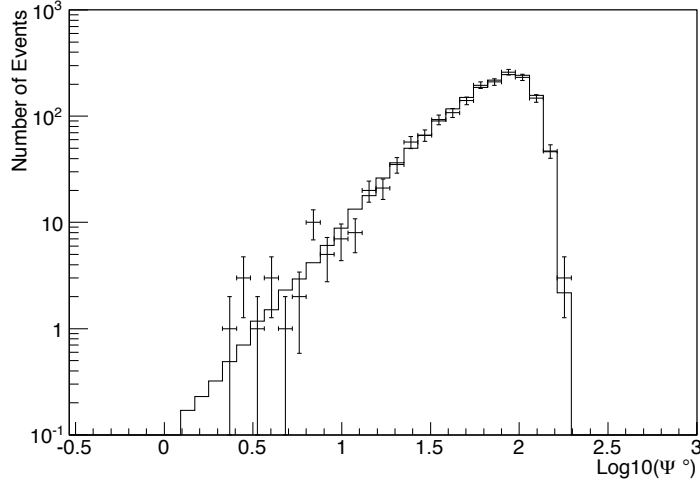


Figure 7.2: A comparison of the distribution of the angular distance of the reconstructed muon track to the source for the background estimate (histogram) and the data (crosses) for BBFit multi-line events. A quality cut of $\chi^2 < 1.4$ has been used. The error bars on the data are statistical errors only.

Naturally, these populations of low TS value experiments do also appear in TS distributions for pseudo-experiments with a small number of inserted signal events. With the Neyman method of limit calculation it is possible that nonphysical limits are produced. This happens when the TS of the unblinded data is at the position or below the aforementioned population of low TS PEs. For this reason the limits are truncated to the sensitivities.

The TS values of the unblinded data are below the median of the background TS distributions for most WIMP masses and annihilation channels. For the remaining WIMP masses and annihilation channel combinations, the TS values are very close to the median of the background TS distribution and are treated as equal to the median, taking into account the binning of the histograms where the TS distributions are saved. Therefore the limits are equal to the sensitivities.

7.2 Optimum cuts

As mentioned in Section 6.2.5, the data selection criteria ("cuts") on the reconstruction quality have been optimised with respect to the cross-section sensitivities. This optimisation leads to the same optimum cuts

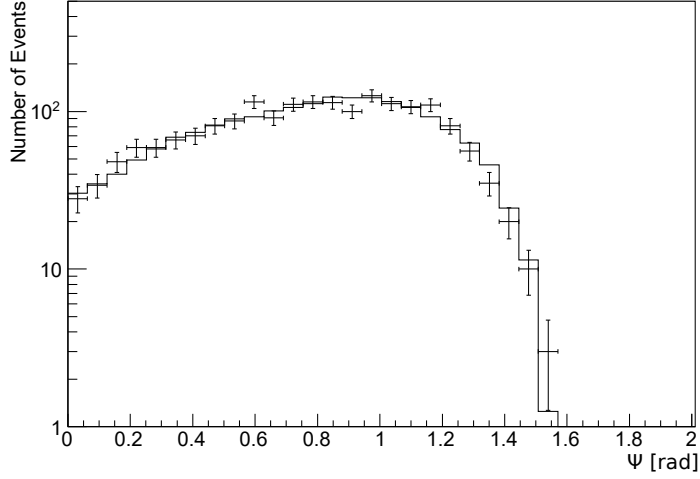


Figure 7.3: A comparison of the distribution of the difference in zenith of the reconstructed muon track and the source for the background estimate (histogram) and the data (crosses) for BBFit single-line events. A quality cut of $\chi^2 < 0.8$ has been used. The error bars on the data are statistical errors only.

for both the spin-dependent and the spin-independent cross-sections.

The optimum cuts are very stable for all strategies over the entire WIMP mass range considered. Only for the BBFit multi-line the optimum cuts change for high WIMP masses from $\chi^2 < 1.3$ to $\chi^2 < 1.4$ at $M_{WIMP} = 1$ TeV for the W^+W^- channel and at $M_{WIMP} = 750$ GeV for the $\tau^+\tau^-$ channel, for which the cut then returns to $\chi^2 < 1.4$ at $M_{WIMP} = 1$ TeV. This is summarised in Table 7.1.

The optimum value of the cut only depends on two things: the limit in terms of the number of detected events and the acceptance. Both change for different quality cuts and WIMP masses. The limits on the number of detected events largely depend on the PSF, which worsens for lower WIMP masses as does the acceptance due to the decrease of the effective area for smaller energies.

Since the energy resolution of ANTARES for muons is not very good it is to be expected that the optimum quality cut only slowly changes with the WIMP mass. As can be seen in Table 7.1 the optimum quality cuts only change for BBFit multi-line events at the highest WIMP masses.

m_{WIMP} [GeV]	Channel	AAFit λ	BBFit single-line χ^2	BBFit multi-line χ^2
< 750 GeV	all	-5.4	0.8	1.3
750 GeV	$b\bar{b}$	-5.4	0.8	1.3
750 GeV	W^+W^-	-5.4	0.8	1.3
750 GeV	$\tau\bar{\tau}$	-5.4	0.8	1.4
1 TeV	$b\bar{b}$	-5.4	0.8	1.3
1 TeV	W^+W^-	-5.4	0.8	1.4
1 TeV	$\tau\bar{\tau}$	-5.4	0.8	1.3
> 1 TeV	all	-5.4	0.8	1.4

Table 7.1: The final data selection criteria for which the optimal cross-section sensitivity is obtained.

7.3 Initial sensitivities

In Fig. 7.4 the 90% confidence level limits on the number of detected events can be seen. For the BBFit multi-line events these limits only show very small variations over the considered WIMP mass range for all annihilation channels. Jumps in the BBFit multi-line limits are due to changes in the optimum cut. The TS distributions are different for the different quality cuts, which in turn leads to different sensitivities. The multi-line limits otherwise change very smoothly. The single-line limits are more unstable due to larger uncertainties in the angular reconstruction of events. These changes are not relevant for the final limits, since the BBFit single-line results are only the best ones for a very narrow mass range ($M_{WIMP} < 250$ GeV for the $b\bar{b}$ channel and $M_{WIMP} < 150$ GeV for the other two).

In the case of AAFit there is a rise of the limits at low WIMP masses, exactly where the BBFit results are more stringent than those of AAFit. As a consequence AAFit gives very stable results for the mass range where they are relevant.

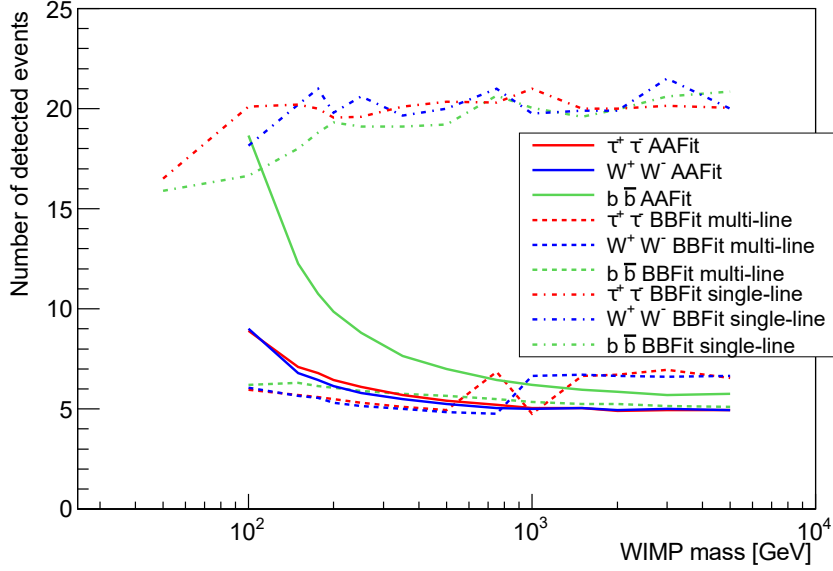


Figure 7.4: 90% confidence level limits on the number of detected events as a function of the WIMP mass for the different reconstruction strategies and annihilation channels considered in this analysis. The quality cuts used for these plots are those obtained from the optimisation of the sensitivity.

7.4 Acceptance

The acceptances for the optimum quality cuts for all annihilation channels are shown in Fig. 7.5. Some jumps in the acceptance for the BBFit multi-line analysis can be seen. These can be explained by changes in the optimum cut. The acceptances for both multi-line analyses are close to each other with the AAFit acceptances always being slightly better.

The BBFit single-line acceptance behaves much more smoothly than the limit on the number of detected events, indicating that the optimum cut does not change in this case. It is also more stable than the other acceptances over the whole mass range, making it clearly better than the other strategies for WIMP masses below 100 GeV for the two hard channels or below 250 GeV for the $b\bar{b}$ channel.

All acceptances decrease for the lowest WIMP masses following the behaviour of the effective area, as can be seen in Fig. 5.14.

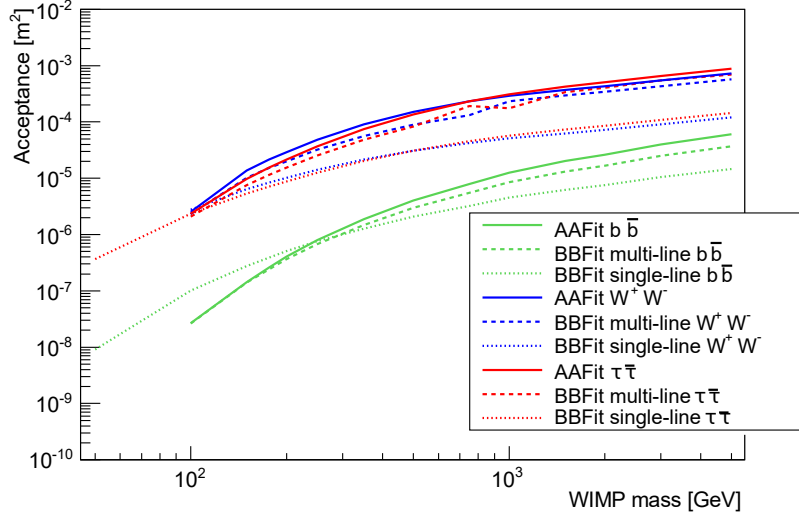


Figure 7.5: The acceptance as a function of the WIMP mass for the different reconstruction strategies and annihilation channels. The quality cuts used for these plots are those obtained from the optimisation of the sensitivity.

7.5 Neutrino Flux

Using equation 5.10 and the acceptance, shown in Fig. 7.5, 90% confidence level limits on the neutrino flux are calculated. In Fig. 7.6 the limits on the neutrino flux from dark matter annihilations in the Sun as a function of the WIMP mass are shown. The limits on the signal strength are relatively stable over the different WIMP masses. This means that the shape of the flux limit almost entirely depends on the behaviour of the acceptance.

The limits in Fig. 7.6 are the combined limits of both reconstruction strategies. For each WIMP mass considered the lowest of the available limits has been used. For the $\tau^+\tau^-$ and the W^+W^- channels, the limits for $M_{\text{WIMP}} \leq 100$ GeV are taken from the BBFit single-line limits; the rest are taken from the AAFit limits. The $b\bar{b}$ limits are taken from the BBFit single-line events for $M_{\text{WIMP}} \leq 250$ GeV. The BBFit multi-line events were not used for the final limits, although for the $\tau^+\tau^-$ and the W^+W^- channels the two BBFit limits are approximately equal for $M_{\text{WIMP}} = 100$ GeV.

The limits on the neutrino flux from the Sun are independent of the dark matter halo model used and other assumptions, like the equilibrium

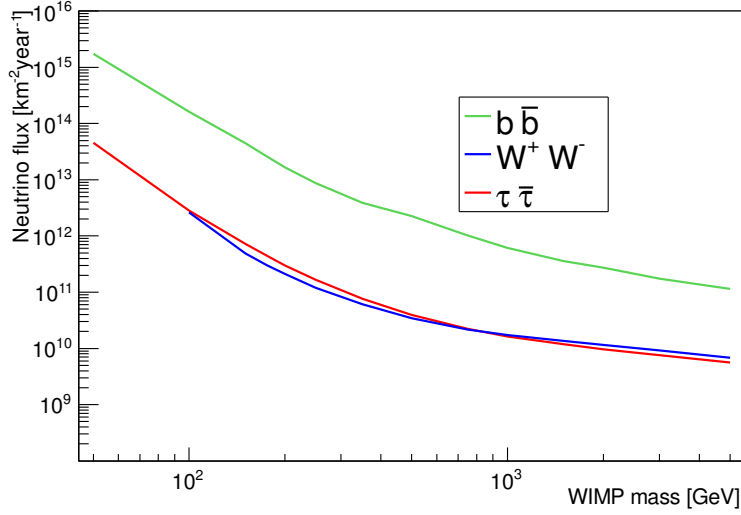


Figure 7.6: 90% C.L. limits on the signal neutrino flux from WIMP annihilations in the Sun as a function of the WIMP mass. This plot shows the combined results for the AAFit events and the BBFit multi- and single-line events. Limits for all the annihilation channels considered are shown.

between annihilation and accumulation of dark matter in the Sun. These further assumptions become relevant when the limits on the flux are converted to limits on the scattering cross-sections. For the flux limits, besides the signal spectra, only processes in the detector itself are relevant.

7.6 Systematics

Systematic errors in this analysis have a variety of sources that range from the uncertainties that stem from the astrophysical conditions to those linked to the detector operation and performance. Firstly there are uncertainties on astrophysical parameters. For the Sun this is mostly the local DM density, $\rho_{DM,loc}$. For this search a typical value of $0.3 \frac{\text{GeV}}{\text{cm}^3}$ was assumed for the local density. This is a very conservative number and a more realistic value would be around $0.4 \frac{\text{GeV}}{\text{cm}^3}$ [61]. The conversion from neutrino fluxes to WIMP-nucleon scattering cross-sections scales with $\frac{1}{\rho_{DM,loc}}$ (e.g. the higher the density the better the limits). This is the main effect of this parameter and limits for different values can be calculated easily from the limits presented in this thesis.

The DM velocity distribution is not directly observable and can have an effect on the final limits. However, if an equilibrium between annihilation and capture is assumed, a thermal equilibrium between the solar plasma and the DM can be assumed as well.

Further uncertainties exist in parton models for the solar plasma and the oscillation lengths of neutrinos. These parameters affect the expected neutrino spectra and are included in the WIMPSim code used to calculate the spectra. In comparison to the uncertainties on the local DM density these systematics only have a minor effect on the final values.

The second type of uncertainties concern the detector performance and the processes happening inside such as the propagation of photons, neutrino interaction cross-sections, quantum efficiencies of the PMTs and timing uncertainties.

Uncertainties on the quantum efficiency of the PMTs and those coming from the photon and muon propagation in the detector can be checked by comparing the recorded data and the detector simulation. If these effects are treated incorrectly for the calculation of the acceptance, there should be a significant mismatch between data and simulation. Since for the relevant regions of the reconstruction quality parameter the agreement is reasonably good but not perfect, there is some uncertainty on these parameters. In the previous binned analysis [83] these uncertainties were taken into account using the program POLE. It turned out that amongst the uncertainties the systematic of 20% on the angular acceptance of the PMTs was by far dominant. To incorporate this uncertainty a degradation of up to 6% of the acceptance was calculated with POLE. The same degree of degradation was determined for the binned analysis using the data from 2007-2012. Since the dataset of this analysis is the same, an identical degradation was used to account for the systematics of the detector.

The new analysis method does not introduce any sizeable new uncertainties to the search and is thereby justified to use the same systematics as the previous analysis.

7.7 Cross-Section

The sensitivities on the spin-dependent and spin-independent scattering cross-sections are calculated assuming an equilibrium between annihilation and capture via scattering [89] (Section 4.4.2).

The spin-dependent cross-section (SDCS) and the spin-independent cross-section (SICS) differ from each other by about two orders of magnitude (Section 4.4.2). The limits on the SDCS are shown in Fig. 7.8, that on the SICS in Fig. 7.9.

7.7.1 Comparison to the binned analysis

For the ANTARES neutrino telescope previous results exist for a binned search for dark matter in the Sun. The most recent publication prior to this work only considered data from 2007 to 2008 [83]. There are, however, newer results, published in proceedings [90], using the same data that were used in the analysis presented here. A comparison of the results of this analysis to these older ones is shown in 7.7.

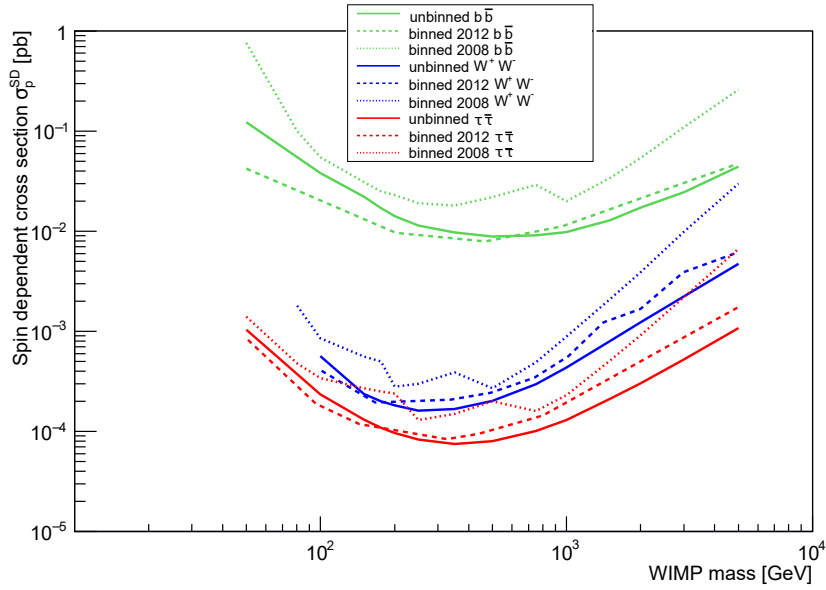


Figure 7.7: 90% C.L. limits on the spin-dependent scattering cross-section for the Sun. The colour-coding shows the annihilation channel; The dotted lines show the limits obtained with the previous “binned method” using data from 2007 to 2008 [83]; the dashed lines show the limits using this same binned method but for the larger data sample from the years 2007-2012 [90] and, finally, the solid lines show the limits obtained by the unbinned method and the 2007-2012 data sample presented in this thesis.

With a worse angular resolution it is more difficult to distinguish between the signal and the background using a likelihood function. With a binned analysis the size of the optimum search bin increases with a worse resolution. These two effects do not increase the limits in equal measure and so, in extreme cases, it is possible that the binned analysis yields better results than the unbinned analysis.

The inclusion of additional data generates an overall improvement over

the old 2007 to 2008 analysis. The change from the binned to an unbinned method however does not always lead to improved results. For masses below 150 GeV for the $\tau^+\tau^-$ and W^+W^- channel or below 500 GeV for the $b\bar{b}$ channel the binned analysis method shows better results. This can be understood as follows. For the low mass ranges, BBFit single-line provides the best limits for both the binned and unbinned methods. The single-line events have a worse angular resolution than those of AAFit multi-line. This worse resolution has a negative impact on the unbinned method, since the likelihood function becomes less powerful to distinguish the signal from the background. On the other hand, in the binned analysis the size of the optimum search bin increases with the worsening of the resolution, but the degradation of the limits in this case is smaller than that of the unbinned method.

7.7.2 Comparison to other experiments

As discussed in Sec. 4.2, there are many ways to search for DM and the results of the experiments are subject to different systematics and have different sensitivities to different hypothesis. Indirect search experiments using neutrinos are generally more sensitive to SDCS than direct detection experiments, which are more sensitive to SICS. As discussed in Sec. 4.2.3 this behaviour of the limits from direct detection experiments on the SDCS can be explained by the target material used in the experiments. Direct detection experiments are often also more sensitive to low WIMP masses. So direct and indirect detection experiments are complementary.

In Fig. 7.8, the limits from this analysis together with those of other experiments (both direct and indirect) on the SDCS can be seen. Since XENON and PICO use target materials with a low density of unpaired spins, their limits do not supersede those from ANTARES for the $\tau^+\tau^-$ and W^+W^- channels. Other direct detection experiments do not provide SDCS limits since they can not expect to supersede indirect detection experiments.

In Fig. 7.9 the comparisons for the SICS is shown. As expected, the results from XENON and LUX are more stringent than those from direct detection experiments at all mass ranges.

To compare between the ANTARES limits and those of other neutrino experiments the $\tau^+\tau^-$ channel is used as a standard. It can be seen that for the SDCS at WIMP masses below 150 GeV the limits from SuperKamiokande are lower than those from ANTARES and remain lower than the direct detection limits even for these low masses. This is not surprising, considering that SuperKamiokande is most sensitive to neutrinos with an energy of 10 GeV or lower.

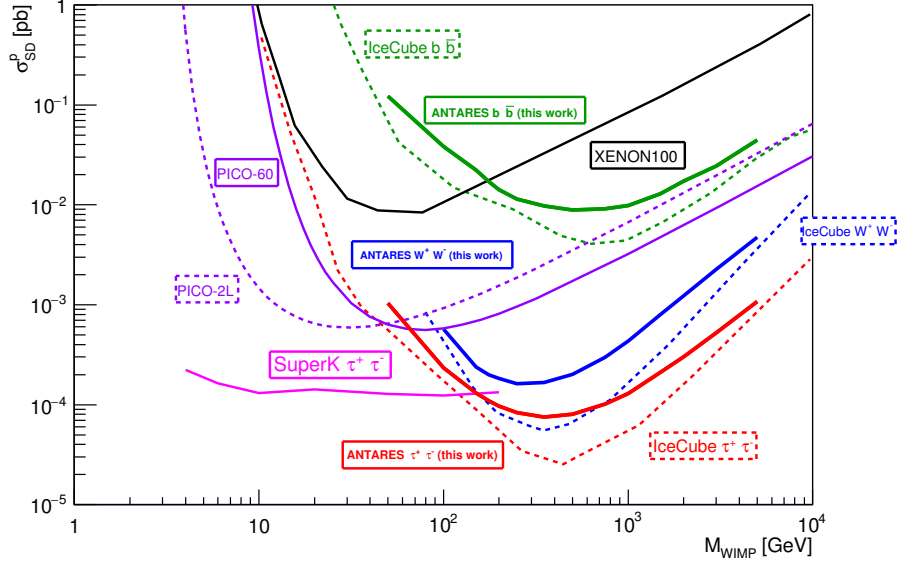


Figure 7.8: 90% C.L. limits on the spin-dependent WIMP–nucleon scattering cross-section as a function of WIMP mass for the $b\bar{b}$ (green), $\tau^+\tau^-$ (red) and W^+W^- (blue) channels. Limits given by other experiments are also shown: IceCube [91], PICO-60 [34], PICO-2L [35], SuperK [92] and XENON100 [93].

The results are also compared to the two most recent IceCube limits. The results from [94] are shown in Fig. 7.9. For those limits one year of data taken from June 2010 to May 2011 has been analysed. The 79 line setup of IceCube, including DeepCore, a volume in the centre of the detector with 6 additional strings, was used. These limits are slightly better than those obtained with ANTARES for WIMP masses below around 800 GeV. For higher WIMP masses the ANTARES limits are better.

The results of IceCube from [91] are also shown. For these limits the same data was used, but including the reconstructed neutrino energy in the likelihood. This leads to an improvement of up to a factor of 4 with respect to the previous results. Because of this improvement the new IceCube limits exceed those of ANTARES at all mass ranges. In that publication only limits on the SDCS were calculated.

The comparisons between the ANTARES and IceCube results raise the question why ANTARES can provide limits close to those of IceCube despite the huge difference in size. Whilst for the ANTARES analysis

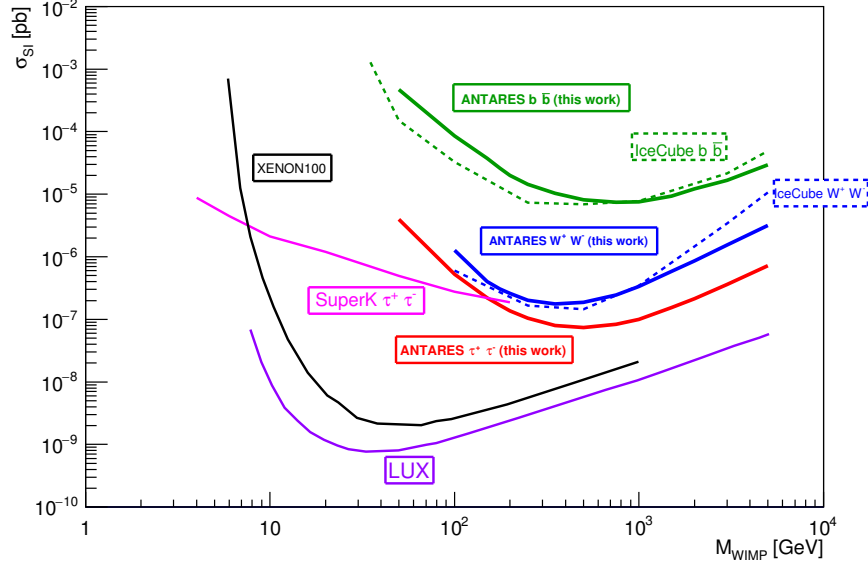


Figure 7.9: 90% C.L. limits on the spin-independent WIMP–nucleon scattering cross-section as a function of WIMP mass for the $b\bar{b}$ (green), $\tau^+\tau^-$ (red) and W^+W^- (blue) channels. Limits given by other experiments are also shown: IceCube [94], SuperK [92], LUX [33] and XENON100 [95].

the AAFit and BBFit single-line samples were used, IceCube uses three samples: Summer low energy (SL), Winter low energy (WL) and Winter high energy (WH). The summer sample uses downgoing low-energy tracks starting in DeepCore (e.g. using the outer detector as a veto), the winter samples use upgoing tracks. The WL sample mainly contains tracks starting in DeepCore, WH contains also longer tracks that may just cross IceCube.

For low WIMP masses ($M_{WIMP} < 100$ GeV) the low energy samples are the most relevant for IceCube, since due to the small size of low energy tracks the outer detector of IceCube has a too large distance between optical modules to provide a good sensitivity. The overall density of OMs in DeepCore is comparable to that of ANTARES, so overall similar limits are expected. At higher WIMP masses absorption of high energy neutrinos in the solar plasma limits the neutrino flux which can again explain similar limits.

Furthermore, the Antarctic ice used in IceCube causes a larger amount of light scattering in comparison to sea water, which is the detector medium

7.7 Cross-Section

of ANTARES. As a result the angular resolution that can be achieved with ANTARES is significantly smaller than the resolution of IceCube, which further increases the reconstruction efficiency.

Chapter 8

Results of the search for dark matter annihilations in the Galactic Centre

In this chapter the final results for the indirect search for dark matter in the Galactic Centre will be presented. For this analysis sensitivities in terms of detected neutrino events were calculated from simulated pseudo-experiments. As explained with more detail in Section 6.1, PEs are simulated maps of detected events with simulated signal events injected into them. They are analysed using the likelihood function to study its capability to distinguish signal and background.

The analysis is then unblinded according to the procedure described in Sec 6.6. The results of this unblinding are shown in Sec. 8.1. In the unblinded analysis quality the cuts that were optimised in the blinded analysis were used. These cuts are presented in Sec. 8.2.

In a first step limits and sensitivities are calculated in terms of signal strength as shown in Section 8.3. They are then converted into sensitivities on the neutrino flux by using the acceptance (Sec. 8.4). The acceptance is the effective area of the detector weighted with the expected signal spectrum. It represents the efficiency of ANTARES to detect a specific signal (Sec. 5.5).

Limits on the thermally-averaged annihilation cross section $\langle\sigma v\rangle$ are then obtained using equation 4.17. These limits are shown in Sec. 8.7. Equation 4.17 relates neutrino fluxes to $\langle\sigma v\rangle$ using the dark matter distribution contained in the so-called J-Factor.

The different dark matter halo models, described in Section 4.4.3, have a large effect on the results. Although the halo of the GC is never small enough to be considered a point source, the NFW profile is much closer to this case than the Burkert profile. Comparisons between limits for these two halo models are shown in Section 8.8.

For the analysis presented in this chapter two datasets were used:

one going from 2007 to 2013 and a larger dataset from 2007 to 2015. Comparisons between the limits for each dataset and to previous analyses performed using ANTARES are presented in Section 8.9.

Finally, the results are compared in Section 8.10 to those of other indirect search experiments, such as IceCube, the FERMI large area telescope and HESS.

8.1 Unblinding results

In the analysis for the Galactic Centre data is blinded by randomising the right ascension of the events, which is equivalent to scrambling the event time in the Sun analysis. Unblinding thus means to use the actual right ascension of the recorded data in the likelihood function and calculate a TS value for the dataset. To visualise the unblinding, Fig. 8.1 shows a comparison between the unblinded data and the expected background. The comparison for the AAFit data taken in the 2007–2015 period has been used as an example using the optimum quality cuts from the analysis. As can be seen, there is no significant excess above the background anywhere, in particular close to the source.

For the BBFit events, different coordinates have to be used. The BBFit events have only a reconstructed elevation angle, but no azimuth, so the declination and right ascension can not be computed. As a consequence, the elevation has to be used directly. The blinding is then achieved by using time-scrambled data for the production of ingredients. This was implemented by choosing random elevations for the GC rather than the actual elevation at the time of the event. Unblinding for the BBFit events means using in the likelihood function the actual position of the GC at the time of detection of an event and calculating the corresponding TS value. Note that this procedure is identical to the unblinding of the BBFit single-line data for the Sun analysis. Just as for AAFit, the unblinding for BBFit shows no significant excess above the background.

The unblinding for both the 2007–2013 (2013 sample) and the 2007–2015 data sample (2015 sample) shows TS values for the actual data below the median of the TS distributions for pure background for any of the WIMP masses and annihilation channels. An example is shown in Fig. 8.2, where the unblinded TS value is at the low end of the TS distributions (red dashed lines). This behaviour is the same for all WIMP masses and annihilation channels. Since here the Neyman method for setting limits was used, the limits were set to the previously calculated sensitivities. In this unblinding the constraint is very necessary since the very low unblinded TS values would always lead to nonphysical low limits.

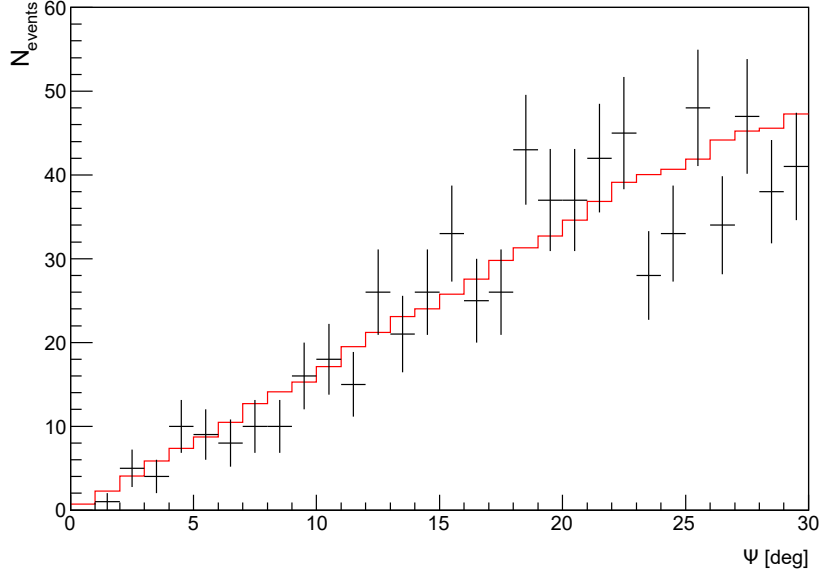


Figure 8.1: Number of events as a function of the distance to the source (crosses) in comparison to the background estimate (red histogram). In this plot a quality cut of $\lambda > -5.2$ was used.

8.2 Optimum cuts

One of the main purposes of blinding the data is to prevent any bias in the selection of the quality cuts. Therefore the optimisation of the quality parameter cuts is done using the PEs. The optimisation was carried out independently for each halo model and annihilation channel considered and can potentially differ for the different models. The optimised cuts were then used in the unblinding.

The cuts that were optimised are those on the reconstruction quality λ of AAFit and χ^2 of BBFit. There was also an optimisation of the cut on the angular error estimate, β , of AAFit in an early stage of the analysis. This cut was set to $\beta < 1^\circ$ for the Sun and the GC analyses.

As in the Sun analysis the final optimised cuts show a large stability over the different WIMP masses. For low WIMP masses the optimum cut for the AAFit analysis using the new NFW profile is $\lambda > -5.4$. This cut changes to $\lambda > -5.2$ at higher masses. This change (the first WIMP mass at which the tighter cut is used) occurs at 0.5 TeV for the W^+W^- and $\nu_\mu\bar{\nu}_\mu$ channels, 0.75 TeV for the $\mu^+\mu^-$ and $\tau^+\tau^-$ channels and 5 TeV for

8.2 Optimum cuts

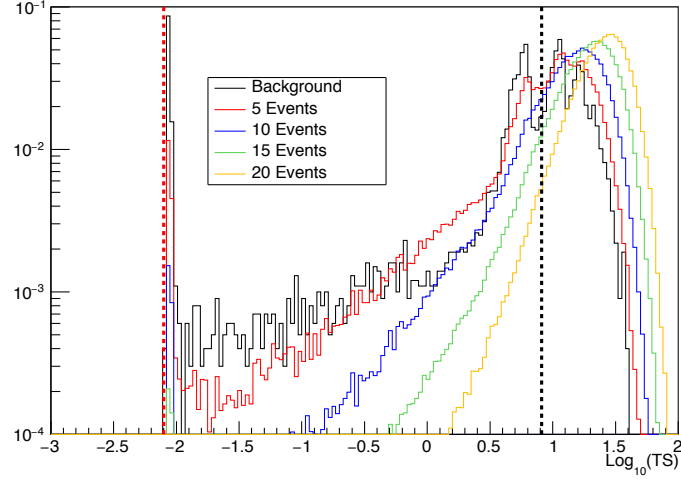


Figure 8.2: TS distributions for different average numbers of events for a WIMP mass of 1 TeV and the $\tau^+\tau^-$ channel. The black dashed line marks the median of the background TS distribution, the red dashed line marks the TS value of the unblinded data.

the $b\bar{b}$ channel. Note that the harder the channel, the earlier the change of cut occurs.

For the Burkert profile this change occurs at lower WIMP masses. For the softest channel, $b\bar{b}$, the change of cut occurs at a WIMP mass of 0.5 TeV. For the harder channels $\tau^+\tau^-$, W^+W^- and $\mu^+\mu^-$ the cut changes at 176 GeV, 150 GeV and 200 GeV, respectively. For the hardest channel, $\nu_\mu\bar{\nu}_\mu$, the cut changes at 180 GeV.

These optimum cuts were the same for both the 2013 and the 2015 data samples. For the 2015 sample, however, it was decided that the final cut would be fixed to $\lambda < -5.2$ for all WIMP masses and annihilation channels. This was done to reduce the amount of background from atmospheric muons and since it almost had no effect on the sensitivity. In Fig. 1 in appendix 1 a comparison between data and simulation is shown and it is visible that the detected events are dominated by atmospheric muons for quality cuts looser than $\lambda < -5.2$.

The BBFit cuts are not relevant at WIMP masses above 1 TeV since the AAFit results lead to the best sensitivities in this region. At the relevant mass range, the prevalent cut is $\chi^2 < 0.7$ with only one exception: at 90 GeV for the $b\bar{b}$ channel the cut jumps to $\chi^2 < 0.9$.

The halo models have an effect on the optimisation of the quality cuts. For the BBFit single-line analysis the cuts at the relevant mass range do

not change for the Burkert profile (it stays at $\chi^2 < 0.7$).

8.3 Initial limits

The sensitivities that are obtained immediately from the TS distributions are sensitivities in terms of the number of detected neutrino events. They can be seen in Fig. 8.3.

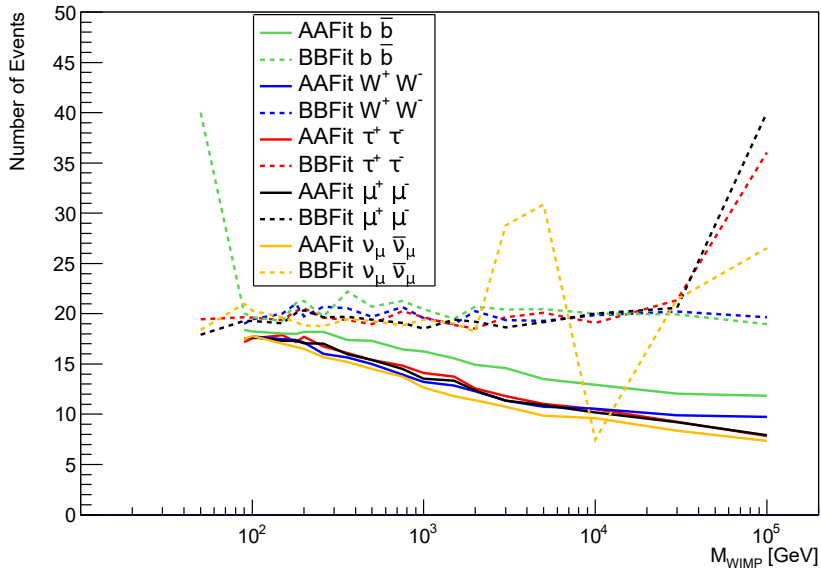


Figure 8.3: Sensitivities on the number of detected neutrino events for the different reconstruction strategies and annihilation channels. The quality cuts used for these plots are the optimised cuts from the calculation of the sensitivity for BBFit and $\lambda < -5.2$ for AAFit. For these sensitivities the NFW profile was used.

These limits depend on the halo model used, since the J-Factors are used to generate the PEs from which they are calculated. The jumps in the BBFit limits stem from the changes in the quality cut described in Sec. 8.2. Even when the cut is stable the BBFit limits change more than the AAFit limits. This can be explained by the lower angular resolution for the BBFit single-line events.

8.4 Acceptance

As in the case of the Sun, the limits in terms of number of detected events are very stable over the range of WIMP masses considered. The shape of the limits on the neutrino flux then depends mostly on the behaviour of the acceptance of the detector.

A plot of the acceptance as a function of the WIMP mass can be seen in Fig. 8.4. The acceptance to signals from WIMP annihilations depends on the neutrino signal spectra and the detector itself but not on the halo model used.

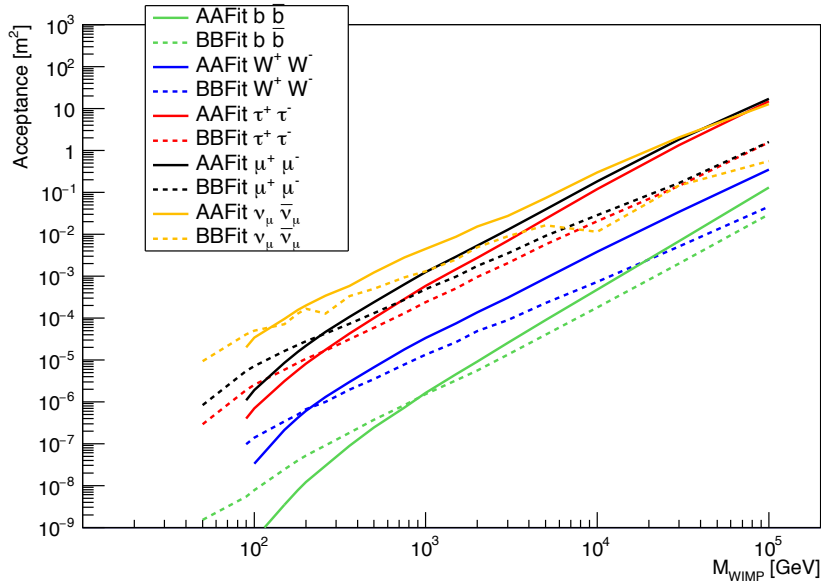


Figure 8.4: The neutrino signal acceptance for the different reconstruction strategies and annihilation channels. The quality cuts used for these plots are the optimised cuts from the calculation of the sensitivity.

A harder channel like the $\nu_\mu \bar{\nu}_\mu$ channel leads to larger acceptances and soft channels like the $b\bar{b}$ channel lead to lower acceptances. The $\mu^+\mu^-$ and the $\tau^+\tau^-$ channels lead to very similar acceptances. At the energy range of the annihilation the mass difference between muons and taus does not seem to be very important for the acceptance, especially for very high WIMP masses.

The acceptance of $\nu_\mu \bar{\nu}_\mu$ also converges for high WIMP masses to those of the $\mu^+\mu^-$ and the $\tau^+\tau^-$ channels. Comparing the spectra of these

channels shown in Fig. 4.16, one can see that the main difference is a bump in the $\nu_\mu\bar{\nu}_\mu$ spectrum at the WIMP mass. At very high WIMP masses this bump is suppressed by the increasing opacity of the Earth (see Fig. 5.5), which explains the convergence of the acceptances.

8.5 Neutrino Flux

As in the case of the Sun analysis, the shape of the limits in terms of the signal neutrino flux depends more strongly on the signal acceptance. The overall level of the flux limits, however, depends strongly on the model assumptions, i.e. the halo models. This is discussed in further detail in Sec. 8.8.

The final limits for the NFW profile are shown in Fig. 8.5. The BBFit limits are used until WIMP masses of 180 GeV for the W^+W^- and $\tau^+\tau^-$ channels, 200 GeV for the $\mu^+\mu^-$ channel, 500 GeV for the $b\bar{b}$ and 100 GeV for the $\nu_\mu\bar{\nu}_\mu$.

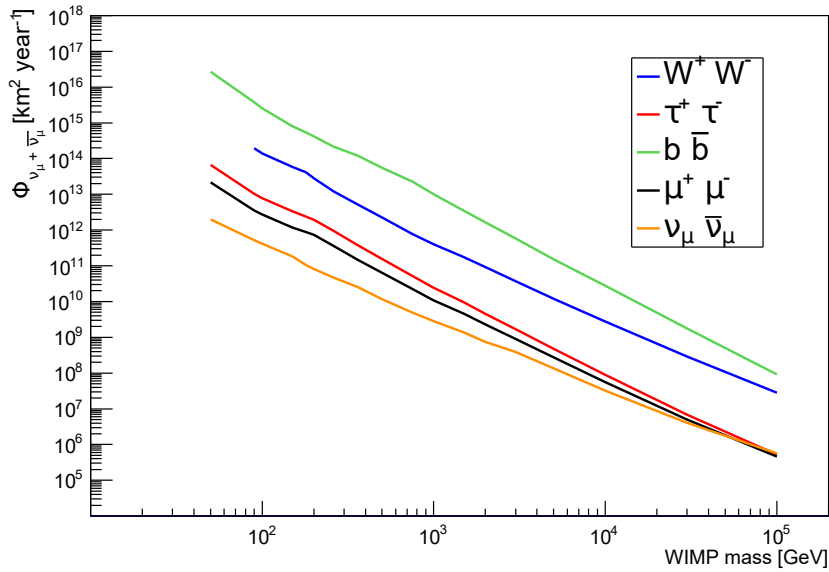


Figure 8.5: 90% C.L. upper limits on the neutrino flux from WIMP annihilations in the Milky Way as a function of the WIMP masses for the different channels considered. In this plot the NFW profile was used.

The sensitivities and limits from other searches with ANTARES [96] show a saturation at neutrino energies of a few 100 TeV. Since most neutri-

nos that result from WIMP annihilations will have an energy proportional to around 10 % of the WIMP mass, the saturation is expected to happen at WIMP masses of the order of 1 PeV and therefore can not be seen here.

8.6 Systematics

There are many sources of systematic errors in this analysis. Similar to the Sun analysis, errors can be divided in model uncertainties and uncertainties from the detector.

To take into account uncertainties from the halo models three very different models were used. The actual errors on the halo parameters were not taken into consideration, since it is inherently difficult to include these in this analysis. The differences in the halo models have a huge impact on the corresponding limits, which can be seen in Sec. 8.8.

Further uncertainties on the neutrino oscillation parameters are included in the signal spectra that were used in the analysis [63, 64].

The detector uncertainties have to be treated differently to the Sun analysis. Since the dataset used for the GC is not the same as the one used in the previous binned analysis, the 6% degradation from that analysis can not be used here. Instead, the approach of previously performed point source searches with ANTARES was applied [97]. In this approach a 15% uncertainty on the angular resolution was assumed based on an uncertainty of 2.5 ns of the arrival time of the photon hits. The actual uncertainty is likely smaller, but not by a large amount.

This systematic was implemented in the analysis at the production of the ingredients. When the PSF and the source morphology were combined as described in Sec. 6.5, the PSF was additionally smeared by this 15% uncertainty.

Uncertainties on the quantum efficiency of the PMTs, photon and muon propagation in the detector can again be investigated using the Monte Carlo simulation. If these were treated improperly a large discrepancy between simulation and data would be apparent. Again a small mismatch can be seen in the comparison in Appendix 1 that indicates a small systematic error, which does not to have a significant effect on the limits.

8.7 Cross–Section

The final results for the search for WIMP annihilations in the Galactic Centre are the limits on the thermally averaged annihilation cross–section. Sensitivities for the three halo profiles were produced. The limits for the NFW profile can be seen in Fig. 8.6 and are also presented in table 3.

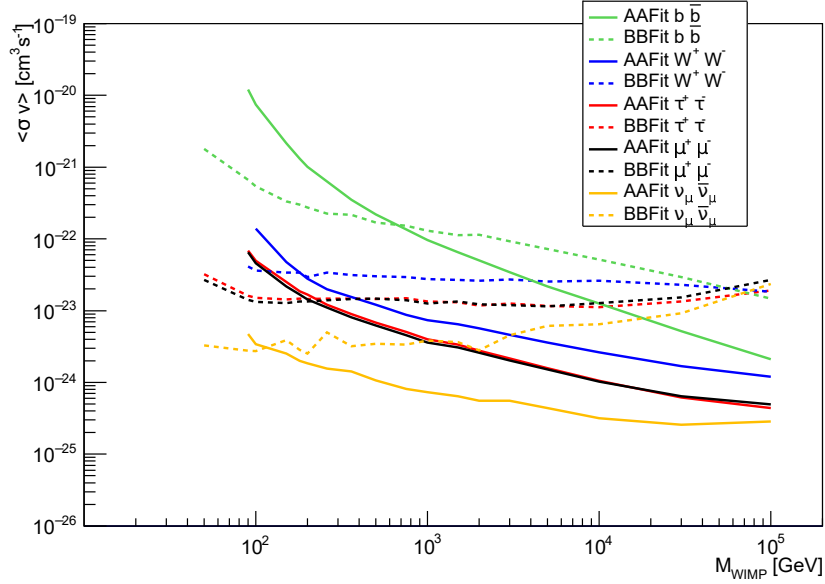


Figure 8.6: Sensitivities for the thermally averaged annihilation cross-section $\langle\sigma v\rangle$ as a function of the WIMP mass. The sensitivities in this plot were calculated for the NFW profile.

The similarity of the limits in terms of the neutrino flux for the cases of the $\nu_\mu\bar{\nu}_\mu$, the $\mu^+\mu^-$ and the $\tau^+\tau^-$ channel is no longer present in the limits on the cross-section. To convert flux to cross-section limits the average number of neutrinos per annihilation has to be taken into account. This number depends on the annihilation channel and breaks the convergence of the three channels.

The limits and sensitivities on the cross-section are calculated from the limits on the signal neutrino fluxes using Equation 4.17. In this equation, the integrated J-Factor is used, adding another dependency on the halo model. As a result, the difference between the neutrino flux sensitivities is further increased in the final limits and sensitivities.

8.8 Comparison between halo models

Three very different profiles were considered in this analysis: the NFW profile, which is a cuspy profile that has a large amount of dark matter concentrated in its centre; the McMillan profile, which is cusped like the NFW profile, but shows a larger halo extension, and the Burkert profile, which is cored and appears much more extended than the NFW and

8.8 Comparison between halo models

McMillan profiles. For the NFW profile, a set of parameters adapted from a survey performed by Nesti [61] that is different from the one used in the previous analysis using ANTARES [98]. This was done in correspondence to recent analyses performed by IceCube [99]. The halo parameters used in this analysis are summarised in Table 4.1. A raw comparison between the halo profiles themselves is presented in Section 4.4.

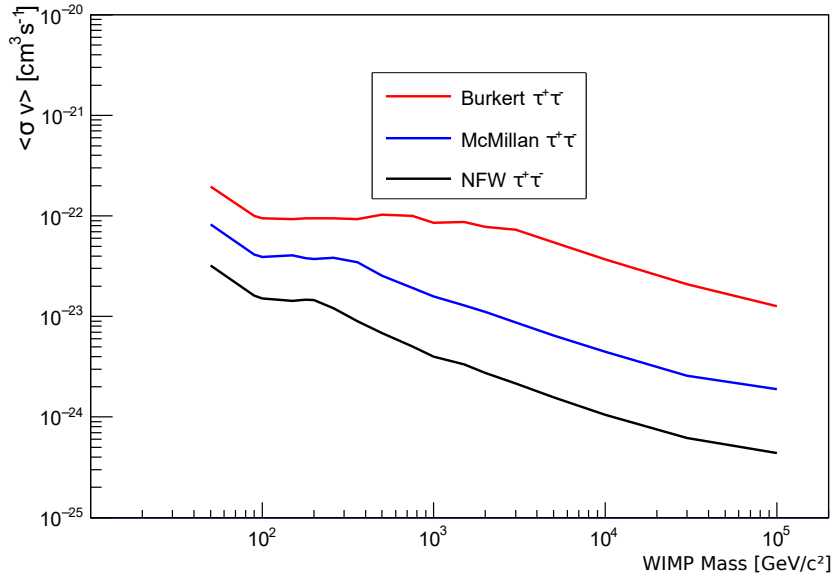


Figure 8.7: Sensitivities on the thermally averaged annihilation cross-section $\langle\sigma v\rangle$ as a function of the WIMP mass for the three Halo models considered for the $\tau^+\tau^-$ annihilation channel.

A more concentrated profile generates a signal that is easier to find with the corresponding likelihood function and therefore affects the limits in terms of the number of detected events and neutrino flux. In addition, in the conversion from neutrino flux to thermally-averaged cross-section (Eq. 4.17) there is also a factor 2.47 between the NFW and the Burkert profiles. This leads to an even larger difference in the final limits which can be seen in Fig. 8.7. The difference between the NFW and the Burkert profiles is up to two orders of magnitude for the highest WIMP masses. The McMillan profile presents an intermediate case between the NFW and the Burkert profiles and produces limits in between.

Since these new limits are very low for the NFW profile at WIMP masses above 100 TeV the limitations from partial-wave unitarity [100] will become relevant, although there is an approach to overcome these

limitations [101].

8.9 Comparison to the binned analysis

In contrast to the comparison for the results on the Sun in section 7.7.1, the comparison between this new analysis and the previous results presented in [62] is subject to a larger number of strong systematics that differ between experiments. A comparison between the limits on $\langle\sigma v\rangle$ from the old analysis and the analysis of this thesis is presented in Fig. 8.8. Firstly, the halo models used in this new analysis differ significantly from those used in the previous analysis. This leads to a factor 2.1 that is introduced through the integrated J-Factor in equation 4.17. Furthermore, a more concentrated source can be identified with fewer signal events. This can cause a difference of a factor 3 to 6 depending on the WIMP mass and the annihilation channel.

The remaining difference can be well explained by the more sophisticated analysis method and the inclusion of the data from 2013 to 2015. The 2013 to 2015 data correspond to 780.6 days of live time, which is 59.91% of the 1321 days of live time in 2007 to 2012. The improvement due to the inclusion of these new data is expected to be below this percentage. It can not be exactly quantified how large the difference is due to the use of the new method, but the overall improvement is within the margin of what can reasonably be expected.

8.10 Comparison to other experiments

Fig. 8.9 shows the limits on the thermally-averaged annihilation cross-section $\langle\sigma v\rangle$ as a function of the WIMP mass for several experiments, including the search with ANTARES described in this chapter. As can be seen, for all WIMP masses the ANTARES limits are more stringent than those provided by IceCube and the difference increases with the WIMP mass. This can be understood as follows. The IceCube search uses a veto to exclude all track-like events starting outside the detector's volume. Therefore, the increase of IceCube's acceptance with WIMP mass is much smaller than that of ANTARES, since the former is limited by the instrumented volume while the latter increases with the muon range, which at high energies can reach hundreds of metres or even a few kilometres. The new ANTARES limits also allow to partly constrain models where extraterrestrial neutrinos observed by IceCube are partly explained in terms of annihilating dark matter candidates [102].

8.10 Comparison to other experiments

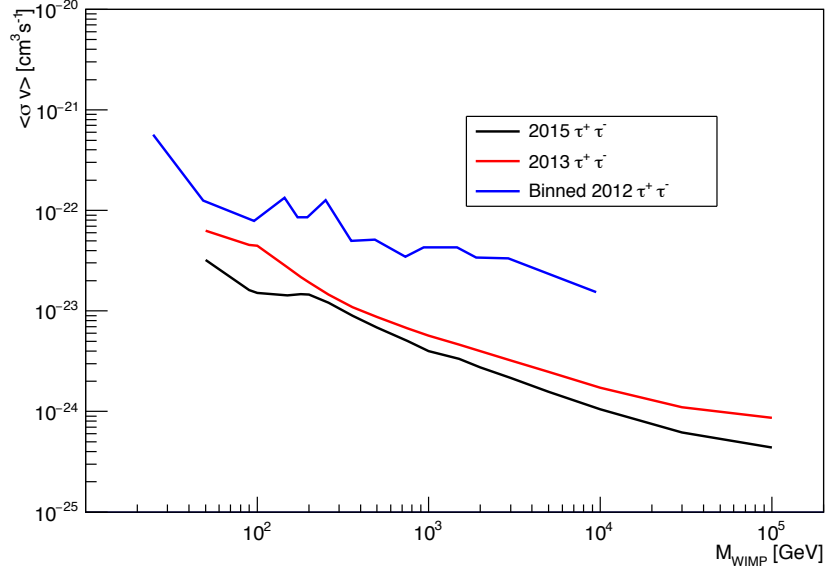


Figure 8.8: Sensitivities for the thermally-averaged annihilation cross-section $\langle\sigma v\rangle$ for different analyses of the ANTARES data. The sensitivities in this plot were calculated for the NFW profile. The limits for the 2013 and 2015 analyses use the new parameters from [61] and the binned limits are taken from [98] and use the old set of halo parameters. The irregular behaviour of the binned analysis is due to the fact that limits (not sensitivities) are shown.

The limit for FERMI is calculated using a stacked analysis with multiple sources, including the Galactic Centre. For the Galactic Centre a generalised NFW profile was used. The halo parameters used for the FERMI GC search are $\rho_{local} = 0.4 \text{ GeV} \cdot \text{cm}^{-3}$ and a scaling radius of 20 kpc. This choice favours both ANTARES and IceCube in this comparison. Further sources that were considered are dark matter dominated dwarf spheroidal galaxies (dSphs) in the Milky Way and other dwarf galaxies.

The HESS limits were calculated for the Galactic Centre alone and assume an Einasto profile with a local density of $0.39 \text{ GeV} \cdot \text{cm}^{-3}$. The comparison favours again ANTARES and IceCube as in the case of the FERMI limits.

These limits supersede all limits generated with IceCube and are the most stringent of all indirect searches for a high WIMP masses.

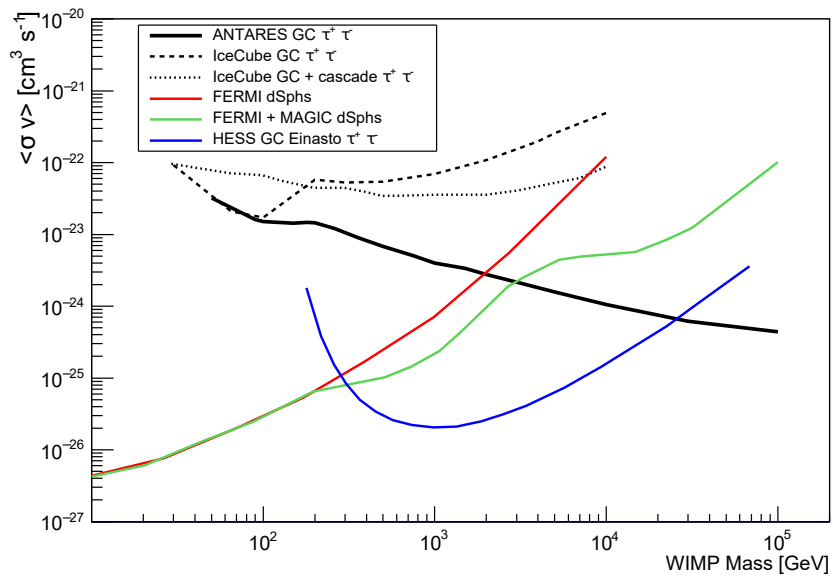


Figure 8.9: Limits on the thermally averaged annihilation cross-section $\langle\sigma v\rangle$. The limits for the IceCube experiment [99, 103] were calculated using the NFW profile. The results of FERMI [104], HESS [105] and MAGIC [106] are also shown.

Chapter 9

Conclusion

9.1 Calibration

The time calibration using optical beacons for the years 2013 to 2015 show the persistent ageing of the detector mainly in the number of OMs that could be calibrated in each period. The spread of the corrections does not show a systematic increase over time and varies around 2 ns. This is concordant with the precision of the order of 1 ns that is required to guarantee the good angular resolution of ANTARES.

Recent studies of the time calibration using ^{40}K decays show a large number of jumps in the time offsets between OMs in the same storey. These jumps do not seem to be correlated to the calibration with OMs, but still show the need for a tighter monitoring of the time calibration than the current calibration every 2 months. Some of these jumps are suspected to be correlated to incidents in the power supply and the communication with the detector.

9.2 Search towards the Sun

Even though the recent results on the search for dark matter in the Sun can not supersede the most recent limits from the IceCube collaboration they are very close in the comparison. Considering the enormous difference in size between ANTARES and IceCube the discrepancy of the limits is small and compared to previous results from ANTARES a significant improvement was achieved. With further data the limits might be improved to the point of competing with the most recent IceCube limits.

9.3 Search towards the Galactic Centre

The search for dark matter in the GC leads to very good results. Not only supersede the new limits those of IceCube, but also the results of indirect searches using γ -rays for WIMP masses larger than 30 TeV, although the comparison is for these other experiments is not perfectly apt. The new method and the inclusion of additional data have achieved a significant improvement over the last results from ANTARES. Overall these new results are a huge success for the ANTARES experiment.

Appendix

1 Comparisons to simulation

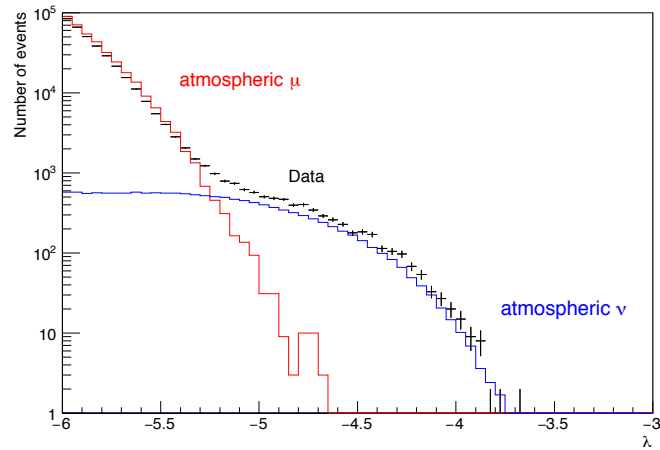


Figure 1: Distribution of the number of events as a function of the event reconstruction quality λ for the AAFit algorithm. The events reconstructed in the 2007-20125 period are shown. The histogram shows the background estimate generated by Monte Carlo simulation, the crosses represent the recorded data.

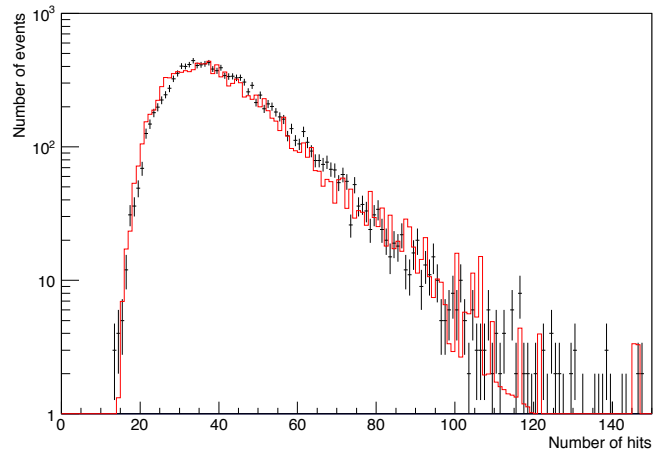


Figure 2: Distribution of the number of events as a function of the number of hits used in the reconstruction. The events reconstructed with the AAFit algorithm in the 2007-2015 period are shown. The line shows the background estimate generated from the Monte Carlo simulation, the crosses represent the recorded data.

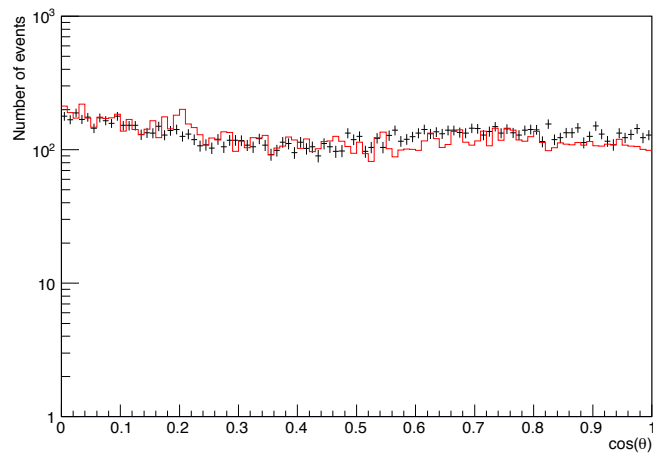


Figure 3: Distribution of the number of events as a function of the event elevation. The events reconstructed with the AAFit algorithm in the 2007-2015 period are shown. The line shows the background estimate generated from the Monte Carlo simulation, the crosses represent the recorded data.

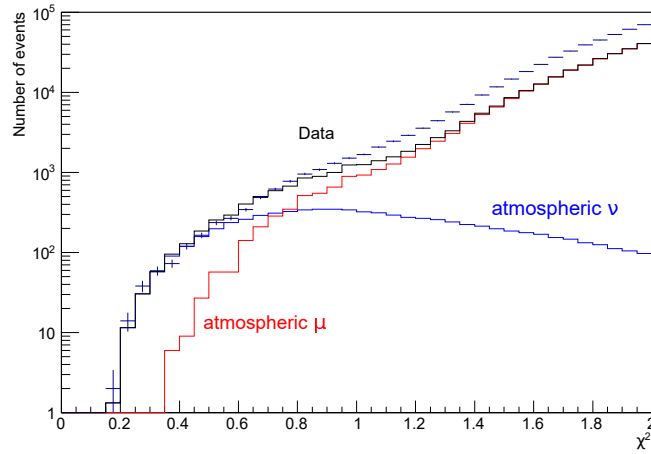


Figure 4: Distribution of the number of events as a function of the event reconstruction quality χ^2 for the BBFit algorithm. The single-line events reconstructed in the 2007-2015 period are shown. The histogram shows the background estimate generated by Monte Carlo simulation, the crosses represent the recorded data.

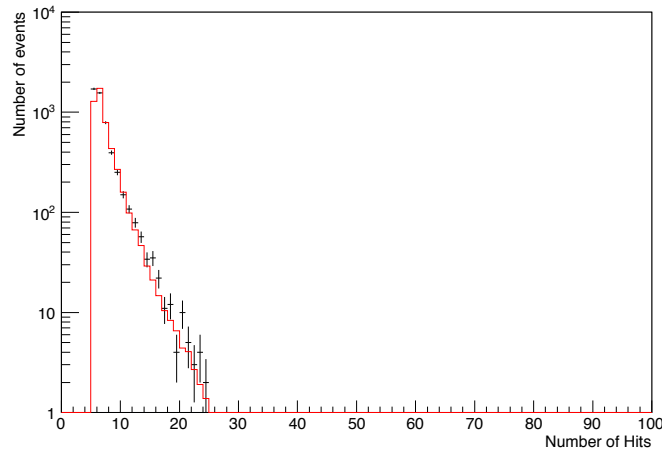


Figure 5: Distribution of the number of events as a function of the number of hits used in the reconstruction. The single-line events reconstructed with the BBFit algorithm in the 2007-2015 period are shown. The line shows the background estimate generated from the Monte Carlo simulation, the crosses represent the recorded data.

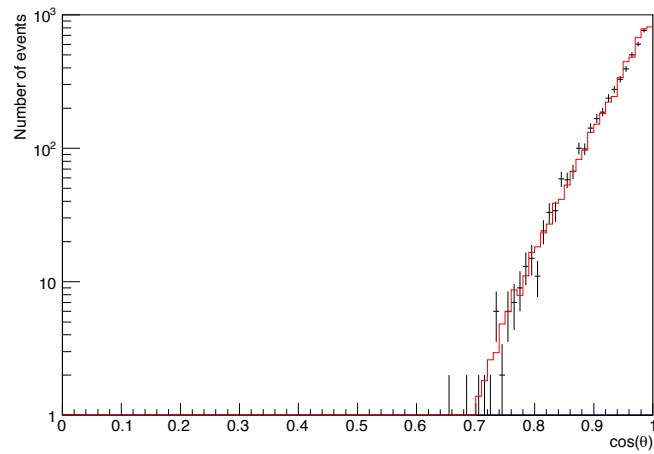


Figure 6: Distribution of the number of events as a function of the event elevation. The events single-line reconstructed with the BBFit algorithm in the 2007-2015 period are shown. The line shows the background estimate generated from the Monte Carlo simulation, the crosses represent the recorded data.

2 Tables

M_{WIMP} [GeV]		Φ_ν [$\text{km}^{-2}\text{yr}^{-1}$]	σ_{SD} [pb]	σ_{SI} [pb]
50	$b\bar{b}$	$1.75 \cdot 10^{15}$	0.122	$4.70 \cdot 10^{-4}$
	$\tau\bar{\tau}$	$4.53 \cdot 10^{13}$	$1.04 \cdot 10^{-3}$	$3.99 \cdot 10^{-6}$
100	$b\bar{b}$	$1.63 \cdot 10^{14}$	$3.81 \cdot 10^{-2}$	$8.54 \cdot 10^{-5}$
	W^+W^-	$2.61 \cdot 10^{12}$	$5.67 \cdot 10^{-4}$	$1.27 \cdot 10^{-6}$
	$\tau\bar{\tau}$	$2.85 \cdot 10^{12}$	$2.34 \cdot 10^{-4}$	$5.24 \cdot 10^{-7}$
150	$b\bar{b}$	$4.51 \cdot 10^{13}$	$2.23 \cdot 10^{-2}$	$3.77 \cdot 10^{-5}$
	W^+W^-	$4.93 \cdot 10^{11}$	$2.38 \cdot 10^{-4}$	$4.02 \cdot 10^{-7}$
	$\tau\bar{\tau}$	$7.25 \cdot 10^{11}$	$1.31 \cdot 10^{-4}$	$2.22 \cdot 10^{-7}$
176	$b\bar{b}$	$2.55 \cdot 10^{13}$	$1.71 \cdot 10^{-2}$	$2.61 \cdot 10^{-5}$
	W^+W^-	$3.00 \cdot 10^{11}$	$2.00 \cdot 10^{-4}$	$3.06 \cdot 10^{-7}$
	$\tau\bar{\tau}$	$4.41 \cdot 10^{11}$	$1.09 \cdot 10^{-4}$	$1.67 \cdot 10^{-7}$
200	$b\bar{b}$	$1.66 \cdot 10^{13}$	$1.42 \cdot 10^{-2}$	$2.01 \cdot 10^{-5}$
	W^+W^-	$2.13 \cdot 10^{11}$	$1.83 \cdot 10^{-4}$	$2.59 \cdot 10^{-7}$
	$\tau\bar{\tau}$	$3.01 \cdot 10^{11}$	$9.65 \cdot 10^{-5}$	$1.37 \cdot 10^{-7}$
250	$b\bar{b}$	$8.75 \cdot 10^{12}$	$1.15 \cdot 10^{-2}$	$1.43 \cdot 10^{-5}$
	W^+W^-	$1.19 \cdot 10^{11}$	$1.62 \cdot 10^{-4}$	$2.03 \cdot 10^{-7}$
	$\tau\bar{\tau}$	$1.65 \cdot 10^{11}$	$8.32 \cdot 10^{-5}$	$1.04 \cdot 10^{-7}$

Table 1: The limits in terms of neutrino flux, spin dependent and spin independent cross-section versus the annihilation channel and wimp mass.

M_{WIMP} [GeV]		Φ_ν [$\text{km}^{-2}\text{yr}^{-1}$]	σ_{SD} [pb]	σ_{SI} [pb]
350	$b\bar{b}$	$3.88 \cdot 10^{12}$	$9.76 \cdot 10^{-3}$	$1.03 \cdot 10^{-5}$
	W^+W^-	$6.10 \cdot 10^{10}$	$1.67 \cdot 10^{-4}$	$1.77 \cdot 10^{-7}$
	$\tau\bar{\tau}$	$7.58 \cdot 10^{10}$	$7.50 \cdot 10^{-5}$	$7.96 \cdot 10^{-8}$
500	$b\bar{b}$	$2.25 \cdot 10^{12}$	$8.83 \cdot 10^{-3}$	$8.15 \cdot 10^{-6}$
	W^+W^-	$3.46 \cdot 10^{10}$	$2.01 \cdot 10^{-4}$	$1.86 \cdot 10^{-7}$
	$\tau\bar{\tau}$	$3.96 \cdot 10^{10}$	$8.00 \cdot 10^{-5}$	$7.38 \cdot 10^{-8}$
750	$b\bar{b}$	$1.02 \cdot 10^{12}$	$9.14 \cdot 10^{-3}$	$7.50 \cdot 10^{-6}$
	W^+W^-	$2.17 \cdot 10^{10}$	$2.98 \cdot 10^{-4}$	$2.44 \cdot 10^{-7}$
	$\tau\bar{\tau}$	$2.24 \cdot 10^{10}$	$1.01 \cdot 10^{-4}$	$8.32 \cdot 10^{-8}$
1000	$b\bar{b}$	$6.15 \cdot 10^{11}$	$9.81 \cdot 10^{-3}$	$7.58 \cdot 10^{-6}$
	W^+W^-	$1.73 \cdot 10^{10}$	$4.33 \cdot 10^{-4}$	$3.35 \cdot 10^{-7}$
	$\tau\bar{\tau}$	$1.63 \cdot 10^{10}$	$1.30 \cdot 10^{-4}$	$1.00 \cdot 10^{-7}$
1500	$b\bar{b}$	$3.58 \cdot 10^{11}$	$1.29 \cdot 10^{-2}$	$9.39 \cdot 10^{-6}$
	W^+W^-	$1.36 \cdot 10^{10}$	$7.99 \cdot 10^{-4}$	$5.80 \cdot 10^{-7}$
	$\tau\bar{\tau}$	$1.19 \cdot 10^{10}$	$2.12 \cdot 10^{-4}$	$1.54 \cdot 10^{-7}$
2000	$b\bar{b}$	$2.72 \cdot 10^{11}$	$1.72 \cdot 10^{-2}$	$1.21 \cdot 10^{-5}$
	W^+W^-	$1.15 \cdot 10^{10}$	$1.23 \cdot 10^{-3}$	$8.65 \cdot 10^{-7}$
	$\tau\bar{\tau}$	$9.68 \cdot 10^9$	$3.02 \cdot 10^{-4}$	$2.13 \cdot 10^{-7}$
3000	$b\bar{b}$	$1.72 \cdot 10^{11}$	$2.45 \cdot 10^{-2}$	$1.68 \cdot 10^{-5}$
	W^+W^-	$9.18 \cdot 10^9$	$2.25 \cdot 10^{-3}$	$1.54 \cdot 10^{-6}$
	$\tau\bar{\tau}$	$7.56 \cdot 10^9$	$5.25 \cdot 10^{-4}$	$3.60 \cdot 10^{-7}$
5000	$b\bar{b}$	$1.14 \cdot 10^{11}$	$4.44 \cdot 10^{-2}$	$2.97 \cdot 10^{-5}$
	W^+W^-	$6.84 \cdot 10^9$	$4.74 \cdot 10^{-3}$	$3.17 \cdot 10^{-6}$
	$\tau\bar{\tau}$	$5.63 \cdot 10^9$	$1.07 \cdot 10^{-3}$	$7.19 \cdot 10^{-7}$

Table 2: The continuation to table 1.

M_{WIMP} [GeV]	$\langle\sigma v\rangle_{b\bar{b}}$ [cm^3s^{-1}]	$\langle\sigma v\rangle_{W^+W^-}$ [cm^3s^{-1}]	$\langle\sigma v\rangle_{\tau^+\tau^-}$ [cm^3s^{-1}]	$\langle\sigma v\rangle_{\mu^+\mu^-}$ [cm^3s^{-1}]	$\langle\sigma v\rangle_{\nu_\mu\bar{\nu}_\mu}$ [cm^3s^{-1}]
50	$1.8 \cdot 10^{-21}$		$3.22 \cdot 10^{-23}$	$2.67 \cdot 10^{-23}$	$3.27 \cdot 10^{-24}$
90	$6.65 \cdot 10^{-22}$	$4.11 \cdot 10^{-23}$	$1.62 \cdot 10^{-23}$	$1.42 \cdot 10^{-23}$	$2.76 \cdot 10^{-24}$
100	$5.38 \cdot 10^{-22}$	$3.61 \cdot 10^{-23}$	$1.51 \cdot 10^{-23}$	$1.33 \cdot 10^{-23}$	$2.72 \cdot 10^{-24}$
150	$3.34 \cdot 10^{-22}$	$3.37 \cdot 10^{-23}$	$1.43 \cdot 10^{-23}$	$1.27 \cdot 10^{-23}$	$2.52 \cdot 10^{-24}$
180	$3.01 \cdot 10^{-22}$	$3.4 \cdot 10^{-23}$	$1.47 \cdot 10^{-23}$	$1.35 \cdot 10^{-23}$	$2.00 \cdot 10^{-24}$
200	$2.75 \cdot 10^{-22}$	$2.95 \cdot 10^{-23}$	$1.45 \cdot 10^{-23}$	$1.35 \cdot 10^{-23}$	$1.84 \cdot 10^{-24}$
260	$2.24 \cdot 10^{-22}$	$2.96 \cdot 10^{-23}$	$1.2 \cdot 10^{-23}$	$1.39 \cdot 10^{-23}$	$1.56 \cdot 10^{-24}$
360	$2.15 \cdot 10^{-22}$	$2.15 \cdot 10^{-23}$	$9.0 \cdot 10^{-24}$	$1.13 \cdot 10^{-23}$	$1.43 \cdot 10^{-24}$
500	$1.7 \cdot 10^{-22}$	$1.66 \cdot 10^{-23}$	$6.83 \cdot 10^{-24}$	$8.66 \cdot 10^{-24}$	$1.06 \cdot 10^{-24}$
750	$2.24 \cdot 10^{-22}$	$1.2 \cdot 10^{-23}$	$5.03 \cdot 10^{-24}$	$6.19 \cdot 10^{-24}$	$8.12 \cdot 10^{-25}$
1000	$1.52 \cdot 10^{-22}$	$1.0 \cdot 10^{-23}$	$4.01 \cdot 10^{-24}$	$4.97 \cdot 10^{-24}$	$7.35 \cdot 10^{-25}$
1500	$8.83 \cdot 10^{-21}$	$8.04 \cdot 10^{-24}$	$3.35 \cdot 10^{-24}$	$3.79 \cdot 10^{-24}$	$6.44 \cdot 10^{-25}$
2000	$6.68 \cdot 10^{-23}$	$7.01 \cdot 10^{-24}$	$2.75 \cdot 10^{-24}$	$3.23 \cdot 10^{-24}$	$5.59 \cdot 10^{-25}$
3000	$4.39 \cdot 10^{-23}$	$5.88 \cdot 10^{-24}$	$2.16 \cdot 10^{-24}$	$2.57 \cdot 10^{-24}$	$5.55 \cdot 10^{-25}$
5000	$2.8 \cdot 10^{-23}$	$4.52 \cdot 10^{-24}$	$1.58 \cdot 10^{-24}$	$1.85 \cdot 10^{-24}$	$4.36 \cdot 10^{-25}$
10000	$1.54 \cdot 10^{-23}$	$3.1 \cdot 10^{-24}$	$1.06 \cdot 10^{-24}$	$1.2 \cdot 10^{-24}$	$3.16 \cdot 10^{-25}$
30000	$6.33 \cdot 10^{-24}$	$1.91 \cdot 10^{-24}$	$6.2 \cdot 10^{-25}$	$7.12 \cdot 10^{-25}$	$2.57 \cdot 10^{-25}$
100000	$2.53 \cdot 10^{-24}$	$1.37 \cdot 10^{-24}$	$4.4 \cdot 10^{-25}$	$5.61 \cdot 10^{-25}$	$2.84 \cdot 10^{-25}$

Table 3: The limits in terms the thermally averaged annihilation cross-section versus the wimp mass for the NFW halo profile.

3 List of Acronyms

3.1 Cosmology and Astrophysics

GC Galactic Centre

RA Right Ascension

DEC Declination

dSphs Dwarf spheroidal galaxy

3.2 Dark matter

DM Dark Matter

CMB Cosmic Microwave Background

3.3 ANTARES

OM Optical Module

OB Optical Beacon

JB Junction Box

BSS Bottom String Socket

ARS Analogue Ring Sampler

LCM Local Control Module

PMT Photo Multiplier Tube

IL Instrumentation Line

3.4 Statistics and Analysis

PE Pseudo-experiment

TS Test Statistic

Resumen

La búsqueda de materia oscura es actualmente uno de los temas de investigación más candentes en física fundamental. Sabemos de su posible existencia únicamente por los efectos gravitatorios que causa, pero desconocemos su naturaleza real.

Una de las hipótesis más estudiadas es la de que pueda estar compuesta por partículas elementales aún no descubiertas. Diversas consideraciones sobre su abundancia actual a partir de su producción térmica en el Universo primitivo conducen a la posibilidad de que dichas partículas sean muy masivas e interaccionen muy débilmente con la materia ordinaria, lo que se ha dado en llamar WIMPs (*Weakly Interacting Massive Particles*). Varios modelos teóricos (supersimetría, teorías de dimensiones extra Kaluza-Klein, etc.), propuestos por otras razones, ofrecen candidatos naturales a WIMPs. La búsqueda de WIMPs se puede llevar a cabo de diversas formas: produciéndolas y observándolas en los aceleradores de partículas, detectando aquellas que están presentes en nuestro entorno (búsqueda directa) u observando partículas estándar muy energéticas (rayos X o rayos gamma, rayos cósmicos, neutrinos) procedentes de grandes objetos astrofísicos donde los WIMPs se concentrarían y acabarían aniquilándose (búsqueda indirecta).

El trabajo de investigación de esta tesis doctoral se centra en la búsqueda indirecta de materia oscura a través de neutrinos de alta energía producidos por la auto-aniquilación de WIMPs acumulados en el interior del Sol o en el centro de la Vía Láctea.

1 El detector ANTARES

ANTARES está ubicado en las profundidades del mar Mediterráneo a 40 km de la costa, cerca de Toulon, y consiste en 12 líneas con 25 módulos de detección cada una, llamados *storeys* (pisos). Las líneas están sujetas al fondo marino (que se encuentra a 2500 m bajo la superficie) mediante un peso muerto que hace las veces de ancla y se mantienen verticales gracias

a grandes boyas en su parte superior.

La longitud de las líneas es de 450 m con un *storey* cada 14,5 m, estando el primero a 100 m sobre el fondo del mar. La distancia entre las líneas es de unos 60 m en promedio. La parte inferior de las líneas contiene, además del ancla, un módulo denominado *Bottom String Socket* (BSS). Estos módulos conectan las líneas con la *junction box* (JB), una caja de conexión que une al detector con la estación de control, situada en el pueblo costero de La Seyne-Sur-Mer, a través de un cable electro-óptico que suministra energía eléctrica al detector, permite enviarle órdenes y transmite los datos adquiridos por el mismo.

Los *storeys* están formados por una estructura metálica que sirve de sujeción a tres módulos ópticos (OMs), que contienen cada uno de ellos un fotomultiplicador de gran superficie. Cada *storey* consta además de un contenedor de titanio (*Local Control Module*, LCM) que alberga la electrónica encargada de la adquisición de los datos y del control del módulo. En cada *storey* hay, asimismo, un transponder acústico para determinar la posición de las líneas gracias a señales sonoras. Además, cada cinco *storeys* hay un *Optical Beacon* (OB) que emite pulsos de luz visible con el fin de sincronizar los relojes en los módulos ópticos.

La estructura básica de los OMs consiste en un fotomultiplicador del tipo R7081-20 de Hamamatsu contenido en una esfera de vidrio (borosilicato) de 17 pulgadas de diámetro. La esfera tiene un grosor de 1,5 cm y está compuesta por dos semiesferas que se mantienen unidas por la presión del agua circundante. Una descripción técnica del detector se encuentra en la Sección 2.3.

Los neutrinos que cruzan el detector o pasan por sus inmediaciones pueden interactuar con la materia, generando un muon relativista que, al desplazarse con una velocidad mayor que la de la luz en el agua, induce emisión de luz Cherenkov. Algunos de estos fotones Cherenkov son detectados por los OMs y registrados como señales (*hits*) cuya información (amplitud y tiempo de llegada) es utilizada para reconstruir la trayectoria del muon y su energía depositada.

El objetivo de ANTARES es la detección de neutrinos procedentes del espacio exterior, sin embargo, debido a la interacción de los rayos cósmicos con los núcleos de la atmósfera, se producen continuamente una enorme cantidad de muones. Pese a que ANTARES está ubicado a una gran profundidad, estos muones suponen la mayor contribución de fondo para eventos que llegan desde la parte superior del detector. Dado que sólo los neutrinos son capaces de atravesar la Tierra sin interactuar, se utiliza la Tierra como filtro para evitar este fondo de muones atmosféricos. Es decir, en este análisis, sólo se consideran los neutrinos que llegan desde abajo.

2 Datos y simulacion

Las trayectorias de los muones producidos por los neutrinos se reconstruyen a partir de la información proporcionada por los *hits* mediante dos algoritmos diferentes que se denominan AAFit y BBFit.

AAFit es un algoritmo que optimiza una función de verosimilitud para reconstruir la traza del muon, mientras que BBFit minimiza el cuadrado de la distancia entre la posición de los *hits* y su posición esperada (véase la Sección 5.1). Además, cada algoritmo tiene su propia estrategia de selección de los *hits* para ser utilizados en los ajustes.

En AAFit se ejecutan múltiples pasos de reconstrucción comenzando con un ajuste preliminar del tipo χ^2 y acabando con un ajuste de una función de máxima verosimilitud. El ajuste preliminar proporciona un punto de partida para el resto del algoritmo. Este ajuste se repite varias veces para diferentes parámetros de partida (dirección, un punto en la traza y tiempo de paso). De todos ellos se selecciona aquel que proporciona el mejor valor de la función de verosimilitud. El resultado final además de los parámetros de la traza ajustada, suministra una estimación del error angular de la traza, calculado a partir de la matriz de covariancia del ajuste. De los dos algoritmos disponibles, AAFit es el que da la mejor eficiencia de reconstrucción para altas energías.

BBFit es un algoritmo cuyo ajuste es de tipo χ^2 , complementado con ciertos pesos que tienen en cuenta de forma empírica la absorción de la luz en el agua. Se trata de un algoritmo de rápida ejecución en términos de tiempo de cálculo, razón por la cual se utiliza para la reconstrucción preliminar en ANTARES a efectos de pre-selección de sucesos. Además, BBFit permite la reconstrucción de sucesos con *hits* en una sola línea y proporciona la mejor reconstrucción a bajas energías.

Para los análisis que se presentan en esta tesis se han utilizando datos correspondientes a tres periodos. El primero contiene datos desde el año 2007 hasta 2012 y se utiliza para la búsqueda de materia oscura en el Sol. Los otros dos corresponden a periodos que van desde 2007 a 2013 o a 2015, respectivamente, y se han utilizado para la búsqueda de aniquilación de materia oscura en la Vía Láctea. En la tabla 5.1 se presenta una lista más detallada de los periodos de toma de datos.

Los datos se organizan en *runs*, que son secuencias ininterrumpidas de adquisición de datos de una duración entre 2 y 12 horas. Su uso es necesario puesto que las líneas de ANTARES se mueven y las condiciones medioambientales pueden cambiar con el tiempo. Para cada periodo de detección o *run* el posicionamiento del detector se determina de nuevo utilizando el sistema de hidrófonos.

La calidad de los runs no es homogénea y han de excluirse aquellos en los

que las condiciones de detección no son buenas. Para cuantificar la calidad de los datos registrados se utiliza un parámetro llamado calidad básica. Este parámetro tiene un valor de cero para los runs de baja calidad. Los criterios para que un run sea considerado o no de baja calidad imponen condiciones sobre la mínima duración del run, mínimo número de ARSs en funcionamiento y ciertos límites sobre las condiciones de trigger, es decir del algoritmo que activa el proceso de registro de los sucesos.

Cada run de datos tiene su propio run de simulación producido con la condiciones medioambientales correspondientes, en particular las de bioluminiscencia. Estas simulaciones se utilizan para calcular las propiedades del detector relevantes para el análisis, tales como la resolución angular (a través de la llamada *point spread function* o PSF) y el área efectiva. El área efectiva es el área que tendría el detector suponiendo una eficacia de detección de neutrinos del 100% y que diera el mismo número de sucesos detectados. A partir del área efectiva podemos calcular límites al flujo de neutrinos a partir del número de sucesos detectados.

La simulación Monte Carlo de ANTARES se utiliza para producir dos muestras de datos correspondientes a cada uno de los fondos: una para muones atmosféricos y otra para neutrinos atmosféricos. La naturaleza del suceso se guarda asignando un código de simulación diferente para cada tipo de partícula.

La simulación de muones atmosféricos se lleva a cabo utilizando los programas CORSIKA y MUPAGE. MUPAGE genera trazas de muones no reconstruidos. Para ello MUPAGE utiliza una parametrización efectiva obtenida de una muestra de muones generada con CORSIKA, lo que ahorra una gran cantidad de tiempo de cálculo y permite la generación de un mayor número de trazas. MUPAGE limita la simulación a un volumen en torno a ANTARES denominado *can*. Las trazas que no atraviesan este volumen tienen una probabilidad muy baja de que la luz que producen sea detectada en ANTARES, de manera que no se consideran.

Los neutrinos atmosféricos se simulan con un programa llamado GENHEN que simula las interacciones entre núcleos y rayos cósmicos usando el modelo de partones CTEQ6. Los neutrinos producidos en estas interacciones se propagan hasta el detector teniendo en cuenta su absorción en la Tierra y otros efectos. El resultado es un flujo isótropo de muones cuyo espectro energético sigue una ley de potencias.

El siguiente paso consiste en la simulación de la propagación de los muones en el detector y la generación y seguimiento de la luz que producen. Esto se hace con los programas KM3 y MUSIC. MUSIC simula la propagación de los muones, mientras que KM3, que está escrito utilizando GEANT, simula la producción y propagación de la luz en el agua, teniendo en cuenta los fenómenos de absorción y dispersión.

Después de la simulación de la luz Cherenkov de los muones es necesario añadir la luz procedente del fondo óptico medioambiental. Esto se realiza con el programa SeaTray. Este código añade luz Cherenkov procedente de las desintegraciones de ^{40}K y de la bioluminiscencia.

La respuesta de los OMs de ANTARES se calcula con el programa TriggerEfficiency, que también calcula la eficiencia de los distintos *triggers*, es decir de los programas que deciden si ha tenido lugar un suceso y si este merece la pena ser conservado. TriggerEfficiency calcula además otros efectos relacionados con la electrónica del detector.

El último paso es la reconstrucción de los sucesos simulados. Los ficheros finales contienen un suceso por cada traza generada. La probabilidad de que un neutrino produzca un muón o por el contrario se absorba en la Tierra se implementa con pesos estadísticos asociados a los sucesos. Estos vienen dados por el peso w_2 , que se define en eq. 5.8, y el peso w_3 que es el anterior multiplicado por el flujo esperado. El w_2 se utiliza para el cálculo del área efectiva y el w_3 para generar estimaciones del fondo y hacer comparaciones entre simulación y datos reales.

3 Calibración temporal

La reconstrucción de los sucesos está basada en la posición y en el tiempo de los hits producidos por los fotones Cherenkov. Para alcanzar una resolución angular de un 1° o menor es necesario conseguir una precisión en la posición de los fotomultiplicadores de unos 10 cm y una precisión temporal de unos pocos nanosegundos. El conseguir y mantener esta última requiere calibraciones regulares de todos los relojes asociados a los OMs para mantenerlos sincronizados con dicha precisión. Para la calibración de los relojes existen diversos métodos que se detallan en el capítulo 3. Como parte de esta tesis se presentan los resultados de la calibración basada en el uso de las balizas ópticas (u *optical beacons*, OBs).

Cada OB contiene 6 tarjetas electrónicas, en cada una de las cuales hay 6 LEDs en su superficie y uno en su borde superior. Estas tarjetas se disponen en un cono hexagonal que asegura una emisión de luz casi isotropa. Los OBs están instalados en los pisos 2, 9, 15 y 21 de cada línea, con la excepción de la línea 12, que no tiene un OB en el piso 21, por encontrarse en él un sistema experimental de detección acústica. Dentro de los OBs hay un pequeño y rápido PMT que detecta los pulsos de luz emitidos por los LEDs de forma independiente de la electrónica que los controla. Una descripción más detallada del sistema de OBs puede encontrarse en la sec. 3.3.

Los pulsos de luz emitidos por los OB se detectan en los OMs en

diferentes instantes debido al tiempo que la luz necesita para llegar a cada OM. Comparando la distribución de las diferencias entre el tiempo de emisión de la luz y su tiempo de llegada al OM, y sabiendo la distancia recorrida por la luz en el agua, se pueden obtener las constantes de calibración temporal necesarias para sincronizar los relojes de los OMs.

El proceso es algo más complejo de lo previamente descrito debido a ciertos efectos experimentales que es necesario considerar. Por ejemplo, dado que el tiempo de llegada registrado es el de los primeros fotones que alcanzan el OM, estos tiempos varían en función de la cantidad de luz recibida, que a su vez cambia en función de la distancia del OM al OB que emitió el pulso debido a la absorción de la luz en el agua. El proceso de calibración consiste en un ajuste de las distribuciones de los tiempos de llegada de los fotones a cada OM y de su incremento con la distancia, lo que permite obtener a partir de las diferencias entre los tiempos de llegada reales y los esperados las constantes de corrección temporales (*offsets*) o constantes de calibración.

Aunque el proceso de la calibración se puede automatizar, en algunos casos los ajustes no se realizan correctamente, como se explica en la sección 3.5, por lo que se tienen que controlar manualmente. A veces se trata de un fallo en el OM que sólo registra unos pocos hits procedentes del pulso de luz del OB, y no es posible realizar la calibración. Otras veces el ruido electrónico de la luz ambiente causa un fondo tan grande que hace imposible distinguir la señal del pulso impidiendo realizar la calibración. En otros casos los límites del rango del ajuste se han puesto incorrectamente y este no converge o ajusta a un máximo local diferente que se produce por una limitación en la memoria del sistema de la adquisición de datos, por lo que se requiere la repetición del ajuste manualmente.

En total hay 1770 relojes que se han de calibrar de los cuales un 30% requieren una revisión manual. De estos, la mayoría tienen una corrección demasiado grande. Alrededor de unos 80 tienen un ajuste mal ejecutado, de los cuales unos 50 requieren un ajuste manual. Después de la revisión manual, entre 798 y 1059 de los OMs (589 en un caso aislado) se pueden calibrar, lo que representa la mayoría de los OMs activos en cada periodo.

Los resultados están recogidos en la figura 3.9 donde se presenta un histograma de las correcciones para los relojes durante el periodo en el que se ha realizado la calibración como parte de esta tesis (desde 2014 hasta 2015 y algunas de las calibraciones de 2013). Como se puede ver en la figura, el estado de la calibración se ha mantenido estable en este periodo.

4 Materia oscura

La búsqueda de materia oscura es uno de los temas más importantes en la física actual. Hay múltiples evidencias de su existencia a través de sus efectos gravitatorios. En 1932 las medidas de Jan Oort de velocidades de estrellas en la Vía Láctea [20] parecían indicar que debía existir más masa que la que se observaba a través de la luz (aunque posteriormente se determinó que estas medidas no eran conclusivas y quizá fuesen erróneas). Poco tiempo después, en 1933, Fritz Zwicky midió las velocidades de rotación de las galaxias en diversos cúmulos galácticos. Evaluando el teorema del virial para el cúmulo de Coma comprobó que debía de existir una gran cantidad de materia no luminosa. Varias décadas después, la medición por Vera Rubin y William K. Ford de la velocidad de las estrellas en varias decenas de galaxias, entre ellas Andrómeda [21], determinó que efectivamente era necesaria mucha mayor masa que la luminosa para explicar las observaciones. Dada la concentración de la materia luminosa, la velocidad de rotación de las estrellas debería disminuir a partir de una cierta distancia, pero las observaciones indicaban que la distribución de velocidades alcanzaba una meseta, lo que se puede explicar mediante la presencia de materia oscura (las teorías de gravedad modificada son otra alternativa que, sin embargo, se enfrenta a diversos problemas para explicar otras observaciones que exponemos a continuación).

Otra evidencia de la materia oscura es la que se extrae del fondo cósmico de microondas (*Cosmic Microwave Background* o *CMB*). El CMB es la radiación que detectamos actualmente procedente de la radiación térmica que se liberó cuando los electrones y protones formaron átomos de hidrógeno por primera vez, el Universo se volvió neutro y, por tanto, transparente a la radiación (este fenómeno se llama recombinación y tuvo lugar unos cuatrocientos mil años después del Big Bang). El espectro de frecuencias del CMB sigue la ley de Planck para la radiación de un cuerpo negro con una temperatura de 2,73 K. El CMB es casi isótropo, con fluctuaciones de temperatura de apenas unas decenas de microkelvin. Estas fluctuaciones o asimetrías proceden de las diferencias de densidades de materia en el momento de la recombinación. A escalas grandes, las produce el efecto Sachs-Wolfe: en las regiones más densas se emiten fotones de menor energía al tener que superar mayores pozos de potencial, y viceversa. A escalas pequeñas, son debidas a las llamadas oscilaciones acústicas: el fluido de fotones y bariones se comprime por gravedad, luego se expande por presión, lo que hace que disminuya esta y vuelva a comprimirse de nuevo. Dependiendo del momento exacto en el transcurso de este ciclo en el que se emita la radiación, los fotones liberados tendrán mayor o menor energía en cada región del espacio. Las fluctuaciones

de temperatura dependerán por tanto de la cantidad de bariones en el momento de la recombinación. Las medidas realizadas por experimentos como WMAP y Planck permiten obtener la densidad de materia total y la de materia bariónica indicando que esta última es sólo un 15% de la materia total.

La materia oscura también tiene un efecto importante en la formación de las estructuras a gran escala en el Universo. Las fluctuaciones de densidad anteriormente mencionadas hacen las veces de semillas para la formación de estructuras mayores a medida que el Universo se expande. Sin embargo, los cálculos y simulaciones de esa formación indican que las fluctuaciones medidas son insuficientes para explicar las estructuras observadas actualmente y su orden de formación (estrellas, galaxias, cúmulos galácticos, etc.). La materia bariónica no habría tenido tiempo de formarlas desde el momento de la recombinación que es cuando desaparecen las fuerzas electrostáticas y la gravedad puede actuar. Sin embargo, la materia oscura, al ser neutra, podría haber empezado este proceso mucho antes de la recombinación.

Hay más evidencias independientes de la existencia de materia oscura. Por ejemplo, la nucleosíntesis primordial, es decir el periodo (de segundos a minutos después del Big Bang) en que los neutrones y protones se fusionaron para formar deuterio, helio y pequeñas trazas de litio y otros elementos, está determinado por la abundancia relativa de la materia bariónica. Los cálculos coinciden con las observaciones solo si suponemos que la materia bariónica era aproximadamente un 20% de la densidad total de materia durante la nucleosíntesis.

En la sección 4.1 hacemos un resumen de las evidencias más importantes de la existencia de materia oscura.

Todas las evidencias de la existencia de la materia oscura indican su presencia mediante efectos gravitatorios. La gravedad afecta a todas las partículas que tienen masa y opera independientemente de las otras propiedades de las partículas. Sabemos que la materia oscura tiene masa y que no tiene carga eléctrica, porque de tenerla ya la hubiéramos detectado por sus efectos electromagnéticos. Tampoco parece sufrir interacción fuerte con el resto de la materia. Para descubrir el resto de las propiedades y qué tipo de partícula constituye la materia oscura hay tres tipos de experimentos: búsquedas directas, búsquedas indirectas y la producción de materia oscura en aceleradores.

Esta tesis está enfocada a la detección indirecta utilizando neutrinos (un resumen de los otros métodos de búsqueda se recoge en la sección 4.2 de esta memoria). En la detección a través de neutrinos (y también en otros métodos de detección indirecta) se asume que la materia oscura consiste en WIMPs y se acumula en objetos celestes masivos como la Tierra o el

Sol, o está presente como remanentes térmicos en estructuras enormes como la Vía Láctea, galaxias enanas o cúmulos de galaxias. También se asume que las partículas de materia oscura se aniquilan entre sí en estos objetos. Estas aniquilaciones producen partículas del Modelo Estándar que en procesos secundarios dan lugar a neutrinos que pueden detectarse en telescopios de neutrinos. Véase la sección 4.3 para un resumen detallado de las ventajas de las búsquedas indirectas de materia oscura.

Además de ANTARES hay otro telescopio de neutrinos que busca neutrinos procedentes de las aniquilaciones de WIMPs. IceCube utiliza el mismo método que ANTARES para detectar neutrinos. El experimento está en el Polo Sur y utiliza el hielo de la Antártida, en lugar del agua del mar, como medio de detección como ANTARES. Con 86 líneas y un volumen de 1 km^3 es mucho mayor que ANTARES y tiene un área efectiva mayor. No obstante, el hielo causa más dispersión de la luz lo que resulta en una resolución angular peor que la de ANTARES. Además no es posible mirar el hemisferio sur directamente con IceCube, que es algo que sí se puede hacer con ANTARES.

Hay dos aspectos de la materia oscura que son bastante importantes para este tipo de búsquedas: el factor-J y el espectro de la señal de las aniquilaciones. El factor-J es la integral sobre la línea de visión de la densidad de la materia oscura al cuadrado. El factor-J tiene en cuenta la distribución de materia oscura, la intensidad de la señal esperada y la forma de la fuente considerada vista desde el detector. Este factor se necesita para convertir límites (eq. 4.17) y para la simulación de la señal. Los modelos de los halos de materia oscura que se utilizan para calcular los factores-J son: el modelo NFW, que es un perfil que da mucha concentración en el centro del halo donde presenta una singularidad, el modelo de Burkert, que da distribuciones extensas y no tiene ninguna singularidad en el centro, y finalmente, el denominado McMillan, que es muy similar al perfil NFW, pero muestra una mayor extensión.

Los espectros de la señal de materia oscura se calculan con el programa WIMPSIM para el Sol y con el programa de Marco Cirelli para aniquilaciones en el vacío (para la búsqueda en el Centro Galáctico). Ambos programas tienen en cuenta las oscilaciones de neutrinos y la absorción en el medio que atraviesan. Los cálculos asumen una anchura de desintegración del 100% en cada canal del Modelo Estándar considerado para las aniquilaciones. Los canales para el Sol son: $b + \bar{b}$, $W^+ + W^-$, $\tau^+ + \tau^-$, $\mu^+ + \mu^-$ y $\nu + \bar{\nu}$. Los dos últimos no se utilizan para el Sol debido a la absorción de las partículas en el plasma solar.

5 Método de análisis

Nuestro análisis utiliza un método de máxima verosimilitud que se describe en detalle en el capítulo 6. En primer lugar estimamos la sensibilidad de ANTARES utilizando pseudo-experimentos (PEs), que son simulaciones Monte Carlo del conjunto de datos que se usan para el análisis. En los PEs, los sucesos de fondo se simulan con datos blindados¹, la señal se simula con los espectros energéticos que se describen en la sección anterior y la simulación Monte Carlo del detector. Para blindar los datos se mantiene oculto el tiempo de detección de cada suceso, utilizando un tiempo aleatorio según una distribución uniforme.

Después de la simulación de PEs para varias intensidades de la señal se analizan los PEs con la función de verosimilitud que se muestra en la ecuación 6.11. Esta función describe la probabilidad de que una muestra de los datos (bien sea de un PE, bien de los datos desblindados), contenga un número dado, n_s , de sucesos. La función de verosimilitud se maximiza con respecto a n_s para cada PE.

Después de obtener el valor máximo de la función de verosimilitud se calcula un test estadístico (TS). El TS que empleamos es el logaritmo del cociente entre la función de verosimilitud maximizada y el valor de esta misma función para la hipótesis nula o hipótesis de solo fondo ($n_s = 0$). Se crean entonces distribuciones de este TS para cada intensidad de la señal considerada y se comparan estas distribuciones con la mediana de la distribución del TS para una muestra de fondo puro. Un ejemplo de estas distribuciones se puede ver en las figuras 6.14 y 6.15. La intensidad que se define como la sensibilidad del experimento es la intensidad más baja para la cual el 90% de la distribución del TS tenga un valor superior a la mediana del caso de solo fondo. Este procedimiento se repite para cada uno de los canales de aniquilación y para cada masa de WIMP. En el caso de ausencia de señal significativa se obtienen límites superiores que se calculan de forma análoga a la sensibilidad pero utilizando el TS de los datos desblindados en lugar del valor de la mediana del fondo puro.

El análisis se repite para diferentes cortes del parámetro de calidad de la reconstrucción de sucesos. Los cortes finales son aquellos para los cuales se obtienen los mejores valores de la sensibilidad, utilizando siempre una estrategia de datos blindados para evitar el introducir sesgos. La selección de cortes optimizada de esta manera es la que se aplica en el cálculo de límites.

Los límites sobre las secciones eficaces se calculan a partir de la ecuación

¹Empleamos el término "blindar" en esta tesis para denotar que no se utiliza toda la información de los datos para evitar sesgos en el posible descubrimiento de una señal.

4.17 para el Centro Galáctico con los factores de conversión que se presentan en la sección 4.4.2.

6 Resultados

Los resultados para la búsqueda en el Sol se presentan en el capítulo 7. En la figura 7.8 se muestran los límites para la sección eficaz dependiente de espín para los tres canales y su comparación con los límites de otros experimentos. Aunque ANTARES tiene un tamaño muy inferior al de IceCube obtenemos límites del mismo orden de magnitud. Para una explicación de este hecho véase la sección 8.10. Además, para estos resultados no se utiliza la muestra total de datos, sino sólo los datos hasta 2012 puesto que los datos registrados con posterioridad no se habían procesado en el momento de este análisis.

Los experimentos como ANTARES que buscan aniquilación de WIMPs en el Sol obtienen mejores límites en esta sección eficaz que los de búsqueda directa, porque la captura de WIMPs en el Sol es muy sensible a dicha sección eficaz, ya que se produce a través de la dispersión elástica de estos sobre el plasma del Sol, que está principalmente compuesto de protones, siendo por tanto un blanco con una alta densidad de materia con espín.

Para la sección eficaz independiente del espín, que se muestra en la figura 7.9, la situación es la opuesta. La detección directa puede producir los mejores límites en comparación con los límites de ANTARES o IceCube. ANTARES genera límites mejores para masas de WIMP más altas. En este caso los límites de ANTARES se comparan con resultados de IceCube más antiguos y por eso la comparación aparece mejor para ANTARES.

En el capítulo 8 se presentan los resultados para el GC. En la figura 8.6 se muestra la comparación entre los diferentes canales. Como en el caso del Sol, el canal $b + \bar{b}$ proporciona el peor límite de los tres, ya que este canal es el más blando (es decir, se esperan neutrinos con energías menores). Los otros canales producen mejores límites, siendo el más restrictivo el obtenido en el canal $\nu + \bar{\nu}$, mientras que los de $\tau^+ + \tau^-$ y $\mu^+ + \mu^-$ son casi idénticos.

En la figura 8.9 se muestran nuestros resultados comparados con los obtenidos por otros experimentos. En dicha figura solo se incluyen los resultados obtenidos por experimentos de detección indirecta, ya que los de detección directa no generan límites sobre la sección eficaz promediada térmicamente. En comparación con IceCube, los resultados de ANTARES son siempre mejores. Aunque ANTARES tiene un volumen menor que IceCube, este no puede utilizar la Tierra como filtro para observar el Centro Galáctico. Por tanto, tiene que utilizar las líneas exteriores del

detector como veto para excluir muones atmosféricos, lo que implica que su área efectiva sea mucho menor. Eso también excluye neutrinos que producen muones fuera del volumen del detector que después pasan por él. Debido a esto, el volumen de detección se limita a su extensión física. La comparación con los otros experimentos muestra que ANTARES puede conseguir los mejores límites para masas por encima de 3 TeV. Hay que hacer la salvedad de que HESS no utiliza un perfil del halo tan concentrado como el utilizado en ANTARES. Además, los límites de FERMI se han obtenido para una lista de galaxias esféricas enanas. Estas galaxias no tienen incertidumbres en la distribución de materia oscura tan grandes como la Vía Láctea, ya que son completamente visibles sin obstrucciones de nubes de polvo y gas.

En conclusión, los resultados de búsquedas de materia oscura en ANTARES son altamente competitivos respecto a los presentados por otros experimentos, tanto en la búsqueda en el Sol como en la búsqueda en el Centro Galáctico. Con el análisis de futuros datos, los límites de ANTARES podrían ser los mejores de su clase durante mucho tiempo.

List of Figures

2.1	A schematic drawing of the ANTARES detector.	5
2.2	A map showing the position of the ANTARES detector.	6
2.3	Illustration of the detection principle of neutrino telescopes [1].	8
2.4	The visibility of the various places to ANTARES on the celestial sky	9
2.5	A schematic of the storeys and their (optional) parts. . .	11
2.6	A schematic of the optical modules used in ANTARES. . .	12
2.7	A schematic of the Data Acquisition System used in ANTARES [9].	13
2.8	A schematic of the time measurement using the TVC. A TVC ramp is generated in synchronicity with the clock signal to allow a more fine determination of the time within a clock cycle.	15
2.9	An image of one of the ARS.	16
2.10	A schematic of the integration process in the ARS. Three capacitors go simultaneously through the different steps of the integration process. Upon fulfilling the L0 condition one of the capacitors will integrate the PMT signal. . . .	17
2.11	The scattering length for typical Cherenkov light measured at the ANTARES site in [11].	19
2.12	The group refraction index as measured in [12].	20
2.13	Number of events versus the event elevation. For $\theta < 0$ the track is reconstructed as upgoing, for $\theta > 0$ the track is downgoing.	22
2.14	Diagram of the trigger levels used in ANTARES. The higher level triggers described in this sections are constructed using L1, L2 and L3 hits and appear as "Majority Triggers and other Triggers".	23

List of Figures

3.1	The time difference between hits in neighboring OMs. The black line shows a gaussian fit to the data shown in red.	27
3.2	A schematic of the clock system used in ANTARES. . . .	28
3.3	A schematic of the on-shore calibration in the Dark Room	29
3.4	An optical beacon of the ANTARES detector	30
3.5	The results of a toy Monte Carlo simulating the early photon effect. On the left the time delay distributions for different OM-OB distances are shown. On the right the medians of such distributions are plotted versus the OM-OB distance can be seen. [19]	32
3.6	On the left the response of all TVCs to a uniform time signal is shown. On the right an example of the multiple peaks generated by the DNL effect for ARS 1 in floor 12 of line 12 can be seen. [19]	33
3.7	An example of the secondary peak produced by the token ring effect from ARS 0 in the fourth floor of line 4.	34
3.8	An overview of the calibration results for Line 2 from February 2015	37
3.9	The time offsets from the calibrations in 2014 and 2015. The rms of these distributions are listed in table 3.1. . . .	39
4.1	The rotation velocity distribution of stars and interstellar gas in the Messier 31 galaxy as measured by Vera C. Rubin and W. Kent Ford [21].	42
4.2	Temperature map of the cosmic microwave background obtained from Planck data [25]. The small scale temperature fluctuations indicate density fluctuations in the early Universe.	43
4.3	Power spectra of the cosmic microwave background for temperature (TT) and temperature-polarization correlation (TE) obtained from 5 years of WMAP data. [26]	44
4.4	The dark matter density field for different models at a redshift of 1. The colour coding indicates the density. . .	45
4.5	The expected two-point correlation function for galaxies in the current cosmological epoch. Red dots show measurements for model galaxies brighter than $M_k = -23$. Data for the large spectroscopic redshift survey 2dFGRS are shown as blue diamonds [28].	46

4.6	An image of the galaxy cluster 1E0657-558 obtained with the Magellan telescope. The white line indicates 200kpc at the distance of the cluster. The green lines show contours of the mass estimate generated from weak lensing observations [29].	47
4.7	An image of the Bullet cluster. The mass distribution estimated by x-rays is displayed as a red hue, the mass distribution estimated by weak lensing as a blue hue [30].	48
4.8	The current and past (at the time of recombination) energy composition of energy and matter in the Universe according to the WMAP data [31].	50
4.9	Diagram of the different types of dark matter searches and the associated interactions.	52
4.10	The main production channels for neutralinos and charginos in accelerator searches [39]. In both cases the incoming particles are fermions (protons in the case of the LHC) and the outgoing particles are in either case a chargino and the second to lightest neutralino. The second channel with a mediating squark (or slepton) gives the best sensitivity in accelerator searches.	54
4.11	The main decay channels for neutralinos and charginos in accelerator searches [39].	54
4.12	The exclusion limits from the CMS collaboration [43]. The most stringent limits come from a search for three-lepton events with large quantities of missing transversal energies and a left handed slepton mediating the production. The red limit is from a search using a production including a right handed slepton, the green and violet lines come from searches, that use for a specific transversal and longitudinal mass instead of a missing energy. The blue line searches for a production without slepton mediation.	55
4.13	The conversion factors from neutrino fluxes to spin-independent (left) and spin-dependent (right) cross-sections. The upper lines show the results of a conservative calculation that includes gravitational effects from the gas giants and assumes less favorable form factors for the scattering and lower bounds for the abundances of more massive elements like oxygen in the Sun [53].	64

4.14	The integrated J-factor computed for the old NFW profile using CLUMPY versus the opening angle α_{int} of the observation window. The blue line is the smooth part of the halo, the red line shows the contribution from substructures (e.g. dark matter satellites) and green line shows the cross-product of the other contributions. The black line shows the sum of the individual contributions.	67
4.15	The integrated, smooth J-factor computed for the old NFW profile and the other three halo profiles used in this thesis as a function of the opening angle Ψ of the observation window.	68
4.16	The number of neutrinos per WIMP annihilation, as a function of the neutrino energy for the different annihilation channels. These spectra have been calculated for WIMP annihilations in vacuum and a WIMP mass of 1 TeV. The peaks stem from a conversion from a logarithmic to a linear energy axis.	69
4.17	The number of neutrinos per WIMP annihilation, as a function of the neutrino energy for the different annihilation channels. These spectra have been calculated for WIMP annihilations in the Sun and a WIMP mass of 1 TeV. The peaks stem from a conversion from a logarithmic to a linear energy axis.	70
5.1	Flow diagram of the AAFit algorithm.	81
5.2	An image of the event display. Each plot shows the hits on one line. The Y-Axes show the position on the line, the X-axis shows the time at which the hit was recorded. The lines on some of the plots visualise the preliminary fit with BBFit. The left part of the image shows a 3D visualisation of the event [73].	82
5.3	Flow diagram of the Monte Carlo simulation chain.	86
5.4	A schematic of the can used in MUPAGE.	87
5.5	The probability for a neutrino to pass through the Earth as a function of the neutrino energy and the zenith angle. (Equation 5.6)	89
5.6	The number of events as a function of the event reconstruction quality λ for the AAFit algorithm. The events reconstructed in the 2007-2012 period are shown. The histogram shows the background estimate generated by Monte Carlo simulation, the crosses represent the recorded data.	94

5.7	The number of events as a function of the number of lines used in the reconstruction. The events reconstructed in the 2007-2012 period with the AAFit algorithm are shown. The histogram shows the background estimate generated by Monte Carlo simulation, the crosses represent the recorded data.	94
5.8	The number of events as a function of the number of hits used in the reconstruction. The events reconstructed in the 2007-2012 period with the AAFit algorithm are shown. The line shows the background estimate generated from the Monte Carlo simulation, the crosses represent the recorded data.	95
5.9	The number of events as a function of the event elevation. The events reconstructed in the 2007-2012 period with the AAFit algorithm are shown. The line shows the background estimate generated from the Monte Carlo simulation, the crosses represent the recorded data.	95
5.10	The number of events as a function of the event reconstruction quality χ^2 . The events reconstructed in the 2007-2012 period with the BBFit algorithm are shown. The line shows the background estimate generated from the Monte Carlo simulation, the crosses represent the recorded data. . . .	96
5.11	The number of events as a function of the number of lines used in the reconstruction. The events reconstructed in the 2007-2012 period with the BBFit algorithm are shown. The line shows the background estimate generated from the Monte Carlo simulation, the crosses represent the recorded data.	96
5.12	The number of events as a function of the number of hits used in the reconstruction. The events reconstructed in the 2007-2012 period with the BBFit algorithm are shown. The line shows the background estimate generated from the Monte Carlo simulation, the crosses represent the recorded data.	97
5.13	The number of events as a function of the event elevation. The events reconstructed in the 2007-2012 period with the BBFit algorithm are shown. The line shows the background estimate generated from the Monte Carlo simulation, the crosses represent the recorded data.	97
5.14	Effective area as a function of the quality cut and the neutrino energy for signals from the Galactic Centre. The AAFit reconstruction strategy has been used.	100

5.15	Effective area as a function of the quality cut and the neutrino energy for signals from the Galactic Centre. This effective area is produced for BBFit single line events. . .	101
5.16	Diagram of the calculation process of the acceptance. . .	102
6.1	Diagram of the likelihood-based analysis procedure for dark matter searches.	104
6.2	A schematic of the celestial coordinate system used in the analysis.	105
6.3	Thermally averaged annihilation cross-section sensitivities for the 2007-2012 AAFit data for a search in the GC [85]. Results using the number of hits (energy information) and β in the likelihood and those not using these parameters are shown.	109
6.4	Distribution of the number of hits and the angular error estimate β for the background for the AAFit data with a quality cut of $\lambda > -5.6$	111
6.5	Distribution of the number of hits and the angular error estimate β for the expected signal for the $\tau^+\tau^-$ annihilation channel and a wimp mass of 5 TeV. The AAFit reconstruction algorithm and a quality cut of $\lambda > -5.6$ is used.	112
6.6	Example of the signal ingredient for the angular separation between event and the centre of the GC for the AAFit data with a quality cut of $\lambda > -5.2$. A WIMP mass of 1 TeV has been used.	113
6.7	Point spread function for the AAFit reconstructed data with a quality cut of $\lambda > -5.2$ for the GC. A WIMP mass of 1 TeV has been used.	114
6.8	Background ingredient for the event declination for the AAFit data with a quality $\lambda > -5.2$. The ingredient is normalised over the solid angle to one.	115
6.9	The angle between the original neutrino and the produced muon (white) and the change of muon direction due to scattering in water before entering the can (red) for different neutrino energies [71].	116
6.10	The median angular error as a function of the WIMP mass for the AAFit reconstructed data with a quality cut of $\lambda > -5.4$ and the BBFit multi-line data using a quality cut of $\chi^2 < 1.3$ for the different annihilation channels for the Sun.	117

6.11	The acceptance versus the reconstruction quality parameter λ for the AAFit reconstruction. A WIMP mass of 1 TeV and a cut on the angular error estimate of $\beta < 1$ degree have been used. The colour coding indicates the annihilation channel: blue: W^+W^- red: $\tau^+\tau^-$ green: $b\bar{b}$	118
6.12	Diagram of the process to obtain sensitivities and limits.	118
6.13	Distributions of the optimum n_s for different numbers of inserted signal events. These distributions were made for the AAFit strategy using a λ cut of -5.4 , a WIMP mass of 1 TeV and for the W^+W^- annihilation channel. The PEs were simulated for the Sun.	120
6.14	The TS distributions for several numbers of inserted signal events. This distribution was made for the AAFit strategy using a λ cut of -5.4 , a WIMP mass of 1 TeV and for the W^+W^- annihilation channel. The PE were simulated for the Sun.	121
6.15	Distributions of x for different average numbers of inserted signal events. This distribution was made for the AAFit strategy using a λ cut of -5.4 , a WIMP mass of 1 TeV and for the W^+W^- annihilation channel.	122
6.16	Fraction of time the Sun spends in each position on the local sky below the horizon. θ is the zenith of the local coordinate system of ANTARES. ϕ is the azimuth shifted by 90° . North is at $\phi = 90^\circ$, South at $\phi = 270^\circ$ and East at $\phi = 0^\circ$. The plot was produced for the data taking periods from 2007 to 2012 described in section 5.2.	123
6.17	The background ingredient for the AAFit reconstruction with a quality cut of $\lambda > -5.6$ used for the generation of background events.	125
6.18	The ingredient for the angular separation of the event to the Sun. AAFit data with $\lambda > -5.6$ was used for the generation of background events.	126
6.19	J-Factor, normalised to one, as a function of the angular separation from the GC, Ψ , multiplied by the solid angle element, $d\Omega$	127
6.20	The effective PSF, i.e. a PSF that also takes the source morphology into account, for the Galactic Centre using the NFW halo profile. The colour coding indicates the annihilation channel used.	128

7.1	A comparison of the distribution of the angular distance of the reconstructed muon track to the source for the background estimate (histogram) and the data (crosses) for AAFit events. A quality cut of $\lambda > -5.4$ has been used. The error bars on the data are statistical errors only. . . .	132
7.2	A comparison of the distribution of the angular distance of the reconstructed muon track to the source for the background estimate (histogram) and the data (crosses) for BBFit multi-line events. A quality cut of $\chi^2 < 1.4$ has been used. The error bars on the data are statistical errors only.	133
7.3	A comparison of the distribution of the difference in zenith of the reconstructed muon track and the source for the background estimate (histogram) and the data (crosses) for BBFit single-line events. A quality cut of $\chi^2 < 0.8$ has been used. The error bars on the data are statistical errors only.	134
7.4	90% confidence level limits on the number of detected events as a function of the WIMP mass for the different reconstruction strategies and annihilation channels considered in this analysis. The quality cuts used for these plots are those obtained from the optimisation of the sensitivity. . .	136
7.5	The acceptance as a function of the WIMP mass for the different reconstruction strategies and annihilation channels. The quality cuts used for these plots are those obtained from the optimisation of the sensitivity.	137
7.6	90% C.L. limits on the signal neutrino flux from WIMP annihilations in the Sun as a function of the WIMP mass. This plot shows the combined results for the AAFit events and the BBFit multi- and single-line events. Limits for all the annihilation channels considered are shown.	138
7.7	90% C.L. limits on the spin-dependent scattering cross-section for the Sun. The colour-coding shows the annihilation channel; The dotted lines show the limits obtained with the previous “binned method” using data from 2007 to 2008 [83]; the dashed lines show the limits using this same binned method but for the larger data sample from the years 2007-2012 [90] and, finally, the solid lines show the limits obtained by the unbinned method and the 2007-2012 data sample presented in this thesis.	140

7.8	90% C.L. limits on the spin-dependent WIMP–nucleon scattering cross-section as a function of WIMP mass for the $b\bar{b}$ (green), $\tau^+\tau^-$ (red) and W^+W^- (blue) channels. Limits given by other experiments are also shown: IceCube [91], PICO-60 [34], PICO-2L [35], SuperK [92] and XENON100 [93].	142
7.9	90% C.L. limits on the spin-independent WIMP–nucleon scattering cross-section as a function of WIMP mass for the $b\bar{b}$ (green), $\tau^+\tau^-$ (red) and W^+W^- (blue) channels. Limits given by other experiments are also shown: IceCube [94], SuperK [92], LUX [33] and XENON100 [95].	143
8.1	Number of events as a function of the distance to the source (crosses) in comparison to the background estimate (red histogram). In this plot a quality cut of $\lambda > -5.2$ was used.	147
8.2	TS distributions for different average numbers of events for a WIMP mass of 1 TeV and the $\tau^+\tau^-$ channel. The black dashed line marks the median of the background TS distribution, the red dashed line marks the TS value of the unblinded data.	148
8.3	Sensitivities on the number of detected neutrino events for the different reconstruction strategies and annihilation channels. The quality cuts used for these plots are the optimised cuts from the calculation of the sensitivity for BBFit and $\lambda < -5.2$ for AAFit. For these sensitivities the NFW profile was used.	149
8.4	The neutrino signal acceptance for the different reconstruction strategies and annihilation channels. The quality cuts used for these plots are the optimised cuts from the calculation of the sensitivity.	150
8.5	90% C.L. upper limits on the neutrino flux from WIMP annihilations in the Milky Way as a function of the WIMP masses for the different channels considered. In this plot the NFW profile was used.	151
8.6	Sensitivities for the thermally averaged annihilation cross-section $\langle\sigma v\rangle$ as a function of the WIMP mass. The sensitivities in this plot were calculated for the NFW profile.	153
8.7	Sensitivities on the thermally averaged annihilation cross-section $\langle\sigma v\rangle$ as a function of the WIMP mass for the three Halo models considered for the $\tau^+\tau^-$ annihilation channel.	154

8.8	Sensitivities for the thermally-averaged annihilation cross-section $\langle\sigma v\rangle$ for different analyses of the ANTARES data. The sensitivities in this plot were calculated for the NFW profile. The limits for the 2013 and 2015 analyses use the new parameters from [61] and the binned limits are taken from [98] and use the old set of halo parameters. The irregular behaviour of the binned analysis is due to the fact that limits (not sensitivities) are shown.	156
8.9	Limits on the thermally averaged annihilation cross-section $\langle\sigma v\rangle$. The limits for the IceCube experiment [99, 103] were calculated using the NFW profile. The results of FERMI [104], HESS [105] and MAGIC [106] are also shown.	157
1	Distribution of the number of events as a function of the event reconstruction quality λ for the AAFit algorithm. The events reconstructed in the 2007-20125 period are shown. The histogram shows the background estimate generated by Monte Carlo simulation, the crosses represent the recorded data.	161
2	Distribution of the number of events as a function of the number of hits used in the reconstruction. The events reconstructed with the AAFit algorithm in the 2007-2015 period are shown. The line shows the background estimate generated from the Monte Carlo simulation, the crosses represent the recorded data.	162
3	Distribution of the number of events as a function of the event elevation. The events reconstructed with the AAFit algorithm in the 2007-2015 period are shown. The line shows the background estimate generated from the Monte Carlo simulation, the crosses represent the recorded data.	162
4	Distribution of the number of events as a function of the event reconstruction quality χ^2 for the BBFit algorithm. The single-line events reconstructed in the 2007-2015 period are shown. The histogram shows the background estimate generated by Monte Carlo simulation, the crosses represent the recorded data.	163
5	Distribution of the number of events as a function of the number of hits used in the reconstruction. The single-line events reconstructed with the BBFit algorithm in the 2007-2015 period are shown. The line shows the background estimate generated from the Monte Carlo simulation, the crosses represent the recorded data.	163

6 Distribution of the number of events as a function of the event elevation. The events single-line reconstructed with the BBfit algorithm in the 2007-2015 period are shown. The line shows the background estimate generated from the Monte Carlo simulation, the crosses represent the recorded data. 164

List of Tables

2.1	The absorption length and effective scattering length measured in [11, 15]	19
3.1	The results of the LED OB calibrations in 2014 and 2015.	38
4.1	Table of dark matter halo parameters for the Milky Way.	67
4.2	Table of particles in the MSSM	76
5.1	Table of the data used in the dark matter analyses	84
7.1	The final data selection criteria for which the optimal cross-section sensitivity is obtained.	135
1	The limits in terms of neutrino flux, spin dependent and spin independent cross-section versus the annihilation channel and wimp mass.	165
2	The continuation to table 1.	166
3	The limits in terms the thermally averaged annihilation cross-section versus the wimp mass for the NFW halo profile.	167

Bibliography

- [1] M. Ageron et al. ANTARES: The first undersea neutrino telescope. Nuclear Instruments and Methods in Physics Research Section A: Accelerators, Spectrometers, Detectors and Associated Equipment, 656(1):11–38, 2011.
- [2] B. T. Cleveland et al. Measurement of the solar electron-neutrino flux with the homestake chlorine detector. The Astrophysical Journal, 496(1):505–526, 1998.
- [3] ANTARES Collaboration, S. Adrian-Martinez et al. The positioning system of the ANTARES Neutrino Telescope. Journal of Instrumentation, 7(08):T08002, 2012.
- [4] ANTARES Collaboration, P. Amram et al. Sedimentation and Fouling of Optical Surfaces at the ANTARES Site. Astroparticle Physics, 19(2):253–267, 2003.
- [5] ANTARES Collaboration, J.A. Aguilar et al. AMADEUS — The acoustic neutrino detection test system of the ANTARES deep-sea neutrino telescope. Nuclear Instruments and Methods in Physics Research Section A: Accelerators, Spectrometers, Detectors and Associated Equipment, 626-627:128–143, 2011.
- [6] ANTARES Collaboration, J.A. Aguilar et al. First results of the Instrumentation Line for the deep-sea ANTARES neutrino telescope. Astroparticle Physics, 26(4–5):314–324, 2006.
- [7] ANTARES Collaboration, P. Amram et al. The ANTARES Optical Module. Nuclear Instruments and Methods in Physics Research Section A: Accelerators, Spectrometers, Detectors and Associated Equipment, 484(1–3):369 – 383, 2002.
- [8] ANTARES Collaboration, J.A. Aguilar et al. Study of large hemispherical photomultiplier tubes for the ANTARES neutrino telescope.

- Nuclear Instruments and Methods in Physics Research Section A: Accelerators, Spectrometers, Detectors and Associated Equipment, 555(1-2):132–141, 2005.
- [9] J.A. Aguilar et al., ANTARES Collaboration. The data acquisition system for the ANTARES neutrino telescope. Nuclear Instruments and Methods in Physics Research Section A: Accelerators, Spectrometers, Detectors and Associated Equipment, 570(1):107–116, 2007.
- [10] ANTARES Collaboration, J.A. Aguilar et al. Transmission of light in deep sea water at the site of the ANTARES neutrino telescope. Astroparticle Physics, 23(1):131 – 155, 2005.
- [11] ANTARES Collaboration, J.A. Aguilar et al. Transmission of light in deep sea water at the site of the ANTARES neutrino telescope. Astroparticle Physics, 26(1):131–155, 2005.
- [12] ANTARES Collaboration, S. Adrian-Martinez et al. Measurement of the group velocity of light in sea water at the ANTARES site. Astroparticle Physics, 35(9):552–557, 2012.
- [13] H. Yepes–Ramírez for the ANTARES collaboration. Water absorption length measurement with the ANTARES optical beacon system. Nuclear Instruments and Methods in Physics Research Section A: Accelerators, Spectrometers, Detectors and Associated Equipment, 626-627, Supplement:S118–S119, 2011.
- [14] ANTARES Collaboration, M. Ageron et al. Studies of a full-scale mechanical prototype line for the ANTARES neutrino telescope and tests of a prototype instrument for deep-sea acoustic measurements. Nuclear Instruments and Methods in Physics Research Section A: Accelerators, Spectrometers, Detectors and Associated Equipment, 581(3):695–708, 2007.
- [15] H. Yepes-Ramírez. Characterization of the optical properties at the ANTARES site using the Optical Beacon system. Influence on the detector performance. PhD thesis, Universidad de Valencia, 2014.
- [16] ANTARES Collaboration, J.A. Aguilar et al. Time calibration of the ANTARES neutrino telescope. Astroparticle Physics, 34(7):539–549, 2011.
- [17] Juan Pablo Gomez Gonzales. Time calibration and search for cosmic sources of high energy neutrinos with the ANTARES neutrino telescope. PhD thesis, Universidad de Valencia, 2013.

-
- [18] ANTARES Collaboration, S. Adrian-Martinez et al. Time calibration with atmospheric muon tracks in the ANTARES neutrino telescope. Astroparticle Physics, 78:43–51, 2016.
- [19] Agustín Sánchez Losa. Search for high energy cosmic muon neutrinos from variable gamma-ray sources and time calibration of the optical modules of the ANTARES telescope. PhD thesis, Universidad de Valencia, 2015.
- [20] J. H. Oort. The force exerted by the stellar system in the direction perpendicular to the galactic plane and some related problems. Bulletin of the astronomical institutes of the Netherlands, 6(238):249, 1932.
- [21] V. C. Rubin, W.K. Ford Jr. Rotation of the Andromeda Nebula from a spectroscopic survey of emission regions. The Astrophysical Journal, 159:379–403, 1970.
- [22] M. Milgrom. Dynamics with a Nonstandard Inertia-Acceleration Relation: An Alternative to Dark Matter in Galactic Systems. Annals of Physics, 229(2):384–415, February 1994.
- [23] R.W. Wilson. The cosmic microwave background radiation. Nobel lecture, 1978.
- [24] R.A. Alpher, R.C. Herman. On the Relative Abundance of the Elements. Physical Review, 74(12):1737–1742, 1948.
- [25] J. Bobin, F. Sureau, J-L Starck. CMB reconstruction from the WMAP and Planck PR2 data. Astronomy and Astrophysics, 591(A50), 2016.
- [26] G. Hinshaw et al. Five-Year Wilkinson Microwave Anisotropy Probe Observations: Data Processing, Sky Maps, and Basic Results. The Astrophysical Journal Supplement Series, 180(2):225, 2009.
- [27] Planck Collaboration: P. A. R. Ade et al. Planck 2015 results. XIII. Cosmological parameters. Astronomy and Astrophysics, 594(A13):63, 2015.
- [28] Volker Springel et al. Simulating the joint evolution of quasars, galaxies and their large-scale distribution. Nature, 435(1):629–636, 2005.
- [29] D. Clowe et al. A direct empirical proof of the existence of dark matter. The Astrophysical Journal Letters, 648(2):L109, 2006.

- [30] J. R. Brownstein, J. W. Moffat. The Bullet Cluster 1E0657-558 evidence shows Modified Gravity in the absence of Dark Matter. Monthly Notices of the Royal Astronomical Society, 382(1):29–47, 2007.
- [31] www.nasa.gov.
- [32] XENON100 Collaboration, E. Aprile et al. First Dark Matter Results from the XENON100 Experiment. Physical Review Letters, 105(13):131302, 2010.
- [33] LUX Collaboration, D. S. Akerib et al. First results from the LUX dark matter experiment at the Sanford Underground Research Facility. Physical Review Letters, 112(9):091303, 2014.
- [34] PICO Collaboration, C. Amole et al. Dark Matter Search Results from the PICO-60 CF3I Bubble Chamber. Physical Review D: Particles and Fields, 93(5):052014, 2016.
- [35] PICO Collaboration, C. Amole et al. Improved Dark Matter Search Results from PICO-2L Run-2. Physical Review D: Particles and Fields, 93(6):061101, 2016.
- [36] G. Angloher et al. Results on light dark matter particles with a low-threshold CRESST-II detector. The European Physical Journal C, 76(1):25, 2016.
- [37] SuperCDMS Collaboration, R. Agnese et al. New Results from the Search for Low-Mass Weakly Interacting Massive Particles with the CDMS Low Ionization Threshold Experiment. Physical Review Letters, 116(7):071301, 2016.
- [38] EDELWEISS collaboration, E. Armengaud et al. Constraints on low-mass WIMPs from the EDELWEISS-III dark matter search. Journal of Cosmology and Astroparticle Physics, 2016(05):019, 2016.
- [39] A. Bharucha, S. Heinemeyer, F. von der Pahlen. Direct Chargino-Neutralino Production at the LHC: Interpreting the Exclusion Limits in the Complex MSSM. The European Physical Journal C, 73(11):2629, 2013.
- [40] ATLAS Collaboration, G. Aad et al. The ATLAS Experiment at the CERN Large Hadron Collider. Journal of Instrumentation, 3(08):S08003, 2008.

-
- [41] CMS Collaboration, S. Chatrchyan et al. The CMS experiment at the CERN LHC. Journal of Instrumentation, 3(08):S08004, 2008.
- [42] L. Evans, P. Bryant. LHC Machine. Journal of Instrumentation, 3(08):S08001, 2008.
- [43] CMS Collaboration, S. Chatrchyan et al. Search for electroweak production of charginos and neutralinos using leptonic final states in pp collisions at $\sqrt{s} = 7$ TeV. Journal of High Energy Physics, 2012(11):147, 2012.
- [44] ATLAS Collaboration, G. Aad et al. Search for direct production of charginos and neutralinos in events with three leptons and missing transverse momentum in $\sqrt{s} = 7$ TeV pp collisions with the ATLAS detector. Physics Letters B, 718(3):841–859, 2013.
- [45] The HESS Collaboration, A. Abramowski et al. Constraints on an Annihilation Signal from a Core of Constant Dark Matter Density around the Milky Way Center with H.E.S.S. Physical Review Letters, 114(8):081301, 2015.
- [46] MAGIC Collaboration, J. Aleksić et al. Searches for Dark Matter annihilation signatures in the Segue 1 satellite galaxy with the MAGIC-I telescope. Journal of Cosmology and Astroparticle Physics, 2011(06):035, 2011.
- [47] W.B. Artwood et. al. The Large Area Telescope on the Fermi Gamma-ray Space Telescope Mission. The Astrophysical Journal, 697(2):1071, 2009.
- [48] W.B. Artwood et. al. Design and Initial Tests of the Tracker-Converter of the Gamma-ray Large Area Space Telescope. Astroparticle Physics, 28(4-5):422–434, 2007.
- [49] L. Feng, R. Yang, H. He, T. Dong, Y. Fan, J. Chang. AMS-02 positron excess: New bounds on dark matter models and hint for primary electron spectrum hardening. Physics Letters B, 728:250–255, 2014.
- [50] S. Adrián-Martínez et. al. Letter of Intent for KM3NeT 2.0. Journal of Physics G: Nuclear and Particle Physics, 43(8):084001, 2016.
- [51] IceCube-Gen2 Collaboration. IceCube-Gen2: A Vision for the Future of Neutrino Astronomy in Antarctica. arXiv:1412.5106v2, 2014.

Bibliography

- [52] K. Abe et. al. Letter of Intent: The Hyper-Kamiokande Experiment — Detector Design and Physics Potential —. [arXiv:1109.3262v1](#), 2011.
- [53] G. Wikström, J. Edsjö. Limits on the WIMP-nucleon scattering cross-section from neutrino telescopes. [Journal of Cosmology and Astroparticle Physics](#), 2009(04):009, 2009.
- [54] A. Gould. Cosmological Density of WIMPS from Solar and Terrestrial Annihilations. [Astrophysics Journal](#), 388(1):338–344, 1992.
- [55] G. Jungman et al. Supersymmetric dark matter. [Physics Reports](#), 267(5):195–373, 1996.
- [56] J. F. Navarro, C. S. Frenck, S. D. M. White. The Structure of Cold Dark Matter Halos. [Astrophysical Journal](#), 462(1):563–575, 1996.
- [57] J. An, H. Zhao. Fitting functions for dark matter density profiles. [Monthly Notices of the Royal Astronomical Society](#), 428(1):2805–2811, 2013.
- [58] Paul J. McMillan. The mass distribution and gravitational potential of the Milky Way. [Monthly Notices of the Royal Astronomical Society](#), 465(1):76–94, 2016.
- [59] A. Burkert; J. Silk. On the structure and nature of dark matter halos. [Proceedings of the second international conference on “Dark matter in astro and particle physics”](#), 1999.
- [60] A. Charbonnier, C. Combet, D. Maurin. CLUMPY: A code for γ -ray signals from dark matter structures. [Computer Physics Communications](#), 183(3):656–668, 2012.
- [61] F. Nesti, P. Salucci. The Dark Matter halo of the Milky Way, AD 2013. [Journal of Cosmology and Astroparticle Physics](#), 2013(07):016, 2013.
- [62] ANTARES Collaboration, S. Adrian-Martinez et al. Search of Dark Matter Annihilation in the Galactic Centre using the ANTARES Neutrino Telescope. [Journal of Cosmology and Astroparticle Physics](#), 2015(10):068, 2015.
- [63] M. Cirelli et al. PPC 4 DM ID: A Poor Particle Physicist Cookbook for Dark Matter Indirect Detection. [Journal of Cosmology and Astroparticle Physics](#), Erratum: [JCAP 1210 \(2012\) E01.](#), 2011(03):051, 2012.

-
- [64] M. Cirelli et al. Erratum: PPPC 4 DM ID: a poor particle physicist cookbook for dark matter indirect detection. Journal of Cosmology and Astroparticle Physics, 2012(10):E01, 2012.
- [65] M. Blennow, J. Edsjo, T. Ohlsson. Neutrinos from WIMP Annihilations obtained using a Full Three-Flavor Monte Carlo Approach. Journal of Cosmology and Astroparticle Physics, 2008(01):021, 2008.
- [66] C. Giunti, C. W. Kim. Fundamentals of Neutrino Physics and Astrophysics. Oxford University Press, 2007.
- [67] L. Wolfenstein. Neutrino oscillations in matter. Physical Review D: Particles and Fields, 17(9):2369–2374, 1978.
- [68] M. Drees, R. M. Godbole, P. Roy. Theory and phenomenology of sparticles. World Scientific, 2004.
- [69] Joakim Edsjo. Aspects of neutrino detection of neutralino dark matter. PhD thesis, Uppsala University, 1997.
- [70] Manuel Drees, Mihoko M. Nojiri, D.P. Roy, Y. Yamada. Light Higgsino Dark Matter. Physical Review D: Particles and Fields, 56(1):276–290, 1997.
- [71] Adriaan Jacob Heijboer. Track Reconstruction and Point Source Searches with ANTARES. PhD thesis, Universiteit van Amsterdam, 2004.
- [72] ANTARES Collaboration, J.A. Aguilar et al. A fast algorithm for muon track reconstruction and its application to the ANTARES neutrino telescope. Astroparticle Physics, 34(9):652–662, 2011.
- [73] <http://www.pi1.physik.uni-erlangen.de/antares/online-display/online-display.php>.
- [74] G. Carminati, M. Bazzotti, A. Margiotta, M. Spurio. Atmospheric MUons from PArametric formulas: a fast GEnerator for neutrino telescopes (MUPAGE). Computer Physics Communications, 179(12):915 – 923, 2008.
- [75] G. Carminati, M. Bazzotti, A. Margiotta, M. Spurio. An update of the generator of atmospheric muons from parametric formulas (MUPAGE). Computer Physics Communications, 181(4):835 – 836, 2010.

- [76] D. Heck, J. Knapp, J.N. Capdevielle, G. Schatz, and T. Thouw. CORSIKA: A Monte Carlo code to simulate extensive air showers. Forschungszentrum Karlsruhe Report, FZKA 6019, 1998.
- [77] D. Heck, J. Knapp. Upgrade of the Monte Carlo code CORSIKA to simulate extensive air showers with energies $> 10^{20}$ eV. Forschungszentrum Karlsruhe Report, FZKA 6097, 1998.
- [78] P. Antonioli et al. Three-Dimensional Code for Muon Propagation through the Rock: MUSIC. Astroparticle Physics, 7(4):357–368, 1997.
- [79] J. Brunner. ANTARES Simulation Tools. In Proceedings of the VLVnT Workshop 2003, Amsterdam, the Netherlands, 109, 2003.
- [80] J. Pumplin, D. R. Stump, J. Huston, H. L. Lai, P. Nadolsky, and W. K. Tung. New Generation of Parton Distributions with Uncertainties from Global QCD Analysis. Journal of High Energy Physics, 2002(07):012, 2002.
- [81] A. Margiotta. Common simulation tools for large volume detectors. Nuclear Instruments and Methods in Physics Research Section A: Accelerators, Spectrometers, Detectors and Associated Equipment, 725(53):98–101, 2013.
- [82] S. Agostinelli et al. Geant4—a simulation toolkit. Nuclear Instruments and Methods in Physics Research Section A: Accelerators, Spectrometers, Detectors and Associated Equipment, 506(3):250–303, 2003.
- [83] ANTARES Collaboration, S. Adrian-Martinez et al. First results on dark matter annihilation in the Sun using the ANTARES neutrino telescope. Journal of Cosmology and Astroparticle Physics, 2013(11):032, 2013.
- [84] R. Barlow. Extended maximum likelihood. Nuclear Instruments and Methods in Physics Research Section A: Accelerators, Spectrometers, Detectors and Associated Equipment, 297(3):496–506, 1990.
- [85] F. Havelock. A Combined Analysis of Data from ANTARES and other Neutrino Telescopes in the Search for Dark Matter. Master’s thesis, Imperial College London, Universidad de Valencia, 2016.

-
- [86] G.C. Hill, K. Rawlins. Unbiased cut selection for optimal upper limits in neutrino detectors: the model rejection potential technique. Astroparticle Physics, 19(3):393 – 402, 2003.
- [87] J.Neyman. A Selection of Early Statistical Papers on J. Neyman. Phil. Trans. Royal Soc. London Series A., 236:250, 1937.
- [88] S.S. Wilks. The Large-Sample Distribution of the Likelihood Ratio for Testing Composite Hypotheses. The Annals of Mathematical Statistics, 9(1):60–62, 1938.
- [89] W. H. Press and D. N. Spergel. Capture by the sun of a galactic population of weakly interacting, massive particles. The Astrophysical Journal, 296(1):679–684, 1985.
- [90] G. Lambard on behalf of the ANTARES collaboration. Indirect searches for dark matter with the ANTARES neutrino telescope. In Proceedings, 21st International Europhysics Conference on High energy physics (EPS-HEP 2011): Grenoble, France, July 21-27, 2011, volume EPS-HEP2011, page 064, 2011.
- [91] IceCube Collaboration, M.G. Aartsen et al. Improved limits on dark matter annihilation in the Sun with the 79-string IceCube detector and implications for supersymmetry. Journal of Cosmology and Astroparticle Physics, 1604(04):022, 2016.
- [92] Super-Kamiokande Collaboration, K. Choi et al. Search for Neutrinos from Annihilation of Captured Low-Mass Dark Matter Particles in the Sun by Super-Kamiokande. Physical Review Letters, 114(14):141301, 2015.
- [93] XENON100 Collaboration, E. Aprile et al. Limits on spin-dependent WIMP-nucleon cross sections from 225 live days of XENON100 data. Physical Review Letters, 111(2):021301, 2013.
- [94] IceCube Collaboration, M.G. Aartsen et al. Search for dark matter annihilations in the Sun with the 79-string IceCube detector. Physical Review Letters, 110(13):131302, 2013.
- [95] XENON100 Collaboration, E. Aprile et al. Dark Matter Search Results from 225 Live Days of XENON100 Data. Physical Review Letters, 109(12):181301, 2012.
- [96] ANTARES Collaboration, S. Adrian-Martinez et al. The first combined search for neutrino point-sources in the southern hemi-

- sphere with the ANTARES and IceCube neutrino telescopes. The Astrophysical Journal, 823(1):65, 2016.
- [97] ANTARES Collaboration, S. Adrian-Martinez et al. Search for Cosmic Neutrino Point Sources with Four Years of Data from the ANTARES Telescope. The Astrophysical Journal, 760(1):53, 2012.
- [98] ANTARES Collaboration, S. Adrian-Martinez et al. Search of dark matter annihilation in the galactic centre using the ANTARES neutrino telescope. Journal of Cosmology and Astroparticle Physics, 2015(10):068, 2015.
- [99] IceCube Collaboration, M.G. Aartsen et al. All-flavour Search for Neutrinos from Dark Matter Annihilations in the Milky Way with IceCube/DeepCore. The European Physical Journal C, 76(10):531, 2016.
- [100] K. Griest, M Kamionkowski. Unitarity Limits on the Mass and Radius of Dark-Matter Particles. Physical Review Letters, 64(6):615–618, 1990.
- [101] S. Profumo. TeV γ -rays and the largest masses and annihilation cross sections of neutralino dark matter. Physical Review D: Particles and Fields, 72(1):103521, 2005.
- [102] M. Chianese, G. Miele, S. Morisi. Dark Matter interpretation of low energy IceCube MESE excess. Journal of Cosmology and Astroparticle Physics, 2017(01):007, 2017.
- [103] IceCube Collaboration, M.G. Aartsen et al. Search for Dark Matter Annihilation in the Galactic Center with IceCube-79. The European Physical Journal C, 75(10):492, 2015.
- [104] FERMI-LAT Collaboration, M. Ackermann et al. Searching for Dark Matter Annihilation from Milky Way Dwarf Spheroidal Galaxies with Six Years of Fermi Large Area Telescope Data. Physics Review Letters, 115(23):231301, 2015.
- [105] H. Abdallah et al., HESS Collaboration. Search for dark matter annihilations towards the inner Galactic halo from 10 years of observations with H.E.S.S. Physical Review Letters, 117(11):111301, 2016.
- [106] R. Caputo, M. R. Buckley, P. Martin, E. Charles, A. M. Brooks, A. Drlica-Wagner, J. M. Gaskins, M. Wood. Search for Gamma-ray

Emission from Dark Matter Annihilation in the Small Magellanic Cloud with the Fermi Large Area Telescope. Physical Review D: Particles and Fields, 93(6):062004, 2016.